



## Durham E-Theses

---

### *NMR studies of water-soluble Dyes*

Birkett, Helen Elizabeth

#### How to cite:

---

Birkett, Helen Elizabeth (2000) *NMR studies of water-soluble Dyes*, Durham theses, Durham University. Available at Durham E-Theses Online: <http://etheses.dur.ac.uk/4286/>

#### Use policy

---

The full-text may be used and/or reproduced, and given to third parties in any format or medium, without prior permission or charge, for personal research or study, educational, or not-for-profit purposes provided that:

- a full bibliographic reference is made to the original source
- a [link](#) is made to the metadata record in Durham E-Theses
- the full-text is not changed in any way

The full-text must not be sold in any format or medium without the formal permission of the copyright holders.

Please consult the [full Durham E-Theses policy](#) for further details.

# NMR Studies of Water-soluble Dyes

The copyright of this thesis rests with the author. No quotation from it should be published in any form, including Electronic and the Internet, without the author's prior written consent. All information derived from this thesis must be acknowledged appropriately.

by

Helen Elizabeth Birkett B.Sc.(Hons. Dunelm)

Collingwood College

University of Durham

*A thesis submitted in partial fulfilment of the requirements for the degree of  
Doctor of Philosophy*

Department of Chemistry

University of Durham

2000



19 JUN 2001

# NMR Studies of Water-soluble Dyes

Helen E. Birkett B.Sc.(Hons.)

Submitted for the degree of Doctor of Philosophy  
2000

## *Abstract*

Solution- and solid-state Nuclear Magnetic Resonance Spectroscopy (NMR) have been used to investigate a series of substituted, triazinylamino azo dyes. Proton,  $^{13}\text{C}$  and  $^{15}\text{N}$  solution-state spectra have been assigned using a variety of techniques and the chemical shifts are discussed. Site-exchange effects have been observed in  $^1\text{H}$  and  $^{13}\text{C}$  spectra for many of the dyes studied but most prominently for compound **13**.

The exchange effects were investigated at different temperatures below ambient, for a  $\text{CD}_3\text{OD}$  solution of compound **13**. The bandshapes were fitted for three-site exchange and the relevant rate constants extracted. The exchange has been attributed to internal rotation of the substituents about the triazine ring. Activation parameters have been calculated: for exchange between one pair of sites  $\Delta H^\ddagger = 76 \pm 8 \text{ kJ mol}^{-1}$  and  $\Delta S^\ddagger = 52 \pm 27 \text{ J mol}^{-1} \text{ K}^{-1}$ , and for a second pair,  $\Delta H^\ddagger = 76 \pm 4 \text{ kJ mol}^{-1}$ ,  $\Delta S^\ddagger = 55 \pm 15 \text{ J mol}^{-1} \text{ K}^{-1}$ . Direct exchange between the remaining pair of sites is negligible. Exchange involving a fourth site affects the spectra at somewhat lower temperatures, which assists in a partial assignment of the observed peaks to the rotamers.

The rotations that are causing the effects observable in the NMR spectra are identified, with the help of molecular modelling investigations. Three out of the four possible energy barriers are found to be a combination of rotation and nitrogen inversion. Exploration of the energy surface shows that nitrogen inversion with rotation actually reduces the rotational energy barrier, compared to the planar rotation. The relative barrier heights can be rationalised, although their exact values are not consistent with those measured using NMR.

Solid-state  $^{13}\text{C}$  spectra have also been recorded but are broad, making detailed assignment difficult. The broadness is found to be mainly due to the amorphous nature of the samples. The resolution is not vastly improved on increasing the spectrometer field and the powder X-ray diffraction exhibits only broad reflections.

# Memorandum

The research presented in this thesis has been carried out in the department of Chemistry, University of Durham, between October 1997 and September 2000. It is the original work of the author unless otherwise stated. None of this work has been submitted for any other degree.

The copyright of this thesis rests with the author. No quotation from it may be published without her prior consent and information derived from it should be acknowledged.

# Acknowledgements

First of all I would like to thank my supervisors Prof. Robin Harris and Dr. A. Margaret Chippendale for their help, support and patience over the last three years. I would also like to acknowledge the EPSRC and Avecia Ltd. for funding.

I would like to thank all the people at Avecia that I have had the pleasure of working with, particularly Kath and Mark for synthesis, Rob and Graham for running the solution-state experiments I could not get the spectrometer time to run in Durham. A big thank you goes to Julian for what probably seemed like endless thesis reading, molecular modelling advice and of course ‘puddings’ on my trips to Manchester!

During my research I have benefited from the experience and help of many people here in the department, particularly: Barry for his unique approach; members of solution world: Alan, Ian and Catherine; those up the hill: David and (over the hill) Phil; and David’s students for putting up with my synthesis efforts in their lab!! John and his group for powder XRD and Mark and Andy at Warwick University.

I would also like to give a special mention to everyone in CG22 past and present for making such a pleasant, friendly, helpful and relaxed atmosphere to work in:

Alison (big Al, for being an example to us all); Susan (Supersoo, Friday evenings in Gradsoc haven’t been the same!), Jon and Julian (how has he got in here again!!) the scary third years who really weren’t that scary!; Lindsey my little conference buddie, for putting up with my paddy feet, disdain of suntan cream and always providing carrying space in Tardis bag on our American adventure; Naser (my year mate); Paolo (the artistic Marvin man) and Alessia, part of our Italian contingent; Debbie (for entertainment, gossip, and distraction – my thesis would have been finished in half the time!!! that’s my excuse anyway!) and Ian (the part-time pieman). I would also like to include our postdocs especially, Paul for help writing the exchange program and for answering my daft questions; Canadian Paul (Honkydonk) for modelling help, thesis advice, reminding me how expensive everything is here and clumsiness (doh!) and Lucy for the musical interlude and probe fixing.

Of course there are many people outside work who have contributed to making my Ph.D. years so enjoyable: David (and most importantly his car! only joking, thanks for being a great friend, the best in fact) and Deb (interesting card playing evenings couldn’t have been provided by anyone else!); Anna (for listening to my whinging), Corinne (for those ice-cream moments) and Helen (housemates); Aline (I couldn’t have got through thesis writing without the trips to M & S and coffee times); Mark (the e-mail and distraction king) and Stuart, for keeping me on my toes, amused, generally looking after me and being a constant reminder that there’s more to life than thesis writing.

Last, but certainly not least I would like to thank my family, mum, dad, grandparents, Ted and Vera for their love, help, support and coping with all my traumas, I do appreciate it.

To my Family

*The great tragedy of science – the slaying of a beautiful  
hypothesis by an ugly fact.*

Thomas Huxley

# List of Abbreviations

AMT	Amplifier Technology
$B_0$	Static magnetic field
$B_1$	Radiofrequency magnetic field associated with the X nucleus
CE	Creative Electronics
CMX	Chemagnetics
COSY	Correlation Spectroscopy
CP	Cross Polarisation
Cpflip	Cross polarisation with flip back
CRAMPS	Combined Rotation and Multiple-Pulse Spectroscopy
CSA	Chemical Shielding Anisotropy
CW	Continuous Wave
DCM	Dichloromethane
DFT	Density Functional Theory
DMF	Dimethylformamide
DMSO	Dimethylsulphoxide
DSS	3-(Trimethylsilyl)-propanesulphonic acid sodium salt
EXSY	EXchange SpectroscopY
FID	Free Induction Decay
FT	Fourier Transform
fwhh	Full Width at Half Height
GARP	Globally optimised Alternating-phase Rectangular Pulses
GIAO	Gauge Including Atomic Orbitals
gs	gradient selected
HETCOR	Heteronuclear Correlation
HF	Hartree-Fock
HH	Hartmann-Hahn
HMB	Hexamethylbenzene
HMBC	Heteronuclear multiple bond coherence
HMQC	Heteronuclear multiple quantum coherence
HPLC	High Power Liquid Chromatography

Kel-F	Proton-free polymer used in rotor accessories ~[CF <sub>2</sub> CFCI]
MAS	Magic Angle Spinning
nOe	Nuclear Overhauser Effect
NQS	Non-Quaternary Suppression
NMR	Nuclear Magnetic Resonance
PDMSO	Polydimethylsiloxane
PTFE	Polytetrafluoroethylene (Teflon)
ppm	Parts Per Million
RDC	Residual Dipolar Coupling
r.f.	Radio Frequency
SCF	Self-Consistent Field Theory
SPI	Selective Polarisation Inversion
SPT	Selective Polarisation Transfer
ssb	Spinning Sideband
TMS	Tetramethylsilane
TTMS	Tetrakis(trimethyl)silane
UDIRL	University of Durham Industrial Research Laboratories
Vespel	Fluorine-free polymer used in rotor accessories
v.t.	Variable Temperature
XRD	X-ray Diffraction
1pda	Single pulse with decoupling during acquisition
1pulse	Single pulse with phase cycling
1pncyc	Single pulse with no phase cycling

Note that all standard symbols used herein follow the IUPAC convention.<sup>1</sup>

---

<sup>1</sup> R. K. Harris, J. Kowalewski and S. C. de Menezes, *Pure & Appl. Chem.*, **12**, 2489 (1997).

---

# Table of Contents

<b>1</b>	<b>Introduction</b> .....	1
1.1	Motivation for the Work.....	1
1.2	Structure of This Thesis.....	2
1.3	Background to NMR.....	3
1.3.1	Origin of the Signal.....	3
1.3.2	Differences Between Solution- and Solid-state NMR.....	5
1.4	Dyes.....	8
1.4.1	Ink-jet Printing.....	8
1.4.2	Ink-jet Inks.....	10
1.4.3	Background to Dyes.....	12
1.5	References.....	20
<b>2</b>	<b>Experimental</b> .....	22
2.1	Solid-state NMR Spectrometers.....	22
2.1.1	Chemagnetics CMX 200.....	23
2.1.2	Sample Handling.....	25
2.1.3	Experimental Set Up.....	25
2.1.4	Varian Unity Plus 300.....	31
2.1.5	CMX 600 Infinity.....	31
2.1.6	Pulse Programs.....	32
2.2	Solution-state NMR Spectrometers.....	32
2.2.1	Probes.....	33
2.2.2	Experimental Set Up.....	33
2.2.3	Referencing.....	34
2.2.4	Variable Temperature.....	34
2.2.5	Pulse Sequences.....	35
2.3	Synthesis of New Compounds.....	41
2.3.1	2-phenylamino-4,6-chloro-1,3,5-triazine.....	41

---

2.3.2	2-phenylamino-4,6-diethanolamino-1,3,5-triazine.....	41
2.3.3	2-phenylamino-4,6-ethanolamino-1,3,5-triazine.....	42
2.3.4	2-(3carboxy-4-chloro-phenylamino)-4,6-chloro-1,3,5- triazine.....	43
2.3.5	2-(3carboxy-4-chloro-phenylamino)-4,6- diethanolamino-1,3,5-triazine.....	43
2.3.6	2-(3carboxy-4-chloro-phenylamino)-4,6-ethanolamino- 1,3,5-triazine.....	44
2.4	References.....	46
<b>3</b>	<b>The Molecules and Their Assignments.....</b>	<b>48</b>
3.1	Introduction.....	48
3.2	Proton NMR Spectral Assignments.....	49
3.2.1	Assignment Methods.....	49
3.2.2	Chemical Shift Comparisons.....	50
3.2.3	Observations.....	55
3.3	Molecular Modelling.....	61
3.4	<sup>13</sup> C Assignment.....	65
3.4.1	Example of <sup>13</sup> C Assignment.....	66
3.4.2	<sup>13</sup> C Chemical Shift Comparison.....	71
3.4.3	Observations.....	74
3.5	References.....	75
<b>4</b>	<b>Observation of Internal Rotation by NMR.....</b>	<b>77</b>
4.1	Introduction.....	77
4.2	Observation of Exchange by NMR.....	82
4.3	Identification of Exchange Processes.....	89
4.4	Exchange Fitting.....	93
4.5	Determination of Activation Parameters.....	101
4.6	Supporting Evidence.....	105
4.6.1	Compound <b>2</b> .....	106

---

4.6.2	Compound 3.....	111
4.6.3	Compound 5.....	118
4.7	Conclusions.....	120
4.8	References.....	121
<b>5</b>	<b>Molecular Modelling of Rotational Energy</b> .....	<b>123</b>
	<b>Barriers</b> .....	
5.1	Introduction.....	123
5.1.1	Molecular Mechanics.....	124
5.1.2	Quantum Mechanics.....	125
5.1.3	Density Functional Methods.....	129
5.1.4	Geometry Optimisations.....	129
5.1.5	Locating Transition States.....	130
5.2	Conformational Studies.....	131
5.3	Rotational Energy Barriers.....	134
5.3.1	Barriers 2, 3 and 4.....	136
5.3.2	Barrier 1.....	151
5.3.3	Summary.....	151
5.4	Discussion.....	153
5.5	Conclusions.....	157
5.6	References.....	158
<b>6</b>	<b>Solid State</b> .....	<b>160</b>
6.1	Introduction.....	160
6.1.1	Experimental Techniques.....	160
6.2	Results and Discussion.....	164
6.2.1	Simplified Compounds.....	164
6.2.2	The Dyes Themselves.....	175
6.3	Conclusions.....	187
6.4	References.....	188

---

<b>7</b>	<b>Future Work</b> .....	189
	<b>Appendices</b> .....	191
A	Conferences attended, work presented etc.....	191
B	Colloquia, Seminars and Lectures given by Invited Speakers.....	193
C	Side-chain chemical shifts of relevant compounds.....	201
D	Compounds studied.....	202

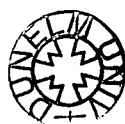
# Chapter 1

## Introduction

### 1.1 Motivation for the Work

The work contained in this thesis examines a variety of ink-jet-printer dyes. Most of the dyes studied are closely related, being magenta substituted triazinylamino azo dyes, differing in the form of the substituent. Many physical properties are required to make a good dye, including lightfastness, wetfastness and brightness. Chemical properties are closely related to physical properties, so understanding the chemical features that affect these physical properties would aid the design of new dyes by allowing synthetic chemists to make a more informed investigation of possible new compounds. NMR is a powerful tool to investigate such features, since information can be gained both in solution and in the solid state so that results from the two states can be directly compared. Dyes are applied in solution and then dry to form a solid, so information about both states is needed. Order, motion and aggregation are just some of the properties it is possible to study using NMR.

This chapter gives some background to the work undertaken in this PhD. Firstly in section 1.2, a brief explanation of the compounds studied is given with a general structure upon which the main dyes considered are based. An outline of the thesis shows how the work described is organised. Section 1.3 gives a simple description of NMR and concentrates particularly upon differences between the solution and solid state. Some information about dyes is contained in section 1.4 to put the dyes



considered into context. The ink-jet printing technique and ink-jet inks are described in sections 1.4.1 and 1.4.2 respectively as the dyes in Appendix D were designed for use in that area. The dyes themselves are described in section 2.4.3, particularly azo dyes as compounds **7-18** are in that class. Dye interactions and properties are also outlined as these are important considerations in the dyestuffs industry.

## 1.2 Structure of This Thesis

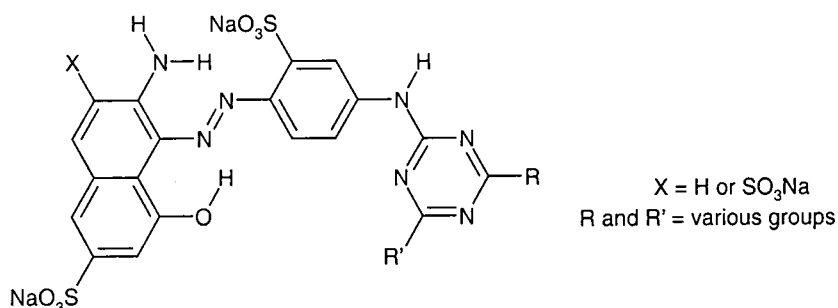


*Figure 1: The general structure upon which the dyes under study in this thesis are based.*

The molecules under investigation are based on the general structure shown in Figure 1. For ease of reference they are displayed again in Appendix D (the last pages of this thesis). Compounds **10** to **17** were initially of interest. Interesting rotational features were observed for many of these compounds, and so compounds **1** to **6** were synthesised as simplified models to help confirm the nature of the rotations suspected. Compounds **7** to **9** were examined as reference material and **18** was used for the spray study described in chapter 6 as a lot of sample was available.

Broad experimental details are given in chapter 2. Chapter 3 describes the methods used to assign solution-state spectra of the dyes in question. A variety of techniques were used to assign the carbon spectra. This is illustrated with reference to compound **9**. A number of observations were made whilst doing this which were investigated to give information about the molecules. A broadness was identified in many proton spectra. This was investigated further (see chapter 4) using variable-temperature proton and <sup>13</sup>C studies to study the compound showing the most prominent exchange features,

namely compound **13**. Conclusions were drawn about the process occurring with the aid of molecular modelling calculations. These were confirmed with reference to the simplified compounds **2**, **3** and **5**. Activation parameters were measured for the accessible processes for compound **13**. Features of the modelling described in chapter 4 are outlined in chapter 5. Information about the rotations occurring is gathered by examining the rotational energy surface. A possible rationalisation in the relative rotational barrier heights is also discussed. Chapter 6 deals with some of the molecules in the solid-state using two nuclei,  $^{13}\text{C}$  and  $^{15}\text{N}$ , and powder X-ray diffraction.

## 1.3 Background to NMR

### 1.3.1 Origin of the Signal<sup>1</sup>

NMR ‘observes’ atomic nuclei to gain information about molecular structure, mobility, hydrogen bonding, aggregation and the local environment of the nuclei. A magnetic nucleus has a spin quantum number,  $I$ , a magnetic (orientation) quantum number,  $m$  (having  $2I+1$  values in integral steps between  $+I$  and  $-I$ ), and angular momentum (known as spin). The last-mentioned is described by a vector quantity,  $\mathbf{I}$ , which is quantised in units of  $\hbar$  ( $=h/2\pi$ ). The z-component of  $\mathbf{I}$  is therefore also quantised as shown in (1).

$$I_z = m\hbar \quad (1)$$

The magnetic moment of a nucleus is directly related to its spin angular momentum defined as in (2).

$$\mu = \gamma\mathbf{I} \quad (2)$$

The proportionality constant,  $\gamma$ , is the gyromagnetic ratio. In the absence of a magnetic field, all  $2I+1$  orientations of a spin- $I$  nucleus have the same energy. When an external magnetic field is applied however, they are no longer degenerate. The energy,  $E$ , in the

magnetic field  $\mathbf{B}_0$  is  $E = -\boldsymbol{\mu} \cdot \mathbf{B}_0$ . In a strong magnetic field, the z-direction is defined as along  $\mathbf{B}_0$  so the energy becomes as in (3).

$$E = -m\hbar\gamma B \quad (3)$$

The  $2I+1$  states for a spin- $I$  nucleus are equally spaced, with energy gap  $\hbar\gamma B$ . The selection rule for an NMR transition is  $\Delta m = \pm 1$ . The allowed transitions therefore have the energy as described in (4).

$$\begin{aligned} \Delta E &= h\nu = \hbar\gamma B \\ \nu &= \frac{\gamma B}{2\pi} \end{aligned} \quad (4)$$

When placed in a magnetic field, the magnetic nuclei in the sample distribute themselves among the  $2I+1$  energy levels according to the Boltzmann Distribution as in (5) for  $\Delta m = 1$ .

$$\frac{n_{\text{upper}} - n_{\text{lower}}}{n_{\text{lower}} + n_{\text{upper}}} = \frac{\Delta E}{2kT} \quad (5)$$

The applied radiofrequency field induces transitions between the lower and upper energy levels. The net absorption energy and hence the intensity of the spectroscopic transition is dependent upon the difference in populations of the two levels. In NMR the upward transitions outnumber the downward transitions by only one in  $10^4$ - $10^6$ , implying that the signals are very weak. It is therefore important to maximise the signal strength by using strong magnetic fields to maximise  $\Delta E$ . Nuclei with a large gyromagnetic ratio and high natural abundance are favoured.

Since the magnetic field experienced by a nucleus is characteristic of the chemical environment of the nucleus as well as the type of nucleus, NMR can be used to give information about the situation of each atom in a molecule.

To perform an NMR experiment, the sample must be placed in a strong magnetic field to produce non-degenerate energy levels. Electromagnetic radiation must then be applied to induce transitions and the signal produced. In NMR radio waves (r.f. field) are in the correct frequency range for this. The signal produced by the sample is then detected using a coil, inside which the sample is placed. This signal is amplified before being transferred to the computer. In the early days of NMR the r.f. field was swept across the frequency region of interest whilst monitoring the signal. This was time consuming, so now a single r.f. pulse is applied which contains all frequencies of interest. The signal produced is a complex decay in the time domain. It contains all the frequencies produced by all the atoms excited in the sample and is called a Free Induction Decay (FID). The frequency domain signal can be extracted by carrying out a Fourier Transformation on the FID.

### ***1.3.2 Differences Between Solution- and Solid-state NMR***

The basic principles of NMR are the same for both the solution and solid states, but it is clear that solution-state NMR is a much more widely used technique, particularly by synthetic chemists, whereas solid-state applications tend to be more specialised.

NMR is related to the nuclear spin energy states and therefore can be described by quantum mechanics using the Schrodinger equation as in (6).

$$\hat{H}\Psi = E\Psi \quad (6)$$

where  $\hat{H}$  is the nuclear spin Hamiltonian. This is composed of a summation of all the internal and external factors effecting the system as outlined below:

$\hat{H}_z$  Zeeman interaction due to  $B_0$ , the static magnetic field

$\hat{H}_{r.f.}$  The effect of the r.f. magnetic field

The following represent the internal interactions of the nucleus:

$\hat{H}_{cs}$  chemical shift

$\hat{H}_Q$  quadrupole term due to electric field gradients

- $\hat{H}_{SR}$  spin rotation, molecular moments associated with molecular angular momentum
- $\hat{H}_D$  dipole coupling, mutual and direct coupling via magnetic dipole moments
- $\hat{H}_J$  scalar coupling, mutual but indirect coupling through electrons.

In liquids and solutions, there is isotropic tumbling of the molecules which averages to zero all the interactions apart from  $\hat{H}_{CS}$  and  $\hat{H}_J$ . This is because all but  $\hat{H}_{CS}$  and  $\hat{H}_J$ , possess the orientational dependence of  $(3\cos^2\theta-1)$  where  $\theta$  is the angle between a fixed molecular axis and the static magnetic field,  $B_0$ .

The signals in solid-state spectra are usually much broader than solution-state spectra, mainly due to the presence of the dipolar coupling, which is averaged to zero in the solution state. Solid-state spectra contain more information than those for solutions, as the effects of the interactions are still present. It is difficult to extract this information, however, and in many cases it is more useful to make the solid-state peaks as narrow as possible, i.e. 'solution like'. There are three techniques commonly utilised to help achieve this.

- 1) In a powder all the molecules are distributed with random values of  $\theta$  and so the resulting spectrum forms a broad 'powder pattern' due to the chemical shift anisotropy (CSA).<sup>2</sup> The shape of this depends on the symmetry of the molecule. The envelope has three turning points, but if the molecule is axially symmetric it will have only two. To overcome this CSA effect, the sample is spun rapidly at the 'magic angle'  $54.7^\circ$  to  $B_0$ ,<sup>3</sup> simulating molecular tumbling. If the spinning speed is greater than the maximum CSA for a particular peak, a single, isotropic peak will result. If the frequency of rotation is less than this then sidebands will appear, equally spaced by the spinning speed. Magic-angle spinning (MAS) also partially averages dipole-dipole and quadrupolar interactions.
- 2) Dipolar interactions can be approximately 1000 times greater than scalar coupling and so cause vast broadening of signals. Therefore their effects on the spectra must be removed if individual peaks are to be resolved. High-power decoupling is used to achieve this. Decoupling is used in the solution state to remove J-coupling but

requires a power of 1-2 Watts whereas dipolar coupling uses powers of 100-150 Watts. Homonuclear decoupling is desirable in the solid state when observing protons, but decoupling cannot be applied to a resonance band which is being simultaneously observed. Multiple-pulse sequences have been devised to do this, e.g. combined rotation and multiple pulse spectroscopy (CRAMPS).<sup>4</sup> These cause an averaging of the dipolar coupling in 'spin space' by changing the phases of the pulses.

- 3) Many nuclei to be observed have a low natural abundance, for example  $^{13}\text{C}$ . This means a large number of acquisitions are crucial, so the time for each acquisition must be as short as possible. Spin-lattice relaxation times are the main limiting factor in this, and unfortunately they can be very long, in extreme cases of the order of hours. The solution to this problem is 'cross polarisation'.<sup>5</sup> A  $90^\circ$  pulse is first applied to the proton channel (but can be applied to another abundant nucleus to give information about structure, or to help the assignment of spectra) and then spin locked. The  $^1\text{H}$  magnetisation is therefore in the 'y' direction in the rotating frame of reference. The  $^{13}\text{C}$  radio-frequency is then switched on while maintaining the proton spin-lock field. The powers of the two channels must obey the Hartmann-Hahn matching condition,  $\gamma_{\text{H}}B_{1\text{H}}=\gamma_{\text{C}}B_{1\text{C}}$ , which ensures the proton and carbon magnetisation are precessing at equal rates, so allowing good transfer of magnetisation. As the carbon magnetisation was generated by the protons, the recycle delay is dependent upon the  $T_1$  of the protons, which is generally much lower than that of carbon. This sequence can be included at the beginning of more complex pulse programs, for example to allow  $T_1$  measurements to be made more rapidly.

Recording solid-state spectra often incorporates the above techniques, but there are some other, less obvious differences in the practicalities between experiments in these two states. Due to the inherent broadness of the spectra, even when high-power proton decoupling and magic-angle spinning are applied, shorter acquisition times are needed as broad peaks give rise to fast signal decay. This is fortunate as high-power proton decoupling is applied during the acquisition time and so a short acquisition time means high power does not have to be entering the probe for a long time. Solid-state probes, and indeed hardware generally, must be able to withstand higher r.f. powers than

solution-state equipment due to the decoupling required and, during the contact time (of the order of ms), two channels are carrying power. As the sample is oriented at the magic angle to the magnetic field, solid-state probes tend to be wider than those for the solution state. Shimming is not as sensitive in solids as solutions as the resolution is not as high so, generally, it does not have to be carried out after every sample change. Tuning the probe however must be carried out every time the sample or temperature are altered.

Spectra recorded for this thesis observe nuclei with dilute spins. In general these can be made more 'solution like' with the techniques described above, than can spectra observing abundant spins. Abundant nuclei undergo efficient spin diffusion, which makes differentiating between individual sites difficult. As mentioned previously, CRAMPS can be used to decrease this problem.

## **1.4 Dyes**

In this section, the ink-jet printing process will be described, followed by an outline of dyes in general, and then some background to azo dyes, the class containing the molecules in this thesis.

A dye is a coloured molecule, whereas an ink is the solution used to apply the dye to the substrate. Inks are composed of an organic solvent or water, in which the pigment is suspended or the dye is dissolved, with added emulsifiers and preservatives.

### ***1.4.1 Ink-jet Printing***<sup>6</sup>

Ink-jet printing, the application for the dyes in this thesis, is the only true primary non-impact printing process whereby a liquid ink is squirted through very fine nozzles and

the resultant ink droplets form an image directly on the substrate. There are two main technologies:

1. Continuous, where a continuous stream of ink is ejected from the nozzle. There are two types:
  - i) 'Sweet-based' designs: Some of the droplets are selectively charged. These are then deflected when passed through high-voltage deflection plates. The charged droplets form the image and the uncharged ones go into the gutter.
  - ii) Hertz technology: a fine mist of irregular-sized ink droplets is formed which forms the image. This is more suited to colour printing.
2. Drop-on-demand where every drop is used to form the image. Drops are not charged and they are fired in a straight line, therefore the print head should be placed as close as possible to the substrate. This allows more accurate positioning of the dots so that higher quality prints are obtained, which means this technique is more suitable for office printers.

### **General features**

The most important general factors required of all ink-jet printers are high reliability and the ability to produce good print quality.

More specific attributes of the ink-jet output are:<sup>7</sup>

- 1) Satellites - These are small drops of ink produced in addition and near to the desired characters.
- 2) Linear resolution – Ink-jet printers with poor linear resolution cannot print separate lines that are close together. Printers can be tested by printing parallel lines and the quality is defined numerically as being the number of separated lines printed within the distance of 25.4 mm without connecting lines.
- 3) Linearity - The uniformity of the characters such that rows or columns appear straight and continuous.
- 4) Stepping - The imperfections when drawing long lines sloped at a very small angle. These are most pronounced at approximately 7°.
- 5) Circular uniformity - Imperfection of drawing circular and curved lines.

- 6) Overlapping - A displacement on the edge of an image of primary coloured dots.

### **2.4.2 Ink-jet Inks**

There are several types of ink: dye based aqueous or solvent, hot melt and pigment based aqueous or solvent. Solvent-based inks are used mainly with continuous printers in industry whereas the most common inks for drop-on-demand office printers are aqueous based and so consequently the colorant is a water-soluble dye.

#### **Aqueous Inks**

Aqueous-based inks normally contain water-miscible co-solvents. These help to minimise the evaporation of water and prevent crystallisation, which would block the printer nozzles. They can also control the viscosity and surface tension and improve the solubility of the inks, making them more stable. A biocide is added to prevent the growth of micro-organisms which would also block the nozzles.

Pure dyes must be used and a pH compatible with the materials in the ink must be chosen as certain electrolytes, for example chloride ions, will accentuate water's corrosive properties. Inks must be filtered before use to prevent insoluble material causing problems. Chelating agents may be added to solubilise certain metal salts.

#### **Solvent Inks**

These are mainly encountered in the industrial segment of ink-jet printing. They are used when fast drying times are required or when printing on to hydrophobic substrates such as metals, plastics or glass. Solvent choice is determined by how flammable and toxic it is.

## Hot-melt Inks

Hot-melt inks are similar to wax crayons, being solid at room temperature and molten when heated. Long-chain fatty acids, alcohols or sulphonamides are used as vehicles. The colorants used are solvent dyes that are soluble in the particular ink vehicle or pigment dispersions.

## Pigments

Pigments as used in inks are ultra-small solid particles with a diameter between 500 and 50 nm.<sup>8</sup> Each pigment particle contains a multitude of colour molecules. Dyes by contrast are liquid, i.e. are dissolved in the carrier liquid.

Although dyes may be lacking in some respects, they are the most used colorant of choice because they perform better than conventional pigments. These standard pigments are generally not used in industrial ink-jet systems due to deficiencies, e.g. ink stability, non-uniform jetting characteristics and solidification at the nozzle. A suitable dispersion stabiliser can be added to the dispersion medium with stirring to disperse the carbon black.

An attempt is being made to apply a pigment-type ink using a pigment like a carbon black as a colouring agent in the place of the dye-type ink for ink-jet printers. This has been done but there are some problems.<sup>9</sup>

Kodak has created a pigment whose particle size is 1/10<sup>th</sup> the size of other pigments.<sup>10</sup> Smaller particles form more stable dispersions with higher optical densities and a more uniform gloss. These pigments have not yet reached the market, however, and so the choice between dyes and pigments is still of major importance and likely to continue to be so in the future.

### **Features to consider when developing inks**

- 1) Curl - This is a property of a coated material to curve from the flat state into a certain direction under outside influencing factors: for ink-jet inks the 3 main ones are:
  - i) Humidity - At low humidities of the ambient air, the binders of the ink-jet layers will desorb their residual humidities, resulting in high internal tension forces within the ink-jet paper. If these forces are not compensated for, the ink-jet paper will react by curling more or less strongly towards the side coated with the ink receptive layer. Generally this happens at <20% humidity.
  - ii) Memory - Before printing, paper may, especially in the case of large-scale printing, be wound around cores for long periods of time. This may lead to the paper exhibiting 'memory curl'.
  - iii) Drying - This is concerned with surface drying, not complete drying throughout the ink-jet layer. Investigations have revealed that even after two hours an ink-jet layer is not completely dry. Ink-jet inks are formulated to prevent plugging of the printheads, a common problem with rapid drying inks. They therefore often contain solvents of low volatility which require longer drying times than for volatile solvents and so clog less readily.
- 2) Banding and bleeding - Banding is streak formation when printing full density areas. Bleeding is the diffusion of a coloured ink into a directly adjacent colour spot. The occurrence of 'puddles' and the spreading of different colours into one another is strongly determined by the type of printer, the inks, and the type of ink-jet media. To prevent both banding and bleeding it has been found to be beneficial if the rate of absorption of the ink-jet inks by the layer, directly after deposition of the ink drops, is rapid.

### **2.4.3 Background to Dyes**

Ink-jet printing uses yellow, magenta and cyan. Black is also used for text. Initially carefully selected food dyes were used. The yellow dyes are the largest group of natural dyes but they have poor fastness properties and are made of unstable chromogens.

Consequently they have been replaced by purely synthetic dyes. A chromogen is the complete arrangement of atoms which gives rise to the observed colour. The term chromophore describes the various chemical units from which the chromogen is built.<sup>11</sup>

The rise of the dyestuffs industry closely paralleled advances made in organic chemistry. The dyestuffs industry solved many of the problems of doing large-scale synthesis, and a high percentage of the modern organic chemical industry is an offshoot of the dyestuffs industry. The second half of the nineteenth century saw the introduction of many new classes of dyestuffs. Since then very few chromogens have been added to the range, due to the increasing costs of oil and energy, together with tougher toxicological and environmental constraints. Instead, dye manufacturers are focussing on new, cheaper routes to existing dyes.

### **Azo Dyes<sup>12</sup>**

All the dyes considered in this thesis belong to this class of compound.

#### Synthesis

Usually the different components of the chromophore are prepared separately and then attached together as the final step of the synthesis, for example the diazotisation and coupling of aromatic amines to give azo dyes.<sup>13,14,15</sup>

The azo dyes are the largest group of dyes, comprising 50% of the total world dyestuff production. They have a high tinctorial strength, are easy to prepare from cheap starting materials, cover the whole shade range and have good fastness properties. Their disadvantages are that they are often duller in shade and do not have as good lightfastness characteristics as their main rivals, the anthraquinones. The advantages however outweigh the deficiencies.

They exist in the more stable trans form rather than the cis form. Both nitrogen atoms are  $sp^2$  hybridised, meaning that the C-N-N bond angles are approximately  $120^\circ$ . Trans-azobenzene is essentially planar in the solution and solid states. There are contributions

from resonance forms, causing the carbon-nitrogen bond lengths to be slightly shorter than expected and the nitrogen-nitrogen bond lengths slightly longer. The phenyl rings show some quinoid character.

### Azo-hydrazo Tautomerism

Dyes capable of undergoing azo-hydrazo tautomerism are those in which the hydroxyl group is conjugated to the azo group i.e. ortho- or para-hydroxylaryl but not meta-hydroxylaryl, see Figure 2.

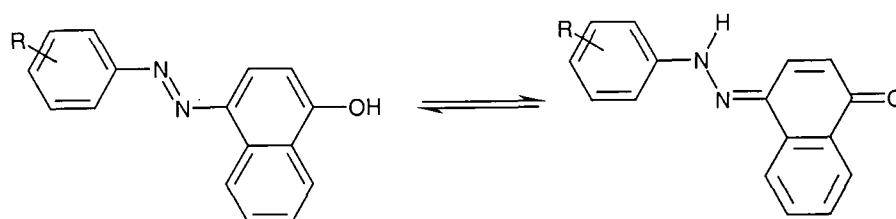


Figure 2: Azo-hydrazone tautomerism in naphthalene systems.

The azo and hydrazone tautomers have different physical properties such as lightfastness and colour, for example in the 4-phenylazo-1-naphthol system the azo tautomer is yellow ( $\lambda_{\max} \sim 410$  nm) whereas the hydrazone tautomer is orange ( $\lambda_{\max} \sim 480$  nm). The main factor determining if this tautomerism is observed is the relative thermodynamic stability of the azo and hydrazone tautomers. If these energies are similar, tautomerism will be observed but if one is much more stable then the dye will exist exclusively in that form. The hydrazo tautomer is more susceptible to aggregation than the azo tautomer.

The solvent can have a huge influence on the position of the equilibrium. Usually a more polar solvent favours the hydrazone form.<sup>16</sup> It is not the bulk solvent properties which determine the proportion of azo and hydrazone forms, it is the solvent structure and the environment of the dye in the solvent matrix. The hydrazone form is favoured in solvents capable of forming a 3-dimensional structure, e.g. water, whereas the azo form is favoured by solvents that form a 2-dimensional structure or are unstructured,

e.g. liquid alcohols.<sup>16</sup> In protic solvents the interconversion of the tautomers occurs through participation of protons available from the solvent.

The steric effects of ortho substituents R in the phenyl ring prevent effective solvent stabilisation of the hydrazone form which gives rise to an anomalous solvent effect: Polar, strongly hydrogen-bonding ‘hydrazone-favouring’ solvents now favour the azo form.

### Amino-imino tautomerism

Unlike the hydroxy analogues, 4-phenylazo-1-naphthylamine dyes exist totally in the aminoazo form of the possible equilibrium, shown in Figure 3.

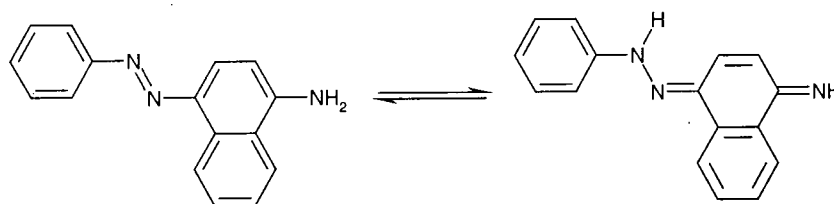


Figure 3: Amino-imino tautomerism of 4-phenylazo-1-naphthylamine.

It has not been established whether tautomerism exists in o-phenylazonaphthalene dyes but it is probable that these dyes also exist in the aminoazo form. It is not clear why this is the case as the thermodynamic stability of the aminoazo form is less than the iminoazo form.

### **Second-generation Colorants**

A step-change in the waterfastness of ink-jet dyes arose as a result of a collaboration between ICI (now Avecia) and Hewlett Packard in 1987. The approach used was that of differential solubility. Here a dye was used that had high solubility in the aqueous ink media but low solubility when on the paper. Aqueous ink-jet inks are normally slightly

alkaline (in the pH range 7.5-10.0) whereas most plain papers are slightly acidic (in the pH range 4.0-6.5). All of the first-generation dyes used in ink-jet printing contain an abundance of strongly acidic sulphonic groups as the water solubilising substituent, and these dyes are often still soluble even under acidic conditions. By selectively replacing some of the sulphonic acid groups by less acidic substituents, for example carboxylic acids, then dyes can be produced that have high solubility in an alkaline ink (where the carboxylic group is ionised and therefore confers extra water-solubilising properties) but which have relatively low solubility on the acidic paper.

### **Dye Interactions**

There are several interactions that influence the behaviour and properties of a dye:

#### Covalent bonding:

This is the strongest interaction that can occur and results from a chemical reaction between the colorant and the substrate. The electrophilic reactive group on the dye reacts with a nucleophilic group (e.g. a primary hydroxyl group on the cotton) producing an irreversible chemical reaction. This produces a print with excellent fastness properties but is only used on textiles.

#### Electrostatic or ionic:

Anionic dyes contain water solubilising groups such as  $\text{SO}_3^-$ ,  $\text{CO}_2^-$  etc. and these are attracted by cationic groups on the media, e.g.  $\text{Ti}^{4+}$ ,  $\text{Al}^{3+}$  etc., producing a strong interaction and effectively immobilising the dye molecules, giving excellent image quality.

#### $\pi$ - $\pi$ :

These are important in dye-dye interactions rather than between the dye and the substrate and can lead to dye aggregation or crystallisation in extreme cases. These are relatively strong interactions and may occur for media containing aromatic groups capable of interaction with the colorants. Phthalocyanines aggregate in such ways.

#### Hydrogen Bonding:

This is fairly weak interaction. However, for cellulosic substrates this is often the most important interaction between colorant and media. For a large dye molecule a large number of sites for these interactions may exist, increasing the strength of the binding. In addition there may be a number of H-bonding interactions involving the OH of the cellulose interacting with the  $\pi$ -cloud of the aromatic group on the colorant.

#### Hydrophobic:

This attraction occurs for solvent-soluble dye systems which contain hydrophobic groups such as alkyl chains. These interact with similar hydrophobic groups on the substrate and this is quite favourable, particularly when the colorant is applied from an aqueous phase.

#### Dipole-dipole:

These are relatively weak and result from the induced polarity in the interacting groups.

#### Van der Waals:

These tend to be quite weak at long range but become stronger when the interacting groups are brought close together. A weak repulsion occurs between cellulosic substrates and anionic dyes when they are far apart. However, as the water-soluble dyes are absorbed then the interaction between colorant and media becomes quite strong.

#### Plain Paper

All these modes of interaction are present in textile ink-jet operation. However, for plain papers H-bonding and Van der Waals are the key interactions, whereas for coated papers and films ionic or coulombic forces are also important.

#### Image Properties

When the dye-dye interactions compete with the dye-substrate interactions, then the colorant can aggregate or crystallise on the paper surface leading to a loss in optical density.

## Dye Properties

### Lightfastness<sup>17,18,19</sup>

Many factors have an effect on the lightfastness of dyes such as humidity, aggregation, pH media type and atmospheric conditions (for example the presence of ozone and oxides of sulphur and nitrogen). There has been limited progress in the research into lightfastness because of the practical problems associated with studying the fading mechanism. Removing the degraded products from the substrate is difficult without removing impurities present on the substrate when there is only a small amount of compound there. The products from the reaction of the dye with light may react further and may even be volatile enough to evaporate from the fibre.

The first test methods used sunlight as the light source but this is not very satisfactory as, particularly in Britain, the duration and intensity of sunlight varies tremendously from day to day. Lightfastness tests can therefore take months or years and may not be very reliable. Procedures were investigated to expose the dye to a light source for 24 hours but the light output may not correspond very well to the output from the sun. This may lead to dyes appearing to have good lightfastness properties in the test but in a real situation they may fade in hours.

The aggregation of the dye seems to have a strong bearing on its rate of fading. Experimental evidence supports this theory. In one study the lightfastness of a series of dyes was measured in ultra-thin films of viscose after the degree of aggregation had been measured. Highly aggregated dyes had good lightfastness whereas dyes existing in the monomolecular form had poor lightfastness properties.

### Photochromism<sup>20,21</sup>

This effect is when dyes change colour reversibly on exposure to light. In azo dyes this is caused by trans to cis isomerism about the azo linkage.

### Solvatochromism

This is the effect of solvent on dye colour and is also seen when printing onto different media.

### Liquid Crystals and Aggregation

Dyes have been considered for use in liquid-crystal displays<sup>22</sup> as they readily aggregate. This aggregation has been studied.<sup>23</sup> Mono, di and tri sulphonic acids were examined with variation in the position of the sulphonic acid groups. The aggregates have a 'ladder' or 'staircase' arrangement of anions in which the aromatic planes can stack alternately one on top of the other. As the concentration increases the stacks increase in length, whilst each aggregate or stack maintains an independent existence.

## 1.5 References

- <sup>1</sup> P. J. Hore, '*Nuclear Magnetic Resonance*', Oxford University Press, Oxford, 1995.
- <sup>2</sup> R. J. Iuliucci and D. M. Grant, *Solid State NMR*, **6**, 55 (1996).
- <sup>3</sup> E. R. Andrew, A. Bradbury and R. G. Eades, *Nature*, **182**, 1659 (1958).
- <sup>4</sup> B. C. Gerstein 'CRAMPS' *Encyclopedia of NMR*, Eds. D. M. Grant and R. K. Harris, Wiley, **3**, 1501 (1996).
- <sup>5</sup> S. R. Hartmann and E. L. Hahn, *Phys. Rev.*, **128**, 2042 (1962).
- <sup>6</sup> P. F. Gordon and P. Gregory, '*Organic chemistry in colour*', Springer-VerlagBerlin Heidelberg, 1987, Ch. 5 by R. W. Kenyon.
- <sup>7</sup> L. Buczynski, *1997 International Conference on Digital Printing Technologies*, 638 (1997).
- <sup>8</sup> H. P. Stockamp, *1997 International Conference on Digital Printing Technologies*, 427 (1997).
- <sup>9</sup> N. Ando and M. Takeuchi, *1997 International Conference on Digital Printing Technologies*, 655 (1997).
- <sup>10</sup> D. E. Bugner and A. D. Bernet, *1997 International Conference on Digital Printing Technologies*, 667 (1997).
- <sup>11</sup> P. F. Gordon and P. Gregory, '*Organic chemistry in colour*', Springer-VerlagBerlin Heidelberg, 1987, Ch. 1.
- <sup>12</sup> P. F. Gordon and P. Gregory, '*Organic chemistry in colour*', Springer-VerlagBerlin Heidelberg, 1987, Ch. 3.
- <sup>13</sup> R. N. Butler, *Chem. Revs.*, **75**, 241 (1975).
- <sup>14</sup> J. H. Ridd, *Quart. Revs.*, **15**, 418 (1961).
- <sup>15</sup> H. Zollinger, *Chem. Revs.*, **51**, 347 (1952).
- <sup>16</sup> A. Burawoy, A. G. Salem, A. R. Thompson, *J. Chem. Soc.*, (1952) 4793.
- <sup>17</sup> C. H. Giles and R. B. McKay, *Textile Research Journal*, **33**, 528 (1963).
- <sup>18</sup> N. A. Evans and I. W. Stapleton, Structural factors affecting the lightfastness of dyed fibres. In, *The chemistry of synthetic dyes*, Venkataraman Vol. VIII pp. 221 New York. Academic Press 1978.
- <sup>19</sup> M Fryberg R Hofmann P A Brugger International conference on digital print technology, p595
- <sup>20</sup> J. Griffiths, *Chem. Soc. Reviews*, **11**, 481 (1972).

<sup>21</sup> D. L. Ross and J. Blanc, Photochromism by *cis-trans* isomerism. In, techniques of chemistry, Vol. III, G. H. Brown p 471 New York, Wiley-interscience 1971.

<sup>22</sup> G. W. Gray, *Dyes and Pigments*, **3**, 203 (1982).

<sup>23</sup> F. Jones and D. R. Kent, *Dyes and Pigments*, **1**, 39 (1980).

# Chapter 2

## Experimental

A range of Nuclear Magnetic Resonance (NMR) spectrometers varying in field strength have been used throughout this Ph.D., for both solids and solutions. Working at different field strengths can be advantageous as line separations in hertz are usually increased with increasing field, meaning better resolution (depending on the origin of the linewidths). For solids more spinning sidebands are observed for the same sample and same spinning rate at higher field. This can be a disadvantage if it causes overlap of sidebands and isotropic peaks. Different solid-state probes with a range of spinning speeds and decoupling fields can also be used depending on the specification of the probes. Gradients can be used with some of the solution-state spectrometers. All spectrometers will be briefly described in this chapter but the majority of the discussion will surround the Chemagnetics CMX 200 belonging to the Durham University NMR group as this requires the most interaction for set up.

### 2.1 Solid-state NMR Spectrometers

Three solid-state spectrometers have been used, namely a Chemagnetics CMX-200 situated in Durham University, a Varian Unity Plus 300 situated in the UDIRL (University of Durham Industrial Research Laboratories) and a Chemagnetics CMX 600

Infinity at Warwick University. The solid-state spectra recorded on the 300 MHz spectrometer were obtained by David Apperley.

### 2.1.1 Chemagnetics CMX 200<sup>1</sup>

This triple-channel spectrometer has a magnetic field of 4.7 T and operates at 200.13 MHz for protons. It is controlled by a Sun workstation running Chemagnetics Spinsight software.<sup>2</sup> The workstation controls the spectrometer by transmitting the pulse program details, timings, phases, frequencies etc. to the synthesisers, transmitters, amplifiers and receiver.

Four amplifiers have been used: a middle-frequency broad-band AMT (AMplifier Technology) amplifier, a low-frequency broad-band AMT; a CE (Creative Electronics) narrow-band amplifier and a Bruker amplifier.

When selecting the amplifier to be used its tuning frequency, pulse shape, maximum power output and duration of maximum power output must be considered, as shown in Table 1.

	Tuning frequency / MHz	Maximum power output / W	Maximum power 'on' time / ms
CE	188.288-200.13	500	no limit
Broad-band AMT (top)	6-220	500	20
Low-frequency AMT	30-122	500	11
Bruker	8-200	variable	no limit

*Table 1: Amplifier specifications.*

The CE amplifier is used for <sup>1</sup>H and may operate in class A/B mode (input power is proportional to output power) or class C mode (non-linear). It must be tuned to give the maximum power output possible in that mode of operation.

The Bruker amplifier operates in class C mode. The transmitter power output is used at maximum because the overall power output is controlled at the amplifier via coarse and fine gain dials. The Bruker amplifier cannot be controlled using the software. It does not require any blanking. The frequency range is altered by changing the tuning circuit which has a narrow frequency range, reducing noise output.

The low-frequency AMT requires blanking when it is not pulsing due to the way it calculates its duty cycle. All amplifiers can be controlled by a hardware power control on the transmitter. This is usually used for the set-up procedure but the powers can also be set using the software, allowing more freedom in pulse sequences. Powers are measured by connecting the output to an oscilloscope and measuring the peak-to-peak voltage, then converting this to Watts. It is important to know the power going into the probe as too large a power can cause degradation. The specification for each probe is different.

### **Probes - HX**

Only one probe was employed during the course of this work for observing  $^1\text{H}$ ,  $^{13}\text{C}$  and  $^{15}\text{N}$ , namely the HX, which is a double-channel probe. This probe can be used for magic angle spinning (MAS) or static work. Each probe contains a spinning module that can be set at the magic angle. All probes use zirconia rotors, shown in Figure 1, but the size of these depends on the probe to be used. Rotors contain an end cap, spacer and drive tip made of Kel-F protruding out of the bottom. Two spacers can be placed so as to limit the sample to the central portion of the rotor. The end caps and spacers are both made from Teflon. Different length end caps and spacers can be used.

The X channel in this probe is tunable in the range 19.4-82.6 MHz and is used in conjunction with 200.13 MHz for protons. The frequency to which the X channel is to be tuned is altered by changing 'top' and 'bottom' plug-in capacitors designed for the probe.  $^1\text{H}$  decoupling powers equivalent to about 60 kHz (4  $\mu\text{s}$  90° pulse) are possible for this probe.

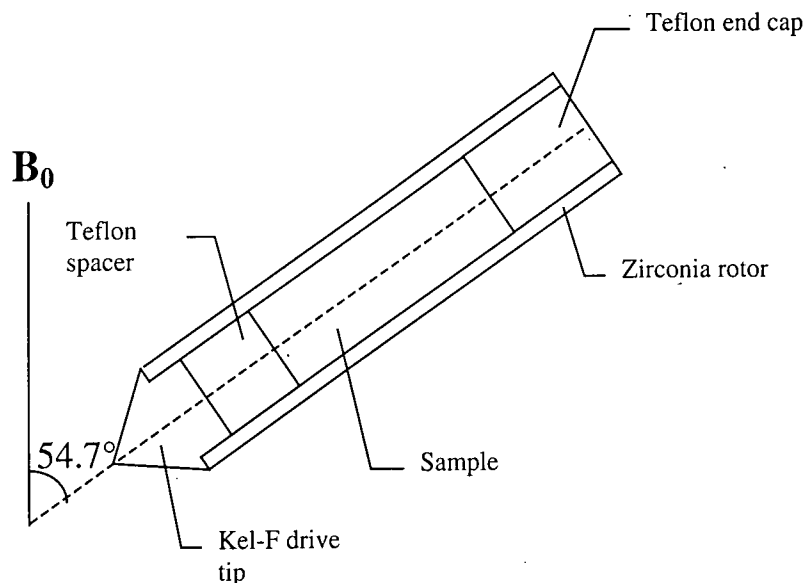


Figure 1: A rotor used for MAS.

The rotors are 7.5 mm in outer diameter with a maximum sample length of 1.5 cm. A spin rate of up to 6.5 kHz is possible. The rotors for the Doty probes used in the Varian spectrometer, see section 2.1.4, are of a similar design but the two end caps are flat – one fluted, the other marked half black, half white for optical speed measurement.

### 2.1.2 Sample Handling

None of the compounds discussed in this thesis are air or moisture sensitive, so rotors could be packed in a normal laboratory environment. Care must be taken when packing the sample to enable smooth spinning. Several of the compounds used here needed to be ground gently to allow even packing.

### 2.1.3 Experimental Set Up

The following section will detail the set-up procedure for  $^1\text{H}$  to  $^{13}\text{C}$  cross polarisation<sup>3</sup> (CP) using the HX probe. The arrangement of the hardware used for observation is the same for all probes and is shown in Figure 2.

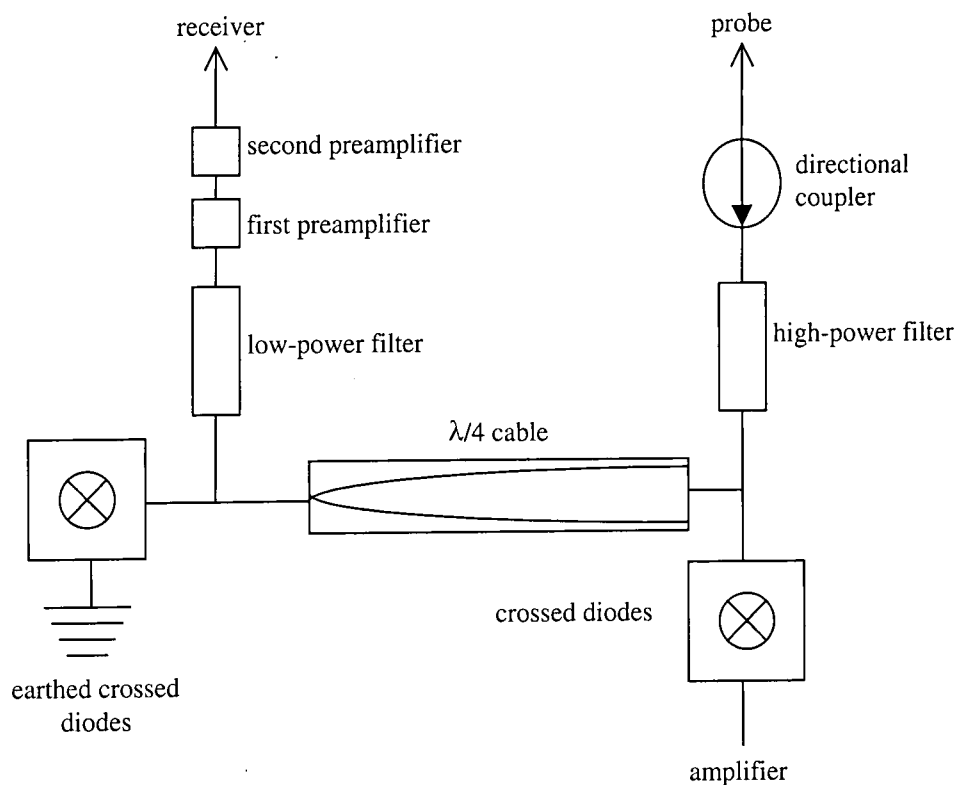


Figure 2: Hardware arrangement used in the CMX 200 spectrometer.

A high-power band-pass 200 MHz filter is used for protons and a high-power low-pass 100 MHz filter is required for the  $^{13}\text{C}$  and  $^{15}\text{N}$ . A low-power filter can be placed before the preamplifier to remove noise further.

## Tuning

Inside the probe is a wire coil that surrounds the sample. This wire transmits the r.f. pulses to the sample and then receives the NMR signal back. It is vital that the impedance of the wire be identical to those of the transmitter and receiver for maximum power transfer. To match the impedance (of  $50\ \Omega$ ) correctly, two capacitors deep inside the probe resonant circuit can be adjusted. Adjusting one of the capacitors changes the resonance frequency of the circuit. This adjustment is carried out so the circuit resonance frequency matches the precessional frequency of the observed nucleus. The other capacitor controls the impedance of the circuit and is adjusted to match the probe impedance. The inductance of the coil will vary from sample to sample, so in solid-

state work it is necessary to tune the probe separately for each sample. Both capacitors must be altered in conjunction with each other as changes in one affect the other.

Tuning is done using a directional coupler between the probe and transmitter output. A pulse program called 'tune' that uses a low power is used. The reflected power, observed using the directional coupler, is minimised by altering the tune and match on the probe to produce a 'dip' which rests on the baseline at 0.5 virtual units on the display scale on the screen. This process is carried out taking the r.f. directly through the directional coupler without taking it through the crossed diodes or filter. This is done because the crossed diodes and filters are designed for high-power r.f. but the tune program uses low power. The circuit is then tuned again using high power to optimise the tuning at the conditions to be used. This is done by minimising the reflected power observed on an oscilloscope.

### Setting proton 90° pulse duration and power

Polydimethylsiloxane (PDMSO) is used to set the  $^1\text{H}$  90° pulse. The sample does not need to be spun as it is a viscous solution giving relatively large intrinsic linewidths. It is desirable to set a 4-5  $\mu\text{s}$  90° pulse for adequate decoupling on the HX probe. This is measured by observing a 180° null signal at twice the desired 90° pulse value. The r.f. output dial on the transmitter is altered while repetitively pulsing and processing a single-pulse experiment and observing how the pulse height changes. This value is checked by a pulse duration array.

When observing  $^{13}\text{C}$ , this value for the  $^1\text{H}$  90° pulse may be used for cross polarisation and decoupling. If cross polarisation to  $^{15}\text{N}$  is required, however, a 4-5  $\mu\text{s}$  90° pulse must be used for adequate decoupling. However, a lower power is essential for cross polarisation because the  $\gamma_{^{15}\text{N}}$  is much lower than that for  $^1\text{H}$  ( $\gamma_{^{15}\text{N}} = -2.712 \cdot 10^7 \text{ rad T}^{-1} \text{ s}^{-1}$ ,  $\gamma_{^{13}\text{C}} = 6.7283 \cdot 10^7 \text{ rad T}^{-1} \text{ s}^{-1}$ ,  $\gamma_{^1\text{H}} = 26.7520 \cdot 10^7 \text{ rad T}^{-1} \text{ s}^{-1}$ ). This means the probe would not withstand the high power that would have to be applied on the X channel to achieve a match ( $\gamma_{^1\text{H}} B_{1\text{H}} = \gamma_{^{15}\text{N}} B_{1\text{N}}$ ). A 7  $\mu\text{s}$   $^1\text{H}$  90° pulse must be set using the software power amplitude control.

## Setting the X channel

All the experiments performed on the CMX 200 used cross polarisation to reduce the recycle delay and increase sensitivity by  $\gamma_{1H}/\gamma_{13C}$ . This means that setting up the X channel involves finding the Hartmann-Hahn matching condition, which allows efficient transfer of magnetisation from  $^1H$  to X. The r.f. output dial on the transmitter for the correct channel is altered while maximising a repetitively pulsing FID.

Adamantane is used for  $^{13}C$  set-up. It must be spun slowly, 1-1.5 kHz, as at higher speeds the matching profile breaks down into sidebands.<sup>4</sup> At the match  $B_{1C} \approx 4 B_{1H}$  as  $\gamma_{1H} \approx 4 \gamma_{13C}$ . Doubly labelled  $NH_4NO_3$  is used to set up for  $^{15}N$ .

## Shimming

Inhomogeneities in  $B_0$  produce a range of precession frequencies as different parts of the sample experience a different field. This means that broad and unsymmetrical lines can be observed. These inhomogeneities are compensated for by altering the current going down the shim coils situated in the bore of the magnet while monitoring the lineshape and width of a standard which responds well to changes in the shims such as adamantane for  $^{13}C$ . If shimmed acceptably this should have a linewidth of less than 5 Hz. This process is called shimming. There are two types of shims, superconducting and room temperature. The cryogenic shims are adjusted when the magnet is initially run up to field. The other set is adjusted as described above.

## Magic Angle Spinning<sup>5</sup>

The magic angle is set using a sample chosen for its sensitivity to orientation in a magnetic field. The probes used only allow the angle to be altered by a few degrees either side of the magic angle. When observing  $^{13}C$  (50.329 MHz), the magic angle (54.7°) is set observing the  $^{79}Br$  (50.143 MHz) signal from KBr at a MAS rate of 2-3 kHz. The number of rotational echoes observed in the FID for this sample is

maximised. These are present due to the effect of MAS on the quadrupolar interaction. This interaction is non-zero because of imperfections in the KBr lattice (cubic). The lineshape of the aromatic carbon signal in hexamethylbenzene spinning at  $\sim 4$  kHz can also be used to set the magic angle. If the angle is a long way from its correct value the asymmetry of this peak indicates whether the angle is too large or too small. When observing  $^{15}\text{N}$  it is more convenient to observe the lineshape of the nitrate peak in doubly labelled  $\text{NH}_4\text{NO}_3$ .

The MAS rate is controlled using a spinning speed controller which allows manual or automatic control. This can be operated using the software or the controller itself. Control of the speed is possible to within  $\pm 1$  Hz of the desired value. The speed is read using optical fibres situated at the top of the spinning module which observe a black mark on the top of the rotor as it spins.

## Referencing

The samples in Table 2 are used in setting powers and for referencing.

Nucleus	Frequency / MHz	Reference sample	Primary standard at 0 ppm	$\delta$ with respect to primary standard / ppm
$^1\text{H}$	200.130	$\text{PDMSO}_{(l)}$	TMS	0
$^{13}\text{C}$	50.329	Adamantane $_{(s)}$	TMS	38.4 <sup>a</sup>
$^{15}\text{N}$	20.288	$^{15}\text{NH}_4^{15}\text{NO}_{3(s)}$	$\text{CH}_3\text{NO}_{2(l)}$	-5.1 <sup>b</sup>

<sup>a</sup> High frequency resonance

<sup>b</sup> Nitrate peak

*Table 2: Standard samples used for referencing.*

Nitrogen-15 referencing is rather more complicated than referencing for other nuclei due to the different standards used in the solid and solution-state. Figure 3 shows how these systems are related.

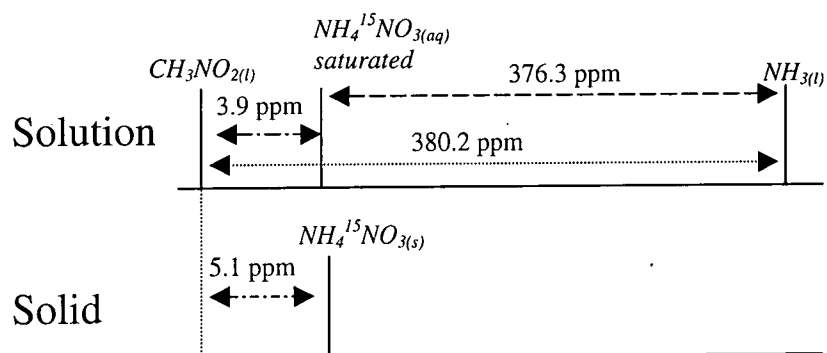


Figure 3: Summary of shift comparison between solid and solution NMR.<sup>6,7</sup>

### Variable Temperature

The CMX probes used in this work are able to perform variable temperature (v.t.) experiments in the range 123-523 K.

#### Variable-temperature operation

There are two gas supplies entering the probe; one is used for spinning, the other for v.t. operation. The temperature of the sample is altered by passing  $N_{2(g)}$  over the rotor. This  $N_{2(g)}$  is cooled or heated by passage through a copper coil. If high temperature is required the  $N_{2(g)}$  is heated inside the v.t. stack (which is itself inside the magnet and attached to the probe). If low temperature is required, the copper coil is immersed in a dewar of liquid nitrogen to cool it, and it is then heated to the required temperature. A thermocouple measures the temperature of the outlet gases and this value is displayed on the v.t. controller.

Usually the spinning gas used is dry air. For v.t. operation above 373 K and below 273 K  $N_{2(g)}$  must be used for spinning as well as for the v.t. gas. If air is used above 373 K there is a danger that the  $O_{2(g)}$  present would oxidise parts of the probe. Below 273 K  $O_{2(g)}$  may be condensed.

#### Variable-temperature calibration

In solid-state NMR there are effects that must be taken into account when doing v.t. experiments. There may be heating and pressure effects due to MAS, and temperature gradients may exist within the rotor due to the bearing and drive gasses being at room

temperature. These effects mean the reading of the thermocouple and the actual sample temperature may be considerably different.

It is therefore necessary to calibrate the sample temperature with the reading from the thermocouple. To do this a sealed sample of absolute ethanol absorbed onto TTMSS (tetrakis(trimethyl)silane) was used. The method of Aliev et. al. was followed<sup>8</sup> in which the separation of the methyl and hydroxyl peaks are measured as a function of temperature. Experiments were performed at temperatures ranging from 173 to 313 K on all probes and at different MAS rates to examine the effects of sample spinning.<sup>9</sup> For the HX probe, which uses 7.5 mm outer diameter rotors, it was found that there was a large difference between the actual sample temperature and thermocouple reading, particularly at the higher spin rates. For example a thermocouple reading of 173 K spinning at 1 kHz has an actual sample temperature of 195.6 K, whereas when spinning at 5 kHz this increases to 210.4 K. For further detail see the thesis of Nordon.<sup>10</sup> All v.t. temperatures quoted in this thesis have been corrected to give the actual sample temperatures.

#### ***2.1.4 Varian Unity Plus 300***

This system uses Doty probes with a double bearing, one of which takes 7 mm zirconia rotors and the other 5 mm rotors for faster spinning. Both these probes operate in double channel mode, one for X observe and the other for cross polarisation from, and decoupling of, protons. A Varian console with VNMR software is used to control the system.

#### ***2.1.5 CMX 600 Infinity***

This spectrometer is very similar in operation to the CMX 200. A triple-channel probe which accepts rotor of 4 mm diameter was used. This has a maximum spinning speed of 20 kHz, maximum <sup>1</sup>H power of 125 kHz (2 μs 90° pulse) and maximum X channel power of 100 kHz (2.5 μs 90° pulse). The Y channel was not used.

The probe is tuned by minimising the reflected power so that the ratio of forward to reflected power is greater than 20:1. These powers are measured on an oscilloscope. Powers are set using only software control. The amplifiers used are a CE for  $^1\text{H}$  and an AMT for  $^{13}\text{C}$ . A separate preamplifier is used for each channel.

There is a need for variable amplitude cross-polarisation sequences to increase the cross polarisation efficiency for the high spinning speeds used.

### ***2.1.6 Pulse Programs***

**1pulse:** This was used on the CMX spectrometers. It consists of a single pulse on one channel followed by acquisition and then a recycle delay.

**1pda:** This was used on the CMX spectrometers. This is a single pulse on one channel with decoupling on the other during acquisition followed by a recycle delay.

**cpflip:** This was only used on the CMX 200 spectrometer. It is simple CP sequence with flip back of the proton magnetisation into the z-direction.

Similar sequences were used on the 300 and 600 MHz spectrometers.

## **2.2 Solution-state NMR Spectrometers**

Four solution-state spectrometers have been used in this work: a Varian Unity 300, VXR 400S and a Varian Inova 500 all situated in Durham University and a Bruker AMX 400 situated at Avecia, Blackley. Solution-state spectra recorded on the Varian VXR 400S and Varian Inova 500 and were obtained by Catherine Heffernan and Ian McKeag respectively. The Bruker AMX 400 spectrometer was operated by Robert Glover and latterly by Graham McPherson.

### 2.2.1 Probes

The Varian Unity 300 and Varian Inova 500 spectrometers both use 5 mm switchable probes which are tuned to  $^1\text{H}$  and  $^{13}\text{C}$ . The VXR 400S spectrometer uses a 4 nucleus probe tuned to  $^1\text{H}$ ,  $^{19}\text{F}$ ,  $^{13}\text{C}$  and  $^{31}\text{P}$ . The Varian Inova 500 also has an inverse probe which has the  $^1\text{H}$  coil inside the  $^{13}\text{C}$  coil. This is useful if doing HETCOR experiments as it means the  $^1\text{H}$  signal can be observed, which increases the signal:noise ratio.

### 2.2.2 Experimental Set Up

A number of standard parameters are stored in the spectrometer which can be recalled by entering the nucleus and solvent for rapid set up. This is done after locking and shimming have been carried out as explained below.

#### Deuterium Lock<sup>11</sup>

FIDs have to be accumulated and stored over long periods to obtain an acceptable signal:noise ratio. During this time there may be small drifts in the magnetic field. The signal is therefore locked to a standard to compensate. The deuterium line of the solvent is used for this as well as for the shimming process. The deuterium lock maintains a constant ratio between the static field and the r.f. If the receiver phase is adjusted correctly, then the signal will be exactly on resonance. The lock frequency remains fixed and the lock field is changed.

Two other parameters that need to be considered when using solution-state NMR are:

1) r.f. power and 2) the gain of the lock signal. If too much power is applied the deuterium nucleus will be saturated, which will produce line broadening and variation of signal amplitude. It is desirable to achieve the highest transmitter power level that is just below the saturation limit to obtain a good lock-signal amplitude. The gain of the lock signal should be optimised, since too high a lock gain will result in over amplification of the lock signal, causing excessive noise.

## Shimming

The shimming of solution-state spectrometers is the same as for solids except that the intensity of the deuterium lock is monitored while altering the shims. Also, significantly higher resolution (and therefore magnetic field homogeneity) is required. However, this may be achieved because narrow-bore magnets are used.

### 2.2.3 Referencing

All proton spectra are referenced to TMS (tetramethylsilane), which is added to the solution under investigation. TMS is not soluble in D<sub>2</sub>O so DSS (3-(trimethylsilyl)propanesulphonic acid sodium salt) is used in this case. Carbon-13 spectra were referenced to the same compounds via DMSO (dimethylsiloxane) at 40.48 ppm or if d<sub>6</sub>-DMSO was used as the solvent the DMSO peak is referenced at 39.50 ppm.

### 2.2.4 Variable Temperature

#### Variable-temperature operation and calibration

A Varian temperature controller was used to regulate the temperature when doing variable temperature experiments. Nitrogen gas was used as the v.t. gas for temperatures below ambient and above 90 °C, as with v.t. using the CMX 200 spectrometer. The v.t. gas was cooled using the same method as for the CMX 200. Care must be taken to keep the sample depth small when doing v.t. experiments to ensure the whole sample is at the correct temperature. To calibrate the v.t. controller below room temperature, a short sample of methanol was used and the difference between the methyl and hydroxyl peaks was measured at different temperatures.<sup>12,13</sup> Above room temperature 1,2-ethanediol was used.<sup>12,13</sup>

### 2.2.5 Pulse Sequences

#### COSY

COSY (CORrelation SpectroscopY)<sup>14</sup> is a common method of assigning proton spectra. It is a 2D technique in which cross peaks occur if spin coupling is present. The basic COSY experiment consists of two  $90^\circ$  pulses separated by an incremental time  $t_1$ .<sup>15</sup> The first pulse (the preparation pulse) transforms z-magnetisation into transverse magnetisation for all allowed transitions. During  $t_1$  (the evolution period) the magnetisation components are labelled with their characteristic precession frequencies. The spins evolve due to their respective chemical shifts. Spin-spin coupling also develops. The second r.f. pulse (the mixing pulse) causes transfer of magnetisation components among all those transitions which belong to the same coupled spin system. The distribution of labelled magnetisation components is determined by measuring their new precession frequencies during the acquisition period,  $t_2$ .<sup>16,17</sup>

The standard COSY works best for spin-spin coupling constants between 3 and 15 Hz. There are several variations on this pulse sequence. The pulse sequence actually used in the present work is shown in Figure 4. In this case the third pulse acts in combination with the second pulse as a double quantum filter.<sup>16</sup>

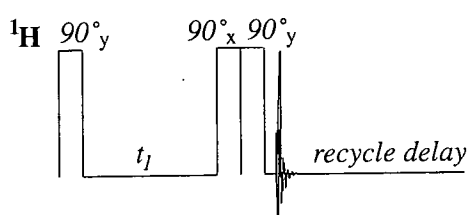


Figure 4: DQF-COSY pulse sequence.

#### EXSY

EXSY (Exchange SpectroscopY), shown in Figure 5, is a 2-dimensional experiment to detect chemical exchange.<sup>18</sup>

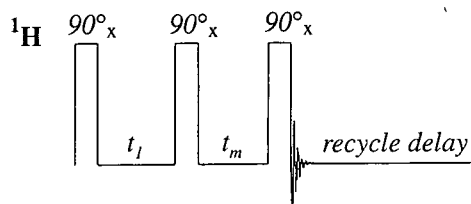


Figure 5: EXSY pulse sequence.

In this pulse sequence,  $t_1$  is the evolution time and  $t_m$  (the mixing time) is the time during which chemical exchange occurs. The first pulse, in the x direction, puts the magnetisation along the y axis. During  $t_1$  the transverse magnetisation precesses about  $B_0$  and is sampled incrementally to provide the second dimension. The second pulse, which is also applied along the x axis, rotates the magnetisation into the xz plane, of which the z component is significant. During  $t_m$  the magnetisation undergoes spin-lattice relaxation and chemical exchange. The third pulse (x) put the instantaneous z-magnetisation onto the y axis to allow it to be measured during the acquisition.

Each site produces a 2D peak at its Larmor frequency in both dimensions i.e. along the diagonal. If there is exchange between two sites at frequencies of  $\omega_A$  and  $\omega_B$ , during the mixing period, nuclei that are in site A during  $t_1$  (so having a precessional frequency of  $\omega_A$ ), will exchange to site B during  $t_m$  (so having a precessional frequency of  $\omega_B$ ). The result is that they will produce a cross peak at  $\omega_A, \omega_B$ .

### Decoupled $^{13}\text{C}$

Carbon-13 spectra are usually obtained while applying  $^1\text{H}$  decoupling. Figure 6 shows the pulse sequence typically used.<sup>16</sup> The benefits of proton decoupling are two-fold. Firstly decoupling during the acquisition leads to simplification of the spectrum as splittings arising from  $^{13}\text{C}$  coupling to  $^1\text{H}$  are removed. Decoupling during the recycle delay leads to nOe (nuclear Overhauser effect) enhancement, and therefore increased signal intensity. The recycle delay is often chosen to be shorter than that which allows total relaxation of the quaternary carbons to save time, i.e. accepting lower signal intensity.

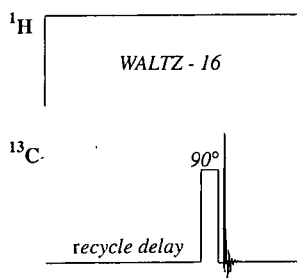


Figure 6: Broad-band decoupled  $^{13}\text{C}$  pulse sequence.

### Coupled $^{13}\text{C}$

To provide information about  $^1\text{H}$ - $^{13}\text{C}$  spin-spin coupling constants, the gated decoupled pulse sequence is implemented (see Figure 7).<sup>16</sup> Proton decoupling is used during the recycle delay only, which maintains the advantages of nOe enhancement. After the decoupler is switched off (at the beginning of the acquisition)  $^1\text{H}$ - $^{13}\text{C}$  coupling is observed.

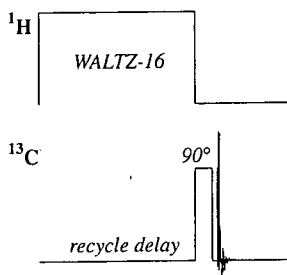


Figure 7: Gated-decoupled  $^{13}\text{C}$  pulse sequence.

### J-MOD-X

To obtain information about the  $^{13}\text{C}$  multiplicities, the J-modulated spin-echo (J-MOD-X) pulse sequence is employed, see Figure 8.<sup>19</sup> Proton decoupling provides nOe enhancement and simplifies the spectrum.  $\text{CH}_n$  spin vectors develop differently after a  $90^\circ$  pulse depending how many hydrogens are attached. If the delay  $d1$  is set to  $1/J(\text{C})$ ,

H) then CH and CH<sub>3</sub> vectors will have the opposite phase to C and CH<sub>2</sub>. The 180° pulse refocuses chemical shifts.

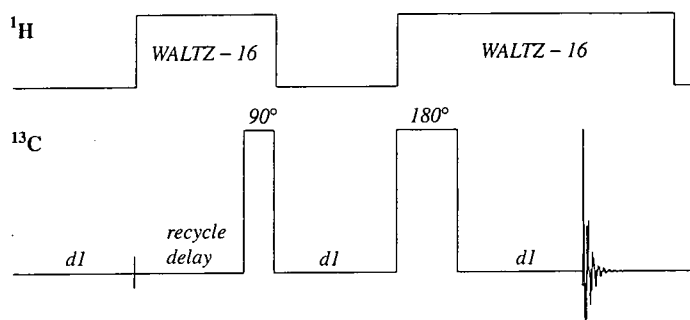


Figure 8: J-MOD-X <sup>13</sup>C pulse sequence.

### gs-HMQC

The HMQC (Hetero Multinuclear Quantum Coherence) sequence, Figure 9, is a 2D pulse sequence designed to correlate the chemical shifts of directly bonded <sup>1</sup>H and <sup>13</sup>C nuclei via <sup>1</sup>J(CH). It is inversely detected to reduce the acquisition time.<sup>20</sup> Here a gradient version is shown (gs=gradient selected). The gradient strength ratio is chosen so that only the selected pathway can be detected and all other coherences are effectively dephased.<sup>21</sup> The coherence pathways are shown in Figure 9, I<sub>H</sub> and I<sub>C</sub> are the density matrix elements of interest. The first proton pulse creates transverse proton magnetisation. The delay time, dl, is chosen to be  $1/\{2J(C, H)\} = 3.5$  ms, corresponding to <sup>1</sup>J(C, H) = 145 Hz.

To improve signal-to-noise and reduce the complexity of the 2D data acquired, the gs-HMQC is acquired using the GARP technique (Globally optimised Alternating-phase Rectangular Pulses; a multiple-pulse, broadband decoupling scheme). If no decoupling was utilised, splitting in the <sup>1</sup>H dimension would be observed, with a magnitude of the spin-spin coupling constant. Furthermore, by reducing the correlated peak to a single line for each CH<sub>n</sub> group, the signal intensity is increased, improving the overall signal-to-noise.

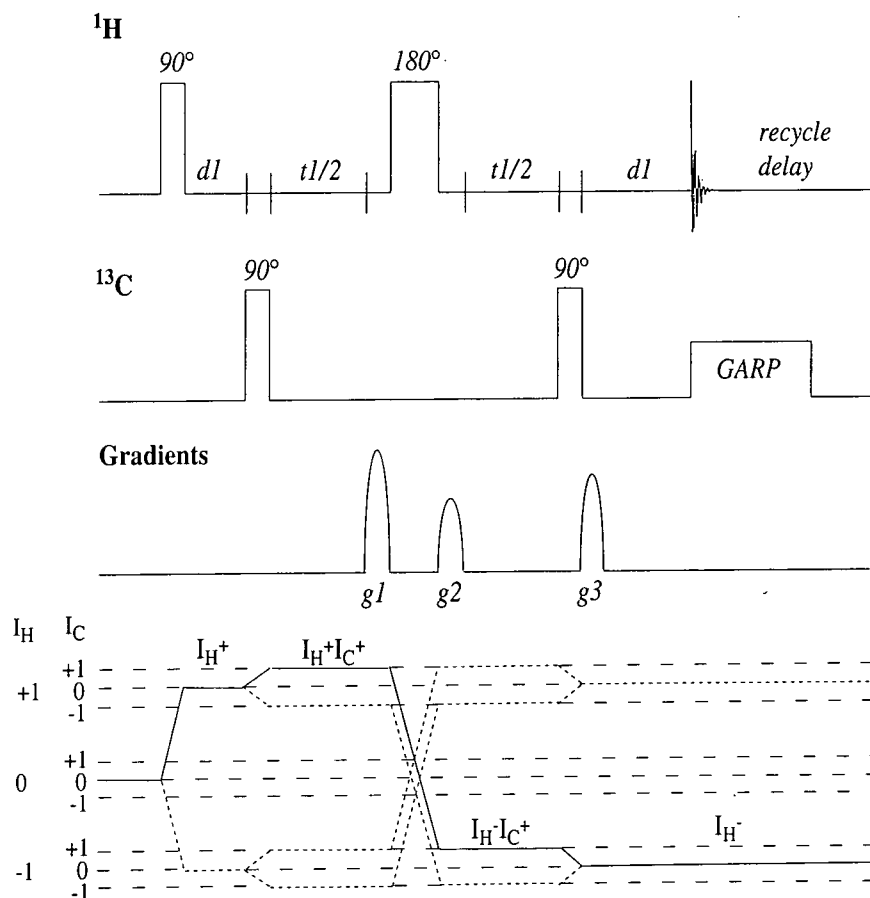


Figure 9: gs-HMQC  $^1\text{H}$ - $^{13}\text{C}$  pulse sequence.

### gs-HMBC

To obtain long-range H, C correlations via  $^2J(\text{C}, \text{H})$  and  $^3J(\text{C}, \text{H})$  one can set the delay ( $d1$ ) in a HMQC sequence to 60 ms, corresponding to a spin coupling constant of 8 Hz. Alternatively a different pulse sequence called HMBC (Heteronuclear Multiple Bond Correlation) can be used,<sup>22</sup> which allows suppression of correlations via  $^1J(\text{C}, \text{H})$  using a low-pass filter. A gradient version of this is shown in Figure 10.<sup>23</sup>

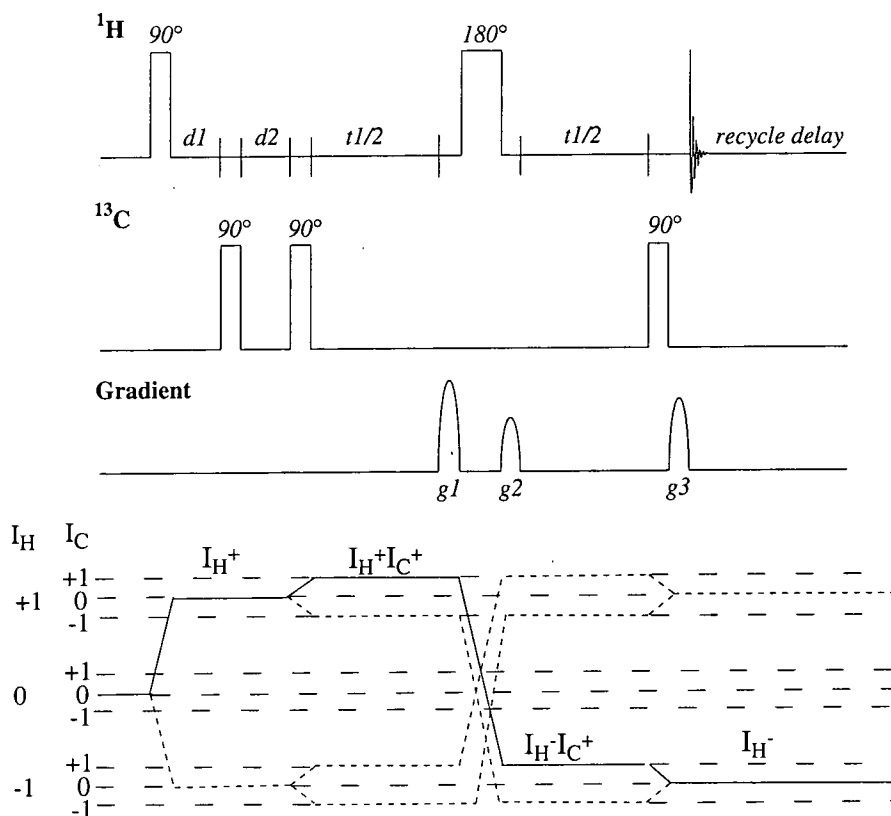
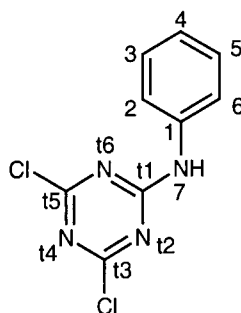


Figure 10:  $gs$ -HMBC  $^1H$ - $^{13}C$  pulse sequence.

The delay,  $d1$ , is set to  $1/2^1J(C, H)$ , and acts as a low-pass filter to suppress one-bond couplings. As  $^1J(C, H)$  is a variable figure between 125 and 163 Hz, some one-bond couplings are not effectively suppressed. Therefore, GARP decoupling is not applied, which enables these signals to be identified. The second  $^{13}C$  pulse selects proton signals experiencing long-range C, H coupling. The rest of the sequence is similar to the  $gs$ -HMQC sequence shown in Figure 10 but a delay ( $d2$ ) of 60 ms, equivalent to a coupling of 8 Hz to allow the evolution of long-range couplings, is implemented.

## 2.3 Synthesis of New Compounds

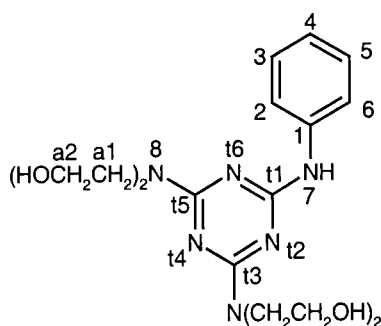
### 2.3.1 2-phenylamino-4,6-chloro-1,3,5-triazine



1

A solution of aniline (10 g, 108.4 mmol) in acetone (150 ml) was added to a solution of cyanuric chloride (20 g, 108 mmol) in acetone (183 ml) at 0 °C. Aqueous sodium hydrogen carbonate (9.2 g in 111 ml, 108.4 mmol) was then added to the mixture over 30 minutes whilst maintaining a temperature of 0–5 °C. The solution was stirred for 1.5 hours. Reaction was shown to be complete by HPLC (High Pressure Liquid Chromatography).  $\text{HCl}_{(\text{aq})}$  (20 ml, 2M) was added until a precipitate formed which was filtered and washed with acetone.

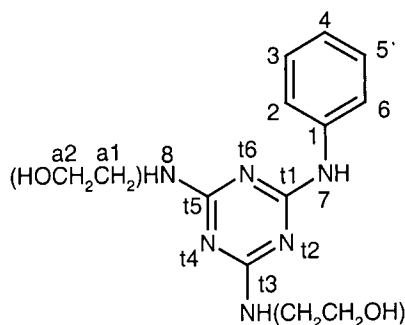
### 2.3.2 2-phenylamino-4,6-diethanolamino-1,3,5-triazine



2

Compound **1** (5 g, 92.21 mmol) was added to diethanolamine (50 ml) and heated at 90 °C for 4 hours. The solution was poured into water (500 ml) and  $\text{HCl}_{(\text{aq})}$  (30 ml, 2M) was added until an acidic suspension was formed, which was then filtered and dried. It was recrystallised from ethyl acetate. m.p. 107.5 – 109.0 °C;  $\nu_{\text{max}}(\text{neat})/\text{cm}^{-1}$  3264 (OH), 2926 ( $\text{CH}_2$ ), 2860 ( $\text{CH}_2$ ), 1578 (t), 1424 (t), 803 (t);  $\delta_{\text{H}}(300 \text{ MHz}; \text{d}_7\text{-DMF}; \text{Si}(\text{CH}_3)_4)$  3.73 and 3.76 (16 H, m, a1 and a2), 4.87 (4 H, m, OH), 6.93 (1 H, m, H4), 7.28 (2 H, m, H3 and H5), 7.90 (2 H, m, H2 and H6), 8.15 (1 H, s, NH);  $\delta_{\text{C}}(100.03 \text{ MHz}; \text{d}_7\text{-DMF})$  51.72 and 51.81 (a1), 60.78 and 60-81 (a2), 119.88 (C2 and C6), 121.77 (C4), 129.04 (C3 and C5), 141.87 (C1), 164.83 (t1), 165.86 (t3 and t5);  $m/z$  (ES+) 379 ( $\text{M}^+ + 1$ ); [Found: C, 53.79; H, 6.94; N, 22.18.  $\text{C}_{17}\text{H}_{26}\text{N}_6\text{O}_4$  requires C, 53.95; H, 6.93; N, 22.21%].

### 2.3.3 2-phenylamino-4,6-ethanolamino-1,3,5-triazine

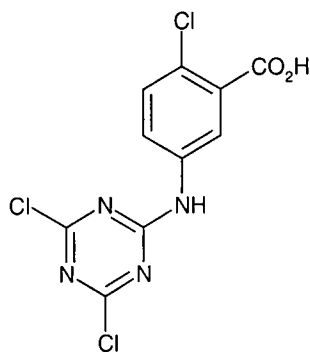


**3**

Compound **1** (5 g, 92.21 mmol) was added to ethanolamine (50 ml) and heated at 90 °C for 4 hours. The reaction mixture was poured onto water (500 ml) and the product extracted into dichloromethane (DCM, 200 ml).  $\text{HCl}_{(\text{aq})}$  (50 ml, 2M) was added until the aqueous layer was acidic. The product was washed until the aqueous layer was clear and colourless and the solvent then removed. The product was recrystallised from ethanol. m.p. 128.0 – 128.5 °C,  $\nu_{\text{max}}(\text{neat})/\text{cm}^{-1}$  3424 (NH), 3291 (OH), 2971 ( $\text{CH}_2$ ), 2941 ( $\text{CH}_2$ ), 2897 ( $\text{CH}_2$ ), 1550 (t), 1420 (t), 800 (t);  $\delta_{\text{H}}(300 \text{ MHz}; \text{d}_7\text{-DMF}; \text{Si}(\text{CH}_3)_4)$  3.50 (4 H, m, a2), 3.67 (4 H, m, a1), 4.84 (2 H, s, OH), 6.76 (2H, s, H8), 6.93 (1 H, m, H4), 7.26 (2 H, m, H3 and H5), 7.91 (2 H, m, H2 and H6), 8.86, 9.04 and 9.19 (1 H, s, H7);  $\delta_{\text{C}}(100.03 \text{ MHz}; \text{d}_7\text{-DMF})$  43.92 (a1), 61.51 and 61.61 (a2), 120.07 (C2 and C6),

121.79 (C4), 128.94 (C3 and C5), 141.87 (C1), 165.15 (t1), 166.90 (t3 and t5);  $m/z$  (ES+) 291 ( $M^+ + 1$ ); [Found: C, 53.53; H, 6.31; N, 28.67.  $C_{13}H_{18}N_6O_2$  requires C, 53.78; H, 6.25; N 28.95%].

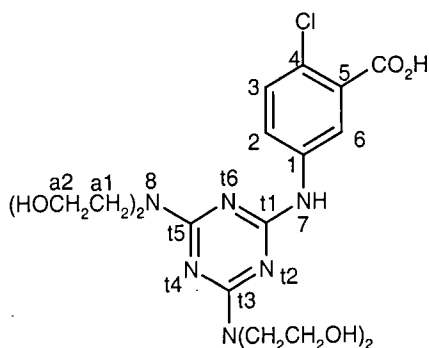
### 2.3.4 2-(3-carboxy-4-chloro-phenylamino)-4,6-chloro-1,3,5-triazine



4

To an aqueous solution of the 3-carboxy-4-chloroaniline (25.6 g, 108.4 mmol in 360 ml water), basified to pH 7 with  $NaOH_{(aq)}$  (40 ml, 2M) at 0 °C, was added a solution of cyanuric chloride (20 g, 108.4 mmol) in acetone (180 ml) and the system was stirred for 2 hours. The reaction was shown to be complete by HPLC. This product was not isolated.

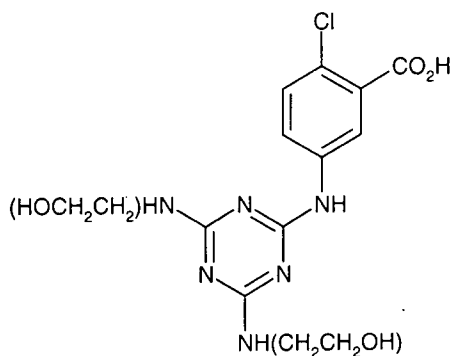
### 2.3.5 2-(3-carboxy-4-chloro-phenylamino)-4,6-diethanolamino-1,3,5-triazine



5

Diethanolamine (12.5 g, 119.2 mmol) was added to a solution of compound **4** (17.3 g, 54.2 mmol in 90 ml acetone, 180 ml water, 20 ml of 2M NaOH<sub>(aq)</sub>) at room temperature and pH 7 and the reaction stirred for 18 hours. The reaction was shown to be complete by HPLC. HCl<sub>(aq)</sub> (20 ml, 2M) was added until a precipitate formed, which was filtered and washed with HCl<sub>(aq)</sub> (50 ml, 2M). The product was dissolved in 200 ml water to form a white suspension. Diethanolamine (17.0 g, 162.6 mmol) was added and the pH adjusted to pH 9 with NaOH<sub>(aq)</sub> (10 ml, 2M). The solution was stirred for 4 hours at 70 °C and the reaction shown to be complete by HPLC. The product was recrystallised from ethanol. m.p. 169.0 – 171.0 °C;  $\nu_{\max}(\text{neat})/\text{cm}^{-1}$  3212 (NH), 2886 (OH), 2588 (CH<sub>2</sub>), 1710 (CO<sub>2</sub>H), 1550 (t), 1504 (Ph), 1428 (t), 828 (t), 750 (CCl);  $\delta_{\text{H}}(300 \text{ MHz}; \text{d}_7\text{-DMF}; \text{Si}(\text{CH}_3)_4)$  3.75 and 3.078 (16 H, m, a1 and a2), 7.44 (1 H, d J=8.70 Hz, H3), 7.96 (1 H, m, H2), 8.65 (1 H, d J=2.68 Hz, H6), 9.51 (1 H, s, H7);  $\delta_{\text{C}}(100.03 \text{ MHz}; \text{d}_7\text{-DMF})$  52.64 (a1), 60.33 (a2), 123.02 (C6), 124.33 (C2), 127.59 (C5), 132.23 (C3), 132.37 (C4), 137.47 (C1), 115.8 (t1, t3 and t5), 166.99 (CO<sub>2</sub>H); m/z (ES-) [Found: 455.1463 (M<sup>-</sup>1). C<sub>18</sub>H<sub>25</sub>N<sub>6</sub>O<sub>6</sub>Cl requires 455.1446]; [Found: C, 43.37; H, 5.47; N, 16.57. C<sub>18</sub>H<sub>25</sub>N<sub>6</sub>O<sub>6</sub>Cl requires C, 47.31; H, 5.52; N, 18.40%].

### 2.3.6 2-(3-carboxy-4-chloro-phenylamino)-4,6-ethanolamino-1,3,5-triazine



**6**

Ethanolamine (20 g, 325.2 mmol) was added to a solution of compound **4** (17.3 g, 54.2 mmol in 90 ml acetone, 180 ml water, 20 ml of 2M NaOH<sub>(aq)</sub>) at room temperature and stirred for 18 hours, after which time the temperature was increased to 90 °C and the

system stirred for a further 4 hours. When the reaction was shown to be complete by HPLC, it was allowed to cool and the solution acidified using  $\text{HCl}_{(\text{aq})}$  (10 ml, 2M) to pH 4 to produce the precipitate which was filtered and dried.

The other compounds used were obtained from the compound collection maintained by Avecia Ltd.

## 2.4 References

- <sup>1</sup> Chemagnetics User's Guide © Otsuka Electronics (U.S.A) Inc. 1996.
- <sup>2</sup> Chemagnetics Spinsight. Version 3.5.2 © Otsuka Electronics (U.S.A.) Inc.
- <sup>3</sup> A. Pines, M. G. Gibby and J. S. Waugh, *J. Chem. Phys.*, **59**, 569 (1973).
- <sup>4</sup> E. O. Stejskal, J. Schaefer, J. S. Waugh, *J. Magn. Reson.*, **28**, 105 (1977).
- <sup>5</sup> E. R. Andrew, A. Bradbury and R. G. Eades, *Nature*, **182**, 1659 (1958).
- <sup>6</sup> S. Berger, S. Braun and H. O. Kalinowski, '*NMR spectroscopy of the non-metallic elements*', Wiley, 113, 1997.
- <sup>7</sup> S. C. Campbell, *Ph.D. Thesis*, Pharmaceutical polymorphism: an investigation using solid-state nuclear magnetic resonance spectroscopy, Durham, 1998.
- <sup>8</sup> A. E. Aliev and K. D. M. Harris, *Magn. Reson. Chem.*, **32**, 366, (1994).
- <sup>9</sup> X. Wu and K. W. Zilm, *J. Magn. Reson.*, **A. 104**, 154 (1993).
- <sup>10</sup> A. Nordon, *Ph.D. Thesis*, Durham, 1997.
- <sup>11</sup> Atta-ur-Rahman and M. I. Choudhary, '*Solving Problems with NMR Spectroscopy*', Academic Press, London, 1996.
- <sup>12</sup> A. L. Van Geet, *Anal. Chem.* **40**, 2227 (1968).
- <sup>13</sup> A. L. Van Geet, *Anal. Chem.*, **42**, 679 (1970).
- <sup>14</sup> W. P. Aue, E. Bartholdi and R. R. Ernst, *J. Chem. Phys.*, **64**, 2229 (1975).
- <sup>15</sup> K. Nagayama, A. Kumar, K. Wutherich and R. R. Ernst, *J. Magn. Reson.*, **40**, 321 (1980).
- <sup>16</sup> S. Baun, H. O. Kalinowski and S. Berger in *100 and More Basic NMR Experiments*, VCH Verlagsgesellschaft and VCH Publishers, Weinheim and New York, 1996.
- <sup>17</sup> H. Friebolin in *Basic One- and Two-Dimensional NMR Spectroscopy*, Ed. 2, VCH Verlagsgesellschaft and VCH Publishers, Weinheim and New York, 1993.
- <sup>18</sup> J. Jeener, B. H. Meier, P. Bachmann and R. R. Ernst, *J. Chem. Phys.*, **71**, 4546 (1979).
- <sup>19</sup> D. W. Brown, T. T. Nakashima and D. L. Rabenstein, *J. Magn. Reson.*, **45**, 302 (1981).
- <sup>20</sup> L. Muller, *J. Am. Chem. Soc.*, **101**, 4481 (1979).
- <sup>21</sup> R. E. Hurd and B. K. John, *J. Magn. Reson.*, **91**, 648 (1991).
- <sup>22</sup> A. Bax and M. F. Summers, *J. Am. Chem. Soc.*, **108**, 2093 (1986).

<sup>23</sup> W. Wilker, D. Leibfritz, R. Kerssebaum and W. Bermel, *Magn. Reson. Chem.*, **31**, 287 (1993).

## Chapter 3

# The Molecules and Their Assignments

### 3.1 Introduction

The molecules introduced in chapter 1 and shown in Appendix D are complex, with several different possibilities of hydrogen bonding, which may influence visible spectral parameters,<sup>1</sup> tautomerism and rotation. This chapter will discuss the molecular modelling and  $^1\text{H}$  and  $^{13}\text{C}$  solution-state NMR data accumulated whilst investigating these molecules. Conclusions can be drawn from the appearance of these spectra and comparison of chemical shifts. The systems under consideration are known to aggregate,<sup>2,3</sup> at high concentrations in aqueous conditions, perhaps involving intermolecular hydrogen bonding or aromatic plane stacking, as observed by variations of their chemical shifts and linewidths with increasing concentration.

Azo-hydrazo tautomerism is well known for related compounds,<sup>4</sup> and it has been found that the tautomeric structure has a profound influence on the properties of azo dyes.<sup>5</sup> The two forms of such molecules have different colours and different properties such as lightfastness. Lightfastness is usually better in the azo form and the hydrazo form usually has a stronger colour,<sup>6,7</sup> and appears to be favoured in more polar solvents.<sup>8</sup> Wetfastness also changes because the electronic properties change. In the hydrazo form there are usually more hydrogen bonds, making the sample more crystalline and so less soluble. It is therefore useful to have information about this tautomerism. In the compounds discussed in this chapter the hydrazone tautomer may be formed by

participation of the  $\text{NH}_a$  proton rather than the OH proton, see compound **14** on page 50, as the latter case would lead to complete removal of the aromatic character of the naphthalene ring system.<sup>9</sup> Many of the compounds considered contain a sulphonic acid sodium salt, the parent acid being highly acidic. Benzene sulphonic acid has a pKa of approximately 2 in aqueous solution.

## 3.2 Proton NMR Spectral Assignments

### 3.2.1 Assignment Methods

Various deductions can be made about molecules and how they behave by looking at their NMR spectra. Broadening of signals for example may mean exchange of some kind or aggregation. Chemical shifts themselves can give information about hydrogen bonding, electronic effects, tautomerism and conformation.

Proton spectra can be assigned to a certain extent by simply measuring coupling constants and chemical shifts and comparing them to the known parameters of related compounds, or (for shifts) to values calculated using substituent effects. It has been found however, that the simple theories that account for the origins of substituent chemical shifts in benzene derivatives must be applied with caution for naphthalene systems.<sup>10</sup> When more complex spectra have to be assigned, various well-known techniques can be used. When using a non-protic solvent, labile protons are visible in the  $^1\text{H}$  spectrum. These can be identified easily by adding a drop of  $\text{D}_2\text{O}$  to the NMR tube, shaking vigorously, recording the  $^1\text{H}$  spectrum and comparing it with the original. The labile protons will exchange rapidly with the deuterium in the  $\text{D}_2\text{O}$  leading to a loss of signal. This exchange may be slow, for example if the labile proton is strongly hydrogen bonded. Another common method of assigning proton spectra is using COSY<sup>11</sup> (COrrrelation SpectroscopY), described in chapter 2 section 2.2.5.

### 3.2.2 Chemical Shift Comparisons

Table 1 shows  $^1\text{H}$  chemical shifts at room temperature and  $90^\circ\text{C}$  in  $d_6$ -DMSO for the compounds shown in Appendix D that contain a naphthalene ring attached via an azo group to a substituted phenyl ring. It is only feasible to make comparison between the chemical shifts quoted in the table, as other protons present in the molecules are specific to particular compounds. The aliphatic peaks are not discussed here as they are specific to individual molecules and in some cases the aliphatic range is obscured by the  $\text{H}_2\text{O}$  and solvent peaks. They are listed in Appendix C. Where appropriate, the chemical shifts in Table 1 are corrected for roofing effects.<sup>12</sup> Various features can be observed in the spectra and by comparing the chemical shifts. An example spectrum of compound **14** is shown in Figure 1.

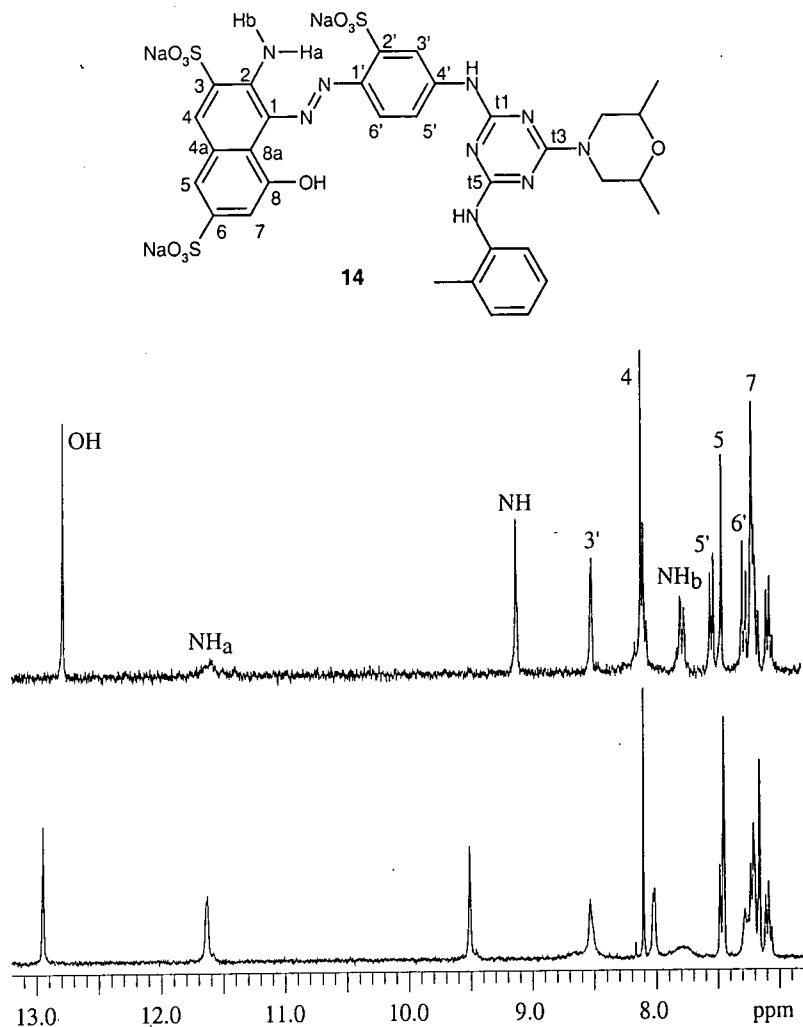


Figure 1: Solution-state  $^1\text{H}$  spectrum of compound **14** in  $d_6$ -DMSO, aromatic and hydrogen-bonding region only, recorded on a Varian Unity Plus 300 spectrometer with a recycle delay of 1 s,  $30^\circ$  pulse width and 120 acquisitions. Bottom: Spectrum recorded at room temperature. Top: Spectrum recorded at  $90^\circ\text{C}$ .

The first thing to notice Figure 1 is the high-frequency chemical shift of the OH and NH<sub>a</sub> proton signals in the room temperature spectrum. This indicates they are hydrogen bonded. The NH<sub>a</sub> peak can be seen to be strongly hydrogen bonded by comparison to similar compounds.<sup>13</sup> At 90 °C the OH proton signal remains sharp. The NH<sub>a</sub> and NH<sub>b</sub> signals are broad at 90 °C however, indicating that they are exchanging. Rotation is probably occurring about the C-NH<sub>2</sub> bond, leading to breaking of the hydrogen bond. As the rotation occurs protons NH<sub>a</sub> and NH<sub>b</sub> become equivalent so the corresponding signals broaden and move towards each other. Eventually an average shift would be observed but 90 °C is not a high enough temperature for this to occur. This rotation of the NH<sub>2</sub> group was observed in most of the molecules studied.

The naphthalene proton signals are sharp at both temperatures showing no motion is occurring in this region of the molecule. This was the case in all the molecules observed.

For most of the compounds studied the peaks due to the H3', H5' and H6' protons are broad at room temperature but are sharper at 90 °C, although the extent of this broadening is very dependent upon the molecule in question. Broadening suggests exchange of some sort and will be discussed further in chapter 4. In some cases it is the H3' peak that undergoes the most significant changes and in other compounds the H5' signal has the larger linewidth. In all cases the peaks are sharp at 90 °C.

When looking at Table 1 it should be highlighted that compounds **8** and **9** do not contain a triazine ring. Compound **8** does not contain a sulphonic acid salt in the 2' position unlike the rest of the compounds; indeed it is found not to contain sodium at all but the sulphonic acid groups are present as the free acid, see section 3.2.3. Compound **13** does not contain a sulphonic acid salt in the 3 position.

	OH	NH <sub>2a</sub>	NH <sub>2b</sub>	H4	H5	H7	H3'	H5'	H6'	H3'-H5'
8	rt	br	br	8.13	7.48	7.16	7.07	4.07	7.62	3.00
	+93 °C	br	br	8.12	7.48	7.19	6.88	6.88	7.52	0.00
9	rt	11.27	7.71	8.04	7.41	7.09	7.24	6.67	7.23	0.57
	+93 °C	~11.2	~7.9	8.06	7.42	7.14	7.29	6.67	7.22	0.62
10	rt	11.71	8.11	8.13	7.48	7.21	~8.6	~8.0	~7.4	~0.6
	+93 °C	~11.7	~8.2	8.13	7.48	7.25	~8.2	~8.1	7.38	~0.1
11	rt	12.96, 12.81	8.02	8.12	7.47	~7.1	8.08	7.63	7.42	0.45
	+93 °C	12.71	~8.2	8.12	7.47	7.23	8.25	~7.8	~7.2	~.45
12	rt	12.88	~7.9	8.14	7.48	7.19	8.68	7.77	7.40	0.91
	+93 °C	12.74	~7.7	8.14	7.48	7.23	~8.3	~7.9	7.39	~0.7
13	rt	12.93	~8.0	7.71	7.46	7.14	~8.5	~8.0	7.31	~0.5
	+93 °C	12.72	~9.2	7.63	7.46	7.19	8.42	7.95	7.31	0.47
14	rt	12.95	8.02	8.11	7.45	7.16	8.53	~7.8	~7.3	~0.7
	+93 °C	12.78	br	8.11	7.45	7.21	8.51	7.77	7.27	0.74
15	rt	12.98	8.01	8.12	7.47	7.17	8.82	7.67	7.34	1.15
	+93 °C	12.82	~11.60	8.12	7.47	7.21	8.71	7.65	7.32	1.06
16.1	rt	12.97	8.02	8.11	7.46	7.16	~8.7	~7.7	7.33	~1.0
	+93 °C	12.83	~11.6	8.12	7.47	7.21	8.76	7.69	7.32	1.07
17	rt	12.92	8.03	8.12	7.47	7.17	9.03	7.57	7.33	1.46
	+93 °C	12.80	~11.6	8.12	7.47	7.21	8.94	7.53	7.32	1.41

~ is used to refer to the approximate chemical shifts of peaks that are broad. br indicates peaks too broad to be observed.

Table 1: <sup>1</sup>H chemical shifts in ppm of a range of compounds in a 0.007 ± 0.00M solution in d<sub>6</sub>-DMSO referenced to TMS all recorded on a Varian Unity Plus 300 spectrometer.

The OH proton signal lies in the range of 12.71 – 13.30 ppm, although in compound **8** this broadens at higher temperature in contrast to the other compounds. It also appears that the rate of exchange of the NH<sub>2</sub> protons is faster than in other compounds, as seen by the broadness of both the NH<sub>2</sub> protons at both temperatures which may be due to weaker hydrogen bonding. These two observations will be discussed in section 3.2.3. Attempts have been made in the literature to use the chemical shifts of the OH<sup>14</sup> and NH<sub>2</sub><sup>15</sup> to determine hydrogen bond strength but there are some difficulties with this method, as the chemical shifts may be influenced by factors other than hydrogen bonding.<sup>16</sup>

As described previously, the naphthalene ring proton signals remain sharp in all compounds at ambient temperature and higher. This is reinforced by the fact that there is little variation in the chemical shifts of these protons, as can be seen in Table 1. The peak due to H4 has a range of 8.11 – 8.13 ppm. Although the H4 signal for compound **13** lies outside this region it does not have a sulphonic acid salt in the 3 position as already highlighted, accounting for this discrepancy. Compound **9** also lies slightly outside this range but the reason for this is not known. The H5 peak has a range of 7.45 – 7.48 ppm. Again compound **9** lies outside this range but compound **13** does not, implying that the absence of the sulphonic acid salt in the 3 position does not have an effect on the H5 chemical shift. The H7 signal lies in the range 7.14 – 7.23 ppm, a slightly larger variation than for the other two naphthalene protons. Again compound **9** lies outside this range.

In comparing the shifts of H3', H5' and H6' compounds **8** and **9** will be discounted as they do not contain a triazine ring. A comment which can be made however is that the presence of the triazine ring increases the phenyl ring proton chemical shifts as expected. The difference in the H3' and H5' proton shifts is quite variable. To observe this difference a graph can be plotted (shown in Figure 2).

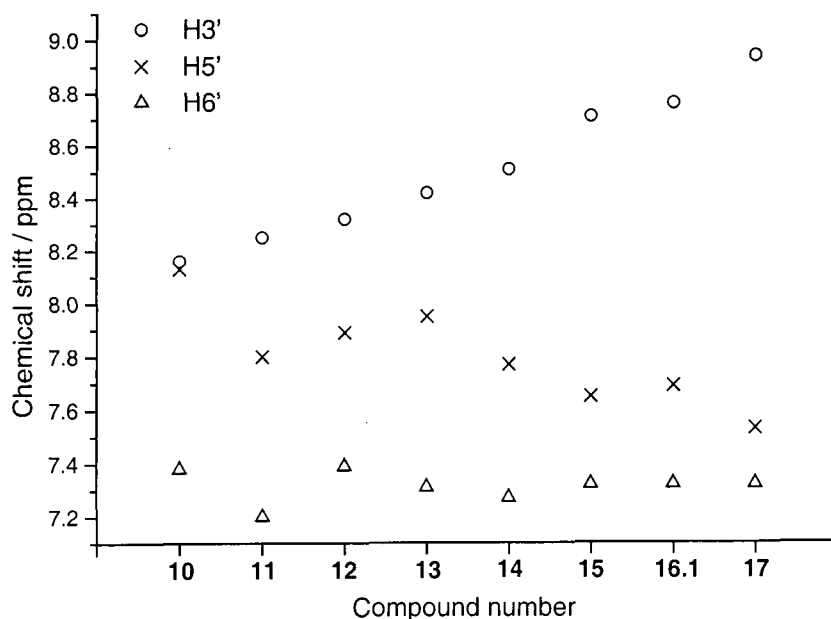


Figure 2: Comparison of some  $^1\text{H}$  chemical shifts at  $90^\circ\text{C}$  from Table 1.

The shifts plotted in Figure 3 are the  $90^\circ\text{C}$  values rather than those for room temperature, as at  $90^\circ\text{C}$  broadening effects have been removed for most of the compounds. It can be seen that although the chemical shift of  $\text{H6}'$  remains reasonably constant, the shift of  $\text{H5}'$  decreases as  $\text{H3}'$  increases. This information, considered with the fact that the  $\text{H3}'$  and  $\text{H5}'$  protons are often broad, indicates there are changes occurring around the triazine ring. The chemical shift variation suggests some averaging process resulting in an equilibrium situation for each compound.

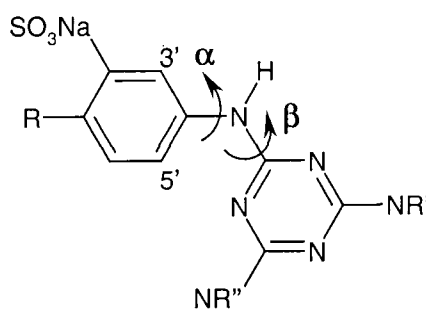


Figure 3: Possible rotations leading to averaging of  $\text{H3}'$  and  $\text{H5}'$ .

As the molecule is drawn in Figure 3,  $\text{H5}'$  is closer to the triazine ring than  $\text{H3}'$  therefore presumably affecting the chemical shift of  $\text{H5}'$  more than that of  $\text{H3}'$ . Rotation about  $\alpha$  leads to  $\text{H3}'$  lying closer to the triazine ring, so influencing the shift of  $\text{H3}'$  more than  $\text{H5}'$ . This effect would account for the simultaneous increase in the shift of  $\text{H3}'$  and decrease in the shift of  $\text{H5}'$ . Either: one of the two planar conformations is

present for each compound, or, the rotation is rapid with an equilibrium position favouring one of the two rotamers (the more likely explanation).

### 3.2.3 Observations:

#### Compound 8

Figure 4 shows the variable temperature spectra of compound **8** in  $d_6$ -DMSO.

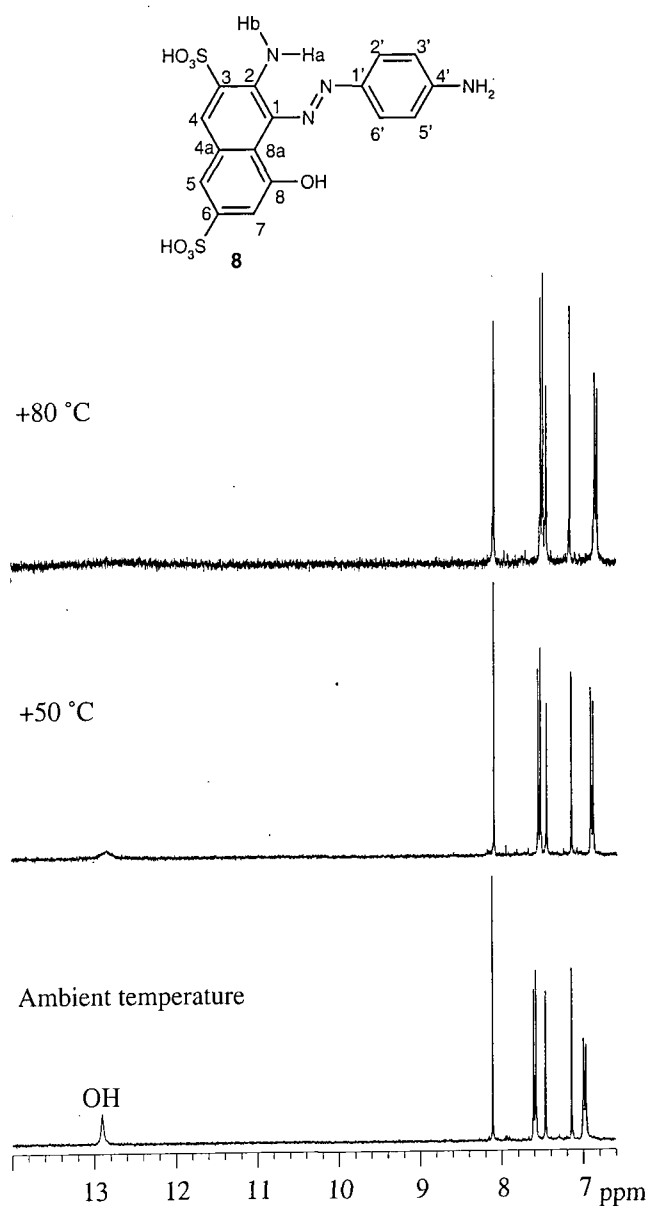


Figure 4: Variable-temperature solution-state  $^1\text{H}$  spectra of **8** in  $d_6$ -DMSO on a Varian Unity Plus 300 spectrometer with a recycle delay of 5 s, pulse width of 30° and 64 acquisitions.

As can be seen from Figure 4, the OH in compound **8** has broadened considerably by 50 °C. In the other compounds in Table 1 the OH proton peak is still sharp at 90 °C. The NH<sub>2</sub> protons are not visible in Figure 4. The presence of the free acid rather than the sodium salt would lead to differences in the spectra of this compound, and promotion of exchange of the labile protons, compared to the other compounds examined in this chapter. Na<sub>2</sub>CO<sub>3</sub> was added to convert the free acid to the sodium salt to check that the presence of the free acid is the cause for the observed spectral differences. The spectra with and without Na<sub>2</sub>CO<sub>3</sub> are compared in Figure 5.

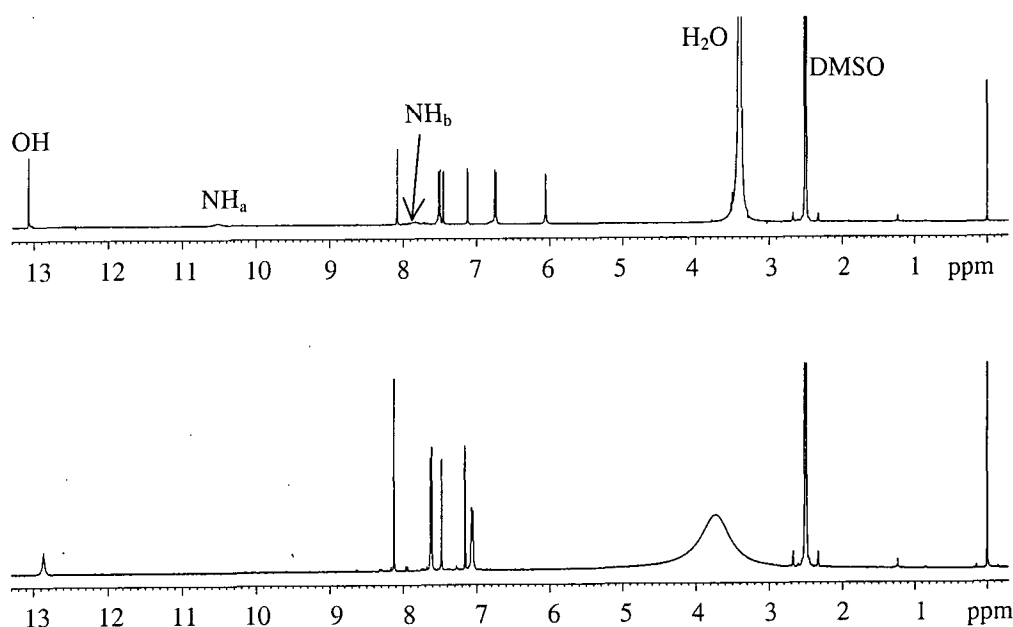


Figure 5: Solution-state <sup>1</sup>H spectrum of compound **8** in d<sub>6</sub>-DMSO at ambient temperature recorded on a Bruker AMX 400 spectrometer with a recycle delay of 7 s, 30° pulse width and 64 acquisitions. Bottom spectrum: Without sodium carbonate. Top: With sodium carbonate added.

It can be seen that the labile NH<sub>2</sub> proton signals become visible with the addition of sodium carbonate, implying that the rate of exchange of the labile protons was indeed increased by the presence of the free acid. The NH<sub>2</sub> proton signals are broader than for the other compounds studied. This suggests that the hydrogen bonding may be weaker in this case, the difference in molecular structure being the absence of the sulphonic acid in the 2' position on the phenyl ring. This effect will be explored further in section 3.2. There are changes in the chemical shifts of the <sup>1</sup>H peaks upon the addition of sodium carbonate. These are shown in Figure 1. The water peak sharpens, indicating

that the labile protons were exchanging with the water when present as the free acid but not when present as the sodium salt.

	Chemical shift in $d_6$ -DMSO / ppm		Difference / ppm
	Without $\text{Na}_2\text{CO}_3$	With $\text{Na}_2\text{CO}_3$	
OH	12.87	13.08	-0.21
$\text{NH}_{2a}$		~10.5br	
$\text{NH}_{2b}$		~7.8br	
H4	8.12	8.08	0.04
H5	7.48	7.44	0.03
H7	7.16	7.12	0.04
H2' & H6'	7.62	7.51	0.11
H3' & H5'	7.06	6.74	0.32
$\text{NH}_2$		6.05	
$\text{H}_2\text{O}$	3.7br	3.4	0.3

br indicates broad peaks.

Table 2: Proton chemical shifts for **8** in  $d_6$ -DMSO with and without the addition of  $\text{Na}_2\text{CO}_3$ .

It can be concluded that compound **8** was present as the sulphonic acid and not as the salt. In such a situation, it may be wholly or partly present as a zwitterion, with sulphonate anions and  $\text{NH}_3^+$  groups, leading to an increase in the rate of exchange between the amino protons and the water in the solvent and therefore broad peaks for all the protons concerned. Zwitterion formation will not occur in basic solution, so the rate of exchange of the labile protons with the water is reduced upon the addition of sodium carbonate, allowing the amino and water resonances to be observed separately and the OH peak to be more evident. The aromatic proton shifts are affected by the presence of the zwitterion, resulting in changes in their chemical shifts upon the addition of sodium carbonate. The substituent effect of an  $\text{NH}_2$  group to a benzene ring is:

ortho: -0.75 ppm, meta: -0.25 ppm and para: -0.65 ppm.

For  $\text{NH}_3^+$  these are:

ortho: +0.4 ppm, meta: +0.2 ppm and para: +0.2 ppm.

This means that in changing from  $\text{NH}_3^+$  to  $\text{NH}_2$  the chemical shifts of the aromatic protons would be expected to change by:

ortho: = -1.15 ppm, meta: -0.45 ppm and para: -0.85 ppm.

It can be seen from Table 2 that:

ortho peaks to the  $\text{NH}_2$  ( $\text{H}3'$  and  $\text{H}5'$ ) change by  $-0.32$  ppm

meta peaks to the  $\text{NH}_2$  ( $\text{H}2'$  and  $\text{H}6'$ ) change by  $-0.11$  ppm on addition of  $\text{Na}_2\text{CO}_3$  i.e. in changing from  $\text{NH}_3^+$  to  $\text{NH}_2$ . These changes are not as great as predicted but this is not too surprising as either one, or both solutions may be a mixture of the free acid and the salt. This would mean that the changes in chemical shift between the two are not as great as if changing from purely the  $\text{NH}_2$  to purely the  $\text{NH}_3^+$  form. Also the other substituent present on the phenyl ring may affect the substituent effects. The changes in shift observed are in the correct direction and the change observed for the ortho proton signals is greater than that for the meta, as expected.

The effect of the zwitterion on the naphthalene proton chemical shifts are a little more difficult to predict as the substituent effects are not documented. Also the naphthalene ring is heavily substituted so there would probably be large deviations from expected behaviour.

### Compound 7

To help with the assignment of **7** in  $\text{d}_6$ -DMSO (shown in the bottom spectrum in Figure 6), two drops of  $\text{D}_2\text{O}$  were added to the solution to identify the labile protons. The peaks at 7.03, 7.20 and 7.37 ppm are due to the ammonium cation, so these exchanged quickly upon the addition of  $\text{D}_2\text{O}$ . A series of spectra were recorded different lengths of time after the addition of the  $\text{D}_2\text{O}$ . These are shown in Figure 6. It can be seen that other changes occur but slowly. These changes are shown in Table 3. The HOD and TMS peaks are also included in the table.

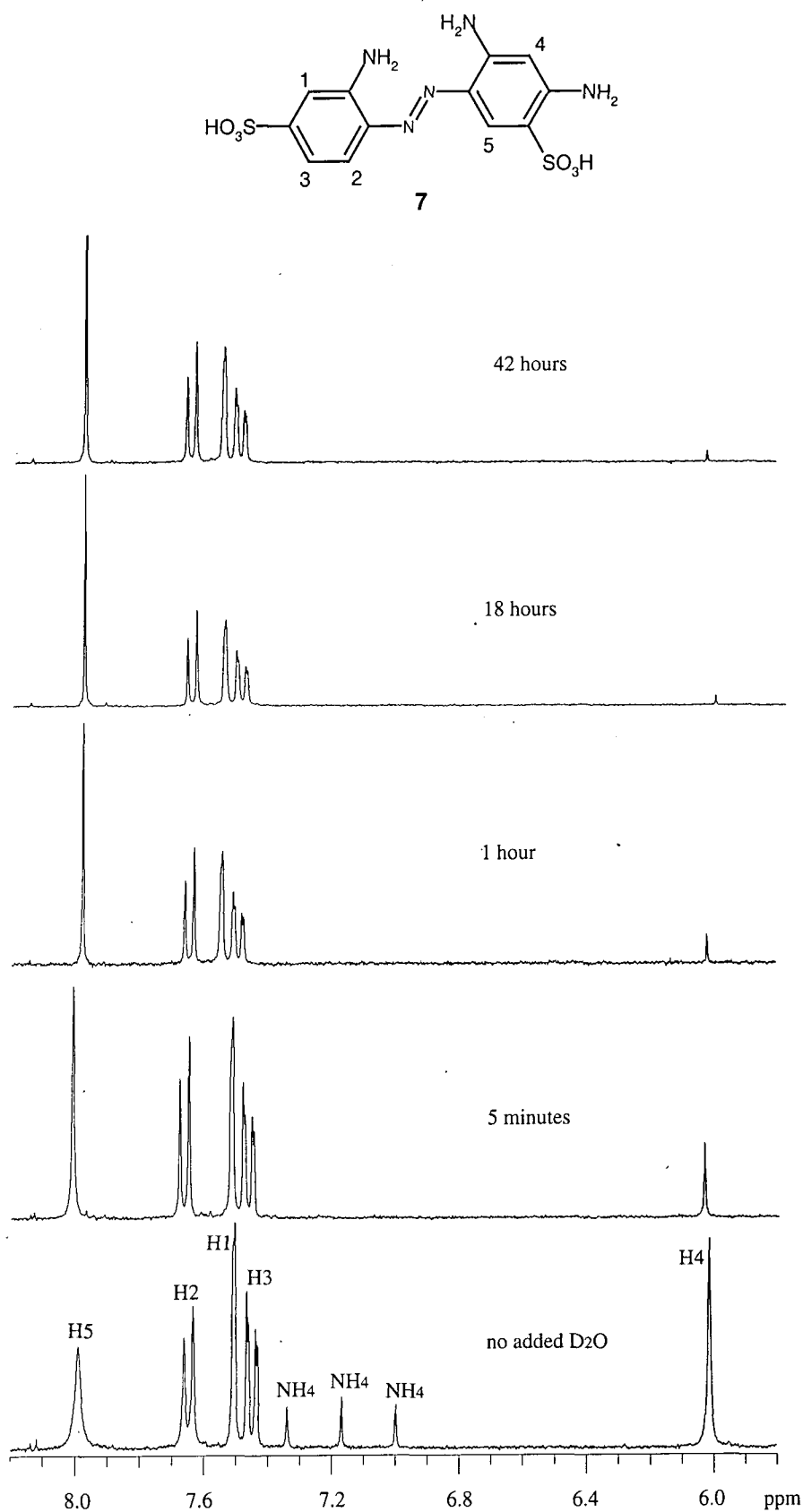


Figure 6: Solution-state <sup>1</sup>H spectra of 7 in d<sub>6</sub>-DMSO at ambient temperature on a Varian Unity Plus 300 spectrometer with a recycle delay of 1 s, pulse width of 30° and 64 acquisitions. The times quoted on the spectra are the length of time after addition of 2 drops of D<sub>2</sub>O.

		No D <sub>2</sub> O	Length of time after addition of 1 drop of D <sub>2</sub> O			
			5 minutes	1 hour	18 hours	42 hours
Integral ratios	H1 and H3	1.9	2.0	2.2	2.0	2.0
	H2	1.0	1.0	1.1	1.1	1.0
	H4	0.9	0.2	0.1	0.2	0.02
	H5	1.0	1.0	1.0	1.0	1.0
Linewidth / Hz	H1	3.8	3.8	3.8	3.8	3.8
	H2	2.8	1.9	1.8	1.7	1.8
	H3	3.5	3.5	3.7	3.7	3.6
	H4	3.0	1.6	1.3	1.0	1.3
	H5	6.3	2.3	1.4	1.0	1.3
	HOD	60.1	11.7	3.5	4.9	3.7
	TMS	0.6	0.7	1.1	0.7	1.1
Shift HOD /ppm		3.58	3.48	3.74	3.74	3.74

Table 3: Data for <sup>1</sup>H spectra of compound 7 in d<sub>6</sub>-DMSO with 2 drops of D<sub>2</sub>O added.

The chemical shifts of the peaks do not change significantly with the addition of D<sub>2</sub>O but the integrals and linewidths do. As can be seen from Table 3, the linewidth of the HOD peak decreases dramatically on addition of D<sub>2</sub>O because exchange between D<sub>2</sub>O and the NH<sub>2</sub> protons of compound 7 increases on the addition of D<sub>2</sub>O so their average signal sharpens. The integral of the H4 peak drastically decreases and the linewidth also decreases suggesting H4 was exchanging with the deuterium in the added D<sub>2</sub>O. It is thought the shift at 6.02 ppm due to H4, disappears slowly due to imino/amino tautomerism shown in Figure 7.

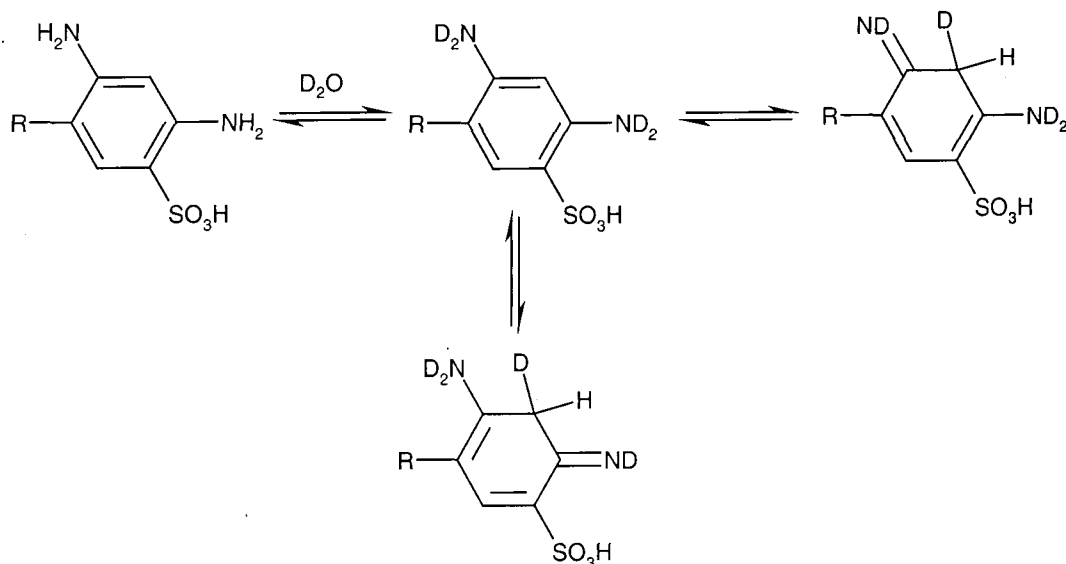


Figure 7: Imino/amino tautomerism of compound 7.

This tautomerism will eventually lead to total deuteration of H4, even if only a small amount of the imine form is present in d<sub>6</sub>-DMSO/D<sub>2</sub>O. The signals due to the NH<sub>2</sub> protons are part of the HOD peak.

As with compound **8** the addition of sodium carbonate showed the sulphonic acid was present as the free acid not the sodium salt.

### 3.3 Molecular Modelling

The NH hydrogen bonding was seen to be relatively strong by looking at the chemical shifts of NH<sub>a</sub> in Table 1. In all the compounds studied, except compound **8**, there is a sulphonic acid salt in the 2' position. It may be possible that this group could contribute to the hydrogen bonding of NH<sub>a</sub> considering that when it is not present, the hydrogen bonding is possibly weaker. This is thought because the NH<sub>a</sub> signal is broad at room temperature, even when the free acid has been converted to the sodium salt (see Figure 5) due to exchange with water. The other compounds exhibit a sharp NH<sub>a</sub> signal, suggesting exchange with water is easier for compound **8** than other compounds investigated, possibly due to weaker hydrogen bonding. To investigate this further

molecular modelling was used and will be discussed here. A lot of information can be obtained from molecular modelling, the most important for this project are conformational details and energies (see chapter 5). The many different modelling techniques will be discussed in chapter 5.

A series of compounds, shown in Figure 8 have been fully optimised using the Hartree-Fock method in Gaussian 94.<sup>17</sup> There are several different positions for the sulphonic acid groups in the molecules studied. These were examined separately by adding a sulphonic acid group in turn at each position to the basic aromatic azo structure shown in the diagram as structure 't'. This was repeated with an NH<sub>2</sub> group present to investigate the NH<sub>2</sub>-sulphonic acid interactions.

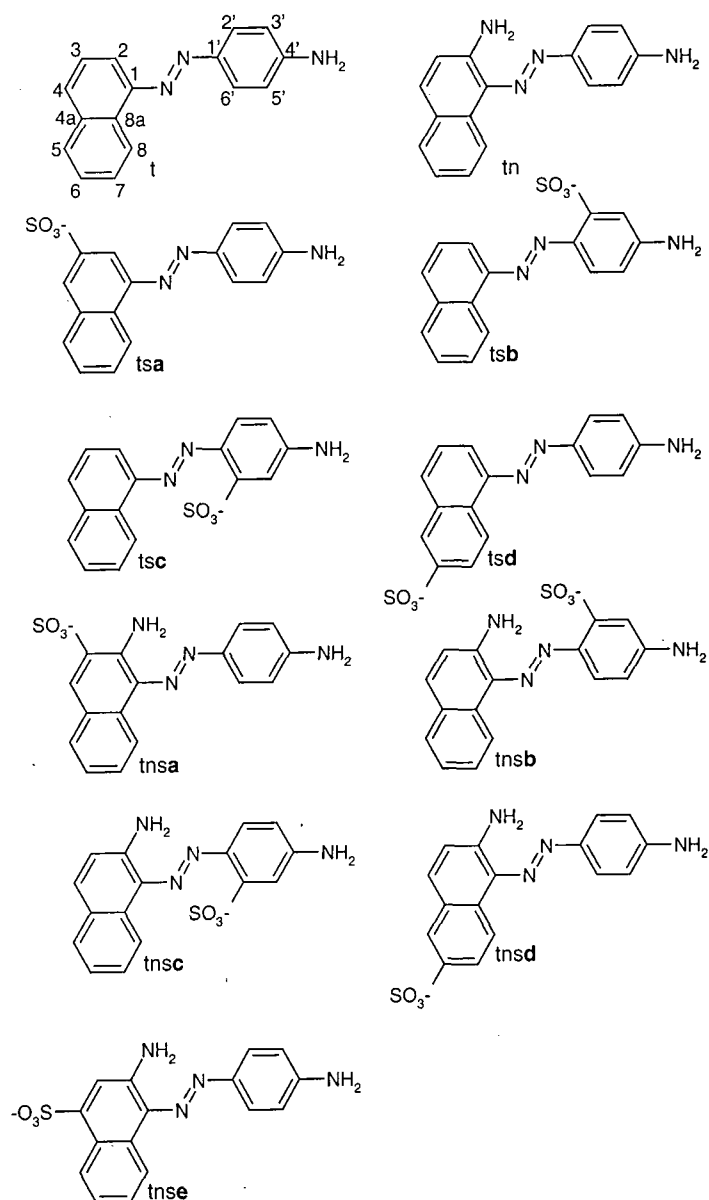


Figure 8: The series of compounds used to investigate the role of the sulphonic anion.

The label 't' denotes the fact that all the structures contain a trans azo bond. 'n' is included when the NH<sub>2</sub> group is present ortho to the azo group on the naphthalene ring and 's' denotes the sulphonic acid anion. 'a-e' are labels for the different places the sulphonic anion can be.

'tsb' and 'tsc' are rotational isomers and these were examined to see which rotamer is the lower energy conformation. 'tnse' was examined – although it is not in a position occupied by a sulphonic acid group in any of the molecules studied – to compare differences in energy between adding a substituent to an already substituted ring and adding the same substituent to an unsubstituted ring with the NH<sub>2</sub> group present, the structure 'tse' was therefore not necessary. The sulphonic acid group has been modelled as an SO<sub>3</sub><sup>-</sup> group as in the actual compounds in solution the sulphonic acid will be anionic.

Energies can only be compared when calculated with the same method, basis set and molecular formula. Although this means none of the values can be directly related in Table 4, they are quoted to show convergence. As the basis set is increased using the same method, the optimised energy of a molecule decreases to a value limited by that basis set, in this case the Hartree-Fock limit, this is called the basis set convergence. It can be seen that for both 't' and 'tn' this is indeed occurring, although the limit has not been reached. Approaching convergence can be seen for 't', as the difference in energy between using basis sets 3-21G and 6-31G is of the order of 10600, whereas it is 74 when increasing the basis set from 6-31G\* to 6-31G\*\*. All the energies in Table 4 are related to the 6-31G\*\* value for that molecule.

Compound	Energy for each method relative to the lowest energy / kJ mol <sup>-1</sup>			
	3-21G	6-31G	6-31G*	6-31G**
t	11485	844	74	0
tn	12281	900	91	0

Table 4: Comparison of calculated energies with different basis sets.

For Table 5 all optimisations were done using HF/6-31G, as the computational time using 6-31G\* and 6-31G\*\* calculations was too long when sulphonic anions are

present. To investigate the conformational effects the dihedral angles shown in Figure 9 were optimised and their values are shown in Table 5.

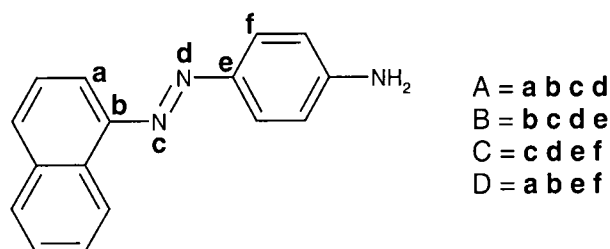


Figure 9: Structure showing measured dihedral angles to investigate deviation from planarity.

Compound	Energy difference from the lowest energy conformation with the same number of atoms / kJ mol <sup>-1</sup>	Dihedral angle / °			
		A	B	C	D
t	0.0	0	180	180	0
tn	0.0	0	180	180	0
tsa	1.9	0	180	180	0
tsb	20.3	-10	178	-177	-6
tsc	36.4	-8	180	161	-30
tsd	0.0	0	180	180	0
tnsa	0.0	3	180	-177	7
tnsb	16.6	8	-178	-171	20
tnsc	65.5	-3	-179	150	-40
tnsd	24.2	0	180	180	0
tnse	23.6	0	180	180	0

Table 5: Comparison of calculated energies with differently positioned sulphonic anion groups.

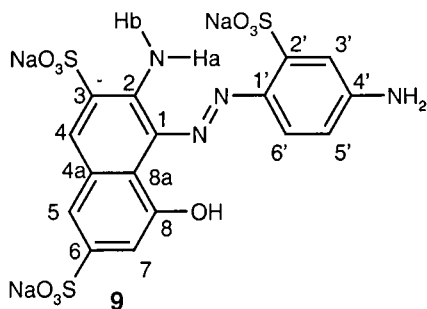
In the 'ts' series it can be seen that when the sulphonic acid group is away from the azo group the structure is planar, i.e. for 'tsa' and 'tsd'. There is a relationship between the deviation from planarity and the energy, the less planar the structure the higher the energy. The highest energy is for 'tsc' and the lowest for 'tsd', with 'tsa' also being low in energy and deviating from planarity by less than 1°. The most likely reason for

this deviation from planarity is steric effects. It can also be seen that 'tsb' is much lower in energy than 'tsc' suggesting that 'tsb' would be the more favoured rotamer.

The 'tns' series is more complex than the 'ts' series. Again 'tnsd' and 'tnsa' are both essentially planar but 'tnsa' is appreciably lower in energy than 'tnsd'. This suggests there is some effect, other than deviation from planarity, leading to the energy stabilisation. The only difference between substituting  $\text{SO}_3^-$  in the 6 position compared to the 3 position (other than the 3 position being near the  $\text{NH}_2$  group), is the fact that the 6 position is on an unsubstituted ring, whereas the 3 position is on an already substituted ring. The energy of 'tnse' is similar to 'tnsd', showing that the sulphonic acid group being near the  $\text{NH}_2$  group is the larger effect, suggesting there is an interaction between the sulphonic acid group at position 3 and the  $\text{NH}_2$  group. 'tnsb' is also now lower in energy than a sulphonic acid group in the 6 position but 'tnsb' is actually less planar than 'tsb'. This suggests there must be an effect decreasing the energy to counterbalance the increase in energy due to the deviation from planarity. It is likely that this effect is interaction between the sulphonic anion at position 2' and the  $\text{NH}_2$  group, the geometry being a balance between reducing steric effects but maximising the interaction. 'tnsa' is more stable than 'tnsb' because it does not have to deviate from planarity but sulphonic anion –  $\text{NH}_2$  interaction is still possible. As with the 'ts' series, 'tnsc' has the highest energy conformation and has the largest deviation from planarity.

### 3.4 $^{13}\text{C}$ Assignment:

There are many techniques to assign  $^{13}\text{C}$  spectra, some of which are described in chapter 2, section 2.2.5. Here it will be illustrated how these techniques can be used to make a full assignment of compound **9** in  $\text{d}_6$ -DMSO.



### 3.4.1 Example of $^{13}\text{C}$ Assignment

The assignment for the  $^1\text{H}$  spectrum of compound **9** has been given earlier, see Table 1. This allows 2-dimensional techniques to be employed to assign the  $^{13}\text{C}$  spectrum. Although the substituent effects of the sodium sulphonate group have been established<sup>18</sup>, a poor correlation for di-substituted benzenes has been found using these parameters.<sup>19</sup> The decoupled spectrum to be assigned is in Figure 10.

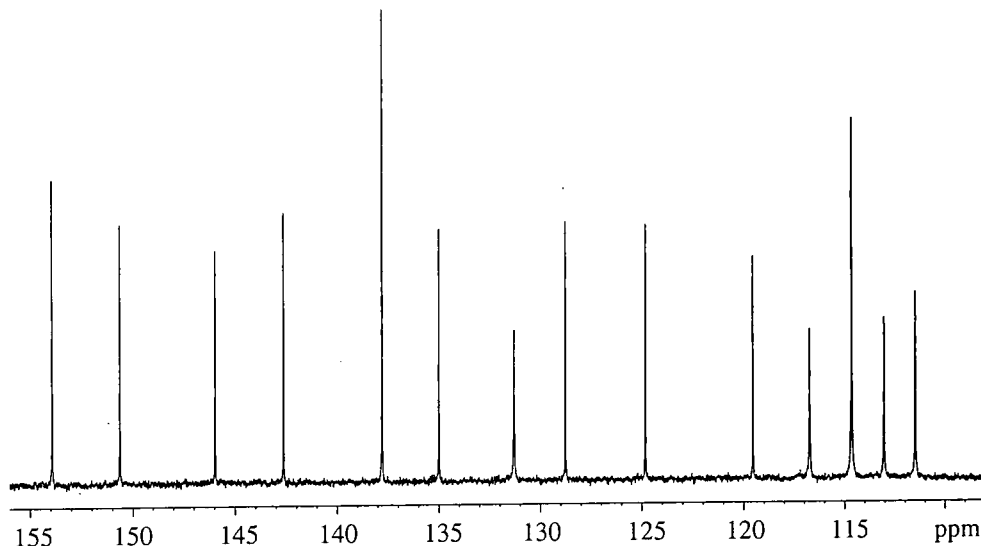


Figure 10: The solution-state proton decoupled  $^{13}\text{C}$  spectrum of compound **9** in  $d_6$ -DMSO on a Bruker AMX 400 spectrometer with a recycle delay of 2 s,  $5.5 \mu\text{s}$   $90^\circ$  pulse and 4096 acquisitions.

The first technique to be used is J-MOD-X which leads to CH (and  $\text{CH}_3$ ) carbon signals to have a negative phase in the spectrum and quaternary (and  $\text{CH}_2$ ) carbon signals to have a positive phase, see Figure 11. As there are a lot of both quaternary and CH carbons, this spectrum does not give a direct assignment. It does give more information

than the simple decoupled carbon spectrum however, and this information can be used to support deductions made using other techniques. It can be seen that although 10 quaternary carbon signals are expected only 9 are observed. Similarly 6 CH signals are expected but 5 are seen. Thus two signals must arise from overlap of two resonances each.

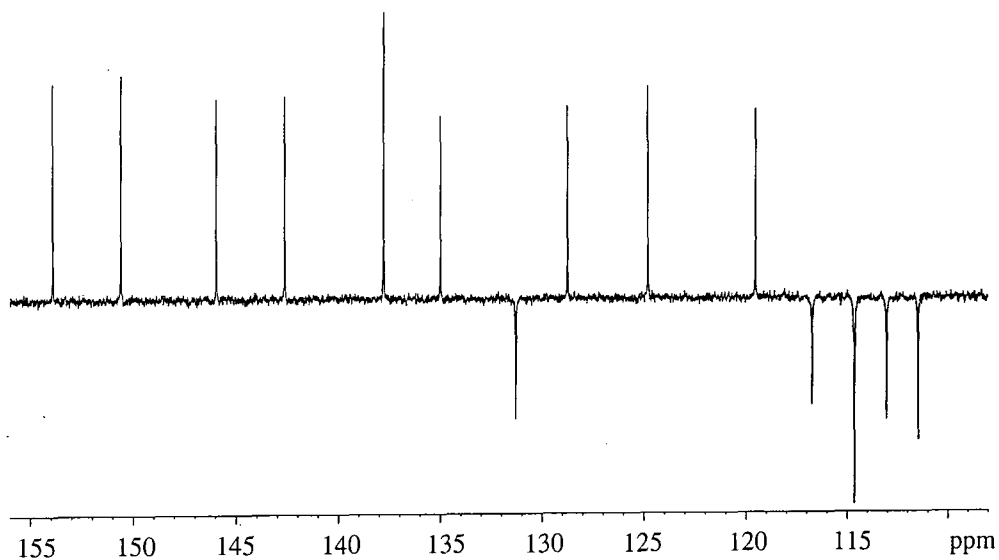


Figure 11: The solution-state J-MOD-X  $^{13}\text{C}\{^1\text{H}\}$  spectrum of **9** in  $d_6$ -DMSO on a Bruker AMX 400 spectrometer with a 2 s recycle delay and 4096 acquisitions.

A partial gs-HMQC spectrum (up to  $\delta_{\text{C}}=140$  ppm, the region containing cross peaks) is shown in Figure 12. As explained in chapter 2, this shows 1-bond correlations and so is useful to assign CH carbons. The quaternary carbons, as identified by the J-MOD-X spectrum shown in Figure 11, are marked with a cross in the gs-HMQC spectrum shown in Figure 12, as they cannot be assigned using this technique. The assignments made from this spectrum are as shown.

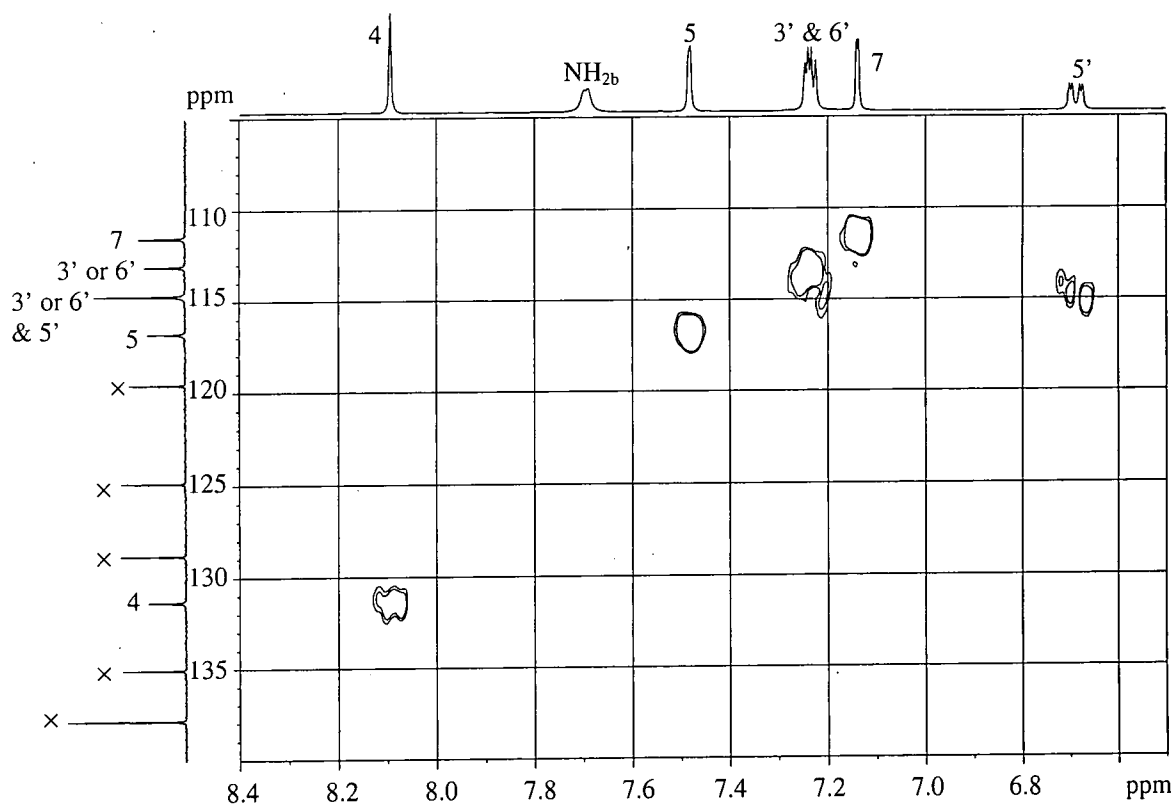


Figure 12: Aromatic part of a solution-state *gs*-HMQC  $^1\text{H}$  -  $^{13}\text{C}$  correlation spectrum of compound **9** in  $d_6$ -DMSO on a Bruker AMX 400 spectrometer using inverse detection with a 2 s recycle delay, 128 increments and 8 acquisitions per increment.

As can be seen 3' and 6' can still not be distinguished.

A *gs*-HMBC spectrum is shown in Figure 13. This allows 2-, 3- and 4- bond correlations to be observed. In aromatic systems such as the ones under investigation here, the 3-bond aromatic couplings are larger than the 2- and 4-bond ( $^1\text{J} \approx 160$  Hz,  $^2\text{J}$  and  $^4\text{J} \approx 1$  Hz and  $^3\text{J} \approx 7$  Hz).<sup>20</sup> This technique can be very powerful when dealing with molecules containing several quaternary carbons. Many of the quaternary carbons being considered here do not have a 3-bond correlation to a proton, meaning unambiguous assignment of these cannot be made with this technique but experiment helps by identifying these.

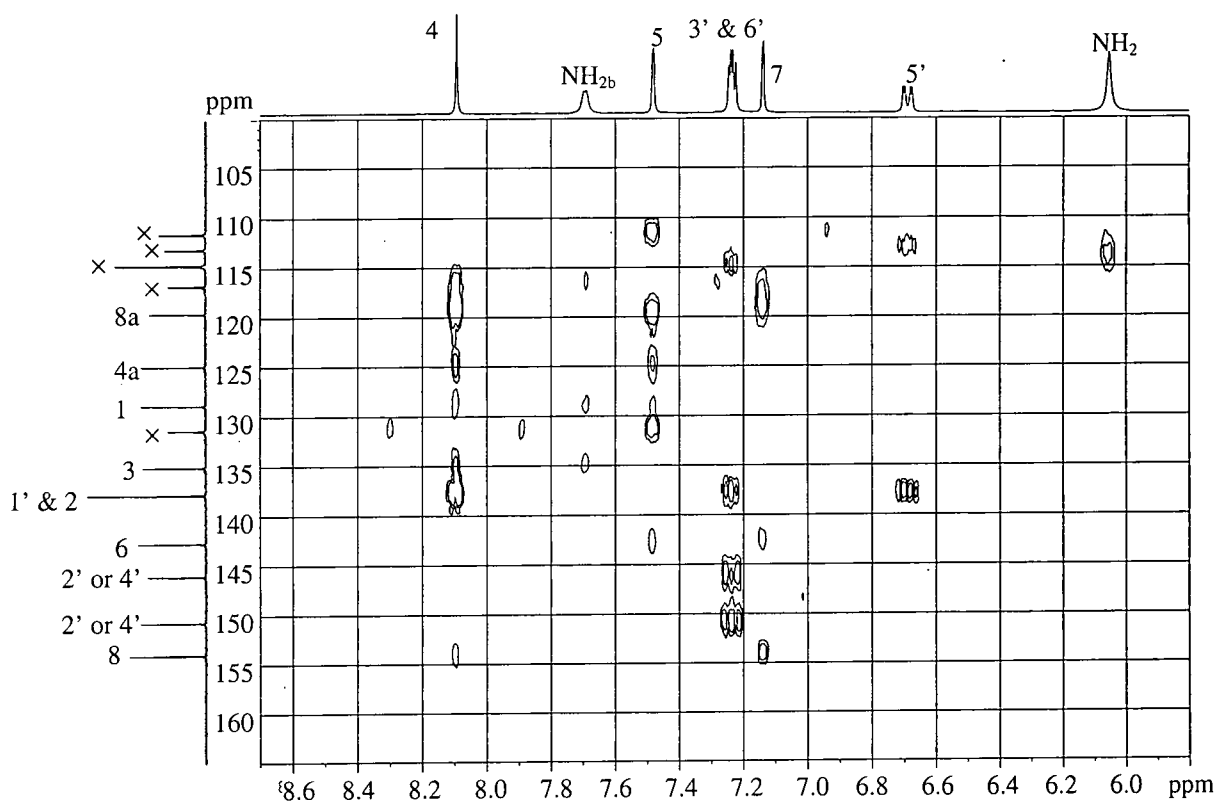


Figure 13: Aromatic part of a solution-state *gs*-HMBC  $^1\text{H} - ^{13}\text{C}$  correlation spectrum of compound **9** in  $d_6$ -DMSO on a Bruker AMX 400 spectrometer using inverse detection with a 2 s recycle delay, 128 increments and 8 acquisitions per increment.

Peaks previously assigned using the *gs*-HMQC method are marked with a cross. Only correlations to peaks not already assigned will be mentioned below in the discussion of the interpretation of the *gs*-HMBC spectrum.

Strong cross-peaks from H4 are expected for C5 (already assigned) C8a and C2. These are observed at 119.5 and 137.8 ppm. Weak cross-peaks are expected at C4a and C3, which can be seen at 124.8 and 135.0 ppm. H5 is expected to strongly correlate with C8a, C4 and C7 (both already assigned) and this is observed at 119.5 ppm so comparing this with the strong correlations for H4, C2 can be assigned to the peak at 137.8 ppm. Weak cross-peaks are also expected for H5 with C6 and C4a. These are observed at 124.8 and 142.6 ppm. Again by comparison with the correlations from H4, C4a can be assigned to 124.8 ppm leaving C3 at 135.0 ppm and C6 at 142.6 ppm. A weak cross peak can be seen with H7 which would be expected to be due to C8.

H5' would be expected to have a strong cross-peak with C1' which is seen at 137.8 ppm (overlapping with the signal from C2). It would also be expected to have a weak

correlation to C4' and C6'. One weak correlation can be observed at 113.1 ppm, which is one of the peaks assigned using the gs-HMQC spectrum to be C3' or C6'. The presence of this weak cross-peak suggests it is C6'. H6' would be expected to have strong cross-peaks to C2' and C4'. These can be seen at 146.0 and 150.6 ppm. A weak peak is also expected with C1' but this has already been assigned. A weak cross-peak is also observed from H6' to C5'. H3' is expected to have a strong cross-peak with C5' (already assigned) and with C1' plus weak cross-peaks with C2' and C4'. These have already been identified and cannot provide any other information to help distinguish between C2' and C4'. Only 1 carbon signal has not been assigned, that of C1. It can therefore be assigned to the only peak not accounted for, that at 131.3 ppm.

As the spectrum was recorded in  $d_6$ -DMSO, the labile protons do not exchange with the solvent. This is helpful because the correlations to the OH proton, shown in Figure 14 can be used to verify some of the assignments. Here some 2-, 3- and 4-bond correlations can be seen.

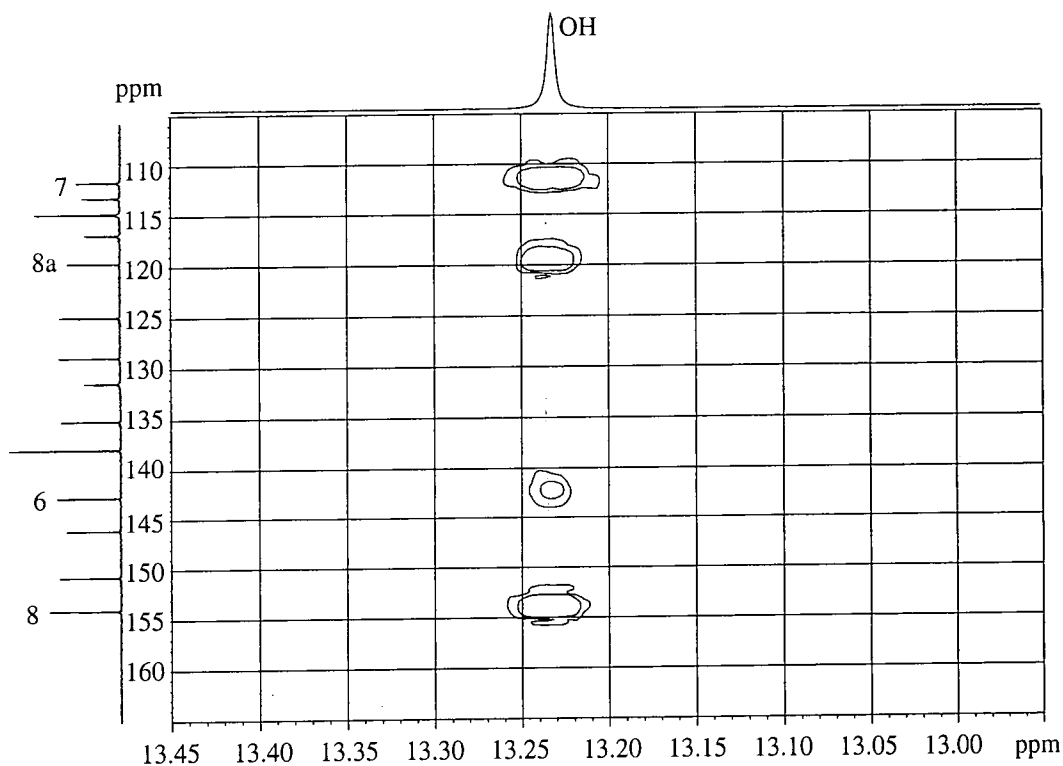


Figure 14: The OH region of a solution-state gs-HMBC  $^1\text{H} - ^{13}\text{C}$  correlation spectrum of compound **9** in  $d_6$ -DMSO on a Bruker AMX 400 spectrometer using inverse detection with a 2 s recycle delay, 128 increments and 8 acquisitions per increment.

A coupled  $^{13}\text{C}$  spectrum can also be used for assignment by looking at coupling constants but this is more difficult and time-consuming to obtain than using 2D spectra because the latter used inverse detection. It is useful to check conclusions or as more evidence to help distinguish between ambiguous assignments. The coupled spectrum for compound **9** is shown in Figure 15.

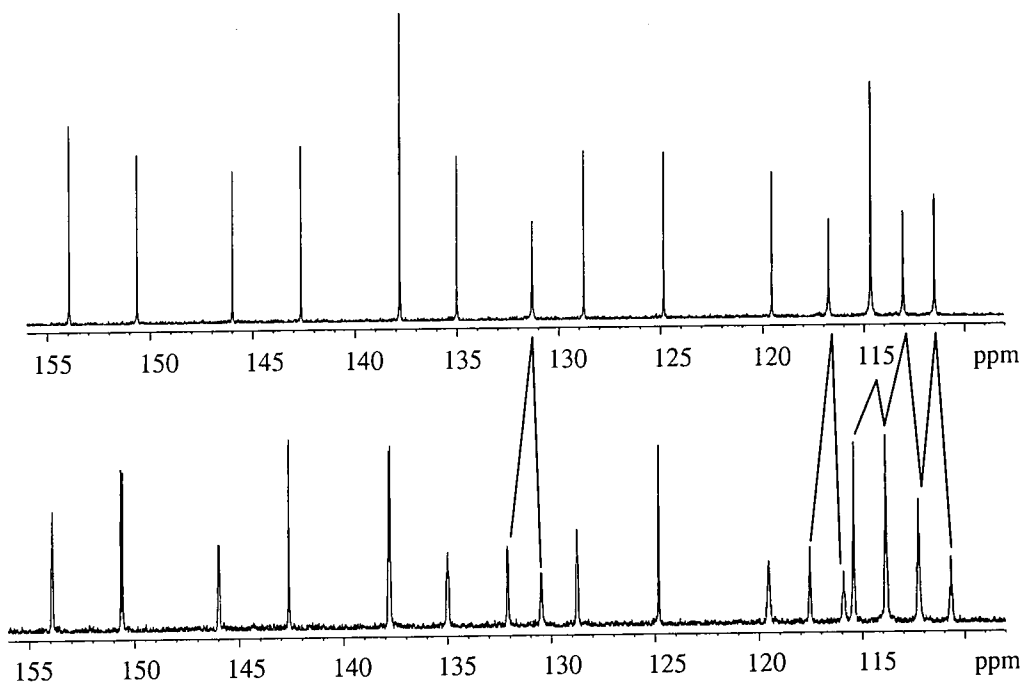


Figure 15: Expansion of a  $^{13}\text{C}$  coupled spectrum of compound **9** in  $d_6$ -DMSO on a Bruker AMX 400 spectrometer with a 2 s recycle delay,  $5.5 \mu\text{s}$   $90^\circ$  pulse width and 6144 acquisitions. The connecting lines show the relationship between the  $^1\text{H}$  decoupled and coupled spectra.

### 3.4.2 $^{13}\text{C}$ Chemical Shift Comparison

Table 6 and Table 7 show  $^{13}\text{C}$  assignments of the compounds soluble enough to record  $^{13}\text{C}$  spectra in  $d_6$ -DMSO and  $\text{D}_2\text{O}$  respectively.

Carbon number	Chemical shift / ppm			
	8 + Na <sub>2</sub> CO <sub>3</sub> room temperature	9 room temperature	13 room temperature	13 363K
t1			164.03	163.82
t3 and t5			165.58	165.40
1	127.93	128.77	128.71	128.51
2	138.05	137.81	141.98	141.42
3	134.92	135.01	120.50 or 120.74	120.15
4	131.33	131.31	135.05	134.12
4a	125.23	124.84	126.85	126.51
5	116.64	116.75	116.60	116.02
6	143.36	142.64	142.59	142.64
7	111.67	111.49	111.60	111.22
8	153.77	153.93	154.08	153.57
8a	119.05	119.55	118.90	118.78
1'	141.86	137.81	142.23	141.98
2'	123.29	145.98	141.33 or 144.05	140.64 or 143.98
3'	114.15	114.66	119.06	118.97
4'	151.55	150.63	141.33 or 144.05	140.64 or 143.98
5'	114.15	114.66	120.50 or 120.74	120.15
6'	123.29	113.05	113.55	112.79
a1			37.00	36.69
a2			50.65	50.34

Table 6: <sup>13</sup>C chemical shifts in d<sub>6</sub>-DMSO, all recorded on a Bruker AMX 400 spectrometer.

Comparison of C2, C3, C4 and C4a with literature data<sup>13</sup> (C2=140.2 ppm, C3=120.1 ppm, C4=133.8 ppm and C4a=126.5 ppm) show that **13** is present as the azo form.<sup>7,21-23</sup> All the molecules considered here will also be in the azo form, as the OH is in a position

All the molecules considered here will also be in the azo form, as the OH is in a position that causes disruption of the aromaticity of the naphthalene ring in forming the hydrazo tautomer. Amino-imino tautomerism exists exclusively in the amino-azo form.

Carbon number	Chemical shift / ppm			
	9 room temperature	12 353K	17 room temperature	17 353K
t1		~158.5	164.13	165.57
t3 and t5		~158.5	166.15	167.65
1	131.21 or 132.40	130.96 or 133.26	131.34 or 132.72	132.35 or 134.37
2	139.89	139.38, 140.19 or 141.54	140.01, 140.45, 141.08 or 142.64	141.39, 141.68, 142.74 or 143.53
3	131.21 or 132.40	130.86 or 133.26	131.34 or 132.72	132.35 or 134.37
4	136.34	136.37	136.88	137.68
4a	126.97	126.97	127.11	128.17
5	120.63	119.82	119.83 or 120.57	121.29 or 121.38
6	139.47	140.72	140.01, 140.45, 141.08 or 142.64	141.39, 141.68, 142.74 or 143.53
7	112.96	113.25	113.48	114.51
8	155.40	154.99	155.54	156.33
8a	123.49	122.29	123.22	124.15
1'	140.99	144.22	143.18	144.79
2'	142.32	139.38, 140.19 or 141.54	140.01, 140.45, 141.08 or 142.64	141.39, 141.68, 142.74 or 143.53
3'	115.60	121.11	119.83 or 120.57	121.29 or 121.38
4'	151.03	139.38, 140.19 or 141.54	140.01, 140.45, 141.08 or 142.64	141.39, 141.68, 142.74 or 143.53
5'	120.40	124.61	124.16	125.15
6'	117.80	115.46	116.41	117.53
a1		41.83	52.17	52.84
a2		69.66	61.92	62.85
a3		72.96		
a4		62.05		

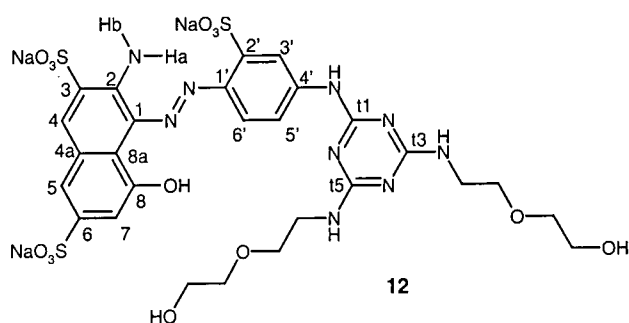
~ refers to approximate shift due to broadness.

Table 7:  $^{13}\text{C}$  chemical shifts in  $\text{D}_2\text{O}$ , all recorded on a Bruker AMX 400 spectrometer.

From the tables it can be seen that the chemical shifts are consistent with each other in the different compounds. Any differences can be accounted for in terms of changes in substituents.

### 3.4.3 Observations

#### Compound 12



A  $^{13}\text{C}$  spectrum in DMSO was recorded at 363K. This temperature had to be maintained for several hours to obtain a good signal-to-noise ratio. It was found that the sample decomposed. DMSO is an oxidising agent and it was thought this was initiating transformation to a triazole, shown in Figure 16.

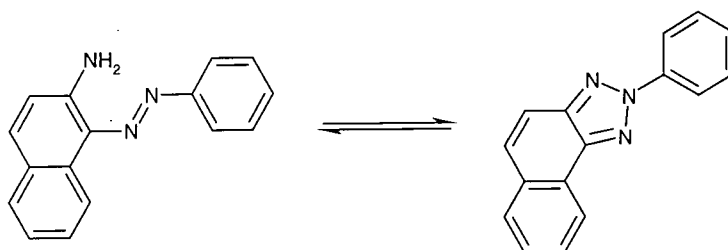


Figure 16: Decomposition of compound 12 in  $d_6$ -DMSO at 363 K.

Heating the sample in  $\text{D}_2\text{O}$  did not lead to decomposition, suggesting that the DMSO is indeed causing sample degradation.

### 3.5 References

- <sup>1</sup> P. Gregory and D. Thorp, *J. Chem. Soc. Perkin Trans. 1*, 1990 (1979).
- <sup>2</sup> T. Asakura and M. Ishida, *J. Colloid Interface Sci.*, **130**, 184 (1989).
- <sup>3</sup> K. Hamada, T. Iijima and S. Amiya, *J. Phys. Chem.*, **94**, 376 (1990).
- <sup>4</sup> A. Lycka, *Annu. Rep. NMR Spectrosc.*, **26**, 247 (1993).
- <sup>5</sup> J. Kelemen, *Dyes and Pigments*, **2**, 73 (1981).
- <sup>6</sup> M. Nepras, M. Titz, M. Necas, S. Lunak jr., R. Hrdina and A Lycka, *Coll. Czech. Comm.*, **53**, 213 (1988).
- <sup>7</sup> J. Kelemen, S. Moss, H. Sauter and T. Winkler, *Dyes and Pigments*, **3**, 27 (1982).
- <sup>8</sup> K. J. Morgan, *J. Chem. Soc.*, 2151 (1961).
- <sup>9</sup> R. A. Cox and E. Buncl, in *The chemistry of the hydrazo, azo and azoxy groups*, ed. S. Patai, London, Wiley (1975).
- <sup>10</sup> J. W. Emsley, J. C. Linden, S. R. Salman and D. T. Clark, *J. Chem. Soc. Perkin Trans 2*, **5**, 611 (1973).
- <sup>11</sup> W. P. Aue, E. Bartholdi and R. R. Ernst, *J. Chem. Phys.*, **64**, 2229 (1975).
- <sup>12</sup> D. H. Williams and I. Fleming, *Spectroscopic methods in organic chemistry*, McGraw-Hill Book Company, Maidenhead, 5<sup>th</sup> Ed., 1995.
- <sup>13</sup> A. Lycka, J. Jirman and P. E. Hansen, *Dyes and Pigments*, **10**, 259 (1989).
- <sup>14</sup> T. Schaefer, *J. Phys. Chem.*, **79**, 1888 (1975).
- <sup>15</sup> J. Reuben, *J. Am. Chem. Soc.*, **109**, 316 (1987).
- <sup>16</sup> P. E. Hansen, *Magn. Reson. Chem.*, **24**, 903 (1986).
- <sup>17</sup> Gaussian 94, Revision E.2, M. J. Frisch, G. W. Trucks, H. B. Schlegel, P. M. W. Gill, B. G. Johnson, M. A. Robb, J. R. Cheeseman, T. Keith, G. A. Petersson, J. A. Montgomery, K. Raghavachari, M. A. Al-Laham, V. G. Zakrzewski, J. V. Ortiz, J. B. Foresman, J. Cioslowski, B. B. Stefanov, A. Nanayakkara, M. Challacombe, C. Y. Peng, P. Y. Ayala, W. Chen, M. W. Wong, J. L. Andres, E. S. Replogle, R. Gomperts, R. L. Martin, D. J. Fox, J. S. Binkley, D. J. Defrees, J. Baker, J. P. Stewart, M. Head-Gordon, C. Gonzalez, and J. A. Pople, Gaussian, Inc., Pittsburgh PA, 1995.
- <sup>18</sup> Y. Kosugi and T. Takeuchi, *Org. Magn. Reson.*, **12**, 435 (1979).
- <sup>19</sup> Y. Kosugi, *Anal. Sci.*, **4**, 353 (1988).
- <sup>20</sup> J. L. Marshall, *Carbon-Carbon and Carbon-Proton NMR Couplings Vol.2*, VCH, Florida, 1983.

<sup>21</sup> J. Seita, J. Sandstrom and T. Drakenburg, *Org. Magn. Reson.*, **11**, 239 (1978).

<sup>22</sup> I. A. McDonald, T. J. Simpson and A. F. Sierakowski, *Aust. J. Chem.*, **30**, 1727 (1977).

<sup>23</sup> A. Lycka and P. E. Hansen, *Org. Magn. Reson.*, **22**, 569 (1984).

## Chapter 4

# Observation of Internal Rotation by NMR

### 4.1 Introduction

Molecules are never stationary. They all undergo vibrational processes but these are too rapid ( $\sim 10^{12}$  to  $10^{14}$  Hz) to be studied by NMR. Slower motions however do have the potential of being NMR observable if they lead to a change in the local environment of an observed nucleus. This is called 'chemical exchange' or, perhaps more descriptively, 'magnetic-site exchange' and includes processes such as internal rotation, ring inversion, dissociation to quote a few. This leads to the possibility of measuring the rate of the process using NMR.<sup>1,2</sup>

There are several different types of exchange: mutual exchange, where two magnetic sites are interchanged by a single process, as opposed to non-mutual exchange. A distinction is also made between coupled and non-coupled exchange, that is exchange of a nucleus between two or more environments where at least two of the sites have different, or potentially different couplings. If it is known that the populations of all the sites in the exchange process are equal, the measurement of rates can be simplified as there are fewer parameters to consider.

When investigating a rate process, it is common to require determination of the rate, activation parameters and/or mechanism of exchange. There are several ways to

achieve this, the most appropriate being dependent on the timescale of the process under investigation.

The NMR timescale usually refers to between 1 s and  $10^{-6}$  s. If the lifetime of the exchanging nuclei are much greater than the NMR timescale, the system is said to be in slow exchange. If this is the case, the NMR spectrum observed is the superposition of the sub-spectra of each of the species present. This occurs because all sites have different precession frequencies and are present for long enough, compared to the difference between those frequencies, to be detected separately in the FID and therefore in the resulting spectrum. If the lifetime of the exchange species is much smaller than the NMR timescale, the process is in the fast-exchange regime. The NMR spectrum appears to contain a single species. This signal is the average of all the species involved in the process, weighted by their individual populations. This is because the exchange is occurring in a time that is short compared to the difference in the frequencies of the sites. The FID is therefore equivalent to the average of those sites.

For processes where the rate of exchange is comparable to the NMR timescale i.e. the intermediate exchange regime, broad lines will result. The reason for this is the Uncertainty Principle: if the lifetime of the species is known, there will be an uncertainty in its energy resulting in broadness of the NMR spectrum. The appearance of the spectrum is therefore a direct indication of the exact rate in this regime. Starting from the slow regime, where there are separate signals, as the rate is increased, these signals broaden, and then start to move together until what is called the coalescence point. When approaching the fast regime this averaged signal gradually sharpens. Effects on exchange spectra will only be noticeable if the lifetimes of the individual species are less than the effective  $T_2$  of the relevant nuclei.

It has been seen that there are three regimes for exchange and the methods to measure rates are different for each one. If determination of activation parameters is desired, then it is advisable to obtain rate measurements in as many regimes, with as many different methods as possible. These different regimes may be reached by changing the temperature of the solution, but depending on the system in question, not all may be observable. The temperature of coalescence is affected by the rate of the process under investigation and the separation of the peaks in the slow exchange regime, which in turn

depends on the spectrometer field. This coalescence temperature may not be accessible if the solvent melting and boiling point, and decomposition temperature of the sample do not permit it to be reached.

In the slow-exchange regime, a method called selective polarisation transfer (SPT) can be used.<sup>3,4</sup> Here, one of the signals involved in the exchange is saturated and the intensity of the other signals are measured and compared to their pre-saturation values by (1):

$$k = \frac{1}{T_{1A}} \left( \frac{M_{0A}}{M_A} - 1 \right) \quad (1)$$

Where  $M_{0A}$  is the equilibrium magnetisation and  $M_A$  is the net magnetisation of A. As well as being dependent on the rate process, the intensities of the unsaturated signals are also dependent upon the spin-lattice relaxation rate, which must be determined for each system at each temperature. An alternative procedure is to invert one signal and monitor the recovery of all exchanging signals (selective polarisation inversion, SPI).

There is also a 2D experiment commonly used called EXSY (Exchange Spectroscopy),<sup>5</sup> the pulse sequence is shown in chapter 2, section 2.2.5. EXSY can indicate chemical exchange by the appearance of cross peaks before line broadening occurs. It can be regarded as a 2D equivalent of the saturation transfer experiment. With this pulse sequence it is trivial to see which groups of peaks are exchanging, therefore obtaining mechanistic information, but it is difficult to extract rate constants using this method. A series of experiments must be recorded at different mixing times, the volume integrals must be evaluated, which is more difficult than the integration of areas, and the  $T_1$ 's of exchanging spins must be known.<sup>6</sup> As a consequence of this it is not commonly used for detailed rate measurements.

Bandshape fitting is applicable in the intermediate-exchange regime, where the linewidth is dominated by the exchange contribution. With this method, spectra are recorded at a series of temperatures. The bandshape of the exchanging peaks will change with temperature. These bandshapes can be fitted using the appropriate theory,

to give values of the rate constants at the different temperatures. There are two levels of theory used in such simulations, the Bloch equations,<sup>7</sup> used for uncoupled exchange, and the density matrix method,<sup>8-11</sup> based on a quantum mechanical treatment, applicable to coupled exchange. Bandshape fitting can only be used when information is available about the chemical shifts of the sites in the slow-exchange regime, and their dependence on temperature.

Information can be obtained directly from the coalescence temperature,  $T_c$ , using (2) for an equally-populated two-site exchange situation.

$$\Delta G^\ddagger = aT_c \left[ 9.972 + \log_{10} \left( \frac{T_c}{\Delta\nu_c} \right) \right] \quad (2)$$

where:

$a = 0.0191 \text{ kJ mol}^{-1}$  and

$\Delta\nu_c$  is the frequency separation in the slow exchange regime.

This, however, requires accurate determination of the coalescence temperature which can be difficult, and is ill-defined if more than two sites are present.  $\Delta G^\ddagger$  can be measured in this way at different spectrometer fields, a straight line plotted and relevant, now corrected,  $\Delta G^\ddagger$  values read off the graph. This procedure will help reduce errors.

In the fast exchange regime rates can be obtained from relaxation methods. In mobile isotropic fluids  $T_1 = T_{1\rho} = T_2$ .  $T_{1\rho}$  is affected by spectral densities at frequencies of  $\gamma B_1 / 2\pi$  i.e. tens of kHz, whereas  $T_1$  is affected by spectral densities dependent upon  $\gamma B_0 / 2\pi$   $\gamma B_0$ , i.e. MHz. Exchange processes may therefore affect  $T_{1\rho}$  and not  $T_1$ . The difference between  $T_{1\rho}^{-1}$  and  $T_1^{-1}$  is then the exchange contribution to  $T_{1\rho}^{-1}$ , called  $T_{1\rho}^{-1}(\text{ex})$  given by (3) for an equally populated  $A \leftrightarrow X$  system in fast exchange resulting in a single averaged line.

$$T_{1\rho}^{-1}(\text{ex}) = \frac{1}{\frac{1}{2}\pi^2(\nu_A - \nu_X)^2 \tau_A} + \frac{\tau_A}{2\pi^2(\nu_A - \nu_X)^2} \omega_1^2 \quad (3)$$

From (3) it can be seen that plotting  $T_{1\rho}(\text{ex})$  vs  $\omega_1^2$  ( $\omega_1 = \gamma B_1$ ) gives information on the lifetimes of one of the species involved in the exchange (A and X will have the same lifetime), and therefore on the rate of the process.

$T_1$  and  $T_2$  can be used in a similar way to the use of  $T_{1\rho}$  to give information about rates in other regimes.<sup>12</sup>  $T_1$  and  $T_2$  can be measured simultaneously using the offset-saturation transfer experiment,<sup>13</sup> or independently using the inversion recovery method,<sup>14,15</sup> and CPMG<sup>16</sup> respectively.

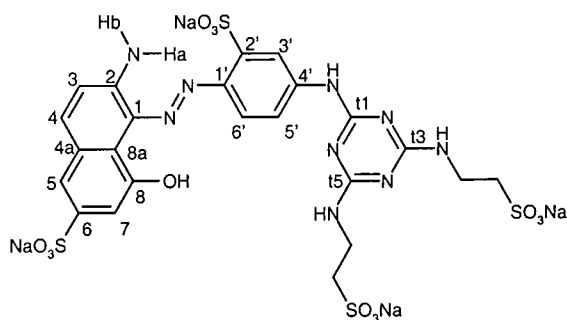
A general guide to methods of use for different exchange rates:

Selective polarisation transfer	$10^{-1} - 10^3 \text{ s}^{-1}$
Bandshape analysis	$10^2 - 10^6 \text{ s}^{-1}$
Relaxation measurements	$>10^6 \text{ s}^{-1}$

These are very approximate, as the regions where the different methods are applicable is very system dependent.

In this study, bandshape analysis was employed as broadening and splitting of the resonances was observed with decreasing temperature. Relaxation measurements could not be applied as the fast exchange regime could not be reached due to the boiling point of the solvent. SPI and SPT methods could not be used because the frequency separation was too small to allow selective irradiation of one conformation at the spectrometer field used (300 MHz).

## 4.2 Observation of Exchange by NMR

**13**

Proton spectra of compound **13** in  $d_6$ -DMSO have been recorded at room temperature and 90 °C, as shown in Figure 1. These have already been assigned in chapter 3.

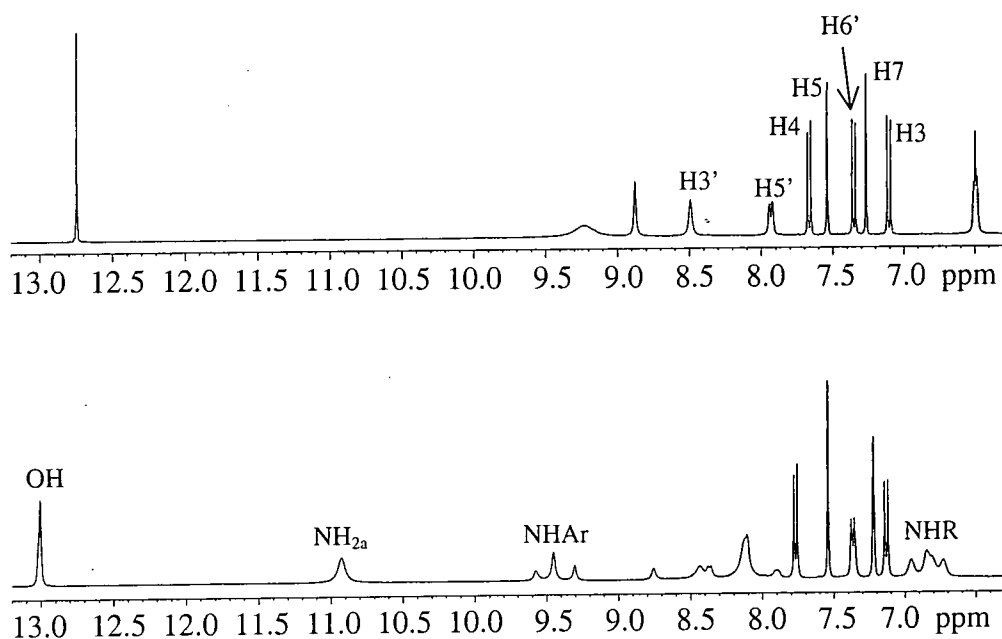


Figure 1: Aromatic region of solution-state proton spectra of compound **13** in  $d_6$ -DMSO recorded using a Bruker AMX 400 spectrometer, using 64 acquisitions, a 7 s recycle delay and a pulse angle of 30°. Bottom spectrum: room temperature; top spectrum: 90 °C.

The <sup>1</sup>H chemical shifts in  $d_6$ -DMSO and their assignments are shown in Table 1.

Proton no.	+90 °C		+23 °C	
	Chemical shift / ppm	Coupling constant / Hz	Chemical shift / ppm	Coupling constant / Hz
3	7.10	9.1	7.12	9.1
4	7.67	9.1	7.77	9.1
5	7.53	1.6	7.53	1.6
7	7.26	1.6	7.21	<sup>b</sup> –
3'	8.48	<sup>b</sup> –	} <sup>a</sup> 8.75, 8.43, 8.33, 8.12, 7.90	
5'	7.94	8.9, <sup>b</sup> –		
6'	7.35	8.9	7.36	8.8
OH	12.78		13.01	
NH <sub>a</sub>	9.24		10.92	
NH <sub>b</sub>	9.24		8.12	
NHAr	8.94		9.30, 9.45, 9.58	
NHR	6.52		6.71, 6.84, 6.96	
NHCH <sub>2</sub>	3.67	6.8, 5.6 to NH	4.55	
CH <sub>2</sub> SO <sub>3</sub> Na	2.81	6.8	2.81	

<sup>a</sup> Assignments of chemical shifts in this range are uncertain and it is difficult to disentangle the spectrum to yield all the coupling constants. First-order analysis is assumed.

<sup>b</sup> Other coupling constants not determined.

Table 1: Proton chemical shifts of compound 13 in *d*<sub>6</sub>-DMSO.

In the spectrum shown in Figure 1, three broad peaks are observed for NHAr, with multiple peaks also observable for H5', H3' and NHR (it is not clear which of the bands in the region of 8.75–7.90 ppm are from H3' and which are from H5'). These multiple resonances are averaged at 90°C, indicating that an exchange process is occurring. This process cannot be probed further in *d*<sub>6</sub>-DMSO due to the constraints of the solvent freezing point (20 °C).

Although  $^{13}\text{C}$  spectra have been used<sup>17,18</sup> in studies of similar compounds to evaluate chemical exchange in detail, this approach was not realistic in the present study as the solubility of compound **13** was not sufficient to obtain the required sensitivity for variable-temperature experiments. A  $^{13}\text{C}$  spectrum in  $d_6$ -DMSO was recorded at 23°C however and is shown in Figure 2 (an assignment of the spectrum is given in chapter 3, table 6). This shows broadening of the resonances of the triazine ring and nearby carbons only, suggesting that the exchange observed is due to a process involving the triazine ring rather than the naphthalene ring.

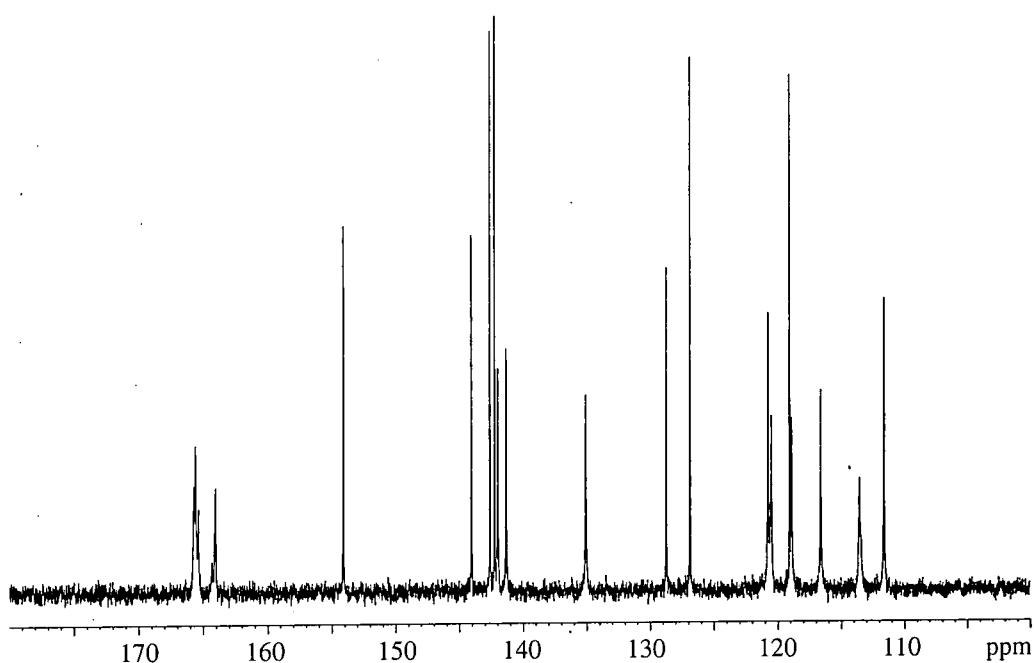


*Figure 2: Aromatic region of a carbon-13 spectrum of compound **13** in  $d_6$ -DMSO at 100.61 MHz, at 23 °C, with 4096 acquisitions, a 2 s recycle delay and 5.5  $\mu$  s 90° pulse.*

A solvent with a lower freezing point,  $\text{CD}_3\text{OD}$ , was chosen, for further study using proton NMR. Variable-temperature proton spectra recorded between  $-11\text{ }^\circ\text{C}$  and  $+61\text{ }^\circ\text{C}$  in  $\text{CD}_3\text{OD}$  are shown in Figure 3. The temperatures were calibrated previously using methanol below room temperature and 1,2-ethanediol above room temperature.<sup>19,20</sup>

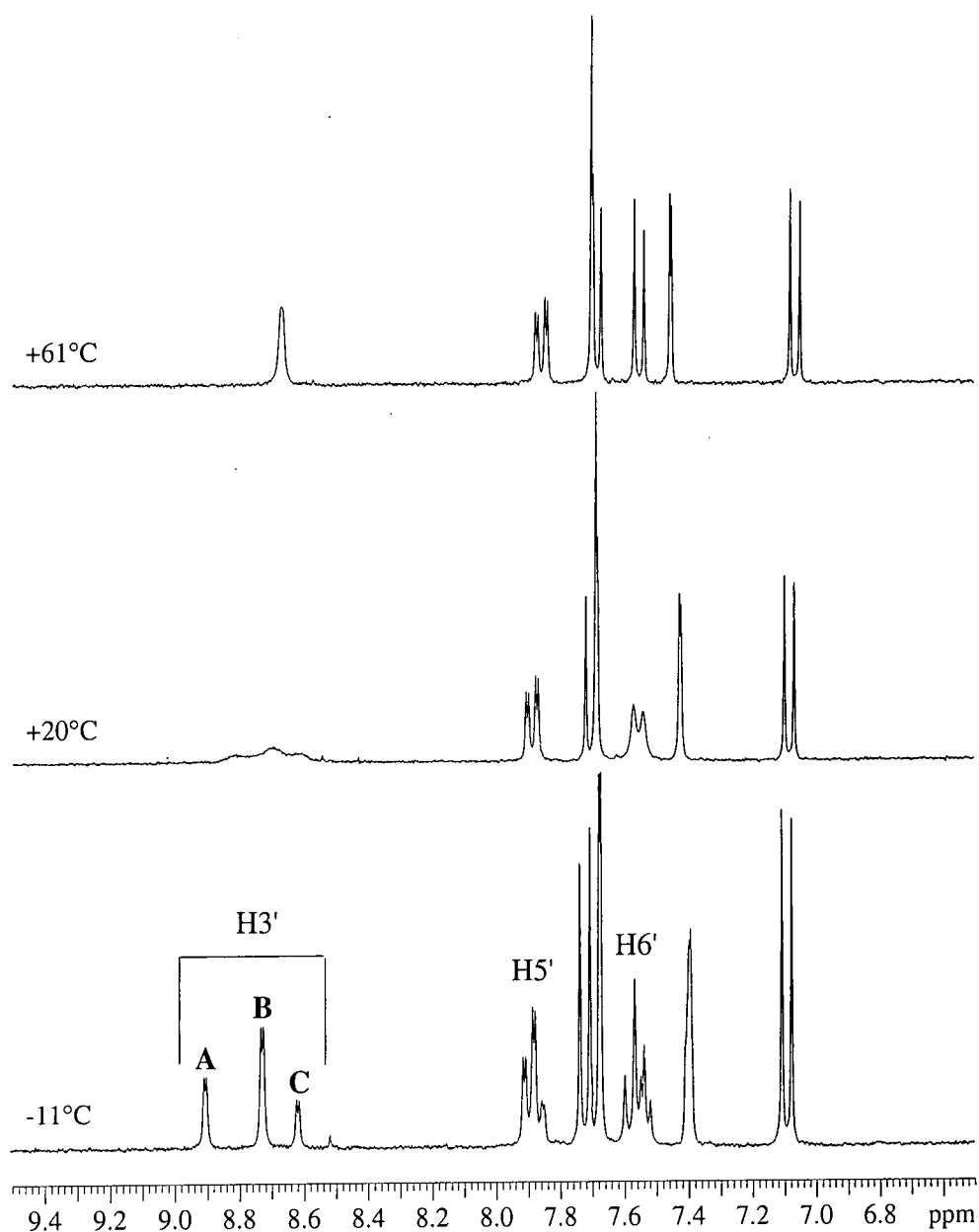
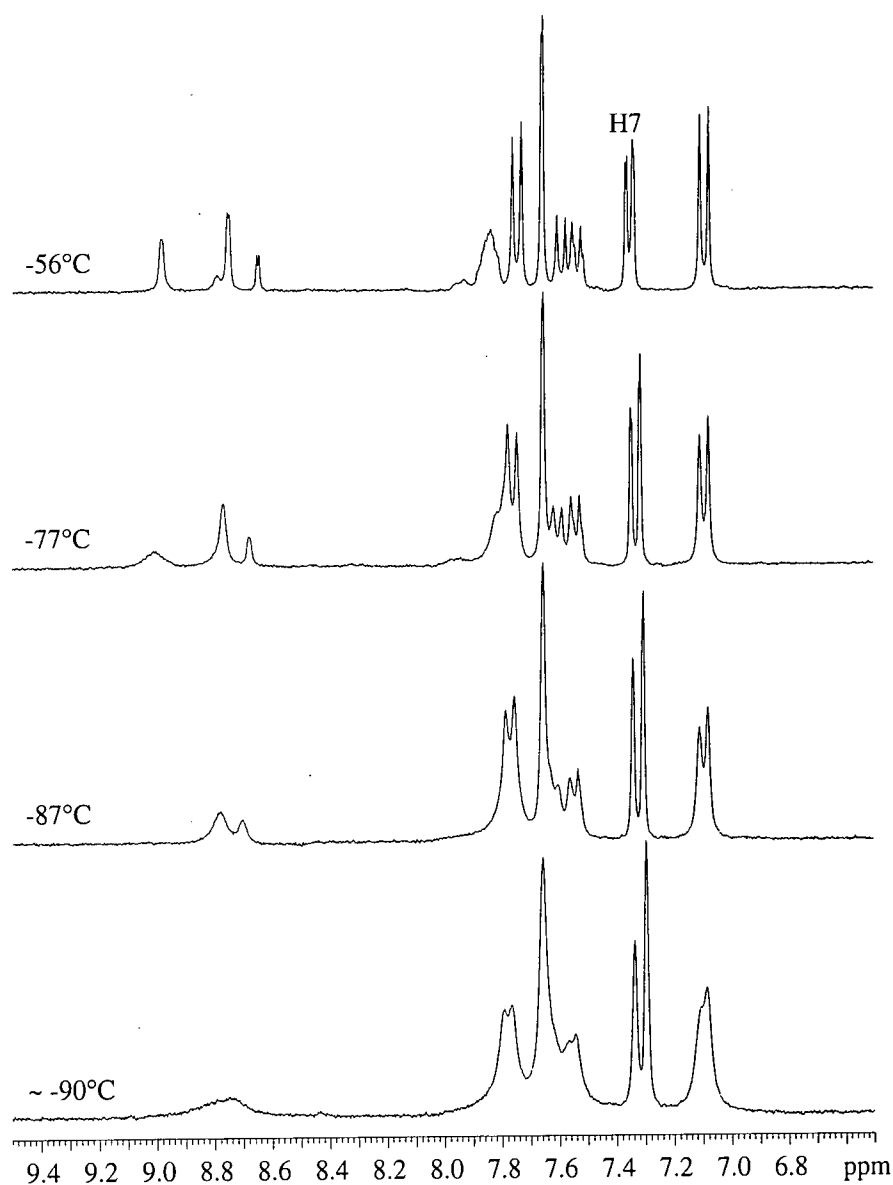


Figure 3: Variable-temperature  $^1\text{H}$  spectra of compound **13** in  $\text{CD}_3\text{OD}$ , at 299.91 MHz, aromatic region only, using 128 acquisitions, with a 1 s recycle delay and a pulse angle of  $28.4^\circ$ .

The spectra exhibit a typical three-site exchange situation for  $\text{H}3'$ : three bands (doublets arising from coupling to  $\text{H}5'$ ) at  $-11^\circ\text{C}$  which broaden, coalesce at approximately  $+20^\circ\text{C}$  and then sharpen to form a single line as the temperature is raised further. These three bands are denoted as A at 8.90 ppm, B at 8.73 ppm and C at 8.61 ppm, all values measured at  $-11^\circ\text{C}$ .  $\text{H}5'$  and  $\text{H}6'$  also show three resonances at low temperatures, but these bands are more complex because of overlap, and also due to a more complicated coupling pattern in the case of  $\text{H}5'$ . Since the three protons  $\text{H}3'$ ,  $\text{H}5'$  and  $\text{H}6'$  are part of the same structural unit, the analysis of the bands arising from the latter two would

not provide any additional information and so they were not fitted. In other studies of related compounds,<sup>17,18</sup> labile protons have been used to examine exchange, but in this investigation the variable temperature work has used a protic solvent, with the result that the labile protons have been exchanged for deuterium and therefore their  $^1\text{H}$  NMR signals are not observed.

As the temperature is decreased below  $-20\text{ }^\circ\text{C}$ , further features in the spectrum of H3' are observed, as shown in Figure 4.



The temperature reading at  $-90\text{ }^\circ\text{C}$  could not be calibrated as pure methanol freezes at  $-93\text{ }^\circ\text{C}$ .

Figure 4: Variable-temperature  $^1\text{H}$  spectra of compound 13 in  $\text{CD}_3\text{OD}$ , at 299.91 MHz, aromatic region only, using 128 acquisitions, with a 1 s recycle delay and a  $28.4^\circ$  pulse angle.

At  $-56\text{ }^{\circ}\text{C}$  a fourth low-intensity peak is seen. However, as the temperature decreases further, broadening occurs for many of the bands so that only two signals are clearly seen for H3' at  $-87\text{ }^{\circ}\text{C}$ . Details of this broadening are summarized in Table 2. The broadening of H3' and H5' is greater than that which would be expected to arise from the increasing viscosity with decreasing temperature. Broadening suggests a motional effect, but this is unexpected as the internal rotation had been frozen out at  $-11\text{ }^{\circ}\text{C}$ . It may be that a rate process that is rapid at room temperature and down to  $-32\text{ }^{\circ}\text{C}$  is frozen out at lower temperatures, this possibility is explored further in section 4.3. An alternative explanation is aggregation. Details of the chemical shifts and coupling constants for a solution of **13** in  $\text{CD}_3\text{OD}$  are shown in Table 2.

To do a kinetic analysis, the exchange mechanism has to be determined. A two-dimensional EXSY spectrum in  $\text{CD}_3\text{OD}$  at  $-11\text{ }^{\circ}\text{C}$  was recorded at a mixing time of 1 s (shown in Figure 5). Strong cross peaks for AB and BC, with a small cross peak for AC were seen. It is possible that the AC cross peak arises from a two-step process (AB followed by BC) rather than from direct AC exchange. The results of the exchange-fitting program detailed in section 4.4 confirm that this possibility is a likely explanation.

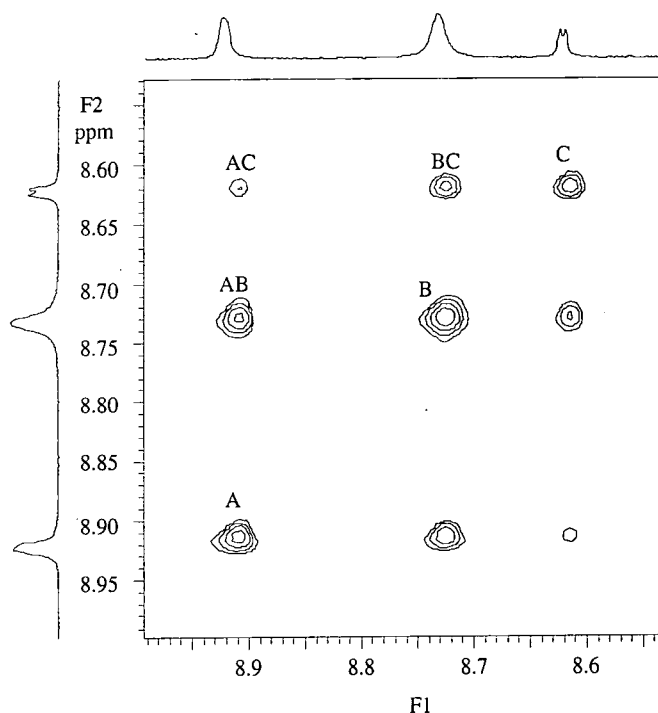


Figure 5: Expansion of the H3' region of a 2D - EXSY  $^1\text{H}$  spectrum of compound **13** in  $\text{CD}_3\text{OD}$  at 399.97 MHz and  $-10\text{ }^{\circ}\text{C}$  with cross peaks as labelled (see text) and using 4 acquisitions,  $2 \times 256$  increments in  $t_1$ , 2 s recycle delay, 1 s mixing time.

Temp / °C	Shift / ppm	Coupling constant / Hz	Integral %	Width / Hz
+61	8.67			6.1
+50	8.68			8.5
+40	8.69			18.7
+31	8.70			35.9
+20	8.81			
+9	8.85			
-1	8.88			
-11	8.90	2.1	30	30
-23	8.92	2.3	30	30
-32	8.94	2.3	32	32
-45	8.97	2.3	34	34
-56	8.99	2.0	33	33
-68	9.0		33	33
-77	9.01		28	28
-87	8.78			
-90 <sup>b</sup>	8.74			
			49	49
			21	21
		2.5	19	19
		2.5	19	19
		2.5	16	16
		2.5	16	16
		2.4	15	15
			15	15
			17	17
			10.2	10.2
			5.9	5.9
			4.8	4.8
			4.4	4.4
			4.7	4.7
			5.1	5.1
			5.9	5.9
			9.0	9.0
			20.9	20.9
			7.6	7.6
			5.7	5.7
			4.7	4.7
			4.1	4.1
			4.3	4.3
			4.2	4.2
			4.5	4.5
			4.8	4.8
			8.2	8.2
			5.7	5.7

<sup>a</sup> Coupling constants, integral and width information not measurable for this peak.

<sup>b</sup> The temperature reading at -90 °C could not be calibrated as pure methanol freezes at -93 °C.

Table 2: Spectral details of H3' for a solution of compound 13 in CD<sub>3</sub>OD with varying temperature.

### 4.3 Identification of Exchange Processes

The explanation of the processes occurring must include a rationalisation for the observations. These are: one peak, splitting into three, then the appearance of a fourth peak followed by general broadening as the temperature is decreased. Internal rotation on the NMR timescale,<sup>21</sup> has been observed for side chains of 1,3,5-triazines. It is therefore likely that this is responsible for the spectral features observed here. There are sixteen possible rotamers, displayed in Figure 6, due to two possible conformations about each of the three triazine C-N bonds and the two orientations possible for the aromatic ring, assuming coplanarity of the two rings.

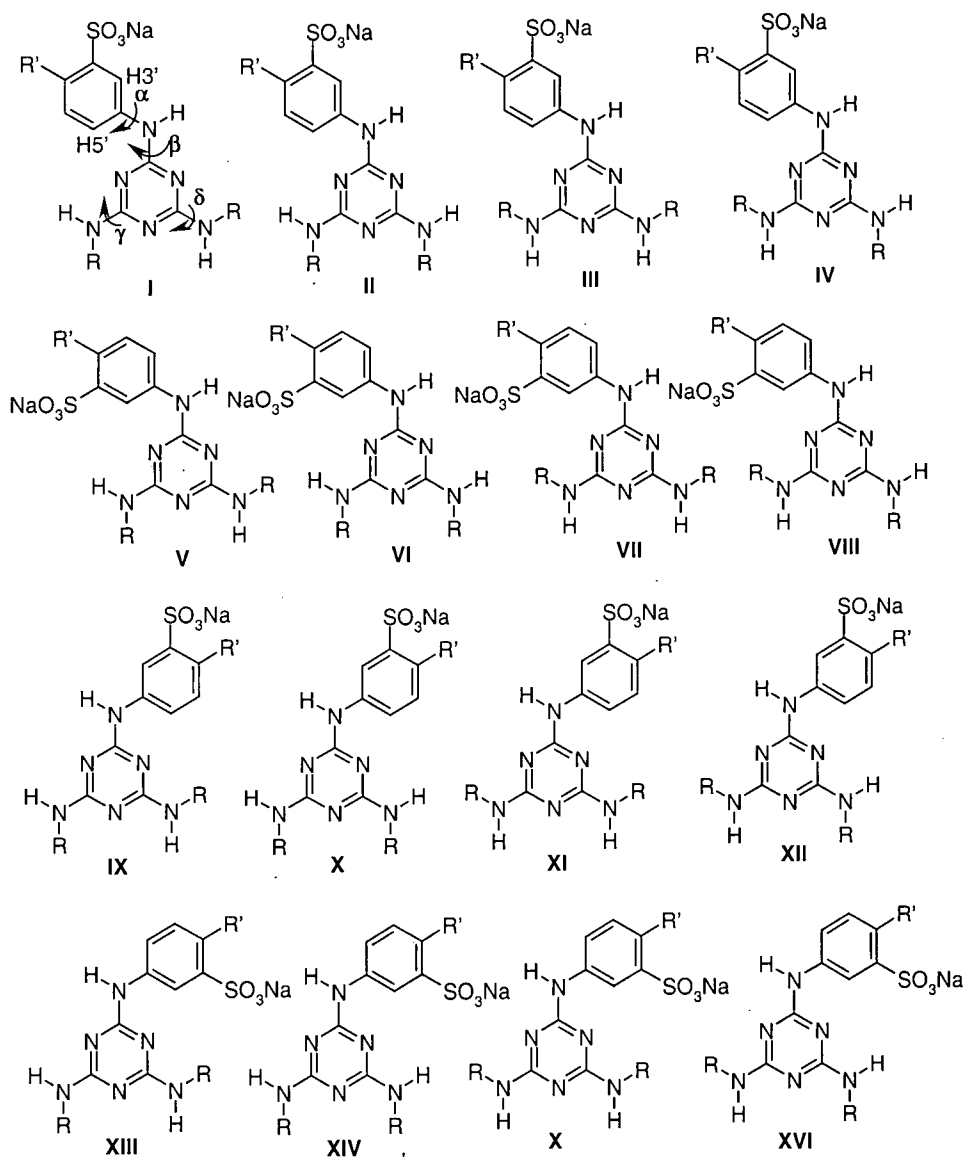


Figure 6: Possible rotational isomers for compound 13. R is  $\text{CH}_2\text{CH}_2\text{SO}_3\text{Na}$  and R' is a substituted naphthalene ring joined to the central aromatic ring by an azo group.

There are two sets of equivalent rotamers: I=XII, II=X, III=XI, IV=IX, V=XVI, VI=XIV, VII=XV and VIII=XIII. This decreases the number of distinguishable rotamers to eight. These are related as shown in Figure 7.

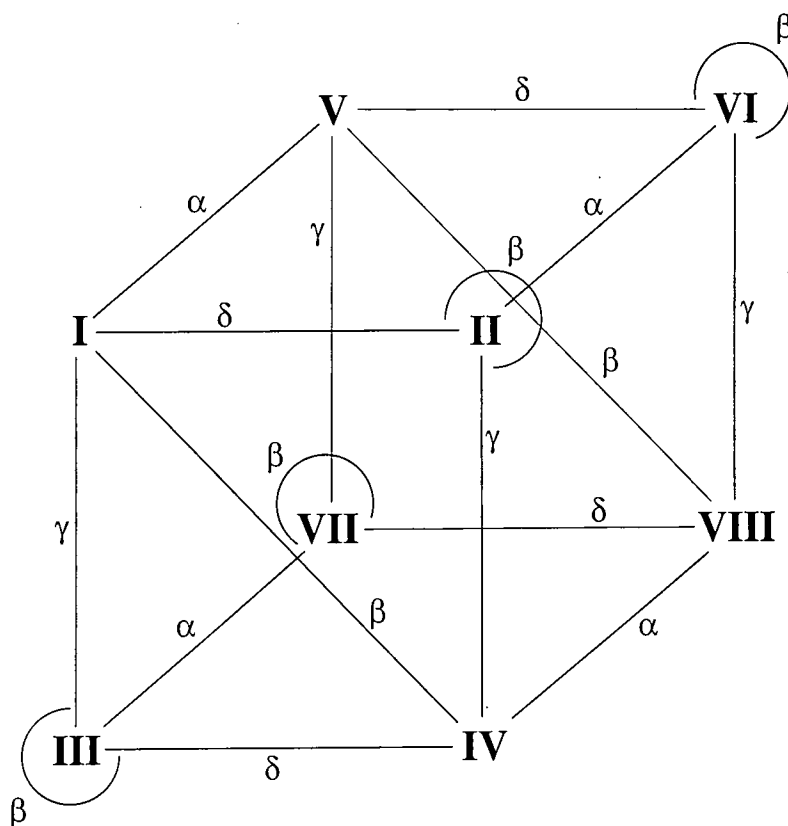


Figure 7: Relationship between rotamers I to VIII shown in Figure 6.

If there is rapid rotation about  $\alpha$ , but slow rotation of the other processes, there are four rapidly interconverting pairs ( $I \leftrightarrow V$ ,  $II \leftrightarrow VI$ ,  $III \leftrightarrow VII$  and  $III \leftrightarrow VIII$ ). The exchange process for compound **13** has been modelled using simplified systems. The specific details of this modelling will be discussed in chapter 5 but the results will be considered here.

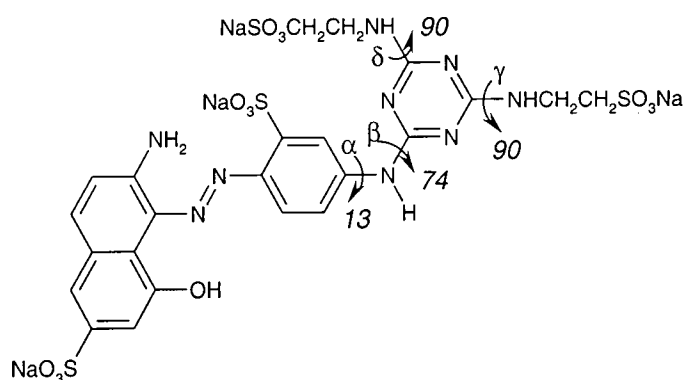


Figure 8: Calculated rotational energy barriers in  $\text{kJ mol}^{-1}$ .

Figure 8 shows that the side chains have the largest barrier to rotation, with  $\alpha$  having the lowest energy barrier. This is surprising but is substantiated by structures in the crystallographic data base which are shown in Figure 9. This figure shows that the smallest barrier,  $\alpha$ , has a large range of angles in the solid state. This indicates that there is a small energy difference between different values for the dihedral angle around this bond and therefore the barrier to internal rotation is low. The dihedral angle of  $\beta$  has a much more limited range of angles, suggesting there is a greater energy difference between the different conformations and therefore a larger energy barrier. This trend in the size of the energy barriers supports the molecular modelling.

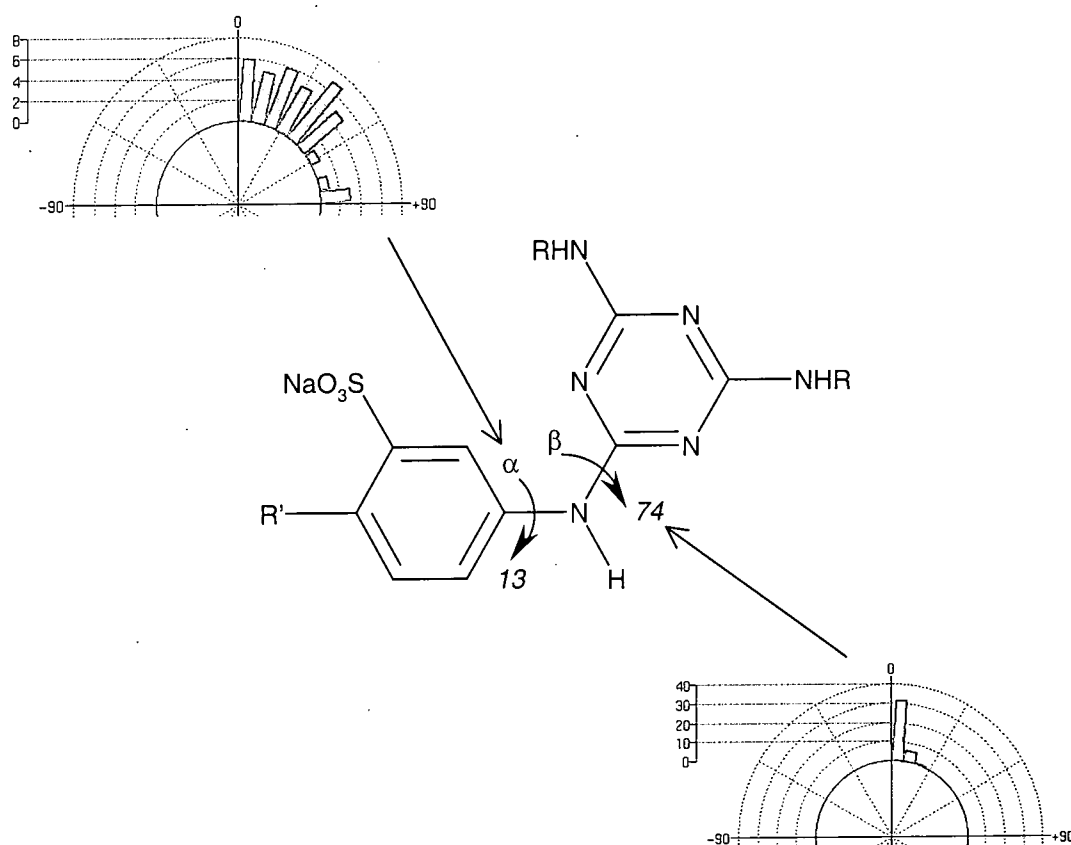


Figure 9: Crystallographic data.

Molecular modelling has shown that there is likely to be fast rotation about  $\alpha$ . There are therefore four possible distinguishable rotamers that can be observed, related as described in Figure 10.

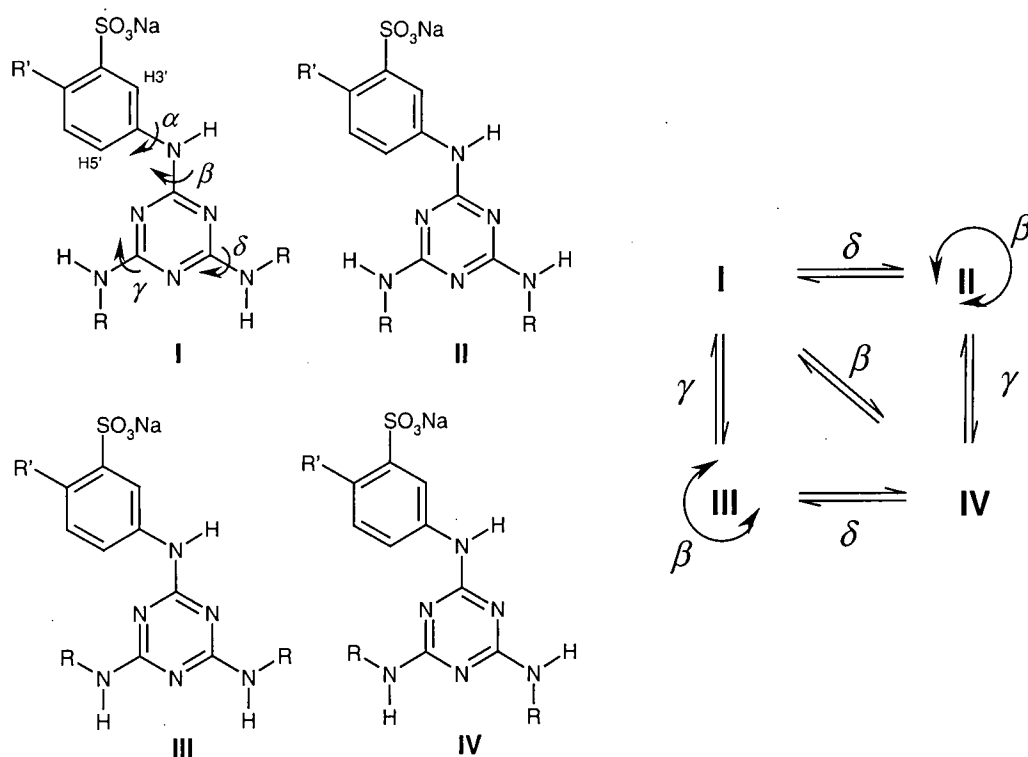


Figure 10: Relationship between four rotamers.

If there is rapid rotation about  $\beta$  then rotamers I and IV become equivalent. This leaves three inequivalent conformations. At high temperatures all four possible rotations are rapid meaning all conformations are equivalent and one band (doublet) is observed in the  $^1\text{H}$  NMR spectrum. As the temperature is decreased, rotations  $\gamma$  and  $\delta$  slow down so that separate signals from three conformations are observed: II, III, and an average of I and IV. As the temperature is decreased further,  $\beta$  begins to slow down, causing the largest intensity peak to split into two, giving four distinguishable conformations, I, II, III and IV. As the temperature is decreased further, the lines broaden again, suggesting yet another active process,  $\alpha$  is slowing down. This leads to four rotamers becoming eight. Further reduction in temperature, to see if there are indeed eight peaks after the broadening, is limited by the freezing point of the solvent.

The populations calculated at 20 °C by molecular modelling, detailed in chapter 5, section 5.1, are I=31.2 %, II=25.0 %, III=21.9 % and IV=21.9 %. In the regime where rotations  $\alpha$  and  $\beta$  are rapid and  $\gamma$  and  $\delta$  are slow i.e. I and IV are in fast exchange, the 3 site populations are therefore expected to be II=25.0 %, III=21.9 % and I+IV=53.1 %. Experimentally they are found to be A=30%, B=49% and C=21%. This suggests that

A=II, B=I+IV and C=III. The populations of the two sites distinguishable as I and IV cannot be accurately determined as they never become fully separated. The higher frequency peak of the two is significantly lower in intensity so it is possibly from IV leaving the lower frequency peak to be I.

Some activation parameters have been calculated for the rotational processes, which are discussed in section 4.3.

## 4.4 Exchange Fitting

Due to the complex situation of several rotational processes and broad spectra below -23 °C, only spectra above -23 °C were simulated. Strictly speaking the process should be treated as a sixteen-site exchange problem but as there are only eight inequivalent situations and it is believed that rotations  $\alpha$  and  $\beta$  are rapid at temperatures above -23 °C, where  $\gamma$  and  $\delta$  are being slowed down, the exchange was treated as a three-site process in this region. It is expected, due to the rationalisation of the origin of the peaks discussed in section 4.3, that there are only two rotational processes linking three rotamers in the spectra at these temperatures. A cyclic three-site exchange process, as shown in Figure 11, was used in the fitting however to check this conclusion, as any processes not occurring would have rates of zero obtained in the fitting. Peak A is defined as the highest frequency peak, B the middle and C the lowest.

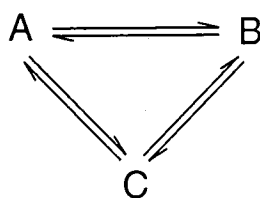


Figure 11: Three-site exchange relationship.

The exchange observed was suitable for bandshape analysis.<sup>22,23</sup> The three sites do not have equal populations, and although coupling is observed to H5', the situation is treated as an un-coupled problem, as the coupling is not effected by the exchange. A

Matlab program<sup>24</sup> was used to fit iteratively the three exchange rate constants ( $k_{AB}$ ,  $k_{AC}$  and  $k_{BC}$ ), together with chemical shifts and populations of each site. A common linewidth, a common coupling constant ( $J$ , the coupling to H5') and a baseline offset, to the experimental spectra were also fitted.<sup>25</sup>

Initially, the parameters required in the simulation were defined. The three natural linewidths ( $W_A$ ,  $W_B$  and  $W_C$ ) were set to be equal to reduce the number of parameters required in the fitting. The three  $T_2$  values were then computed as  $T_2 = 1/\pi W$ .

The timescale of the FID for the experimental spectrum was calculated using the spectral width and the dwell time. The three reverse rate constants are related to the forward rate constants, which are estimated in the program input, by the population ratios, as defined in (4), according to conservation of matter.

$$\begin{aligned} k_{BA} &= \left( \frac{n_A}{n_B} \right) k_{AB} \\ k_{CB} &= \left( \frac{n_B}{n_C} \right) k_{BC} \\ k_{CA} &= \left( \frac{n_A}{n_C} \right) k_{AC} \end{aligned} \quad (4)$$

The trial spectra for three-site exchange were calculated according to a modified Bloch treatment shown in (5).<sup>7,26-29</sup>

$$\mathbf{L} = i\mathbf{\Omega} + \mathbf{K} + \mathbf{R} \quad (5)$$

where:

$$\mathbf{\Omega} = \begin{bmatrix} \nu_A & 0 & 0 \\ 0 & \nu_B & 0 \\ 0 & 0 & \nu_C \end{bmatrix} \text{ is the diagonal matrix of chemical shifts,}$$

$$\mathbf{W} = \begin{bmatrix} -(k_{AB} + k_{AC}) & k_{BA} & k_{CA} \\ k_{AB} & -(k_{BA} + k_{BC}) & k_{CB} \\ k_{AC} & k_{BC} & -(k_{CA} + k_{CB}) \end{bmatrix} \text{ is the kinetic exchange matrix and}$$

$$\mathbf{R} = \begin{bmatrix} -\frac{1}{T_{2A}} & 0 & 0 \\ 0 & -\frac{1}{T_{2B}} & 0 \\ 0 & 0 & -\frac{1}{T_{2C}} \end{bmatrix} \text{ is the relaxation matrix.}$$

$\mathbf{L}$  in (5) is diagonalised and the FID is calculated using (6).

$$\text{FID} = \exp(\mathbf{L}t)\mathbf{M}_0 \quad (6)$$

where:  $\mathbf{M}_0$  is the equilibrium magnetisation.

The J coupling to H5' was included as an additional modulation, by multiplication of the FID by  $\cos\pi Jt$ . This is equivalent to convolution of the spectrum by a stick doublet. The Fourier transform was then taken of the result to produce the simulated spectrum. The Levenberg-Marquardt method was used to find the optimum parameters.<sup>30</sup> This uses the steepest descent method far away from the minimum and the inverse Hessian method close to the optimised parameters.

The standard deviation of the noise in each spectrum as obtained by Matlab, (shown in Table 3) was used to normalise the value of  $\chi^2$  and in the estimates of the errors on the fitted parameters. The correlation matrix was also estimated. This gives a value between -1 and 1 for each pair of parameters. A negative value indicates an inverse correlation i.e. as one parameter increases the other will decrease to give the same spectrum. The larger the value (further from 0 positive or negative), the more strongly correlated the two parameters and therefore the less accurate they are individually.

Temperature / °C	Noise level
-23	1.26
-11	1.43
-7	1.43
-1	1.43
5	2.48
9	2.23
20	2.32
31	2.33
40	2.29
50	3.36
61	3.51

Table 3: The standard deviation of the noise in the spectra to be fitted.

It can be observed that the noise in the spectrum increases as the temperature is raised. This is not unexpected because as the temperature is increased, thermal noise will increase also, therefore producing more noise in the spectrum.

Bain and Cramer<sup>31</sup> have found that in fitting bandshapes, many parameters are correlated. It is not possible under these conditions to use a least-squares fit to obtain the error on one parameter. The most reliable way to do this is to use error profiling. If there are 10 parameters to fit, 1 is kept constant and the data are fitted using the other 9. The value of the fixed parameter is then changed and the other variables optimised. As the value of the fixed parameter becomes more removed from its ideal value, the fit of the spectra will get worse. When the error at that point, divided by the error at the global minimum exceeds a particular value, the fixed variable has reached its confidence limit.

A similar method was used in the optimisation under discussion here. During the fitting, the program calculated how much each parameter can be changed and still give the same fit. This means that if the number of parameters being fitted decreases then it reduces the freedom of the parameters that are being optimised so their error will appear smaller.  $\chi^2$  refers to how the calculated spectrum compares to the experimental. The

correlation matrix shows that as expected the linewidth is closely correlated with the rate constants. It also shows that the J-coupling is fairly independent. This means it can be fitted in cases where appropriate, that is where the coupling can be observed, without it disrupting the fitting of other parameters.

The number of correlated parameters to be fitted had to be reduced over the intermediate exchange regime ( $\sim +20$  °C). In this range there is one broad peak so large systematic errors would be expected when fitting 12 parameters.

The linewidths of all peaks for solutions are usually dominated by  $B_0$  inhomogeneities. Therefore they are all expected to be very similar. This assumption is usually valid at temperatures above ambient but is not as reliable at lower temperatures. If spectra above and below the rate limits can be found, where broadening due to exchange is not an issue, this can be justified.<sup>32,33</sup> This is not possible in the case under discussion here as the fast exchange regime is limited by the solvent boiling point and the low temperature regime is complicated by the slowing down of other exchange processes. The sensitivity of the bandshape to  $T_2$  is largest at the extremes of slow and fast exchange and is smallest around the coalescence temperature.<sup>34,35</sup> To simplify the exchange fitting it will be assumed here that the natural linewidths of all the peaks are comparable. Therefore the natural linewidth of the non-exchanging doublet, H3, was measured as a function of temperature and compared with the linewidth of the TMS signal, shown in Figure 12.

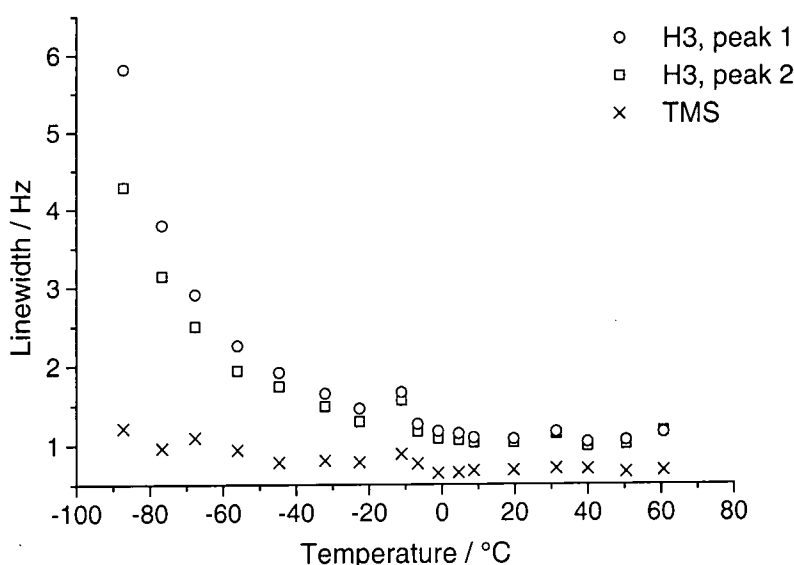


Figure 12: Linewidth of a non-exchanging doublet, H3, and TMS with temperature.

As can be observed from the graph in Figure 12, there is not much variation in the linewidth with temperature in the range observed (-23 to +61 °C). The average value of the linewidth, 1.61 Hz, is comparable to the linewidth of the exchanging peak, H3', obtained by fitting the low temperature spectra, giving confidence to this assumption. Below this temperature range the linewidths of the two peaks of the non-exchanging doublet differ and there is a large deviation from the linewidth of the TMS, presumably due to the reduced mobility of the sample compared with TMS. It is therefore clear that it would be unreliable to fit spectra below -23 °C.

It was assumed that the coupling constants to H3', derived from the low temperature spectra, would be the same for all three bands at all temperatures as explained previously. This parameter was fitted for the low temperature spectra where the 3 peaks to be simulated were well defined and was fixed at a value of 2.48 Hz where the doublet was not clear.

Chemical shifts are strongly correlated with the populations and rates so it is necessary to fix these in the intermediate regime also. The low temperature (-23 to +5 °C) chemical shifts were fitted and can be compared to the chemical shift variation of the non-exchanging doublet, H3, shown in Figure 13. Peak B is actually a combination of two rotamers but as they are in fast exchange here the average chemical shift will be used.

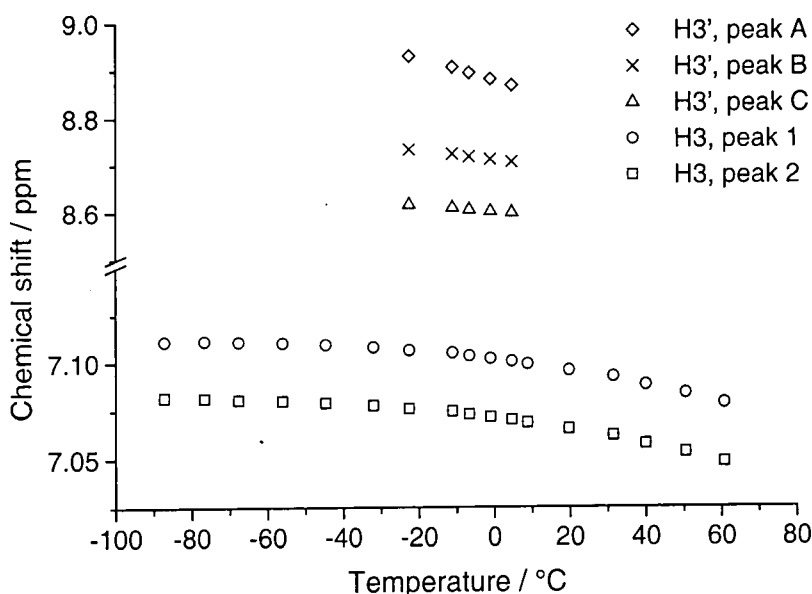


Figure 13: Chemical shift variation.

It can be seen that the chemical shift of the non-exchanging doublet varies smoothly with temperature and appears to be approximately linear in the region of interest. It is feasible therefore to expect that the chemical shift of the exchanging peaks would also vary smoothly. From the graph in Figure 13 it appears that this variation is linear although the change is larger than expected. Chemical shifts may show considerable variation with temperature due to effects such as solute-solute and/or solute-solvent interactions, which can be site-specific, but most importantly due to changes in the nature of the vibrational levels of the molecule or their populations.<sup>21</sup> In most cases these changes in chemical shift can indeed be approximated by a linear relation over a moderate temperature range, although higher order polynomials are sometimes required.<sup>36,37</sup> An equation for each line can be calculated from the graph, in Hz for input into the fitting program:

$$\nu = c_1 T + c_2 \quad \text{where: } c_2 \text{ is in Hz with respect to TMS and:}$$

for peak:	A	$c_1 = -0.22 \pm 0.01$	$c_2 = 2579.6 \pm 0.6$
	B	$c_1 = -0.32 \pm 0.01$	$c_2 = 2612.7 \pm 0.1$
	C	$c_1 = -0.74 \pm 0.01$	$c_2 = 2663.6 \pm 0.1$

N.B. These data were fitted with 5 points and in all cases  $R^2$  was greater than 0.99.

The resulting values from these equations, extrapolated to higher temperatures where required, were used in the fitting routine. To check the validity of the extrapolation, due to the larger variation in shift than expected in the slow exchange regime, the fitted populations were monitored with temperature, as they are strongly correlated with the chemical shifts. The populations were found to vary only to a small extent (probably within experimental error) as expected from the Van't Hoff Isochore.<sup>38</sup> This means they are unlikely to be compensating significantly for errors in the shift extrapolation in the temperature range used in the activation energy measurements (see below) i.e. from -23 °C to +40 °C.

With the constraints imposed, the parameters to be fitted at intermediate and high exchange rates are three rate constants, three populations and a baseline. The absence of a baseline offset may lead to false minima. Examples of fitted spectra are shown in Figure 14.

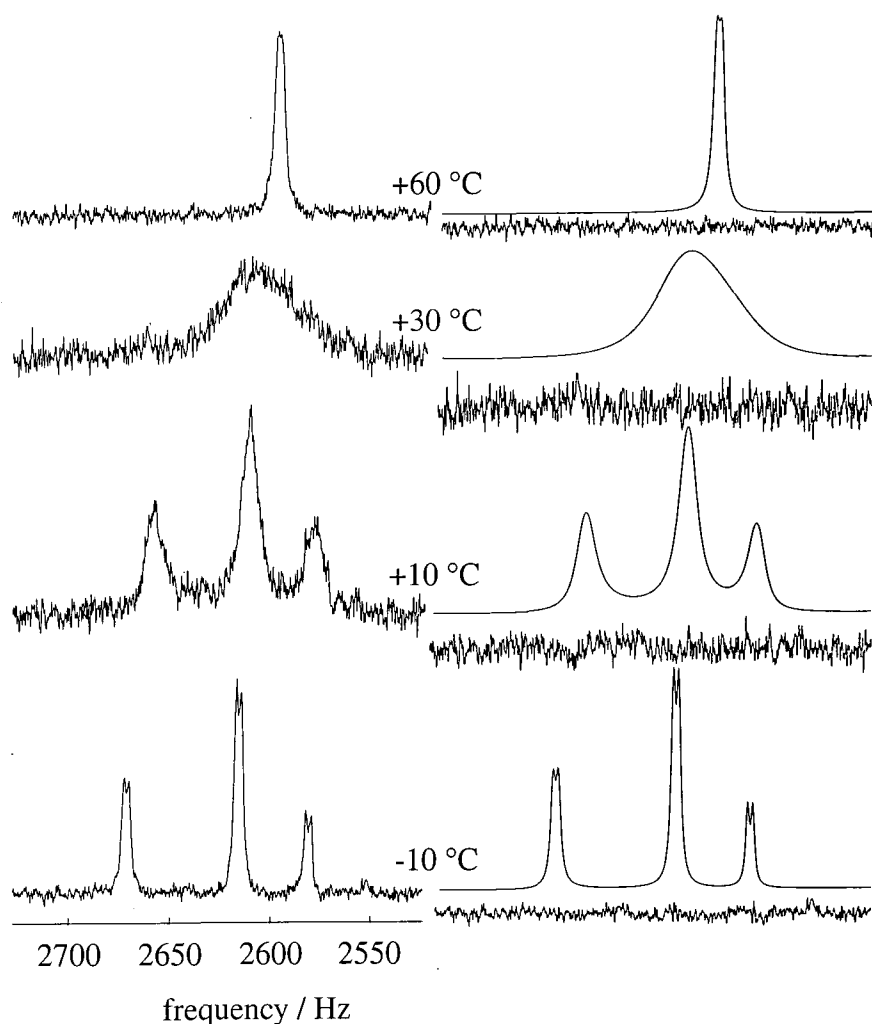


Figure 14: Experimental, theoretical and difference spectra at various temperatures.

It was found that the rate constant AC was indistinguishable from zero at all temperatures, i.e. within the estimate of the error. This is consistent with the rationalisation of the processes discussed in section 4.3. The other calculated rate constants, their statistical errors and percentage populations are shown in Table 4.

Temperature / °C	$k_{AB}$ / s <sup>-1</sup>	Error in $k_{AB}$ / s <sup>-1</sup>	% Error in $k_{AB}$	$k_{BC}$ / s <sup>-1</sup>	Error in $k_{BC}$ / s <sup>-1</sup>	% Error in $k_{BC}$	% Populations		
							A	B	C
-11	2.1	0.1	4.8	1.5	0.1	6.7	31	51	18
-7	1.9	0.1	5.3	2.8	0.2	7.4	28	52	20
-1	3.4	0.1	2.9	5.0	0.3	6.0	28	52	20
5	6.9	0.3	4.3	8.7	0.5	5.7	28	51	21
9	12.4	0.3	2.4	19.0	0.5	2.6	28	50	22
20	35.7	0.8	2.2	55.6	1.6	2.9	26	52	22
31	115.7	31.5	27.2	170.4	31.8	18.7	28	50	22

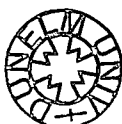
Table 4: Exchange rate constants and their errors, calculated by iterative fitting of the H3' bandshape.

It can be seen from Table 4 that the populations at the temperatures fitted are fairly constant and consistent with the experimental spectra, outlined in Table 2.

## 4.5 Determination of Activation Parameters

The rate constants obtained at +40, +50 °C and +60 °C were not included in Table 4, or in further calculations because in this range the motion is too fast to be measured accurately on the NMR timescale by bandshape fitting. Naively one would think that data points should be chosen at the extremes of the temperature range, but unfortunately these are the least accurate. Data for  $\Delta S^\ddagger$  and  $\Delta H^\ddagger$  were calculated using the statistical mechanics model proposed by Eyring.<sup>39,40</sup> According to this, the exchange rate constant is given by (7).

$$k = \kappa \frac{k_b}{h} T \exp\left(\frac{-\Delta G^\ddagger}{RT}\right) \quad (7)$$



where:

$\kappa$  is the transmission coefficient and is an estimate of the fraction of molecules that successfully pass over the transition barrier and has been assumed to be 0.5

$h$  is the Planck constant

$k_b$  the Boltzmann constant and

$\Delta G^\ddagger$  is the difference in Gibbs free energy between the transition state and the ground state.

$\Delta G^\ddagger$  is related to the enthalpy and entropy of activation by:  $\Delta G^\ddagger = \Delta H^\ddagger - T\Delta S^\ddagger$ . These parameters can be found by plotting a graph of  $\ln(k/T)$  vs  $1/T$  which has an intercept of  $(\Delta S^\ddagger/R + \ln \kappa k_b/h)$  and gradient of  $-\Delta H^\ddagger/R$ . Such a plot, the Eyring plot, is shown in Figure 15.

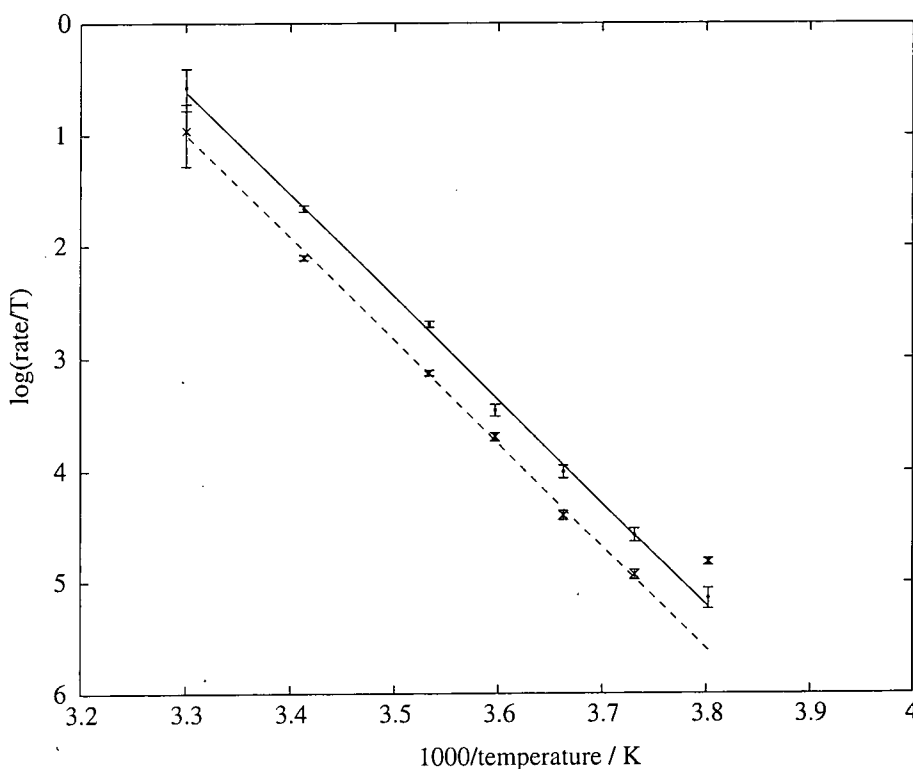


Figure 15: Eyring plot for rates AB and BC for the exchange process in compound 13. The crosses and dotted line represent the AB process and the dots and solid line represent the BC process. The error bars are those calculated from the exchange fitting. Where not indicated, such errors are smaller than the symbol used for the point on the graph.

From the graph shown in Figure 15 it can be calculated that:

$$\begin{aligned} \text{for AB:} \quad \Delta H^\ddagger &= 71 \pm 4 \text{ kJ mol}^{-1} \\ \Delta S^\ddagger &= 33 \pm 15 \text{ J mol}^{-1} \text{ K}^{-1} \\ \text{for BC:} \quad \Delta H^\ddagger &= 72 \pm 5 \text{ kJ mol}^{-1} \\ \Delta S^\ddagger &= 39 \pm 26 \text{ J mol}^{-1} \text{ K}^{-1} \end{aligned}$$

For the BC rate process, all the points plotted on the graph are taken into account, whereas for the AB rate process, the point corresponding to  $-11^\circ\text{C}$  is not used since it is clearly an outlier. The errors quoted are estimated from variations in the fitted line which still give a reasonable fit to the data. Since this method does not take into account systematic errors they are likely to be under estimates. Due to the limitations on the temperature range investigated here, it is more common to compare  $\Delta G^\ddagger$  values to literature data and calculations rather than  $\Delta H^\ddagger$  and  $\Delta S^\ddagger$  individually.<sup>41-44</sup>  $\Delta G^\ddagger$  values around the coalescence temperature are much less sensitive to experimental error. A free energy of  $55.0 \text{ kJ mol}^{-1}$  at a coalescence temperature of  $-3^\circ\text{C}$ , has been quoted in the literature for a triazine ring with three  $\text{NBu}_2$  substituents.<sup>18</sup>  $\Delta G^\ddagger$  values for AB and BC are found to be  $62.1$  and  $61.5 \text{ kJ mol}^{-1}$  respectively at  $-3^\circ\text{C}$ . These values are comparable to the literature values. Modelling calculations give  $\Delta H^\ddagger$  values, so to compare these with experimental data,  $\Delta S^\ddagger$  is often assumed to be zero i.e.  $\Delta G^\ddagger = \Delta H^\ddagger$ . The fitted rotational energy barriers,  $\Delta H^\ddagger$  values, are lower than the modelled barriers (see chapter 5). Crystallographic data show (see Figure 9) that there can be confidence in the trends observed for the energy barriers from the modelling even if the absolute values are not correct.

The errors in  $\Delta S^\ddagger$  are quite large since determination of  $\Delta S^\ddagger$  involves extrapolation over a large temperature range. It is commonly assumed that activation entropies are small for unimolecular processes, so extreme values are suspicious. However, there are cases where  $\Delta S^\ddagger$  is found to be non-zero.<sup>45-47</sup> One example of this is intramolecular reorientation of 2,2-diphenyl-1-(2,4,6-trinitrophenyl)hydrazine in dilute solution.<sup>47</sup> Out of 10 different solvents used,  $\Delta S^\ddagger$  was found to be non-zero for deuterated methanol and nitromethane, due to their ability to form intermolecular hydrogen bonds. This highlights the fact that large values for the entropy, although often unreliable are not

always incorrect. Extreme  $\Delta S^\ddagger$  values however, are usually a sign of having data only over a limited temperature range. In principle SPT or SPI may be used at lower exchange rates, but there would be complications at the slow exchange limit due to the appearance of another rate process, as already discussed.

The fourth peak can be investigated by looking at its coalescence point, approximately -45 °C, and using (2); where  $\Delta\nu_c \approx 15$  Hz, leading to a  $\Delta G^\ddagger \approx 50$  kJ mol<sup>-1</sup>. This can be compared to a  $\Delta G^\ddagger$  value for H3' for AB and BC at -45 °C of 63 kJ mol<sup>-1</sup>. There are large errors associated with measuring the coalescence point of the fourth peak as the frequency separation cannot really be measured with any degree of accuracy due to broadening effects before the slow exchange limit has been reached.

It has been attempted to fit the low temperature spectra to a four-site exchange process. The same natural linewidth and coupling constant were used. The four populations and the rate BD were allowed to vary, as were the chemical shifts I and IV, as their behaviour with temperature was not known, only the average I and IV signal (B) had been monitored previously. The other two chemical shifts were fixed. Rates AB, BC and AC were fixed at zero. The spectra at temperatures of -30 to -50 °C inclusive were fitted. Below these temperatures there is further broadening so a four-site model is not applicable. The fitting routine did not converge at temperatures above these, as there were too many variable parameters. Making any more restraints would mean making assumptions that were not valid; indeed at temperatures higher than -30 °C it is not feasible to fix the rates AB and BC to zero meaning more, rather than less variables. Plotting an Eyring equation with three points (!) yields:

$$\Delta H^\ddagger = 46 \text{ kJ mol}^{-1}$$

$$\Delta S^\ddagger = -16 \text{ J mol}^{-1} \text{ K}^{-1}$$

$$\text{At } -45 \text{ °C } \Delta G^\ddagger = 42 \text{ kJ mol}^{-1}$$

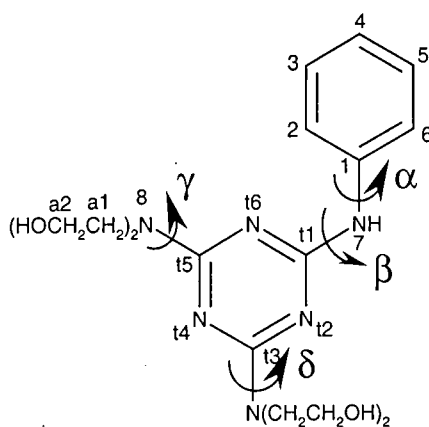
There are large errors associated with these values but the  $\Delta G^\ddagger$  value is significantly less than for the processes AB and BC as expected.

## 4.6 Supporting Evidence

An explanation has been offered in this chapter for the exchange effects observed in many of the spectra studied in this thesis by examining compound **13** in detail. To substantiate this theory a range of simplified molecules were made for study in the latter stages of this research, namely compounds **2**, **3**, **5** and **6**. Proton, carbon-13 and nitrogen-15 spectra were recorded for compounds **2**, **3** and **5**. Solid-state spectra for these compounds can be seen in chapter 6. Compound **6** was not sufficiently soluble in solvents of interest so it was not purified for study. Spectra were recorded in  $d_7$ -DMF, enabling the temperature to be decreased (to  $-40\text{ }^\circ\text{C}$ ) but still allowing the observation of labile protons. Initially a lot of water was present, obscuring the aliphatic proton peaks. Water can exchange with the labile protons in the sample. This water therefore had to be removed as it was desirable to know that any broadening observed was due to internal rotation as opposed to exchange with water. This was achieved by drying each NMR sample (containing solvent, sample and TMS) over a molecular sieve overnight prior to recording the spectrum.

The spectra of the simplified compounds were examined. In each case the spectra expected (if the results discussed in this chapter are correct) are outlined in Table 5-Table 10, for ease of comparison to the spectra actually obtained. In practise there may not be large chemical shift differences between some resonances, meaning some signals cannot be resolved. It is also assumed that there is rapid rotation within the alkyl chains. The aromatic signals are taken as a whole, as are the triazine carbon peaks. Peaks arising due to coupling are not counted in the number of signals expected.

## 4.6.1 Compound 2



2

## Proton Spectra

	Number of peaks expected in $^1\text{H}$ spectra			
	All rapid	$\alpha$ , $\beta$ rapid $\gamma$ , $\delta$ slow	$\alpha$ rapid, $\beta$ , $\gamma$ , $\delta$ slow	All slow
Phenyl	3 <sup>a</sup>	3 <sup>a</sup>	3 <sup>a</sup>	5 <sup>b</sup>
NH	1	1	1	1
a1	1	2 <sup>c</sup>	4 <sup>d</sup>	4 <sup>d</sup>
a2	1	2 <sup>c</sup>	4 <sup>d</sup>	4 <sup>d</sup>
OH	1	2 <sup>c</sup>	4 <sup>d</sup>	4 <sup>d</sup>

<sup>a</sup> 1 signal from H2 and H6, 1 from H3 and H5 and the third from H4.

<sup>b</sup> 1 peak for each aromatic proton.

<sup>c</sup> 1 signal for protons near the NH and 1 for protons away from the NH.

<sup>d</sup> All four chains are different.

Table 5: Number of peaks expected in proton spectra for compound 2 when different rotations are occurring.

The phenyl region remains simple, as 3 peaks, throughout the temperature range studied. This indicates that not all rotations are frozen out at any temperature accessible in  $d_7$ -DMF. a1 and a2 peaks are very similar in chemical shift, causing considerable peak overlap. The number of peaks present for these protons is therefore difficult to deduce. Changes in this region can be observed but they may, at least in part, be due to variation of chemical shift with temperature. The whole spectrum at 19.7 °C is shown in Figure 16.

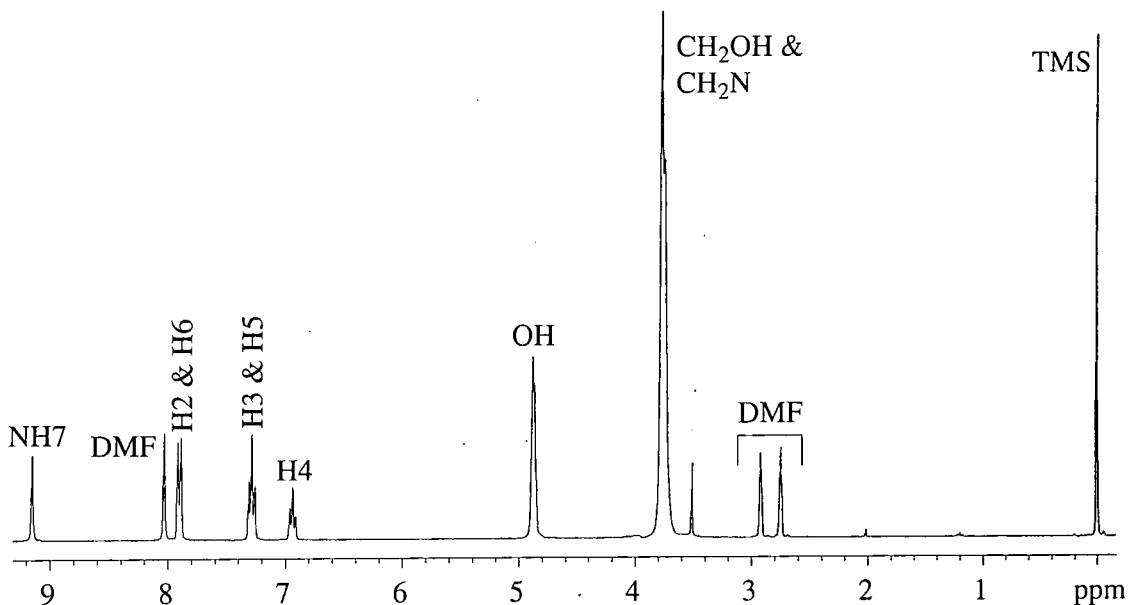


Figure 16: Solution-state  $^1\text{H}$  spectra of compound 2 in  $d_7$ -DMF recorded on a Varian Unity 300 spectrometer at  $19.7^\circ\text{C}$  using a recycle delay of 1 s, pulse width of  $28.4^\circ$  and 100 acquisitions.

The region of the spectra, at different temperatures, showing the OH proton resonances are expanded in Figure 17.

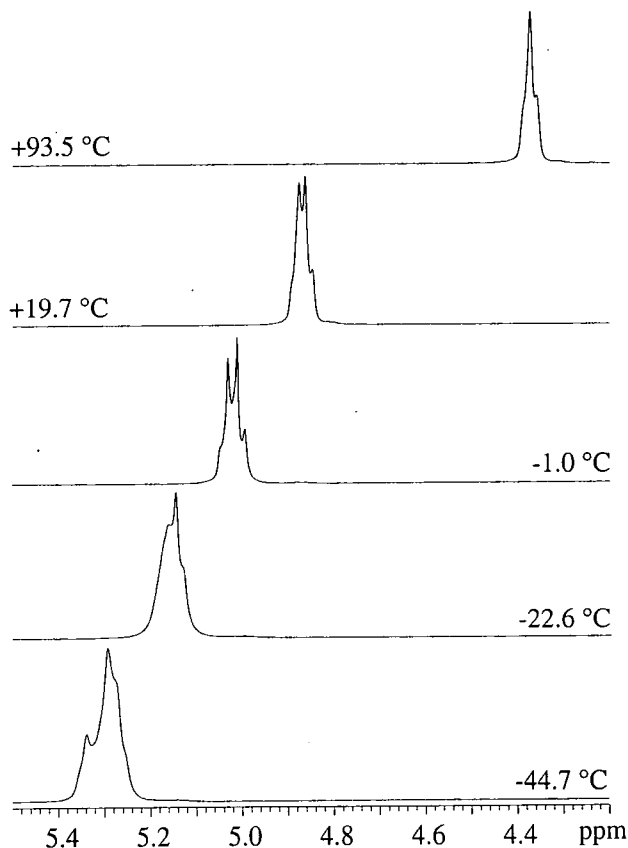


Figure 17: Solution-state  $^1\text{H}$  spectra of the OH protons in compound 2 in  $d_7$ -DMF recorded on a Varian Unity 300 spectrometer using 1 s recycle delay,  $28.4^\circ$  pulse width and 100 acquisitions.

Changes are observed in the OH peak with temperature, shown in Figure 17. There will be complex coupling of the OH protons to the CH<sub>2</sub> protons, increasing the number of OH peaks predicted, so exactly how many are expected in the OH region for each rotational situation is not clear. The OH peak at all temperatures observed appears complex. Decoupling of CH<sub>2</sub> peaks from the OH peak was attempted at room temperature. This can be achieved because a1 and a2 protons give rise to peaks that are close in frequency. A range of decoupling frequencies and powers were used. The OH peak was then deconvoluted to identify how many signals were present. Unfortunately the fit was not conclusive.

### Carbon Spectra

To summarise:

	Number of peaks expected in <sup>13</sup> C spectra			
	All rapid	α, β rapid γ, δ slow	α rapid, β, γ, δ slow	All slow
Phenyl	4 <sup>a</sup>	4 <sup>a</sup>	4 <sup>a</sup>	6 <sup>b</sup>
Triazine	2 <sup>c</sup>	2 <sup>c</sup>	3 <sup>d</sup>	3 <sup>d</sup>
a1	1	2 <sup>e</sup>	4 <sup>f</sup>	4 <sup>f</sup>
a2	1	2 <sup>e</sup>	4 <sup>f</sup>	4 <sup>f</sup>

<sup>a</sup> 1 signal from C1, 1 from C2 and C6, 1 from C3 and C5 and 1 from C4.

<sup>b</sup> 1 for each aromatic carbon.

<sup>c</sup> 1 signal for t1, and 1 for t3 and t5 together.

<sup>d</sup> All triazine carbons are inequivalent.

<sup>e</sup> Carbons near the NH and carbons away from the NH.

<sup>f</sup> All four chains are different.

*Table 6: Number of peaks expected in carbon spectra for compound 2 when different rotations are occurring.*

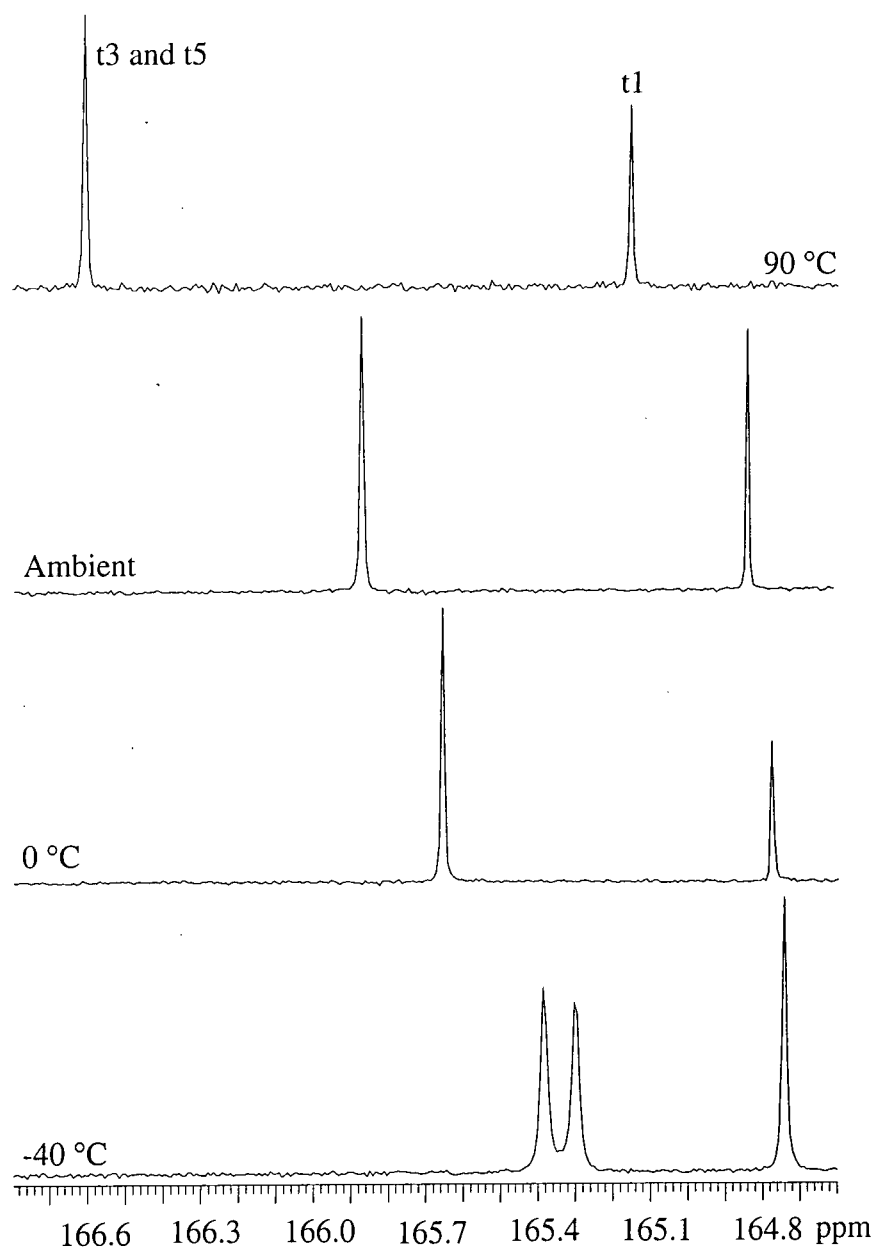
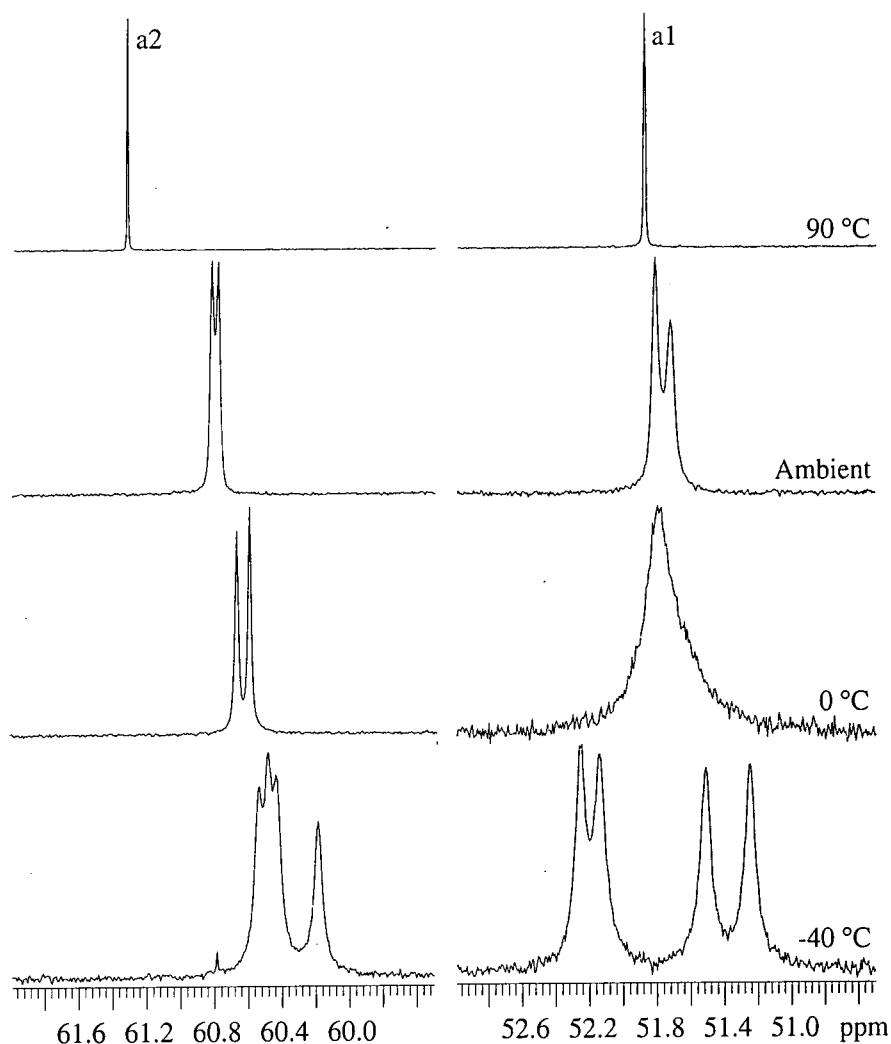


Figure 18: Triazine ring region of a solution-state  $^{13}\text{C}$  spectra in  $d_7$ -DMF of compound 2 recorded on a Bruker AMX 400 spectrometer with recycle delay of 2 s,  $5.5 \mu\text{s}$   $90^\circ$  pulse width and top: 10240 acquisitions; second: 2320 acquisitions; third: 1001 acquisitions and bottom: 4121 acquisitions.

There are 2 triazine peaks at the higher temperatures but at  $-40^\circ\text{C}$  3 peaks are observed, as shown in Figure 18. The higher frequency signal, arising from t3 and t5 together splits into 2, as expected when rotation  $\beta$  slows down. No information can be obtained about any of the other rotations from these peaks as only the  $\beta$  rotation is expected to affect the appearance of this part of the spectrum. There is a change in chemical shift with temperature, particularly for the t3, t5 peak, possibly due to solvent effects.

The number of peaks observed in the phenyl region does not change with temperature, implying that  $\alpha$  is rapid at all accessible temperatures. This agrees with the information gained from the proton spectra.

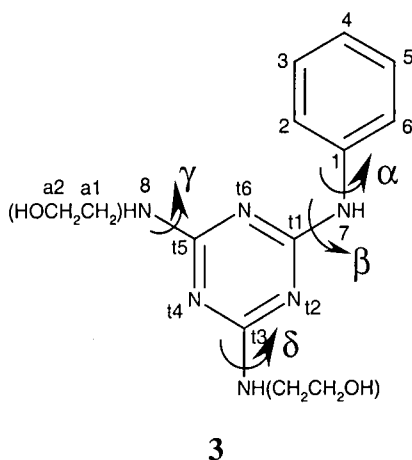


*Figure 19: Aliphatic carbon region of a solution-state  $^{13}\text{C}$  spectra in  $d_7$ -DMF of compound 2 recorded on a Bruker AMX 400 spectrometer with recycle delay of 2 s, a  $5.5\mu\text{ s}$   $90^\circ$  pulse width and top: 10240 acquisitions; second: 2320 acquisitions; third: 1001 acquisitions and bottom: 4121 acquisitions.*

The aliphatic carbon peaks illustrated in Figure 19 show several changes. At  $90^\circ\text{C}$  there is 1 peak for each carbon. At room temperature there are 2 peaks, while at  $0^\circ\text{C}$  the spectrum shows a broad signal for a1, with both peaks from a1 and a2 splitting into 4 at  $-40^\circ\text{C}$ . The chemical shift separation of the 4 a1 peaks at  $-40^\circ\text{C}$  is larger than for a2, meaning the former signal is broad over a larger temperature range. The changes observed with temperature are as expected. 1 peak for both a1 and a2, splitting to form

2 at room temperature, consistent with  $\gamma$  and  $\delta$  rotations slowing down. 4 peaks for each at  $-40\text{ }^{\circ}\text{C}$  is due to the  $\beta$  rotation slowing down as observed for the triazine carbons, and  $\alpha$  rotation remains rapid at all temperatures investigated, in agreement with the proton spectra and the phenyl carbon region.

### 4.6.2 Compound 3



The possible rotamers for this compound are shown in Figure 20, assuming the  $\alpha$  rotation is rapid.

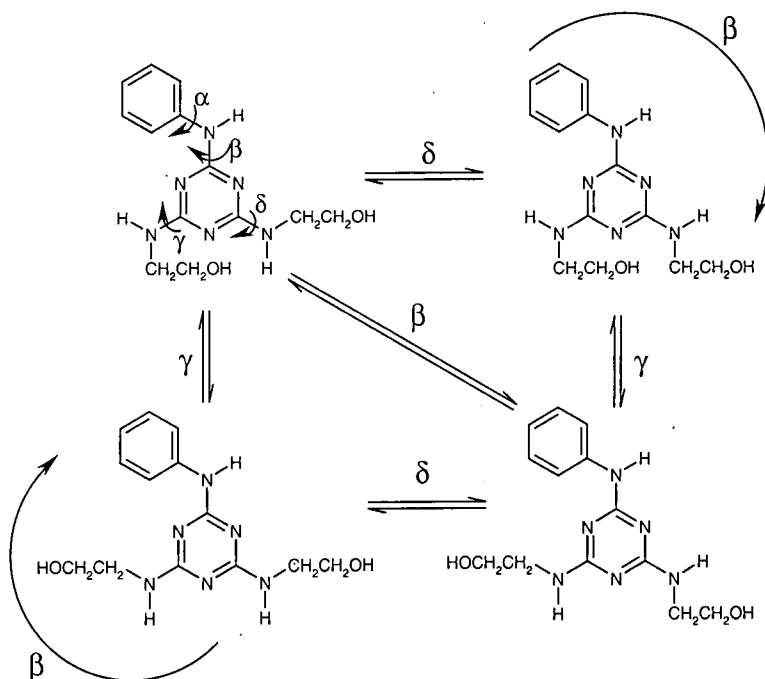


Figure 20: Possible rotamers of compound 3 assuming rapid rotation about  $\alpha$ .

## Proton Spectra

The predictions of the number of  $^1\text{H}$  signals to be seen for compound **3** are set out in Table 7.

	Number of peaks expected in $^1\text{H}$ spectra			
	All rapid	$\alpha$ , $\beta$ rapid $\gamma$ , $\delta$ slow	$\alpha$ rapid, $\beta$ , $\gamma$ , $\delta$ slow	All slow
Phenyl	3 <sup>a</sup>	(3x3) 9 <sup>b</sup>	(4x3) 12 <sup>c</sup>	(4x5) 20 <sup>d</sup>
NH7	1	3 <sup>e</sup>	4 <sup>f</sup>	4 <sup>f</sup>
a1	1	4 <sup>g</sup>	(2x4) 8 <sup>h</sup>	(2x4) 8 <sup>h</sup>
a2	1	4 <sup>g</sup>	(2x4) 8 <sup>h</sup>	(2x4) 8 <sup>h</sup>
NH8	1	4 <sup>g</sup>	(2x4) 8 <sup>h</sup>	(2x4) 8 <sup>h</sup>
OH	1	4 <sup>g</sup>	(2x4) 8 <sup>h</sup>	(2x4) 8 <sup>h</sup>

<sup>a</sup> 1 signal for H2 and H6, 1 for H3 and H5 and 1 for H4.

<sup>b</sup> 3 sets of the 3 signals in <sup>a</sup>, one set for each conformation of the aliphatic side chains but the phenyl sites in two rotamers can be averaged by rotation  $\beta$ .

<sup>c</sup> 4 sets of the 3 signals in <sup>a</sup>, one set for each conformation of the aliphatic side chains as now  $\beta$  is slow.

<sup>d</sup> 4 sets of 5, the 5 signals in each set are composed of one for each aromatic proton.

<sup>e</sup> 1 signal for each conformation of the aliphatic side chain with 2 rotations being made equivalent by rotation  $\beta$ .

<sup>f</sup> 1 signal for each conformation of the aliphatic side chain.

<sup>g</sup> 1 signal for each conformation of the aliphatic side chain.

<sup>h</sup> 2 sets of the 4 signals in <sup>g</sup>, one set when the side chain is close to NH7 and one set when away from NH7.

*Table 7: Number of peaks expected in proton spectra for compound 3 when different rotations are occurring.*

The NH7 region exhibits several changes as shown in Figure 21. 1 peak which is broad at room temperature, splits into 3 peaks at 0 °C and then into 4 at -40 °C. This is as expected, 3 peaks due to the  $\gamma$  and  $\delta$  rotations slowing down and 4 peaks when rotation  $\beta$  is frozen out. Nothing can be said about rotation  $\alpha$  as it has no effect on NH7. There is a chemical shift change with temperature (approximately 0.3 ppm from 90 °C to -40 °C) which is not surprising as NH7 is a labile proton.

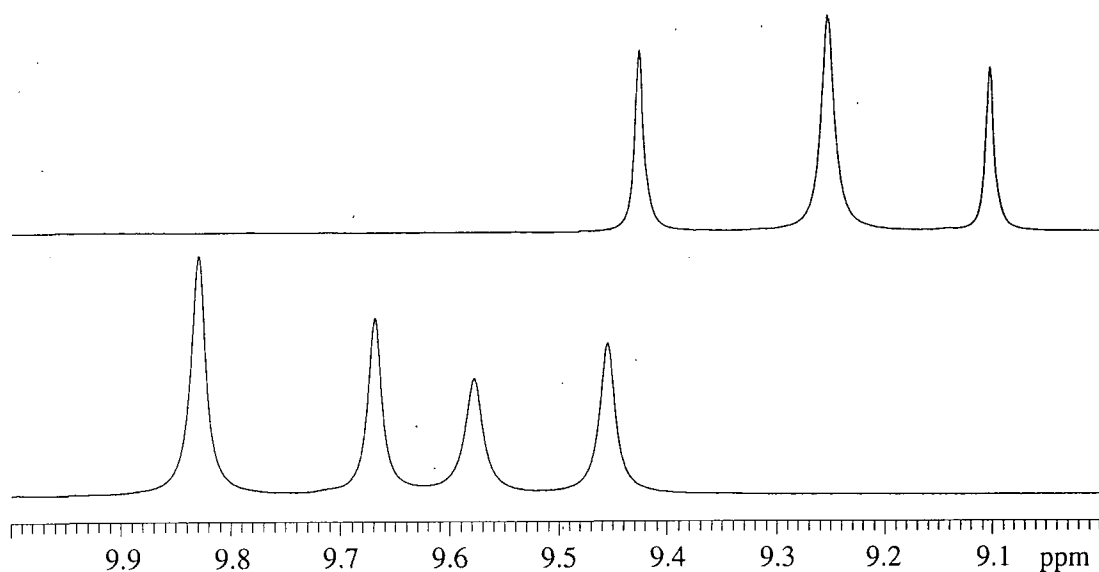


Figure 21: The NH7 region of the solution-state  $^1\text{H}$  spectra in  $d_7$ -DMF of compound **3** recorded on a Bruker AMX 400 spectrometer with a recycle delay of 2 s, pulse angle of  $30^\circ$  and top: 1200 acquisitions and bottom: 3141 acquisitions.

The phenyl proton region for compound **3** is very complex due to coupling. As information about all rotations can be obtained from other spectra, this region was not investigated in detail. The NH8 signal also undergoes broadening and a large chemical shift change with temperature resulting in overlap with the resonance of H4, an aromatic proton. Broadening and then complex splitting of peaks is observed for the resonances of a1, a2 and OH protons but again this was not investigated as it would not contain any extra information.

### Carbon Spectra

The predicted number of  $^{13}\text{C}$  peaks for compound **3** under various assumptions are shown in Table 8.

	Number of peaks expected in $^{13}\text{C}$ spectra			
	All rapid	$\alpha, \beta$ rapid $\gamma, \delta$ slow	$\alpha$ rapid, $\beta, \gamma, \delta$ slow	All slow
Phenyl	4 <sup>a</sup>	(3x4) 12 <sup>b</sup>	(4x4) 16 <sup>c</sup>	(4x6) 24 <sup>d</sup>
Triazine	2 <sup>e</sup>	(3+4) 7 <sup>f</sup>	(4x3) 12 <sup>g</sup>	(4x3) 12 <sup>g</sup>
a1	1	4 <sup>h</sup>	(2x4) 8 <sup>i</sup>	(2x4) 8 <sup>i</sup>
a2	1	4 <sup>h</sup>	(2x4) 8 <sup>i</sup>	(2x4) 8 <sup>i</sup>

<sup>a</sup> 1 from C1, 1 from C2 and C6, 1 from C3 and C5 and 1 from C4.

<sup>b</sup> 3 sets of the 4 signals in <sup>a</sup>, one set for each conformation of the aliphatic side chains but two rotamers can be interchanged by rotation  $\beta$ .

<sup>c</sup> 4 sets of the 4 signals in <sup>a</sup>, one set for each conformation of the aliphatic side chains as now  $\beta$  is slow.

<sup>d</sup> 4 sets of 6, the 4 sets in <sup>c</sup> but now all carbons are inequivalent.

<sup>e</sup> t3 and t5 are equivalent forming 1 peak, t1 forms the other.

<sup>f</sup> Expect the 2 peaks in <sup>c</sup> but now the peak due to t3 and t5 has 4 conformations, for t1, 2 of these conformations appear to be equivalent.

<sup>g</sup> t3 and t5 are now inequivalent; each has 4 conformations.

<sup>h</sup> 1 signal for each conformation of the aliphatic side.

<sup>i</sup> 2 sets of the 4 signals in <sup>h</sup>, one set when the side chain is close to NH7 and one set when away from NH7.

Table 8: Number of peaks expected in carbon spectra for compound 3 when different rotations are occurring.

At 90 °C there are 2 signals for the triazine ring carbons as shown in Figure 22. These are broad at room temperature. The peak for and t1 splits into 3 at 0 °C. The resonances for t3 and t5 also split into 3 but it appears that there is accidental degeneracy, meaning there are likely to be 4 sites, consistent with slowing down of  $\delta$  and  $\gamma$ . The t3 and t5 region divides into at least 7 peaks. However, 8 peaks are expected, due to slowing down of the rotation  $\beta$ . There is probably accidental degeneracy of 2 conformations. Again information about the rotation  $\alpha$  cannot be deduced from these peaks.

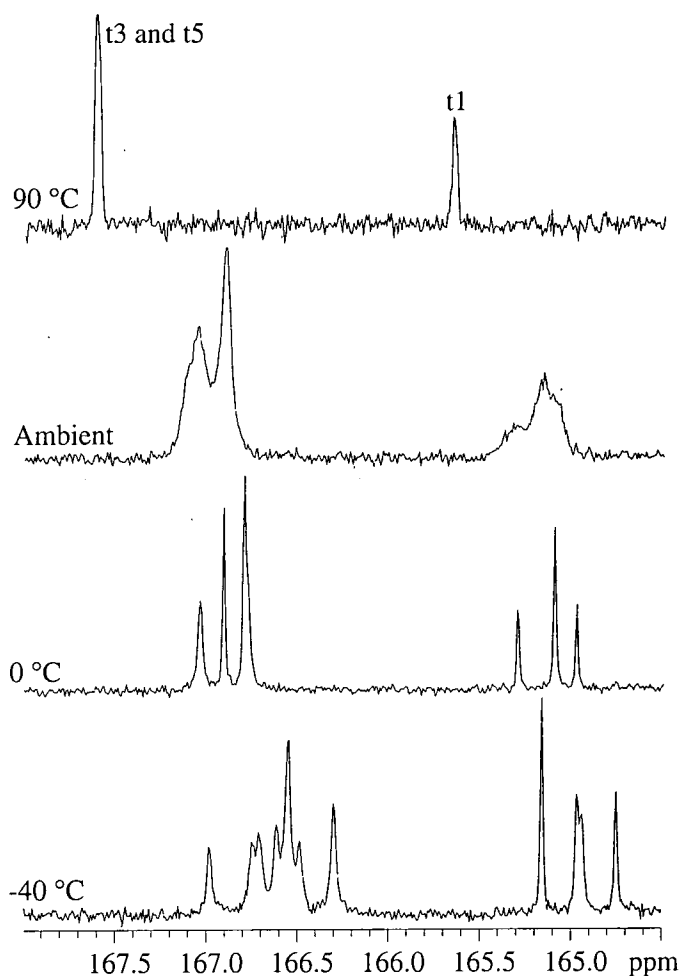


Figure 22: Triazine ring region of solution-state  $^{13}\text{C}$  spectra in  $d_7$ -DMF of compound 3 recorded on a Bruker AMX 400 spectrometer with recycle delay of 2 s, 5.5  $\mu$  s 90° pulse width and top: 5723; second: 10240 acquisitions, third: 1200 acquisitions and bottom: 3141 acquisitions.

All the phenyl signals behave as expected. Those for C4, C2 and C6 are shown in Figure 23. All show 1 peak at 90 °C, broadening at room temperature, splitting into 3 peaks at 0 °C as  $\delta$  and  $\gamma$  rotations slow down. Then freezing out of motion about  $\beta$  at -40 °C leads to 4 peaks.

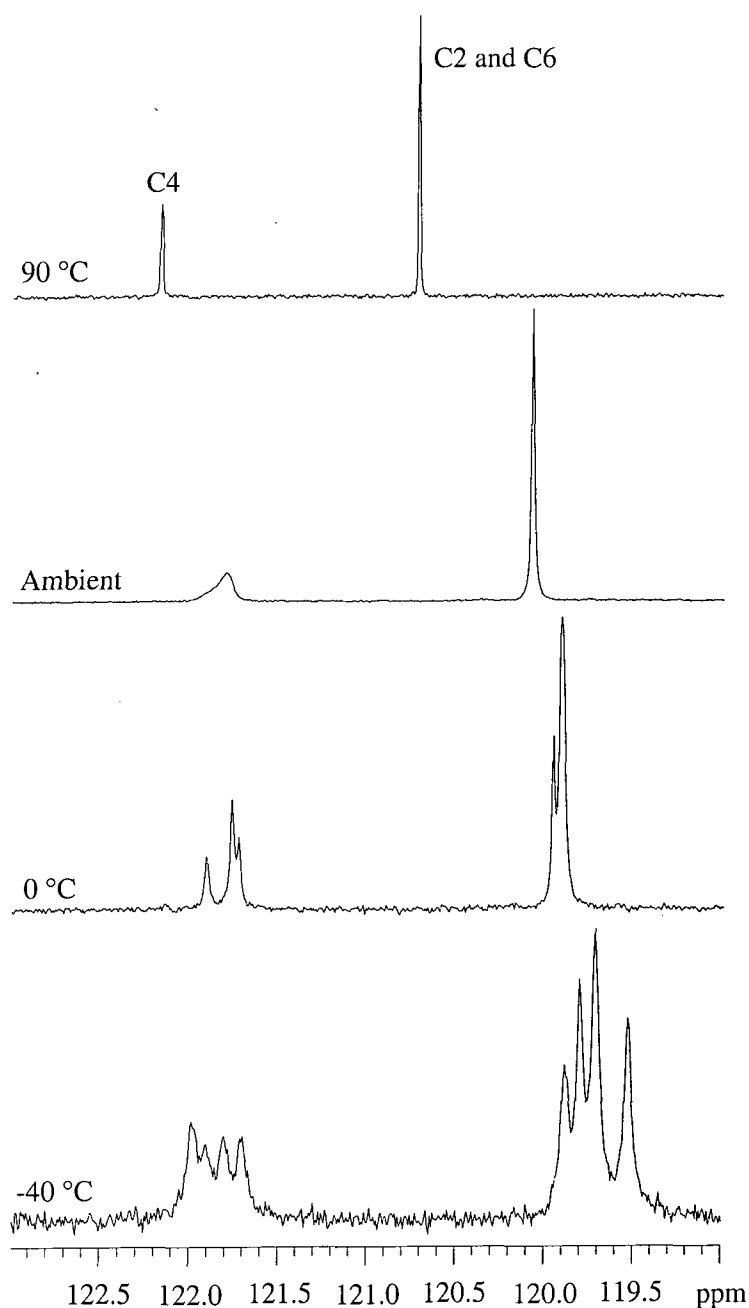


Figure 23: Part of the phenyl carbon region of solution-state  $^{13}\text{C}$  spectra in  $d_7$ -DMF of compound **3** recorded on a Bruker AMX 400 spectrometer with recycle delay of 2 s, 5.5  $\mu\text{s}$   $90^\circ$  pulse width and top: 5723; second: 10240 acquisitions, third: 1200 acquisitions and bottom: 3141 acquisitions.

The a1 and a2s signals also behave as expected as shown in Figure 24. The single peaks for a1 and a2 at  $90^\circ\text{C}$  both become 2 peaks at room temperature as  $\delta$  and  $\gamma$  rotations begin to slow down. This is actually an intermediate stage occurring as 1 peak is splitting into 4. The expected 4 peaks can be seen at  $0^\circ\text{C}$  when rotations about  $\delta$  and  $\gamma$  have been frozen out (the a1 region appears as 3 peaks but it can be seen that the a2 signal has split into 4 so it is likely that a1 has done the same, again with overlap of 2

signals). Splitting into 8 occurs for the peak due to a1 at  $-40\text{ }^{\circ}\text{C}$  as rotation  $\beta$  is frozen out. The a2 signal will also be 8 lines but as the chemical shift difference is much smaller there is more peak overlap.

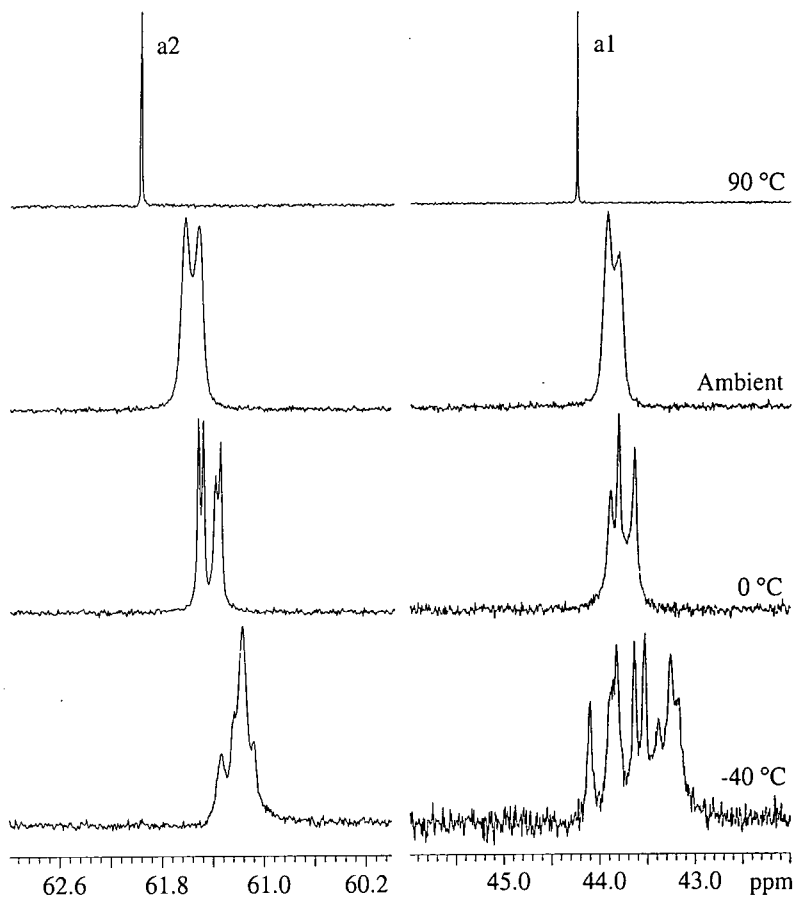
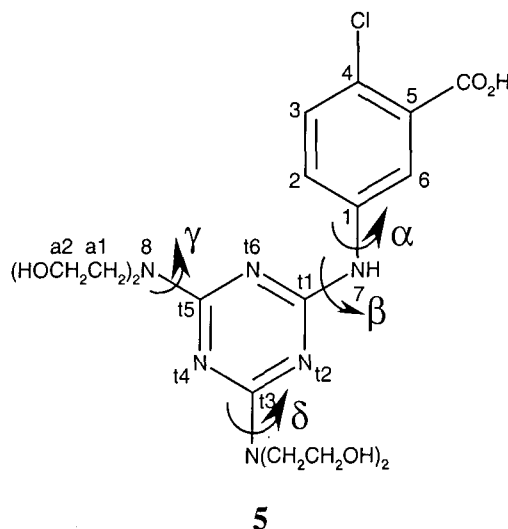


Figure 24: The aliphatic carbon region of solution-state  $^{13}\text{C}$  spectra in  $d_7$ -DMF of compound **3** recorded on a Bruker AMX 400 spectrometer with recycle delay of 2 s and a  $5.5\mu\text{ s}$   $90^\circ$  pulse width and top: 5723; second: 10240 acquisitions, third: 1200 acquisitions and bottom: 3141 acquisitions.

## 4.6.3 Compound 5



## Proton Spectra

Predictions for the proton spectrum of **5** are given in Table 9.

	Number of peaks expected in $^1\text{H}$ spectra			
	All rapid	$\alpha$ , $\beta$ rapid $\gamma$ , $\delta$ slow	$\alpha$ rapid, $\beta$ , $\gamma$ , $\delta$ slow	All slow
Aryl	3 <sup>a</sup>	3 <sup>a</sup>	3 <sup>a</sup>	(2x3) 6 <sup>b</sup>
NH	1	1	1	2 <sup>c</sup>
a1	1	2 <sup>d</sup>	4 <sup>e</sup>	(2x4) 8 <sup>f</sup>
a2	1	2 <sup>d</sup>	4 <sup>e</sup>	(2x4) 8 <sup>f</sup>
OH	1	2 <sup>d</sup>	4 <sup>e</sup>	(2x4) 8 <sup>f</sup>

<sup>a</sup> 1 for each aromatic proton.

<sup>b</sup> 2 for each aromatic proton, one pointing towards the aliphatic chains and one away.

<sup>c</sup> 1 for each orientation of the aromatic group.

<sup>d</sup> Protons near the NH and protons away from the NH.

<sup>e</sup> All four chains are different.

<sup>f</sup> 2 sets of the 4 peaks in <sup>e</sup>, 1 set of each orientation of the aromatic group.

*Table 9: Number of peaks expected in proton spectra for compound 5 when different rotations are occurring.*

No changes are observed in the aryl region or for the NH proton suggesting that rotation  $\alpha$  always remains rapid. As with compound 2, a1 and a2 proton peaks overlap making derivation of the number of rotamers present very difficult. The OH peak broadens,

without showing any structure, as the temperature is increased until it is not visible at 90 °C. This may be due to exchange with the CO<sub>2</sub>H proton as this signal is not visible at any temperature studied. No information can be obtained from these spectra about rotations  $\beta$ ,  $\gamma$  or  $\delta$ .

### Carbon Spectra

Table 10 lists the number of <sup>13</sup>C peaks expected for compound 5.

	Number of peaks expected in <sup>13</sup> C spectra			
	All rapid	$\alpha$ , $\beta$ rapid $\gamma$ , $\delta$ slow	$\alpha$ rapid, $\beta$ , $\gamma$ , $\delta$ slow	All slow
Aryl	6 <sup>a</sup>	6 <sup>a</sup>	6 <sup>a</sup>	(2x6) 12 <sup>b</sup>
Triazine	2 <sup>c</sup>	2 <sup>c</sup>	3 <sup>d</sup>	(2x3) 6 <sup>e</sup>
a1	1	2 <sup>f</sup>	4 <sup>g</sup>	(2x4) 8 <sup>h</sup>
a2	1	2 <sup>f</sup>	4 <sup>g</sup>	(2x4) 8 <sup>h</sup>

<sup>a</sup> 1 for each aromatic carbon.

<sup>b</sup> 2 sets of the 6 signals in <sup>a</sup>, 1 set for each orientation of the aromatic ring.

<sup>c</sup> 1 for t1 and 1 for t3 and t5 together.

<sup>d</sup> All 3 triazine carbons are now inequivalent.

<sup>e</sup> There are 2 signals for each triazine for the two conformations of the aryl ring.

<sup>f</sup> 1 signal for carbons pointing towards NH and 1 signal for those pointing away.

<sup>g</sup> All 4 aliphatic side chains are different.

<sup>h</sup> 2 sets of the 4 signals in <sup>g</sup>, 1 set for each orientation of the aromatic group.

*Table 10: Number of peaks expected in carbon spectra for compound 5 when different rotations are occurring.*

Variable temperature carbon work was not carried out with this sample as it was found to decompose at high temperature. In the room temperature spectrum it can be seen that there are 2 peaks for a2, and the signal for a1 is broad. This is consistent with  $\delta$  and  $\gamma$  rotations being slow.

## 4.7 Conclusions

The effects of internal rotation have been observed for several triazine derivatives. The rotational energy barriers for the different possible rotations have been calculated using molecular modelling to help deductions regarding the motions occurring from the experimental spectra. Energy barriers have been measured using variable-temperature proton NMR for a dye molecule. A set of simplified molecules have been studied to support the rationalisations made. The observations from the proton and  $^{13}\text{C}$  NMR spectra of these molecules were found to fully agree with the predictions about the relative energies of the rotational barrier heights and that the exchange processes observed did not involve the triazine ring. This shows that the conclusions drawn from molecular modelling and the initial NMR study of the dye were correct.

## 4.8 References

- <sup>1</sup> C. L. Penn and T. J. Dwyer, *Chem Rev.*, **90**, 933 (1990).
- <sup>2</sup> A. N. Lane, *Prog. NMR Spec.*, **25**, 481 (1993).
- <sup>3</sup> S. Forsen and R. A. Hoffman, *J. Chem. Phys.*, **39**, 2892 (1963).
- <sup>4</sup> S. Forsen and R. A. Hoffman, *J. Chem. Phys.*, **40**, 1189 (1964).
- <sup>5</sup> J. Jeener, B. H. Meier, P. Bachmann and R. R. Ernst, *J. Chem. Phys.*, **71**, 4546 (1979).
- <sup>6</sup> A. Kumar, G. Wagner, R. R. Ernst, *J. Am. Chem. Soc.*, **103**, 3654 (1981).
- <sup>7</sup> L. W. Reeves and K. N. Shaw, *Can. J. Chem.*, **48**, 3641 (1970).
- <sup>8</sup> C. N. Banwell and H. Primas, *Mol. Phys.*, **6**, 225 (1963).
- <sup>9</sup> G. Binsch, *J. Am. Chem. Soc.*, **91**, 1304 (1969).
- <sup>10</sup> D. A. Kleider and G. Binsch, *J. Magn. Reson.*, **3**, 246 (1970).
- <sup>11</sup> M. Cuperlovic, G. H. Meresi, W. E. Palke and J. T. Gerig, *J. Magn. Reson.*, **142**, 11 (2000).
- <sup>12</sup> L. H. Piette and W. A. Anderson, *J. Chem. Phys.*, **59**, 899 (1959).
- <sup>13</sup> A. D. Bain and G. J. Duns, *J. Magn. Reson. A.*, **109**, 56 (1994).
- <sup>14</sup> R. L. Vold, J. S. Waugh, M. P. Klein and D. E. Phelps, *J. Chem. Phys.*, **48**, 3831 (1968).
- <sup>15</sup> R. Freeman, H. D. W. Hill, *J. Chem. Phys.*, **51**, 3140 (1969).
- <sup>16</sup> H. Y. Carr and E. M. Purcell, *Phys. Rev.*, **94**, 630 (1954).
- <sup>17</sup> A. R. Katritzky, D. C. Ghiviriga and R. A. Barcock, *J. Chem. Soc., Perkin Trans 2*, 785 (1995).
- <sup>18</sup> A. R. Katritzky, I. Ghiviriga, P. J. Steel and D. C. Oniciu, *J. Chem. Soc., Perkin Trans 2*, 443 (1995).
- <sup>19</sup> A. L. Van Geet, *Anal. Chem.* **40**, 2227 (1968).
- <sup>20</sup> A. L. Van Geet, *Anal. Chem.*, **42**, 679 (1970).
- <sup>21</sup> R. K. Harris, *Nuclear Magnetic Resonance Spectroscopy*, Longman Scientific and Technical, Essex, 1986
- <sup>22</sup> H. S. Gutowsky, *Dynamic Nuclear Magnetic Resonance Spectroscopy*, Ed. L. M. Jackman and F. A. Cotton, Academic Press, New York and London, 1975.
- <sup>23</sup> H. S. Gutowsky and C. H. Holm, *J. Chem. Phys.*, **25**, 1228 (1956).
- <sup>24</sup> The Mathworks, Natick, MA, USA
- <sup>25</sup> P. Hodgkinson, unpublished work.

- <sup>26</sup> M. J. Duer and M. H. Levitt, *Solid State Nucl. Magn. Reson.*, **1**, 211 (1992).
- <sup>27</sup> A. D. Bain, D. A. Fletcher and P. Hazendonk, *Concepts Magn. Reson.*, **10**, 85 (1998).
- <sup>28</sup> H. M. McConnell, *J. Chem. Phys.* **28**, 430 (1958).
- <sup>29</sup> A. D. Bain and G. J. Duns, *J. Magn. Reson. A*, **112**, 258 (1995).
- <sup>30</sup> W. H. Press, B. P. Flannery, S. A. Teukolsky and W. T. Vetterling, *Numerical Recipes*, Cambridge University Press, Cambridge, 1986.
- <sup>31</sup> A. D. Bain and J. A. Cramer, *J. Magn. Reson. A*, **118**, 21 (1996).
- <sup>32</sup> R. R. Shoup, E. D. Becker and M. L. McNeal, *J. Phys. Chem.*, **76**, 71 (1972).
- <sup>33</sup> T. Liljefors, *Org. Magn. Reson.*, **6**, 144 (1974).
- <sup>34</sup> D. Hofner, S. A. Lesko and G. Binsch, *Org. Mag. Reson.*, **11**, 179 (1978).
- <sup>35</sup> D. Hofner, I. Tamir and G. Binsch, *Org. Magn. Reson.*, **11**, 172 (1978).
- <sup>36</sup> U. Berg, J. Sandstrom, W. B. Jennings and D. Randall, *J. Chem. Soc. Perkin II*, **1980**, 949 (1980).
- <sup>37</sup> U. Berg, J. Sandstrom, W. B. Jennings and D. Randall, *Tetrahedron Lett.*, **1976**, 3197 (1976).
- <sup>38</sup> E. B. Smith, *Basic Chemical Thermodynamic*, Oxford Science Publications, Oxford, 4<sup>th</sup> Edition.
- <sup>39</sup> Eyring H. *Chem. Revs.* 1935; **17**: 65.
- <sup>40</sup> Glasstone S, Laider KJ, Eyring H. *The Theory of Rate Processes*. McGraw-Hill: New York, 1941.
- <sup>41</sup> W. E. Stewart and T. H. Siddall, *Chem. Rev.*, **70**, 517 (1970).
- <sup>42</sup> M. M. Turnbull, D. J. Nelson, W. Lekouses, M. L. Sarnov, K. A. Taranni and T. Huang, *Tetrahedron.*, **46**, 6613 (1990).
- <sup>43</sup> C. Saurez, C. B. LeMaster, C. L. LeMaster, M. Tafazzoli and N. S. True, *J. Phys. Chem.*, **94**, 6679 (1990).
- <sup>44</sup> K. A. Haushalter, J. Lau and J. D. Roberts, *J. Am. Chem. Soc.*, **118**, 8891 (1996).
- <sup>45</sup> U. Berg and U. Sjostrand, *Org. Magn. Reson*, **11**, 555 (1978).
- <sup>46</sup> T. Belsky, H. Dodiuk and Y. Shvo, *J. Org. Chem*, **42**, 2734 (1977).
- <sup>47</sup> R. L. Randy, J. A. Weil and *J. Am. Chem. Soc.*, **94**, 3951 (1990).

# Chapter 5

## Molecular Modelling of Rotational Energy Barriers

### 5.1 Introduction

This chapter will discuss the molecular modelling that was used in chapter 4 to help identify the rotations occurring in compound **13**. Geometrical information about the rotamers and their expected populations is given in section 5.2, followed by a detailed study of the rotational energy barriers that were of interest in chapter 4. This is explained in section 5.3. First, however, a brief outline of some of the modelling techniques used in this chapter will be given. Some detailed accounts are listed in references 1-7.

There are many ways to model molecules. All are approximations but some are more approximate than others. The method of choice depends on the system size, the types of atom involved, the information required, the time available and the cost. Most calculations are performed 'in the gas phase', meaning no intermolecular forces or solvent effects are considered. Relativistic effects, important for heavier atoms, are also not included. There are two main approaches to these calculations, based on molecular mechanics and quantum mechanics.

### 5.1.1 Molecular Mechanics

This method considers molecules as a collection of atoms held together by elastic or harmonic forces like a ‘ball and spring’. These forces can be described by potential energy functions. The potential functions together comprise the ‘force field’ of the molecule, shown in (1).

$$E_{FF} = E_{str} + E_{bend} + E_{tors} + E_{el} + E_{cross} + \dots \quad (1)$$

Where:

$E_{FF}$  is the total energy of the force field.

The following terms are summed over the whole molecule:

$E_{str}$  is the energy to stretch or compress a bond from its equilibrium value.

$E_{bend}$  is the energy required to distort a 3-centre bond angle from its initial value.

The potential used in most molecular mechanics methods for the above two terms is based on Hooke’s Law.  $E_s = \frac{k^s}{2}(l_{ik} - l_{ik}^0)^2$  for bond stretching and  $E_b = \frac{k^b}{2}(\theta_{ijk} - \theta_{ijk}^0)^2$

for bond bending where:

- $E_s$  and  $E_b$  are the energies of a bond stretch and bend respectively,
- $k^s$  and  $k^b$  are the respective force constants for stretching and bending,
- $l_{ik}$  and  $\theta_{ijk}$  are the respective actual bond lengths and angles, and
- $l_{ik}^0$  and  $\theta_{ijk}^0$  are the natural bond lengths and angles.

$E_{tors}$  is the energy of a torsional angle being distorted from its natural value.

$E_{el}$  is different from the above terms as it is not based upon a reference value but instead represents interactions between non-bonded atoms.

$E_{cross}$  this describes the coupling between the first three terms.

There is no limit to the number of terms that can be included. The more terms that are included, the more accurate the potential. Molecular mechanics methods are quick, inexpensive and can be used for large molecules such as proteins. There are limitations to their application:

- a) they can only be used to look at electronic ground states.

b) since the results are limited by the potential energy functions and parameters used, a specific force field can give good results only for a limited class of compounds.

### 5.1.2 Quantum Mechanics

Here a quantum mechanical theory is employed rather than classical mechanics. Quantum mechanics states that the energy of a molecule can be found by solving the Schrodinger equation, (2).

$$\hat{H}\Psi = E\Psi \quad (2)$$

This can only be solved exactly for one-electron systems, so that approximations must be made to allow it to be used for other systems. There are two main classes of calculation, *ab initio* and semi-empirical. These will both be briefly described.

#### **ab initio methods**

*Ab initio* calculations attempt to approximate the Schrodinger equation from first principles i.e. without reference to experimental parameters. Instead it uses theoretically calculated wavefunctions to find the energy of the system. The way this is done classifies the method. The Variation Principle states that the energy calculated using an approximate wavefunction will never be lower than the true energy. This means the wavefunction giving the lowest energy will be the most accurate. The most commonly used quantum mechanical method used is Hartree-Fock (HF) which usually uses a self-consistent field approach (SCF). The most accurate energy this method can calculate is called the Hartree-Fock limit. This energy is not the true energy (see (3)), however, as two effects, electron correlation and relativistic effects, are not adequately considered.

$$E_{true} = E_{HF} + E_{correlation} + E_{relativistic} \quad (3)$$

Electron motion is correlated. This means the motion of one electron affects every other electron. The HF approach considers one electron interactions with an electron cloud which is only an approximation. Relativistic effects are important for large atoms where especially the core electrons move at velocities approaching the speed of light.

As the Hartree-Fock is the most commonly used method, the idea behind the approach will be described briefly.

As with all quantum mechanical treatments, the aim is to solve the Schrodinger equation, (2). The Hamiltonian can be written as in (4).

$$\hat{H} = -\sum_{i=1}^n \frac{\hbar^2}{8\pi^2 m_e} \nabla_i^2 - \sum_{i=1}^n \sum_{\alpha=1}^N \frac{Z_{\alpha} e^2}{4\pi \epsilon_0 r_{i\alpha}} + \sum_{i<j}^n \frac{e^2}{4\pi \epsilon_0 r_{ij}} \quad (4)$$

where:

$r_{i\alpha}$  are the electron-nuclear distances

$r_{ij}$  is the inter-electron separation

$Z_{\alpha}$  is the number of protons for nucleus  $\alpha$ .

The first term represents kinetic energy, the second the electron-nuclear attraction and the third electron-electron repulsion.

If the third term is ignored, (4) is equivalent to a set of one-electron Schrodinger equations, (5):

$$\hat{h}_i \Psi_i = E_i \Psi_i \quad (5)$$

where  $\psi_i$  are spin orbitals (one electron orbitals that contain a spatial and a spin description) that can be expanded as a linear combination of single-electron orbitals, (6):

$$\Psi_i = \sum_{v=1}^K c_{vi} \Phi_v \quad (6)$$

where  $\Phi_v$  are one-electron orbitals called basis functions and the collection is called a basis set. A solution to (5) can be found by solving the corresponding secular equations.

For more accurate results, the electron-electron repulsion term must be considered. The one-electron operator,  $\hat{h}_i$ , in (5) can be replaced by the Fock operator shown in (7),

$$\hat{F}_i = \hat{h}_i + \sum_j [2\hat{J}_j - \hat{K}_j] \quad (7)$$

where:

$\hat{J}_i$  is the Coulomb operator and

$\hat{K}_i$  is the exchange operator.

to give (8):

$$\hat{F}_i \Psi_i = E_i \Psi_i \quad (8)$$

The secular equations now involve matrix elements.  $[2\hat{J}_i - \hat{K}_i]$  involve molecular orbitals. These can be approximated to a linear combination of atomic orbitals (LCAO), where the coefficients are not known. To overcome this problem a self-consistent approach can be used. This is where an initial estimate of the coefficients in (6) are found. These values of the coefficients are then used in (8) and the secular equations are solved to produce a new set of spin orbitals with new coefficients. The process is iterative and is repeated until it converges on a self-consistent solution. The more basis functions that are included the more accurate the solution.

The atomic orbitals used in (8) have been described by Slater<sup>8</sup> and are found by fitting exponential functions to the atomic wavefunction. If one such function is used for each filled atomic orbital then the set of atomic orbitals is called a minimal basis. If that number is doubled it is called a double zeta basis. Using atomic wavefunctions in energy calculations requires integration of these functions which is difficult for exponentials. To overcome this problem, Gaussian functions are used to approximate

the Slater-type orbitals. Linear combinations of Gaussians are used for each orbital. The time required to perform a calculation increases approximately as  $N^4$ , where  $N$  is the number of basis functions. Examples of some basis sets are:

STO-3G      This is a minimal basis set, approximated by three Gaussians.

HF/3-21G    This uses linear combinations of two types of function (differing in size but not shape) for each atomic orbital and is called a split-valence basis set.

Polarised basis sets add an extra layer of orbitals to the ground state e.g. 6-31G(d) (the same as 6-31G\*) adds 'd' functions to heavy atoms. 6-31G(p,d) (the same as 6-31G\*\*) adds 'p' functions to hydrogens and d functions to heavy atoms.

Diffuse functions can be added when there is electron density far away from the nucleus e.g. for lone pairs e.g. 6-31+G(d) is the 6-31G(d) basis set with diffuse functions added to heavier atoms.

### **semi-empirical**

Semi-empirical methods reduce the computational cost of *ab initio* methods. They do this by using parameters from experimental data for the core electrons, and *ab initio* calculations for only valence electrons. These *ab initio* calculations tend to use minimal basis sets. The accuracy of these methods is limited by how they have been parameterised. They can take account of some relativistic and electron correlation effects by incorporation in the core potential. The first commonly used method of this type was CNDO.<sup>9</sup> This has been followed by many others: Examples are AM1<sup>10</sup> and PM3.<sup>11</sup>

### 5.1.3 Density Functional Methods (DFT)

The main idea behind density functional theory is the proof by Hohenberg and Kohn<sup>12</sup> that the ground-state electronic energy is determined completely by the electron density. In other words the energy of a system is directly correlated with the electron density. This has the advantage that while the complexity of a wavefunction increases with the size of the system the electron density has the same number of variables so is independent of system size and therefore less computationally demanding. This method also has the advantage that it allows for electron correlation. The aim of DFT methods is therefore to design functionals to relate the electron density to the system energy.

DFT is fairly new in computational chemistry, so there is still a lot of research into the calibration of methods and there is no clear standard. Two of the methods available are LDA (Local Density Approximation) and GGA (Gradient Corrected or Generalised Gradient Approximation), in both of which the electron density is treated as an electron gas.

### 5.1.4 Geometry Optimisation

The methods described so far attempt to find the minimum energy of a system with a particular atomic configuration. In many cases geometrical information is required, in other words the lowest energy conformation must be identified. Geometry optimisation is achieved by varying the atom positions, performing an energy calculation at each step, until the minimum is found, i.e. searching the energy surface. The more atoms present in the system the more complex the surface. There are three commonly used search methods for finding optimum geometries:

- 1) Steepest descent method: The path taken follows the steepest gradient towards the minimum.
- 2) Conjugate gradient: This performs a search along a line constructed so it is conjugate to the previous search direction.
- 3) Newton-Raphson: This expands the true function around the current point and uses second derivatives to traverse the energy surface.

The energy surface, unless very simple, consists of many local minima, saddle points and energy barriers of different shapes and sizes. There is only one global minimum but identifying it may prove difficult as the search algorithm may become 'lost' in a local minimum. This must be considered when carrying out geometrical optimisations.

### ***5.1.5 Locating Transition States***

There are two types of transition state: those involving changes in conformation, and those leading to bond breaking. Transition states are saddle points on the energy surface, meaning they are a maximum in at least one co-ordinate and a minimum in all others. They are denoted of order one if the point is a minimum in one co-ordinate only. Locating transition states is non-trivial. No general methods are guaranteed to work. There are two main strategies: those based on interpolation between two minima and those using only local information.

In this chapter, the STQN (Synchronous Transit-guided Quasi-Newton method) was used to locate saddle points, specifically the QST3 method. This requires an initial structure, a final structure (both usually taken to be fairly close to the expected transition state) and a guess at the transition state. The program then automatically looks for a first-order saddle point.

## 5.2 Conformational Studies

To attempt calculations on compound **13** in its entirety would be very time consuming, so it was therefore simplified for study. Initially the geometry and populations of the four rotamers identified by NMR in chapter 4 were explored. The models used for this are shown in Figure 1.

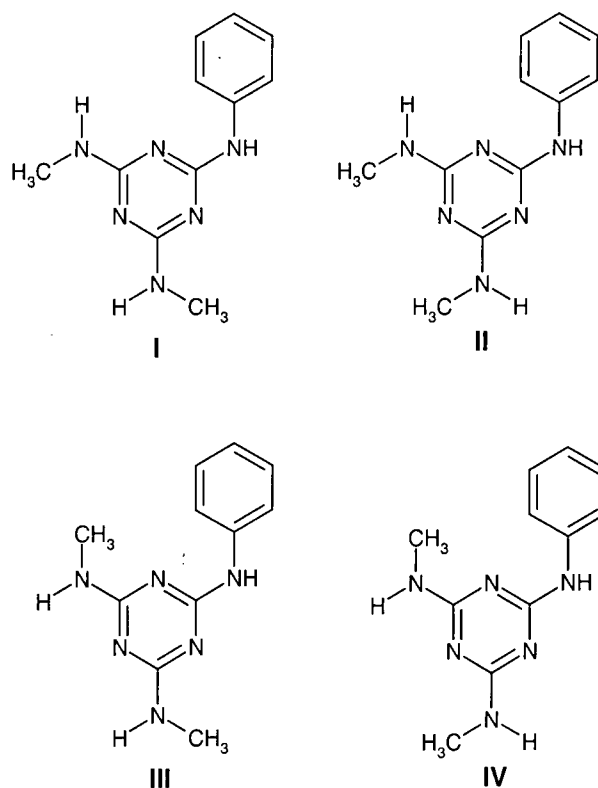


Figure 1: Rotamers of a general molecule representing the triazine region of compound **13**.

The reliability of the energies and geometry optimisations carried out in this chapter can be assessed by comparing the bond lengths and angles with known fragments of the molecule found in the literature.

Although triazine molecules form a flat benzene-like aromatic structure, they have very different properties and are not regular hexagons. The angles are  $\text{N-C-N} > 120^\circ$  and  $\text{C-N-C} < 120^\circ$ . There is strong repulsion between the  $\sigma$ -electrons of each N-C bond and the lone pair on the ring nitrogen atoms, decreasing the C-N-C bond angles.<sup>13</sup> The

increase in the N-C-N angles is due to the attraction of the  $\sigma$  electrons in the C-substituent bond towards the substituent, so reducing the repulsion between these electrons and the ring C-N bonds. The C-N-C bond angles are therefore sensitive to the electronic effects of the substituent. The calculated values in the geometry optimisation are compared to crystallographic data<sup>14,15</sup> in Table 1 (I wish to acknowledge the use of the EPSRC's Chemical Database Service at Daresbury). Various bond lengths are also compared. The fragment used in the crystallographic search is shown in Figure 2.

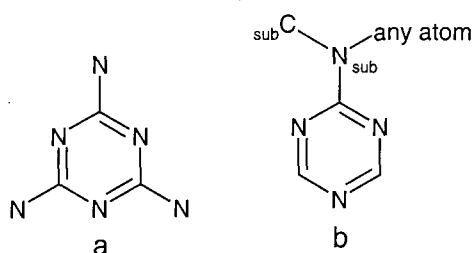


Figure 2: Fragments used to search the crystallographic database.

Fragment 'b' was used to measure the  $N_{\text{sub}}-C_{\text{sub}}$  bond length and fragment 'a' was used for all other measurements. Structures were discounted that contained charged species or other rings that were in a position likely to distort the geometry of the region of interest.

	6-31G	6-31G**	Crystallographic
N-C-N ring / °	124.08-124.41	125.63-125.95	123.45-128.00
C-N-C ring / °	115.60-116.05	114.04-114.45	111.723-115.79
C-N ring / Å	1.331-1.348	1.315-1.339	1.283-1.383
Cring-Nsub / Å	1.337-1.352	1.338-1.356	1.311-1.441
N-C sub / Å	1.406-1.450	1.402-1.444	1.391-1.488

Table 1: Bonds lengths and angles for comparison between calculated optimisations and crystallographic data.

The internal angles of the triazine ring, calculated with both the 6-31G and the 6-31G\*\* basis sets lie within the range of crystallographic data although the 6-31G\*\* produces more separation between the N-C-N angles and the C-N-C angles.

The bond lengths also lie in the range expected by comparison to crystal data. The Tr-NPh bond is longer than the Tr-NMe in the calculated structures, but the N-Ph is shorter than the N-Me lengths. It is expected that the N-Tr bond in all cases would have partial double-bond character. The N-Ph would also be expected to have some partial double-bond character which would result in reduction of the double-bond character of the N-Tr bond in the presence of the Ph ring. The bond lengths can be compared to typical C-N bond lengths with known bonding:<sup>16,17</sup>

Triply covalent nitrogen	$1.472 \pm 5 \text{ \AA}$
N-aromatic	$1.426 \pm 12 \text{ \AA}$
Partial double bond in heterocyclic rings	$1.352 \pm 5 \text{ \AA}$
Partial double bond in for example N-C=O	$1.322 \pm 3 \text{ \AA}$

It can be concluded that, as expected, the triazine ring bond lengths all have a large amount of double-bond character and so do the Tr-N bonds. What is more surprising is that the  $N_{\text{sub}}-C_{\text{sub}}$  bonds also appear to have some double-bond character. This observation is consistent with crystallographic data.

All four conformations were found to be planar,  $360.0^\circ$ , as is supported by the crystal data information which shows that in triazine systems bonded to nitrogen, the sum of the angles around the nitrogen is between  $358.4^\circ$  and  $360.0^\circ$ , with the majority lying between  $359.2^\circ$  and  $360.0^\circ$ .

It can be deduced that the modelled geometries are likely to be fairly accurate.

The energies of these conformations have been calculated using HF/6-31G and HF/6-31G\*\* basis sets and are quoted in Table 2, relative to the lowest energy form, I.

Conformation	Relative energy <sup>a</sup> / kJ mol <sup>-1</sup>		Populations based on HF/6-31G <sup>**b</sup>	
	HF/6-31G	HF/6-31G <sup>**</sup>	Relative	%
I	0.0	0.0	1.0	31.2
II	0.4	0.6	0.8	25.0
III	0.6	1.0	0.7	21.9
IV	0.6	1.0	0.7	21.9

<sup>a</sup> Not corrected for zero-point vibrational energies.

<sup>b</sup> Populations calculated at 20 °C.

Table 2: Relative energies of the four rotamers shown in Figure 1.

Within the error of the modelling all the energies calculated with the 6-31G basis set are the same. Increasing the basis set to 6-31G<sup>\*\*</sup> increases the differences in energy between the conformations, suggesting that the basis set limit using the Hartree-Fock method has not been reached but is clearly not far away. The relative energies are of the order expected based on steric considerations. The populations are estimated based on the energies calculated using the 6-31G<sup>\*\*</sup> basis set and are also shown in Table 2.

### 5.3 Rotational Energy Barriers

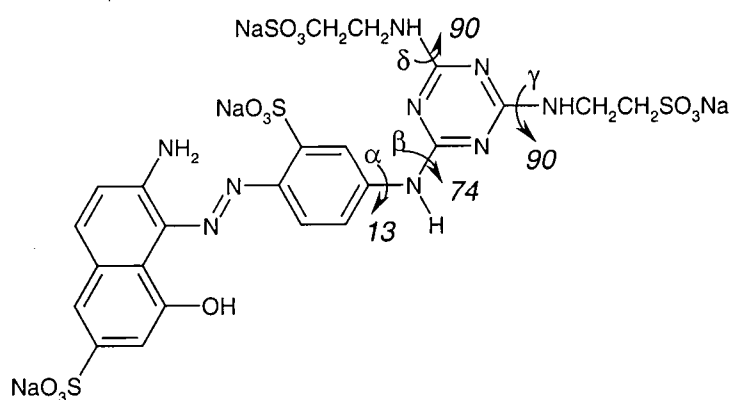
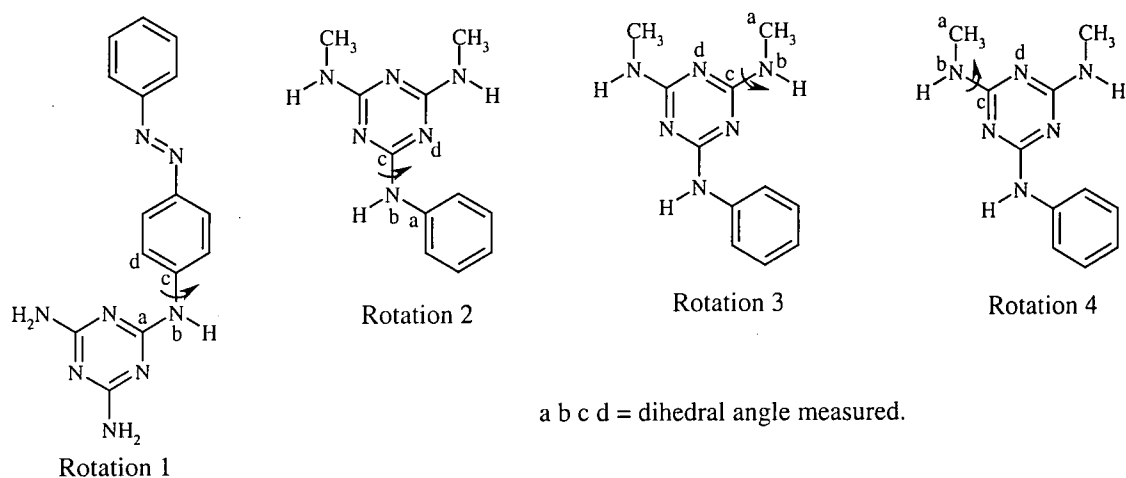


Figure 3: The molecule discussed in chapter 4. The rotational energy barriers in kJ mol<sup>-1</sup> are labelled in the diagram.

The aim of this chapter is to discuss the four rotational energy barriers involved in the exchange that was discussed in chapter 4. These angles are shown in Figure 3. The barriers were modelled initially using HF/6-31G calculations. Many calculations had to

be performed to explore the rotational energy barriers, so using a higher basis set would be very time consuming. The rotations measured are indicated on the models used to calculate them in Figure 4. Rotations 2, 3 and 4, corresponding to  $\beta$ ,  $\gamma$  and  $\delta$  respectively, will be discussed first in section 5.3.1. Barrier 1, corresponding to  $\alpha$  in chapter 4, will be described in section 5.3.2. Rotation 1 is considered separately to the other three as it does not involve rotation of a bond directly attached to the triazine ring. The observations made when investigating barriers 2, 3 and 4 can be used when looking at this barrier. The results obtained from all the barriers are summarised in section 5.3.3.

The dihedral angles used to calculate the rotational barriers 1, 2 and 3 and 4, are also shown in Figure 4. These were constrained at  $15^\circ$  increments for the initial barrier measurement while allowing the rest of the molecule to relax. The optimisation at each new angle used the previous optimised geometry as a starting point. The maximum in the barrier was investigated in more detail by measuring the energy at smaller intervals of rotation. The barrier conformations were found to the nearest  $0.5^\circ$ .



*Figure 4: Rotations measured, as shown on the models used in the calculations. The dihedral angles indicated were those constrained in the calculation; all are shown as  $0^\circ$  in the diagram.*

### 5.3.1 Barriers 2, 3 and 4

The rotational energy plots for barriers 2, 3 and 4, are shown in Figure 5. The energies plotted on the graph are relative to the starting structures described in Figure 4.

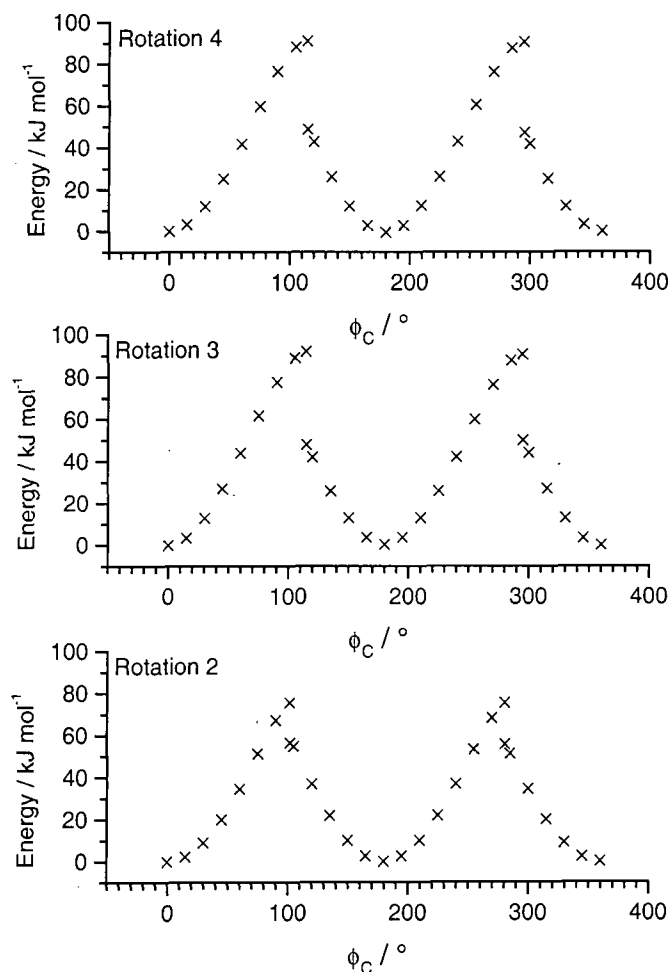


Figure 5: Rotational energy barriers 2, 3 and 4.

It can be seen that these barriers do not have a simple 2-fold energy profile as expected. A change in the dihedral angle by 0.5° at the top of the barrier results in an energy discontinuity in the order of 40 kJ mol<sup>-1</sup> for rotations 3 and 4, and of the order of 20 kJ mol<sup>-1</sup> for rotation 3. Rotation 2 has a lower barrier than 3 and 4: The reason for this will be discussed later in this chapter.

It can be seen that the rotations are approximately symmetrical about 180°. Although the model has a plane of symmetry along the plane of the triazine ring when ϕ<sub>C</sub> = 0°,

rotation of one side chain will disrupt this. The disruption induced is slightly different, strictly speaking, to that caused in the second half of the rotation starting from  $\phi_C = 180^\circ$  (conformer D). Using the 6-31G basis set, however, these differences cannot be distinguished, as already established in Table 2.

The existence of an energy discontinuity in a rotation profile suggests that there is some error in the method of modelling for the rotation. This therefore requires further investigation. Nitrogen has the ability to be planar or pyramidal and all stages in between. It is possible that some artefact of the geometry of the rotating chain nitrogen is responsible for the discontinuity in the rotation profile. The angles around the nitrogens of the side chains were measured at all dihedral angles and for all three rotations. The sum of the angles around one nitrogen is a measure of its planarity. The greater the deviation from  $360^\circ$ , the greater the deviation from planarity.

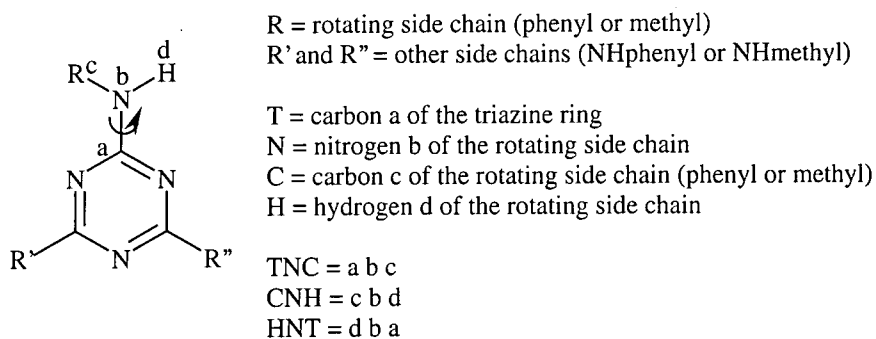


*Figure 6: Angles measured.*

Figure 6 describes the angles that are plotted in Figure 7. The angles around the nitrogen of the non-rotating side chains (R' and R'') were also measured, but the nitrogen in these side chains were found to remain planar in all cases.

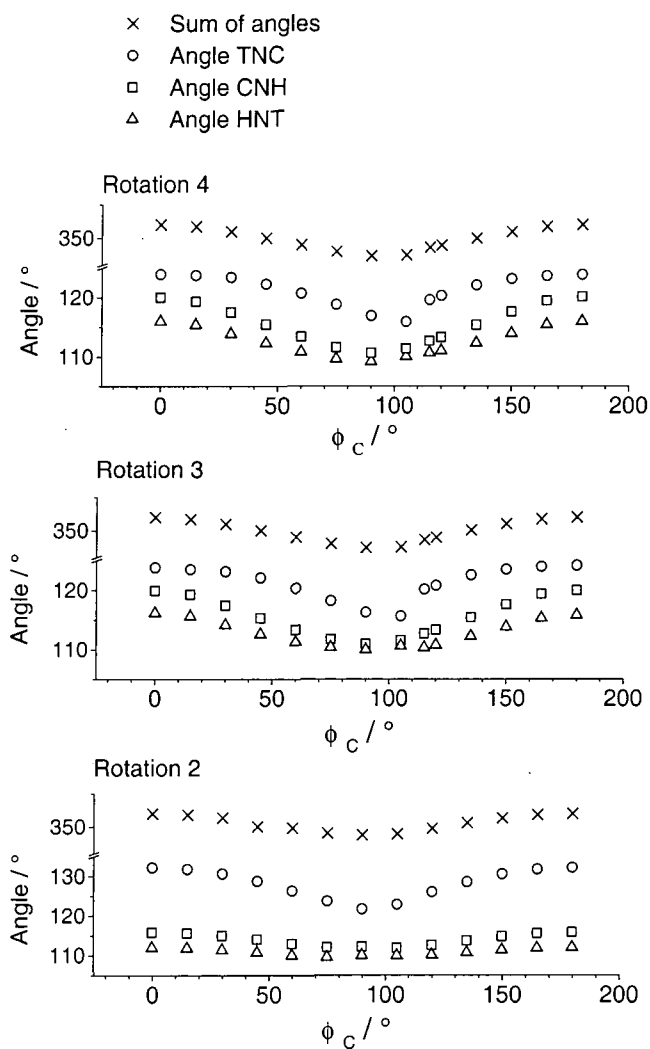


Figure 7: Angles around the rotating side-chain nitrogen.

By looking at the sum of the angles it is found that there is a deviation from planarity as rotation occurs, which is a maximum at the same point in the rotation as the maximum in energy. This deviation is greater for rotations 3 and 4 than for 2. This will be discussed later.

Pyramidalisation of the rotating side-chain nitrogen suggests the possibility of nitrogen inversion. The dihedral angle of the H attached to the nitrogen of the rotating side chain was therefore measured and its variation can be seen in Figure 8.

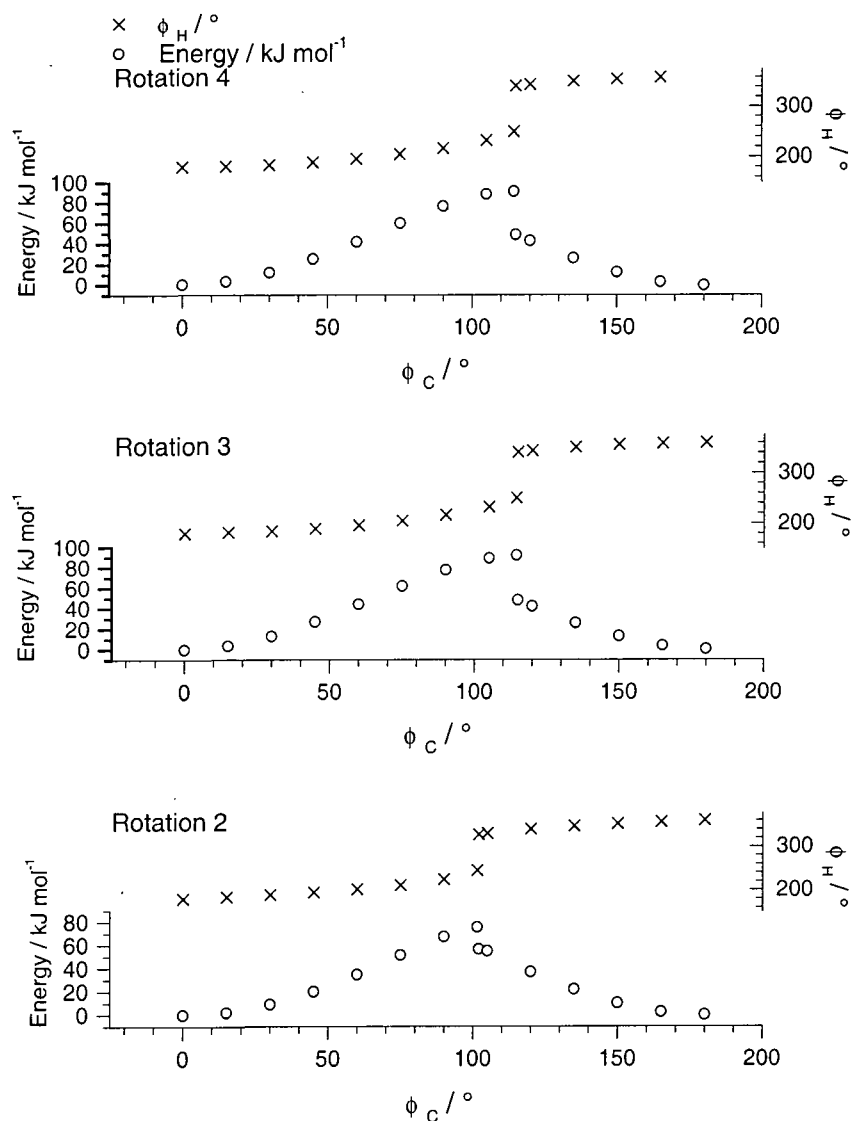
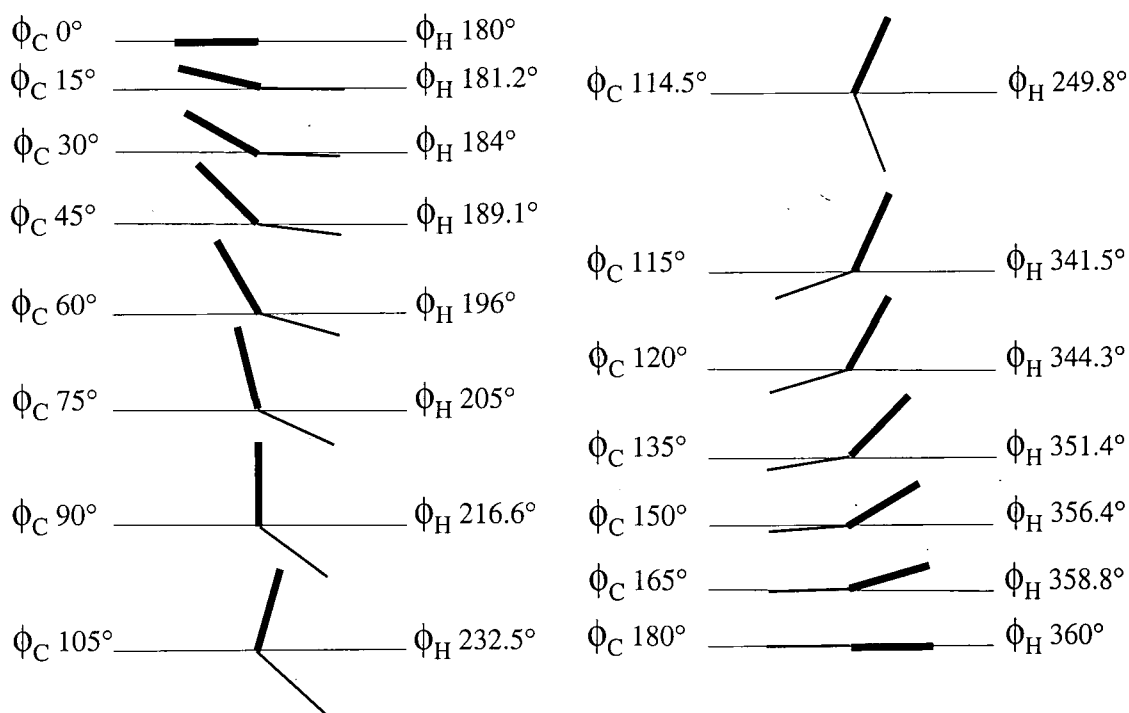


Figure 8: H dihedral angle and energy variation with side-chain rotation.

As can be seen in Figure 8, there is a jump in the H dihedral angle at the same point as the jump in energy. This jump in energy can therefore be interpreted as the nitrogen inverting. The rotation described by the calculations thus far is illustrated in Figure 9.



The horizontal line represents the plane of the molecule, the thick line represents the methyl group and the thin line the hydrogen, both of which are attached to the nitrogen of the rotating side chain.

Figure 9: The rotation calculated by molecular modelling.

The nitrogen inversion appears to be responsible for the discontinuity in the energy profile. Ideally it would be useful to measure separate barriers to rotation and inversion. The rotation actually occurring will involve changes in a combination of bond angles and bond lengths but it must be determined whether the combination of rotation, pyramidalisation and inversion modelled here is indeed an accurate description. We assume that the process is dominated by the two dihedral angles  $\phi_C$  and  $\phi_H$ . The above calculations are mimicking the rotational process as closely as possible by constraining only one dihedral angle and permitting relaxation of all other variables. To understand the cause of the nitrogen inversion, a 'backwards' rotation was modelled i.e. a dihedral angle of  $180^\circ$  was used as a starting point and the dihedral angle was decreased in  $15^\circ$  intervals using the optimised geometry of the previous higher angle as a starting point. The 'forward' and 'backward' energy barriers are shown in Figure 10 for rotations 1, 2 and 3. Only half the total  $360^\circ$  rotation was calculated as it was shown in Figure 5 that the rotations are approximately symmetrical about  $180^\circ$  as discussed previously.

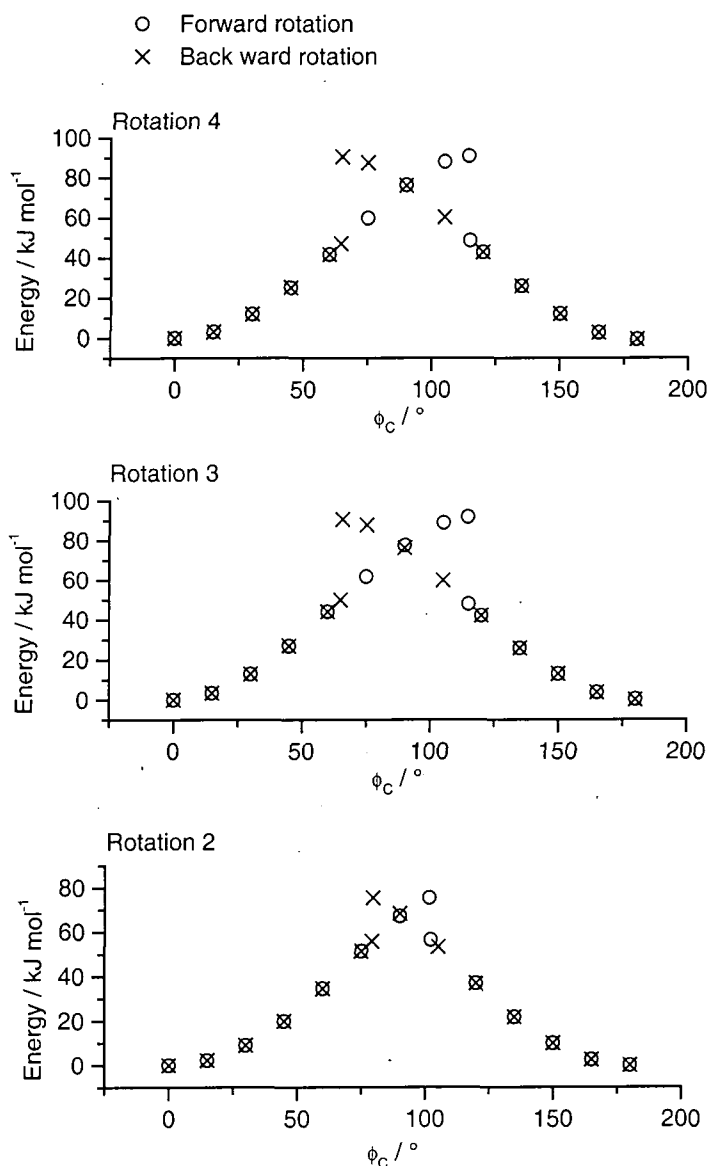


Figure 10: The 'forward' and 'backward' energy barriers.

It can be seen that the 'backward' profile is a mirror image of the 'forward' barrier. The fact that some dihedral angles have two corresponding values for the energy suggests that either or both of the following possibilities are true: 1) there are two possible paths across the energy surface and 2) the higher energy value is due a local minimum rather than the global minimum. Both these possibilities indicate that use of a single variable for the rotational process is inadequate since simultaneous inversion, pyramidalisation and rotation must be considered. This is most readily modelled by treating the dihedral angles between the ring plane and the CH<sub>3</sub> and H substituents on nitrogen as independent variables. An energy surface is therefore required. Due to the large

number of calculations required to achieve this, the model used thus far was simplified further and is shown in Figure 11.

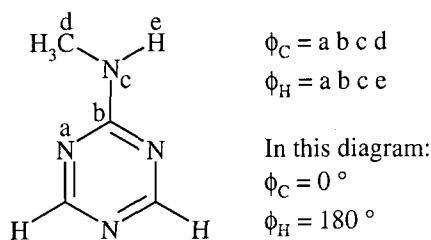


Figure 11: The model used for the 2D energy surface computed over dihedral angles C and H, see Figure 12.

The dihedral angles that were constrained are indicated in Figure 11. These were fixed at  $15^\circ$  intervals, while the rest of the molecule was allowed to optimise using an HF/6-31G calculation. The energy map is seen in Figure 12.

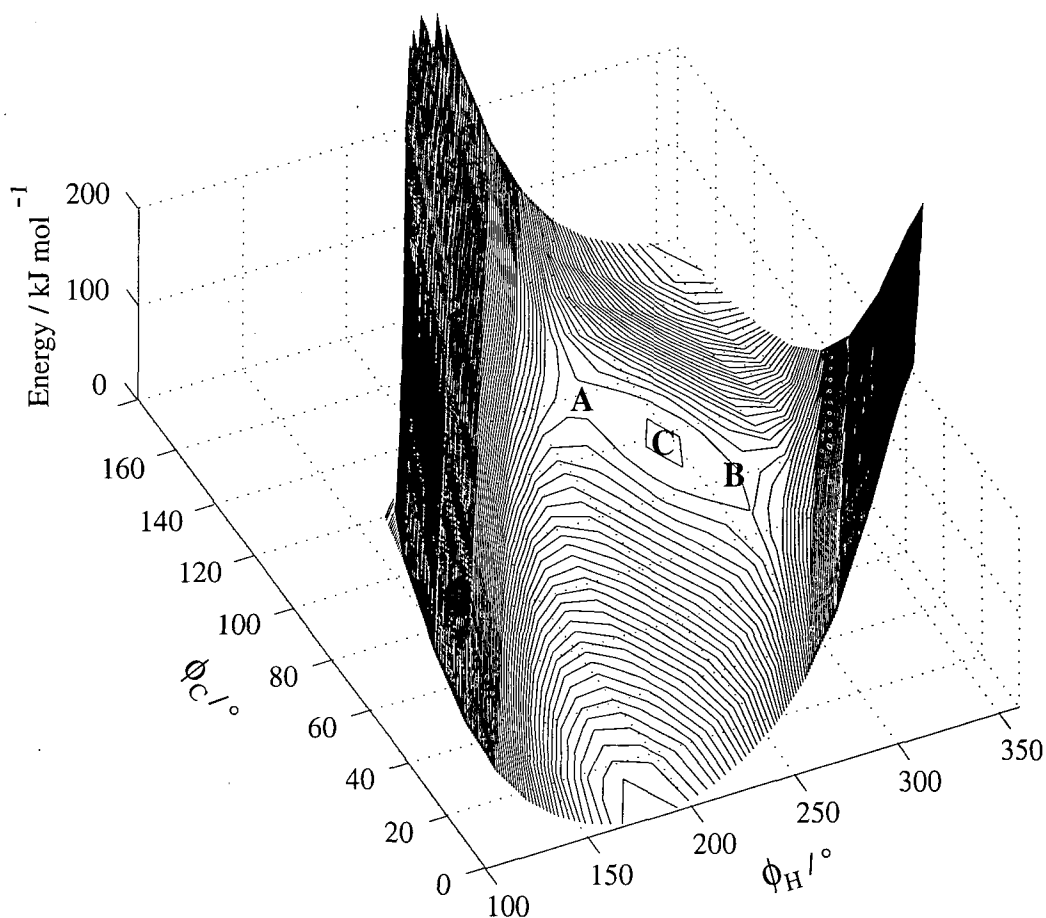


Figure 12: Energy map. The map was calculated using points separated by  $15^\circ$  in each dimension.

The very steep areas on the energy map are where the carbon and hydrogen are becoming close together. There is a comparable trough to that shown in Figure 12, corresponding to rotation in the opposite sense, separated from the section of the map shown by a high-energy area (where the energy is too great to be shown on the graph). At the centre of this region the energy is too large to be calculated (corresponding to atom overlap, which is physically impossible). It can be seen that there are two saddle points for the rotation, of approximately the same energy, 'A' and 'B' in Figure 12, and the central peak between the saddle points corresponds to nitrogen inversion, 'C' in Figure 12. To understand this map more fully, cross sections at constant  $\phi_C$  are displayed in Figure 13.

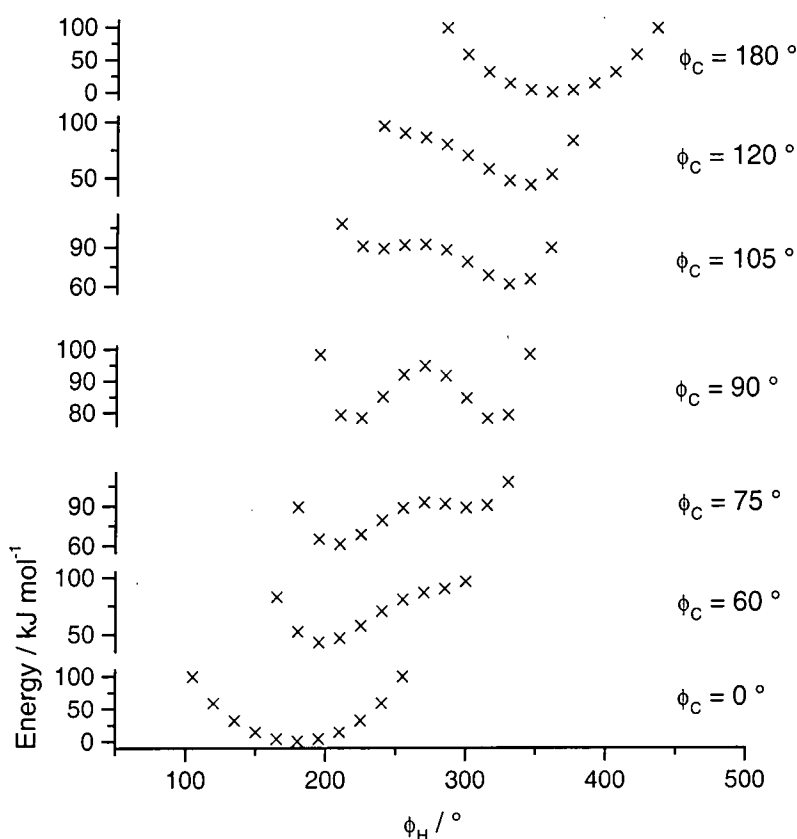
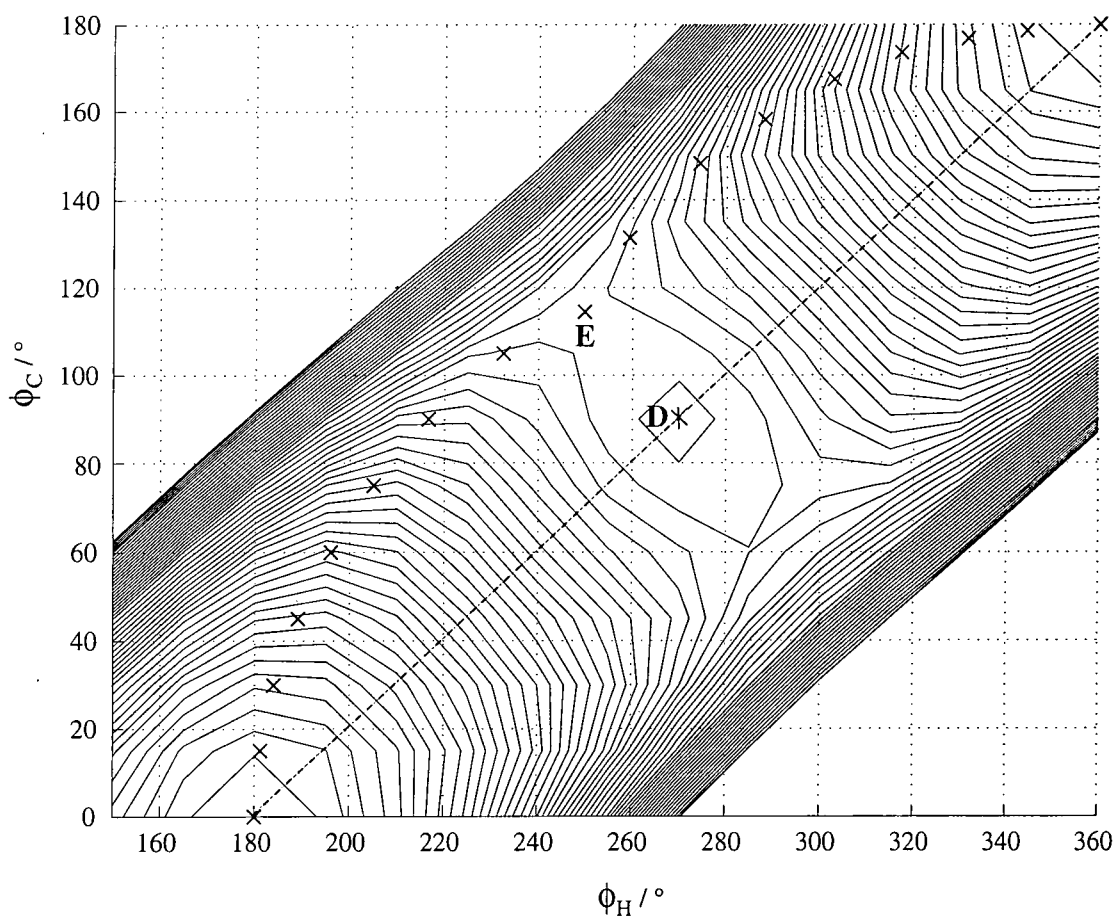


Figure 13: Cross sections of the energy map in Figure 12.

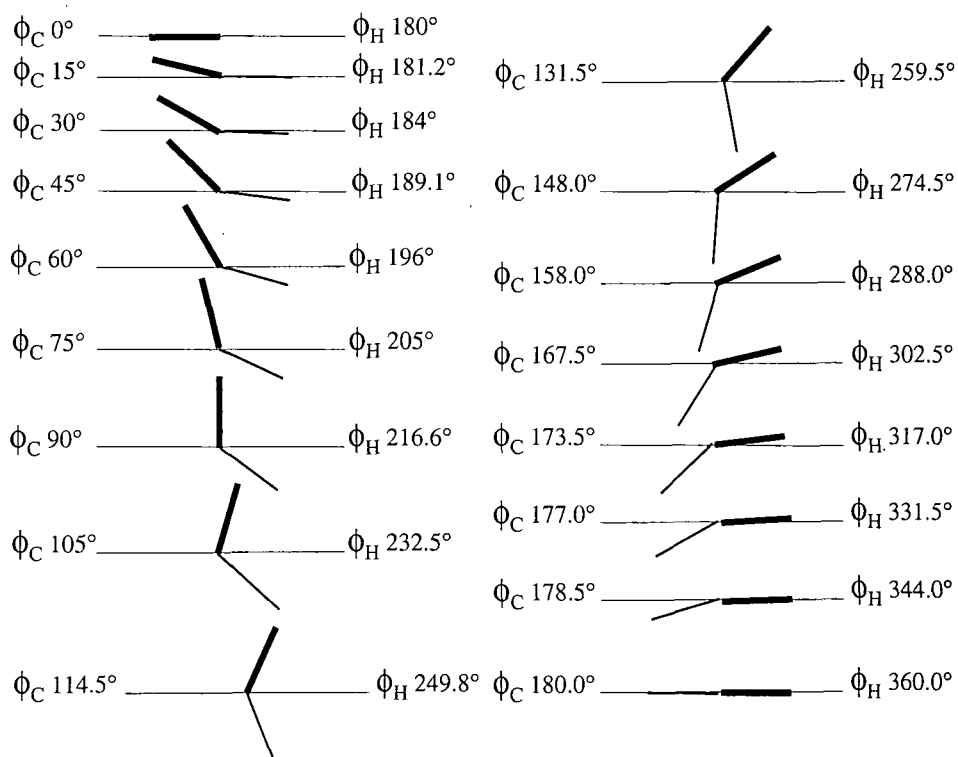
A rotation profile without inversion is indicated on the map in Figure 14.



The crosses represent a rotation path without nitrogen inversion and the dashed line, a planar rotation i.e. without pyramidalisation of the rotating side-chain nitrogen.

*Figure 14: Rotation path without nitrogen inversion. The map was calculated using points separated by  $15^\circ$  in each dimension.*

The difference in energy between point 'D' and point 'E' marked on the map in Figure 14 is the energy barrier to pure inversion. The rotation without nitrogen inversion represented by the crosses in Figure 14 is outlined in Figure 15.



The horizontal line represents the plane of the molecule, the thick line represents the methyl group and the thin line the hydrogen both of which are attached to the nitrogen of the rotating side chain.

*Figure 15: Possible rotation proposed without nitrogen inversion.*

The transition state area has been explored further, as shown in Figure 16. Here  $5^\circ$  steps in both dihedral angles were taken.

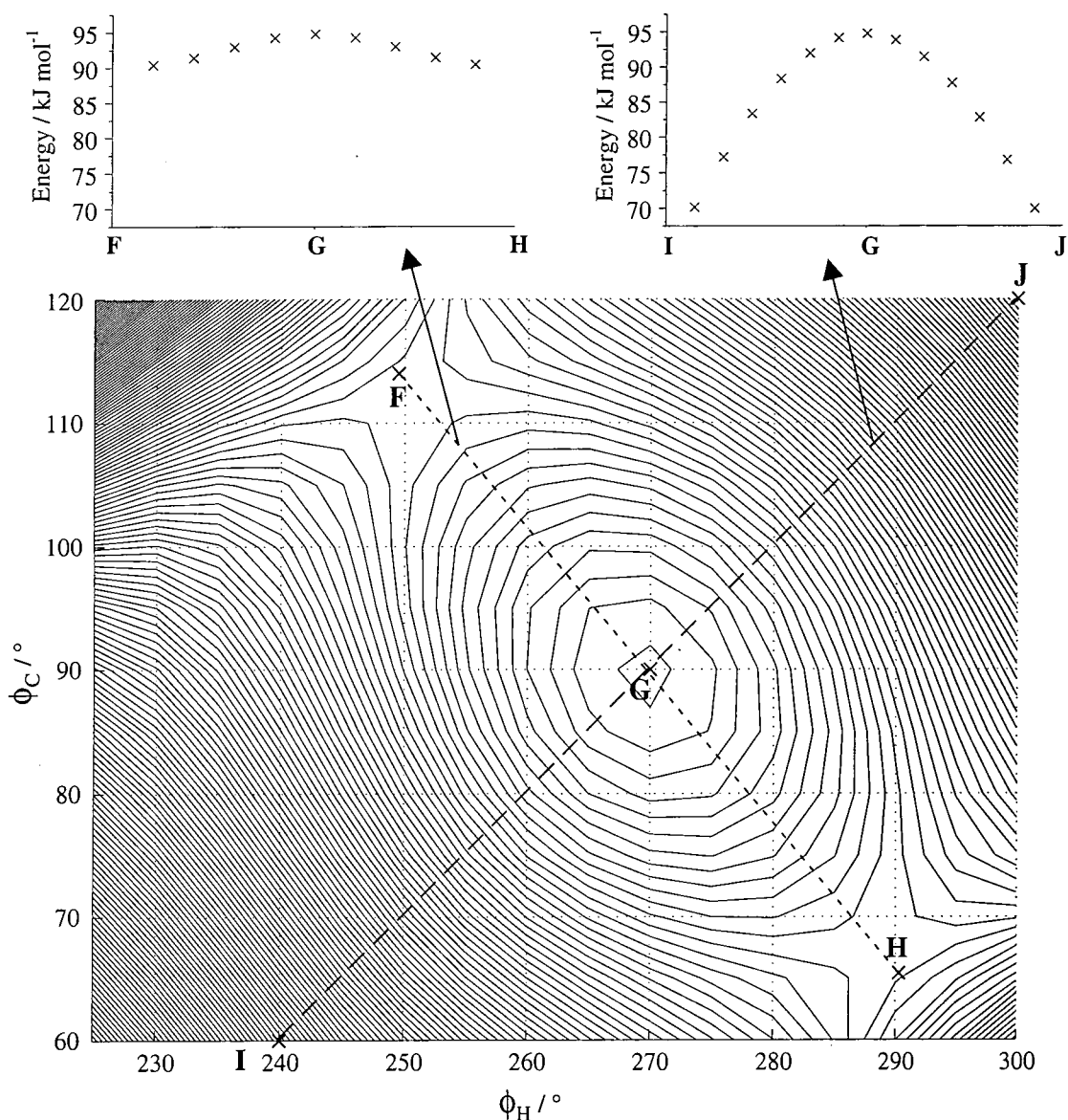
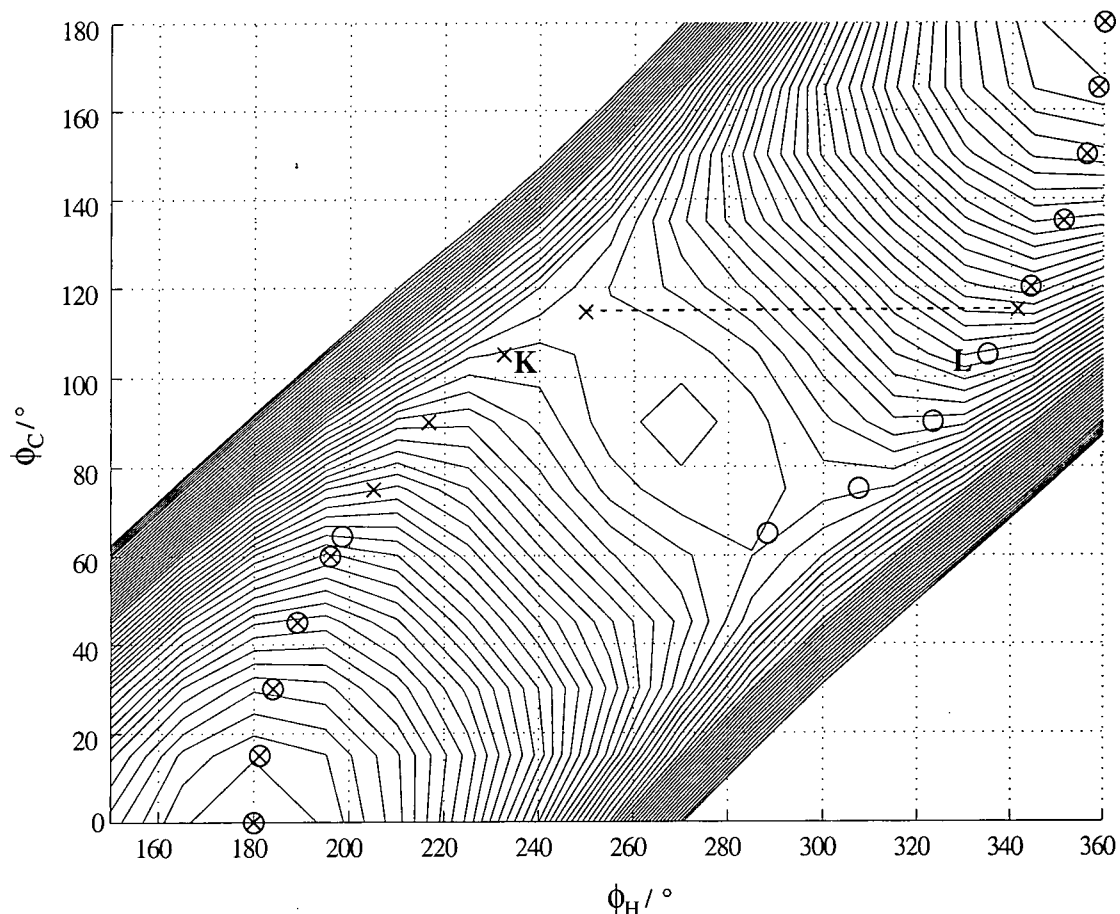


Figure 16: Expanded transition-state area. The map was calculated using points separated by  $5^\circ$  in each dimension.

The transition states of the rotational process can be seen to be approximately at  $\phi_C = 114.0^\circ$ ,  $\phi_H = 250^\circ$  ( $-110.0^\circ$ ), point 'F' and  $\phi_C = 65.4^\circ$ ,  $\phi_H = 290.3^\circ$  ( $-69.7^\circ$ ), point 'H'. There is only a small difference in energy between points 'F' and 'G', corresponding to the energy barrier to pure nitrogen inversion. In fact this barrier only appears to become visible near the transition states. As expected this maximum energy conformation is at C and H dihedral angles of  $90^\circ$  and  $270^\circ$  respectively. The saddle point for the overall rotational process is not at  $\phi_C = 90^\circ$  however. The path of the 'forward' and 'backward' rotations calculated previously are shown on the energy surface in Figure 17.



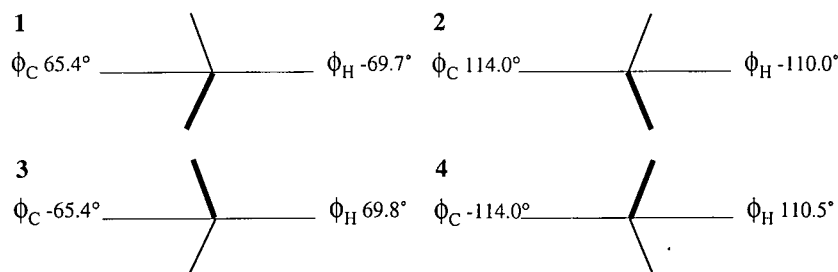
Crosses represent the forward rotation and circles represent the backward rotation.

*Figure 17: Routes of the 'forward' and 'backward' rotations plotted on the energy map. The map was calculated using points separated by  $15^\circ$  in each dimension.*

Point 'K' (marked on the map) is a local minimum compared to 'L' (also on the map) at  $\phi_C = 105^\circ$  but one of the two saddle points must be traversed for full rotation. It can be observed therefore that there are indeed two possible routes over this energy surface, both of which lead to local minima being found for some values of  $\phi_C$ . Rotation with nitrogen inversion has the same transition state as the path shown in Figure 14. These transition states are also the same as the maxima in the energy barriers calculated previously, displayed in Figure 5.

Now the rotation has been explored, the transition states can be found more accurately. This is done using the QST3 method outlined in the introduction to this chapter. There are actually 4 transition-states per rotation due to the lack of symmetry, strictly speaking, of the molecule as shown in Figure 18. Only two will be calculated however due to the symmetry considerations discussed previously. There are also two higher-

energy planar transition states for the nitrogen inversion which are expected to be at  $\phi_C = 90^\circ$ ,  $\phi_H = 270^\circ$  and  $\phi_C = 270^\circ$ ,  $\phi_H = 90^\circ$ . Again only one of the two will be found due to symmetry.



The horizontal line represents the plane of the molecule, the thick line represents the methyl group and the thin line the hydrogen, both of which are attached to the nitrogen of the side chain. Only 1 and 2 have been calculated due to symmetry considerations.

Figure 18: Transition states.

The transition states for the nitrogen inversion could not be found by the QST3 method because they are not saddle points of order 1. The energies at the points  $\phi_C = 90^\circ$ ,  $\phi_H = 270^\circ$  and  $\phi_C = 270^\circ$ ,  $\phi_H = 90^\circ$  were calculated as approximations to the inversion transition states using the 6-31G basis set.

A discrepancy was found for rotation 2 while doing the saddle point search. The initial investigation showed that the barrier behaved similarly to rotations 3 and 4, that is with an energy jump due to nitrogen inversion, although this energy discontinuity was considerably smaller. The transition state search using the QST3 method found only one saddle point that was appreciably different from the two estimated initially by observing the angle at the highest energy before nitrogen inversion when incrementing  $\Phi_C$  only ( $\Phi_C = 90.4^\circ$  in contrast to  $79.5^\circ$  and  $101.5^\circ$ ). The initial barrier search had been found to be fairly accurate for rotations 3 and 4. This rotation therefore needed further investigation. An energy map was constructed by incrementing  $\phi_C$  and  $\phi_H$  by  $5^\circ$  in each dimension to detail the saddle point area using the simpler model shown in Figure 19. As with the other energy maps plotted, all other variables are optimised. The energy map is shown in Figure 20.

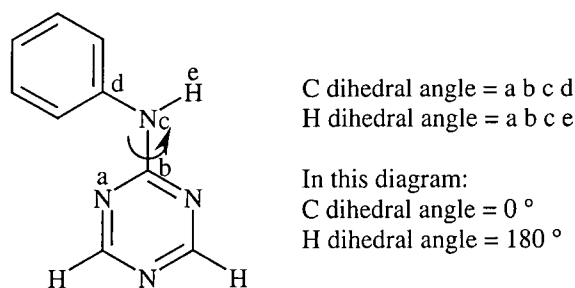
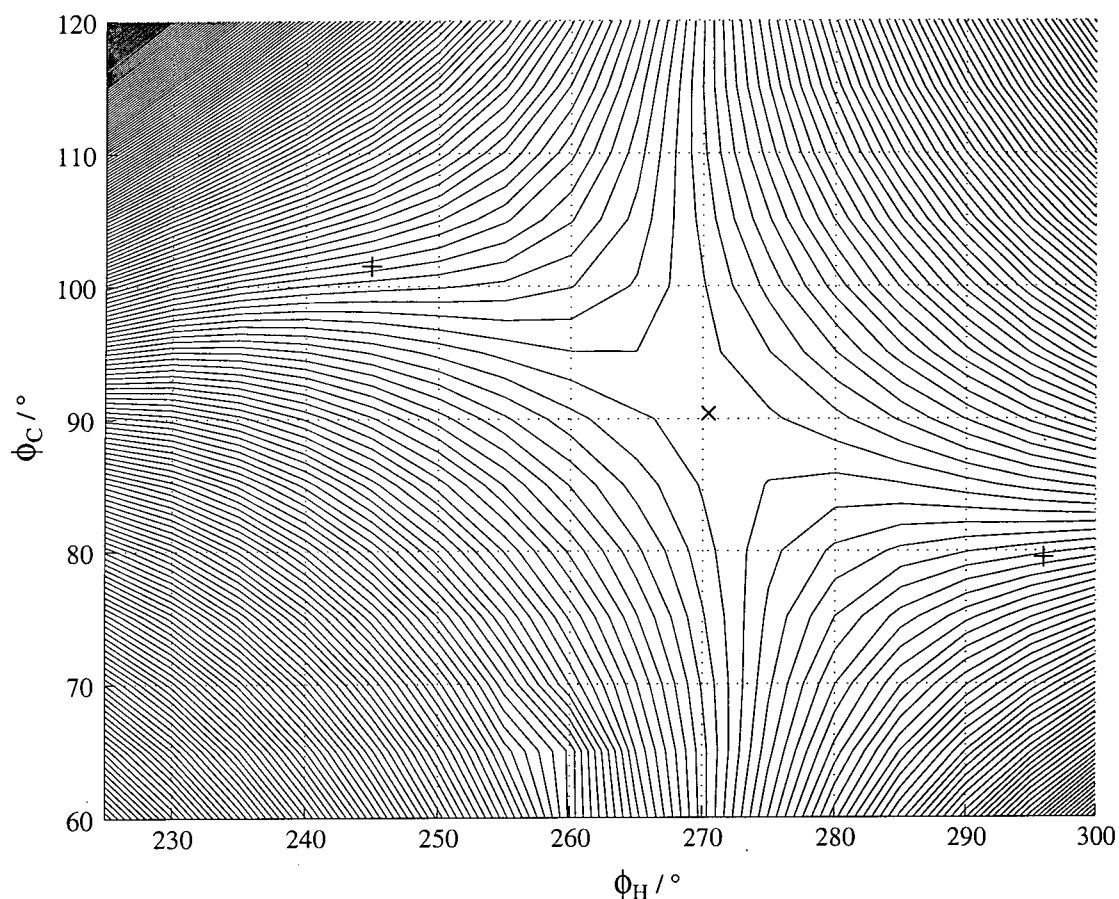


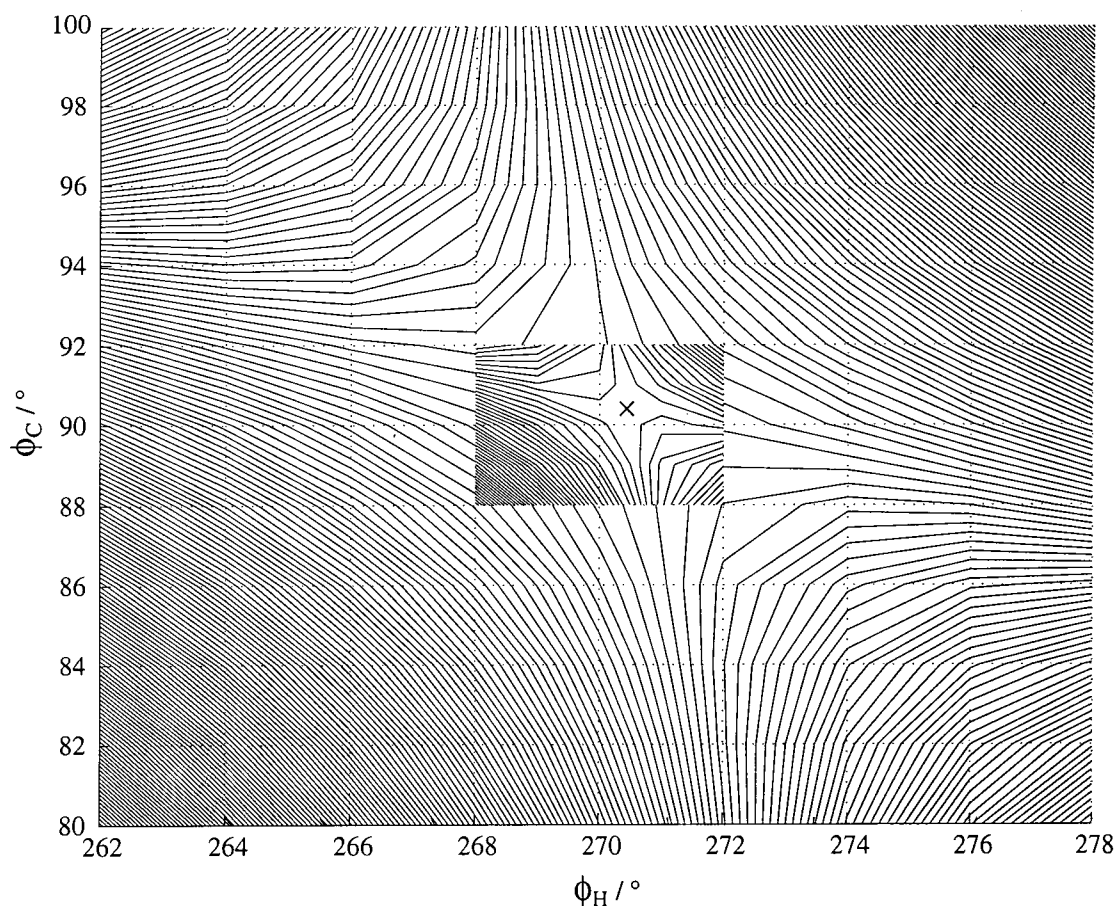
Figure 19: The model used for the 2D energy surface computed over dihedral angles C and H, see Figure 20.



+ marks the top of the 'forward' ( $\Phi_C = 101.5^\circ$ ,  $\Phi_H = 244.9^\circ$ ) and 'backward' ( $\Phi_C = 79.5^\circ$ ,  $\Phi_H = 296.0^\circ$ ) barriers found by incrementing  $\Phi_C$ .  
x marks the saddle point found using the QST3 method ( $\Phi_C = 90.4^\circ$ ,  $\Phi_H = 270.4^\circ$ ).

Figure 20: 2D energy map using the simplified model shown in Figure 19 to model rotation 2. The map was calculated using points separated by  $5^\circ$  in each dimension.

Figure 20 shows that the initial transition state search by incrementing  $\Phi_C$  did not find the optimum path over the energy surface. The saddle points are not as pronounced as for rotations 3 and 4. To see more clearly if there are one or two saddle points, the central region is expanded further in Figure 21.



x marks the saddle point found using the QST3 method ( $\Phi_C = 90.4^\circ$ ,  $\Phi_H = 270.4^\circ$ ).

*Figure 21: 2D energy map using the simplified model shown in Figure 19 to model rotation 2. The contour lines in the central region,  $\Phi_C = 88^\circ$ - $92^\circ$ ,  $\Phi_H = 268^\circ$ - $272^\circ$  are expanded compared to the rest of the map so do not represent the same energy difference. The main body of the map was calculated using points every  $2^\circ$  in each dimension. The central region was calculated using a point separation of  $1^\circ$  in each dimension.*

Looking at Figure 21 it appears that there is only one transition state. The position of this appears to have been calculated correctly using the QST3 method. The existence of a single saddle point indicates that there is not significant pyramidalisation of the nitrogen during this rotation as initially thought and in contrast to rotations 3 and 4. This will be discussed further in section 5.4.

### 5.3.2 Barrier 1

For barrier 1,  $\Phi_C$  was incremented in  $15^\circ$  intervals in the same way as for rotations 2, 3 and 4. The model used is shown in Figure 4. The energy profile is shown in Figure 22.

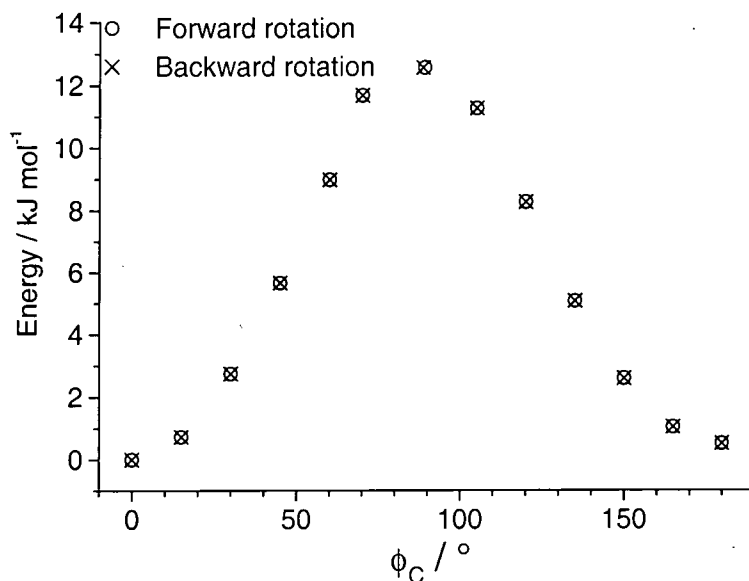


Figure 22: The 'forward' and 'backward' rotational energy barriers of rotation 1.

The energy profile for rotation 1 is smooth and symmetrical. It is expected therefore that there is only one saddle point (with a corresponding one  $180^\circ$  later). This was found using the QST3 search.

### 5.3.3 Summary

The results so far have been summarised in Table 3.

The transition states occur with approximately the same energy and geometry as those found initially by changing only  $\Phi_C$ . One saddle point was found in the 'forward' rotation and the other during the 'backward' rotation.

	$\Phi_C / ^\circ$	$\Phi_H / ^\circ$	Energy / $\text{kJ mol}^{-1}$	
Rotation 1	91.4	271.6	12.6	
Rotation 2	90.4	270.4	74.4	
Rotation 3	1	65.8	-70.4	92.0
	2	114.3	-110.7	90.7
	pure inversion <sup>a</sup>	90.0	-90.0	6.8
Rotation 4	1	65.4	-69.7	90.6
	2	114.0	-110.5	91.0
	pure inversion <sup>a</sup>	90.0	-90.0	6.4

<sup>a</sup> Approximations to the transition state. The barrier quoted in the last column corresponds to the difference in energy between points 'F' and 'G' in Figure 16.

Table 3: Saddle-point energies and geometries.

Rotations 1 and 2 appear to be simple planar rotations whereas rotations 3 and 4 involve nitrogen inversion with rotation. These complex energy surfaces can be defined by four energy barriers per rotation: Planar rotation, rotation with pyramidalisation, rotation with pyramidalisation and inversion, and nitrogen inversion only. The corresponding energies are listed in Table 4.

	Energy of rotation / $\text{kJ mol}^{-1}$			Energy of inversion only / $\text{kJ mol}^{-1}$
	Planar	with pyramidalisation	with pyramidalisation and inversion	
Rotation 1	12.6			
Rotation 2	74.4			
Rotation 3	97.5	92.0	92.0	6.8
Rotation 4	97.0	91.0	91.0	6.4

Table 4: Summary of the energy barriers to different paths of rotation.

Nitrogen inversion rotation is a concerted process<sup>18</sup> for sterically hindered alkylamines which involves effectively an energy-less barrier to nitrogen inversion during rotation. For unhindered alkylamines however the inversion-rotation barrier is dominated by inversion.<sup>19</sup>

## 5.4 Discussion

Now that the rotational process is understood, one can try to account for the different barrier heights.

Nitrogen rotation-inversion processes in amines are well known. Many such barriers have been measured, particularly using dynamic NMR.<sup>20-22</sup> With advances in molecular modelling, these barriers have become subject to theoretical study. A range of methods have been employed, particularly molecular mechanics.<sup>20-25</sup> Much work has been done to attempt to rationalise trends in barrier heights of alkylamines.<sup>20-25</sup>

The barriers under discussion here, although involving amine rotation-inversion, have more similarities to amide rotation due to a change in hybridisation from the equilibrium geometry to the transition state. The nitrogen is planar and pyramidalises upon rotation. Amine barriers to rotation-inversion are dependent upon substituent steric bulk and conformational changes during rotation i.e. trans, gauche, eclipsed etc. It is expected that due to the presence of the planar triazine ring, these features are not the main effects in this investigation.

Hindered rotation of amines involving delocalisation opportunities of the nitrogen lone pair with  $\pi$ -electrons of substituents has been little studied experimentally except in the form of amides and thioamides and none could be found in the literature involving triazines. HF and DFT methods were mainly used in these studies. Of the work done, concerted rotation, inversion barriers were quoted rather than separate ones, as attempted here, so direct comparison of the numerical results with the literature is difficult. DFT has been found to give more accurate results than HF methods for amide rotation<sup>26</sup> although for amine rotation HF/6-31G\* has been found to be adequate.<sup>27</sup> Although in this study electron correlation will be important, it is believed that the *ab initio* method used (HF/6-31G) is sufficient to observe trends in the different barriers of interest and the overall shape of the energy surface. The values of the barriers themselves are not accurate, as can be seen by comparison with the experimentally

measured energies in chapter 4 but the aim of this chapter was to increase the understanding of these barriers, which has been achieved.

There are two descriptions of rotational barriers in amines of this type.<sup>28</sup> The first is the traditional approach of delocalisation, or resonance,<sup>29-33</sup> and the second is a relatively new idea which considers the relative energies of the nitrogen and its substituents.<sup>34-36</sup> This view remains controversial and generally not appreciated.<sup>37-42</sup> A rationalisation of the relative energy barriers of the three processes according to the delocalisation approach will be considered first.

Resonance occurs whenever a molecule can be represented by structures that have the same arrangement of nuclei but a different arrangement of electrons.<sup>43</sup> The molecule will be a hybrid of all these structures and cannot be accurately represented by any one of them. Resonance becomes important if these structures are similar in stability i.e. energy. The contribution each structure makes to the hybrid depends on the relative energy of that structure.<sup>43</sup> The resulting hybrid is more stable than its component structures. This difference in energy is called the resonance energy.<sup>43</sup> The smaller the difference in energy between all the contributing structures, the greater the resonance energy will be.<sup>43</sup>

A lot of work has been carried out on amide rotation so the system under discussion here will be compared to that.

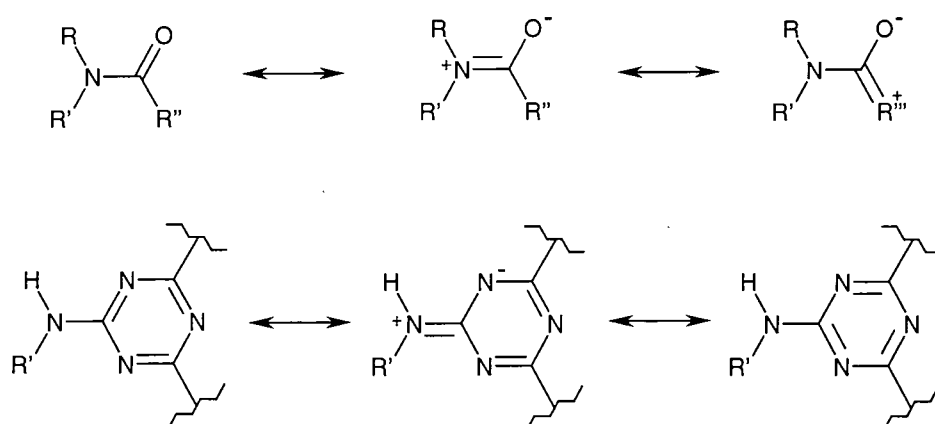


Figure 23: Resonance structures for the amine side chains of the triazine system under investigation, compared with those of amides.

Resonance predicts that in the planar form there is interaction between the triazine  $\pi$  bond and the lone pair on the side-chain nitrogen as seen in Figure 23. As the rotation occurs this interaction is lost when the orbitals become orthogonal. This is analogous to the amide case where the interaction is between the nitrogen lone pairs and the carbonyl  $\pi$  bond.

Calculations on the electron density of formamide show the main electron transfer is from nitrogen to the carbonyl carbon with the oxygen remaining virtually unchanged. This disagrees with the delocalisation description, which suggests the electron density on oxygen would be expected to change considerably. As the rotation proceeds, the nitrogen pyramidalises and the carbon-nitrogen bond lengthens. The carbonyl bond is seen to increase only marginally. This again is not consistent with the resonance approach, where the carbonyl bond order, and therefore length, is expected to change. This anomaly requires a new rationalisation.

It is found that the N-R bonds are shorter in the planar form of formamide compared to the pyramidal form, therefore increasing the repulsive forces between the substituents. The rationalisation for this is that in the planar form, the nitrogen has more 's' character than when in the pyramidal form, because it has  $sp^2$  hybridisation. When in the planar form it therefore requires a net transfer of electrons from its substituents. Decreasing the electron density on these substituents results in a destabilisation.<sup>35,39,40</sup> The nitrogen is more stable in the planar form, but the substituents are less stable due the increased repulsion and the decrease in electron density. The stability of the nitrogen and the stability of the substituents are therefore in opposition, meaning that the energy of the structure at a particular rotational angle, and therefore the overall rotational energy barrier, depends on the balance of these two factors.<sup>44</sup>

To summarise, resonance theory would predict that the N-Tr bond should lengthen as the nitrogen deviates from planarity in rotations 3 and 4. No significant bond length changes are expected between nitrogen and the substituents. As the triazine ring is a delocalised system itself, no significant changes would be expected in triazine bond lengths in contrast to the analogous amide rotation.

The non-resonance model also expects the N-Tr bond length to increase and also no changes in the triazine internal bond lengths, but in contrast to the resonance model, the N-substituent bond lengths are expected to increase as the rotation occurs.

The calculations presented in this chapter show that the N-Tr bond length does indeed increase from 1.34 Å at  $\Phi_C=0^\circ$  to 1.40 Å at the transition state of rotation 4. This is an increase of 5.0 %. There is only a small change in the triazine internal bond lengths, as expected, namely a decrease of 0.8 %. The bond length of the side-chain nitrogen to the aliphatic carbon is where the two theories differ. It is observed, in the calculations described in this chapter, that this bond length does increase with rotation but not dramatically. 1.45 Å when  $\Phi_C=0^\circ$  to 1.47 Å at  $\Phi_C=90^\circ$  which is an increase of 1.37 %. This suggests that the non-resonance model is slightly better at predicting the trends observed but not conclusively so.

The calculations given herein show that rotation 2 is lower in energy than 3 and 4 and that nitrogen remains planar upon rotation, in contrast to becoming pyramidal as observed in rotations 3 and 4. Resonance theory can explain this. In the 'ground state' of rotation 2, the side-chain nitrogen is planar due to the extensive delocalisation of the triazine ring, through the lone pair on the nitrogen to the phenyl ring. As delocalisation with the triazine ring is disrupted on rotation, the nitrogen lone pair can remain delocalised with the phenyl ring. This means it can remain planar in contrast to the situation with the presence of purely aliphatic side-chains where no delocalisation can remain during rotation. The remaining delocalisation also means that some resonance energy is retained at the saddle point, leading to a lower energy barrier than without the presence of the phenyl ring in the side chain. Similarly in rotation 1, the nitrogen remains planar as delocalisation can be maintained with the nitrogen lone pairs and the triazine ring when the phenyl group is rotated. The energy barriers 2, 3 and 4 are large, suggesting that there is a large resonance energy, which is disrupted on rotation, between the triazine ring and the lone pair on the side-chain nitrogens. When this can be maintained (in rotation 1) the barrier is considerably smaller, supporting the idea that the triazine ring provides a large stabilisation. This stabilisation is greater than that provided by the phenyl ring, as when this can participate in resonance during rotation (in rotation 2) the barrier, although lower than for rotations 3 and 4 where no resonance

is possible, is still large. Although the modelled barriers are significantly lower than those measured by NMR, the trends observed appear to be correct.

The non-resonance model can also rationalise the observations made. Nitrogen remains planar during rotation 1. This suggests that the triazine ring is able to donate electron density to the nitrogen without decreasing its stability sufficiently to result in nitrogen pyramidalisation. Rotation 2 requires stable electron density transfer from the phenyl ring if the nitrogen is to remain planar. The phenyl ring is a well-known source of electrons so there will not be a large disruption to the stability of the phenyl ring in doing this. When aliphatic groups are present, the increase in energy of the substituents upon electron density donation to the nitrogen is greater than the decrease in energy of the nitrogen by being planar. This is not surprising, as a phenyl ring is a more stable electron donor than a methyl group. The result is rotations 1 and 2 are planar and lower in energy than 3 and 4.

## 5.5 Conclusions

Molecular modelling has been shown to provide reasonable geometries for triazine systems. The relative energies of the different rotamers have been calculated.

Rotations 3 and 4 of the triazine side chains have been found to occur via a concerted process incorporating nitrogen inversion. This agrees with literature observations. Rotations 1 and 2 have been found to be pure rotations. The differences in these barriers have been rationalised. Values for the energies of the different processes occurring have been calculated. These have been discussed in terms of two theories, the delocalisation idea, and a more recent approach considering the substituent destabilisation.

## 5.6 References

- <sup>1</sup> J. M. Goodman, *Chemical Applications to Molecular Modelling*, RSC., Cambridge, 1998
- <sup>2</sup> A. Hinchliffe, *Chemical Modelling From Atoms to Liquids*, Wiley, Chichester, 1999.
- <sup>3</sup> F. Jensen, *Introduction to Computational Chemistry*, Wiley, Chichester, 1999.
- <sup>4</sup> D. M. Hirst, *A Computational Approach to Chemistry*, Blackwell Scientific, Oxford, 1990.
- <sup>5</sup> J. B. Foresman and A. Frisch, *Exploring Chemistry with Electronic Structure Methods*, Gaussian Inc., Pittsburg, 2<sup>nd</sup> Ed., 1995.
- <sup>6</sup> G. H. Grant and W. G. Richards, *Computational Chemistry*, Oxford University Press, Oxford, 1995.
- <sup>7</sup> J. C. Cherryman, Ph. D. Thesis, University of Durham, 1998.
- <sup>8</sup> J. C. Slater, *Phys. Rev.*, **36**, 57 (1930).
- <sup>9</sup> J. A. Pople and G. A. Segal, *J. Chem. Phys.*, **43**, S136 (1965).
- <sup>10</sup> M. J. S. Dewar, E. G. Zoebisch, E. F. Healy and J. J. P. Stewart, *J. Am. Chem. Soc.*, **107**, 3902 (1985).
- <sup>11</sup> J. J. P. Stewart, *J. Comp. Chem.*, **10**, 209 (1989).
- <sup>12</sup> P. Hohenberg and W. Kohn, *Phys. Rev.*, **136**, B864 (1964).
- <sup>13</sup> M. L. Glówka and I. Iwanicka, *Acta Cryst.*, **C47**, 616 (1991).
- <sup>14</sup> The United Kingdom Chemical Database Service, D. A. Fletcher, R. F. McMeeking, D. J. Parkin, *Chem. Inf. Comput. Sci.*, **36**, 746 (1996).
- <sup>15</sup> 3D Search and Research using the Cambridge Structural Database, F. H. Allen, O. Kennard, *Chemical Design Automation News*, **8(1)**, 1 & 31 (1993).
- <sup>16</sup> Ed. O. Kennard, D. G. Watson, F. H. Allen, N. W. Isaacs, W. D. S. Motherwell, R. C. Pettersen and W. G. Town, *Molecular Structures and Dimensions AI*, International Union of Crystallography with Crystallography Data Centre, Cambridge, 1965.
- <sup>17</sup> J. E. Huheey, *Inorganic Chemistry*, 3<sup>rd</sup> Ed. Harper and Row, New York, 1983.
- <sup>18</sup> A. M. Belostotskii and A. Hassner, *J. Phys. Org. Chem.*, **12**, 659 (1999).
- <sup>19</sup> A. M. Belostotskii, P. Aped and A. Hassner, *Theochem-J. Mol. Struc.*, **398**, 427 (1997).
- <sup>20</sup> J. H. Brown and C. Hackett Bushweller, *J. Am. Chem. Soc.*, **114**, 8153 (1992).
- <sup>21</sup> J. H. Brown and C. Hackett Bushweller, *J. Phys. Chem. A*, **101**, 5700 (1997).
- <sup>22</sup> R. Maharajh, J. P. Snyder, J. F. Britten and R. A. Bell, *Can. J. Chem.*, **75**, 140 (1997).

- <sup>23</sup> A. M. Belostotskii and A. Hassner, *J. Phys. Org. Chem.*, **12**, 659 (1999).
- <sup>24</sup> A. M. Belostotskii, H. E. Gottlieb, P. Aped and A. Hassner, *Chem. Eur. J.*, **5**, 449 (1999).
- <sup>25</sup> A. M. Belostotskii, P. Aped and A. Hassner, *Theochem.*, **398**, 427 (1997).
- <sup>26</sup> I. A. Topol and S. K. Burt, *J. Phys. Chem.*, **99**, 905 (1995).
- <sup>27</sup> M. A. Murcko and B. G. Rao, *J. Comput. Chem.*, **14**, 1446 (1993).
- <sup>28</sup> P. Hazendonk, *Ph.D. Thesis*, McMaster University, 2000.
- <sup>29</sup> H. S. Gutowsky and C. H. Holm, *J. Chem. Phys.*, **25**, 1228 (1956).
- <sup>30</sup> M. T. Rodgers and J. C. Woodbrey, *J. Phys. Chem.*, **66**, 540 (1962).
- <sup>31</sup> K. I. Dahlqvist and S. Forsen, *J. Phys. Chem.*, **73**, 4124 (1969).
- <sup>32</sup> L. L. Graham and R. E. Diel, *J. Phys. Chem.*, **73**, 2696 (1969).
- <sup>33</sup> W. E. Stewart and T. H. Siddall, *Chem. Rev.*, **70**, 517 (1970).
- <sup>34</sup> K. B. Wiberg and K. E. Laidig, *J. Am. Chem. Soc.*, **109**, 5935 (1987).
- <sup>35</sup> K. B. Wiberg and C. Breneman, *J. Am. Chem. Soc.*, **114**, 831 (1992).
- <sup>36</sup> A. D. Bain, P. Hazendonk and P. Couture, *Can. J. Chem.*, **77**, 1340 (1999).
- <sup>37</sup> A. J. Bennet, Q. P. Wang, H. Slebocka-Tilk, V. Somayaji, R. S. Brown and B. D. Santarsiero, *J. Am. Chem. Soc.*, **112**, 6383 (1990).
- <sup>38</sup> C. L. Perrin, *J. Am. Chem. Soc.*, **113**, 2865 (1991).
- <sup>39</sup> K. E. Laidig and L. M. Cameron, *Can. J. Chem.*, **71**, 872 (1993).
- <sup>40</sup> K. E. Laidig and L. M. Cameron, *J. Am. Chem. Soc.*, **118**, 1737 (1996).
- <sup>41</sup> D. Lauvergnat and P. C. Hiberty, *J. Am. Chem. Soc.*, **119**, 9478 (1997).
- <sup>42</sup> G. Fogarasi and P. G. Szalay, *J. Phys. Chem.*, **101 A**, 1400 (1997).
- <sup>43</sup> R. T. Morrison and R. N. Boyd, *Organic Chemistry*, 3<sup>rd</sup> Ed. Allyn and Bacon Inc., Boston, 1973.
- <sup>44</sup> R. F. W. Bader, J. R. Cheeseman, K. E. Laidig, K. B. Wiberg and C. Breneman, *J. Am. Chem. Soc.*, **112**, 6530 (1990).

# Chapter 6

## Solid State

### 6.1 Introduction

The aim of the work in this chapter was to find out how the molecules move and interact in the solid state. The dye is applied in solution, so information in this state is necessary to help stop clogging of print heads etc., but it dries on the substrate, where it is viewed, so information in this state is also important. A brief introduction to solid-state NMR is given in chapter 1, section 1.3.

Before discussing the spectra obtained, some information about the techniques used in this chapter will be mentioned.

#### *6.1.1 Experimental Techniques*

##### **Cross Polarisation**

To record  $^{13}\text{C}$  and  $^{15}\text{N}$  solid-state spectra, cross polarisation from protons is used. The set-up procedure used for this is outlined in chapter 2, section 2.1.3. The pulse sequence used for simple  $^{13}\text{C}$  and  $^{15}\text{N}$  spectra is shown in Figure 1. This consists of

cross polarisation for a time,  $ct$  (contact time), and acquisition (with proton decoupling), followed by flip back of the proton magnetisation.

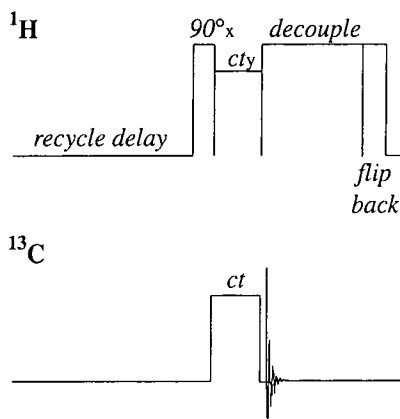


Figure 1: Cross polarisation pulse sequence with proton magnetisation flip back.

### Dipolar Dephasing

There are various spectral editing methods. The one used here is non-quaternary suppression (NQS), sometimes called dipolar dephasing. The pulse sequence used for this is shown in Figure 2.

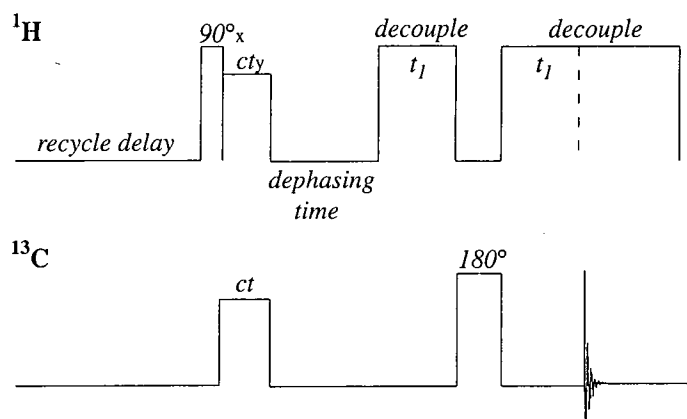


Figure 2: Non-quaternary suppression pulse sequence.

After the contact time there is a decoupling window of some tens of  $\mu\text{s}$  duration. During this time there is transverse relaxation of the  $^{13}\text{C}$  magnetisation. CH and  $\text{CH}_2$  groups are influenced by strong dipolar coupling interactions so their relaxation is fast.

Quaternary carbons, in contrast, have weak dipolar coupling, as there are no directly bonded protons, leading to slow relaxation. Although CH<sub>3</sub> groups have very strong dipolar coupling, rapid rotation often occurs which has the effect of slowing down the carbon relaxation by averaging the dipolar interactions to reduced values. These different relaxation times can be utilised to remove signals originating from CH and CH<sub>2</sub> carbons by increasing the dephasing time to a value large enough to allow CH and CH<sub>2</sub> carbon transverse magnetisation to decay, therefore leaving only quaternary and CH<sub>3</sub> carbon peaks in the spectrum.

## Nitrogen

Nitrogen would be a useful probe to examine molecular properties due to the many nitrogen atoms contained in the molecules. Nitrogen-14 is a quadrupolar nucleus with a spin of 1, meaning spectra are usually too broad to be observed. It is possible to record <sup>15</sup>N spectra, however, as this has a spin of ½. Nitrogen-15 has a low natural abundance, 0.37%, making obtaining spectra very time consuming. It is possible to enrich samples but this is expensive.

## Shielding Anisotropy and Asymmetry Measurements

Static powder patterns and spinning sideband manifolds both contain information about the shielding anisotropy and asymmetry so in principle both can be used to obtain this information. The method of choice will depend on the individual spectra. Static powder patterns take longer to acquire due to the distribution of intensity and if the spectrum contains a lot of sites, overlap may be a problem. Sidebands often result in complex spectra if more than one site is involved but by comparing spectra at a range of spinning speeds, the individual manifolds can usually be extracted (the isotropic shift does not change frequency when the spin rate is varied). If the anisotropy is small, sidebands may only be visible at very low spinning speeds. These low spinning speeds can be difficult to achieve due to their instability. A smooth drive tip or a restrictor on the air supply may be required.

To analyse spinning sidebands, an ‘in house’ program called *ssb97* was used.<sup>1</sup> This is based on the theory by Maricq and Waugh<sup>2</sup> and includes statistical error analysis.<sup>3</sup> For determination of anisotropy and asymmetry using static powder patterns, an ‘in house’ program called ‘*fitstatic*’ was used.<sup>4</sup>

The definitions of shielding anisotropy and asymmetry that are used herein are given below:

$$\xi = \sigma_{33} - \sigma_{iso}$$

$$\eta = \frac{\sigma_{22} - \sigma_{11}}{\sigma_{33} - \sigma_{iso}}$$

where  $\sigma_{iso}$  is the isotropic shielding value and  $\sigma_{11}$ ,  $\sigma_{22}$  and  $\sigma_{33}$  are the shielding components, defined such that:

$$|\sigma_{33} - \sigma_{iso}| \geq |\sigma_{11} - \sigma_{iso}| \geq |\sigma_{22} - \sigma_{iso}|$$

$T_{1\rho}$

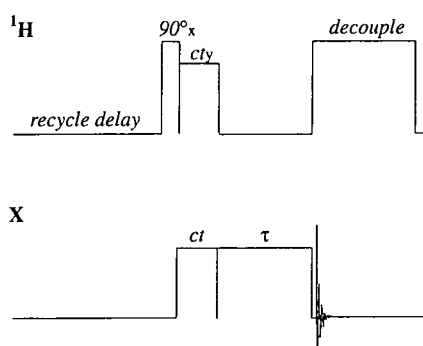


Figure 3: Pulse sequence for the measurement of  $T_{1\rho}$  for nucleus X.

$T_{1\rho}$  values have been measured using the pulse sequence shown in Figure 3. This involves cross polarisation from  $^1\text{H}$  to  $^{15}\text{N}$ . The  $^{15}\text{N}$  magnetisation is then spin locked for a variable time,  $\tau$ . During this time the  $^{15}\text{N}$  magnetisation will decay according to  $T_{1\rho}$ . The  $^{15}\text{N}$  FID is then recorded with proton decoupling.  $T_{1\rho}$  values can be calculated using the equation:

$$\text{Intensity} = \text{Amplitude} * \exp\left(\frac{-\tau}{T_{1\rho}}\right)$$

where  $T_p$  is the spin-lattice relaxation time in the rotating frame, *Intensity* is the intensity of the relevant peak in the spectrum and *Amplitude* is a scaling factor.

As with all arrayed spectra it is important to randomise the  $\tau$  periods to ensure that spectrometer drift contributes to a random rather than a systematic error.

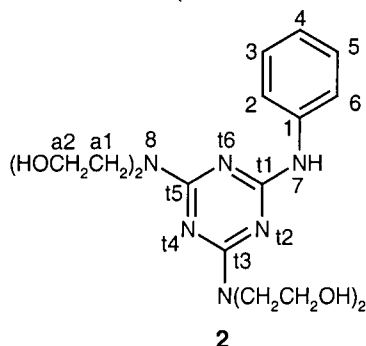
## 6.2 Results and Discussion

This section will first discuss the compounds that were made as simple model compounds for the dyes in which internal rotation was observed. Their solid-state chemical shift information will be compared to the solution-state data described in chapter 4, section 4.6. The more complex dyes themselves will then be discussed in section 6.2.2.

### 6.2.1 Simplified Compounds

Carbon-13 and  $^{15}\text{N}$  CPMAS spectra were obtained for compounds **2**, **3** and **5**. Information about the asymmetric unit can be deduced and chemical shifts can be assigned and compared with solution-state information.

## Compound 2



The  $^{13}\text{C}\{^1\text{H}\}$  full and NQS spectra of compound **2** are shown in Figure 4.

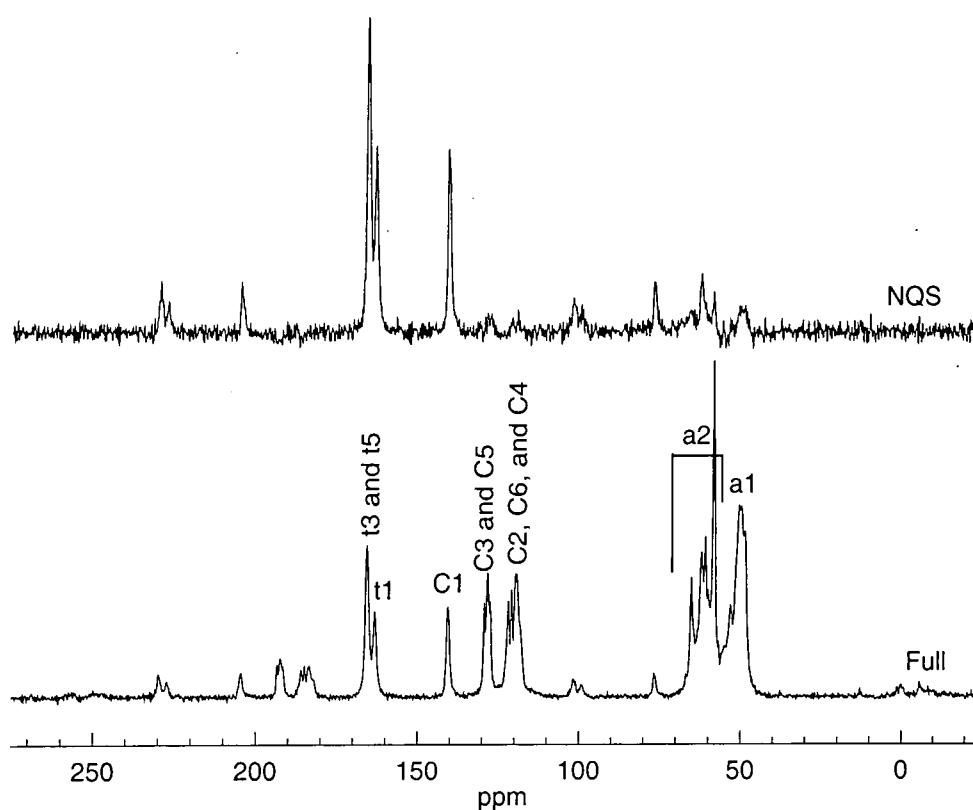


Figure 4: Solid-state  $^{13}\text{C}\{^1\text{H}\}$  full and NQS spectra of compound **2** recorded on a Varian 300 spectrometer. Full spectrum: Used a recycle delay of 3 s, contact time of 1 ms, 240 acquisitions, proton decoupling power of 60 kHz and spin rate of 3.87 kHz. NQS spectrum: Used a recycle delay of 3 s, contact time of 1 ms, 192 acquisitions, proton decoupling power of 60 kHz, spin rate of 4.80 kHz and dephasing time of 40  $\mu$  s.

The assignment of t3 and t5 to the approximately double intensity peak at 165.7 ppm seems to be the most likely situation as the local chemical environment around t3 is similar to that of t5 with t1 being different.

The peaks from the carbons directly bonded to nitrogen atoms are broader than the signals from carbons further away from nitrogen i.e. C1, t1, t3, t5 and a1. This is due to residual dipolar coupling (RDC).<sup>5</sup> This is where second-order quadrupolar effects are transferred to spin-1/2 nuclei by dipolar interactions, resulting in an asymmetric lineshape when the quadrupolar interaction is comparable in size to the Zeeman interaction. This phenomenon prevents complete narrowing of the dipolar broadening by MAS but the magnitude of the residual coupling is inversely dependent upon the magnetic field strength. As the mechanism for the transfer of quadrupolar effects is dipolar coupling, proportional to inter-nuclear distance, residual dipolar coupling also depends on inter-nuclear distance rather than chemical bonding.

There are at least three signals from the carbons ‘meta’ to the NHTr on the phenyl ring (C3 and C5). There may be more, some of which cannot be resolved. C3 and C5 are not chemically equivalent. There are two explanations for this part of the spectrum:

- 1) The three signals may be due to three molecules in the asymmetric unit, with C3 and C5 being indistinguishable.
- 2) C3 and C5 may be observed independently producing only two signals, but if there are two molecules in the asymmetric unit, at least one of C3 and C5 would be expected to give rise to two signals leading to at least three observable signals. There may be two signals from both C3 and C5 but with some accidental degeneracy.

In both the above cases there is more than one molecule in the asymmetric unit.

There are at least four peaks from C2, C4 and C6. There are two possible combinations of peaks: Two peaks from C4 and two peaks from C2 and C6 together (the ortho peaks), or one peak from C4 leaving three from C2 and C6. With this combination there are the same possibilities for the ortho peaks (C2 and C6) as there were for the meta signals described above. This therefore seems to be the more likely explanation given the appearance of the C3 and C5 signals. Also, changes in the asymmetric unit are likely to affect C2, C3, C5 and C6 more than C4, as neither rotation of the phenyl ring, or different environments of the side chains, will have as much effect on C4 as on the other phenyl carbons.

There are many peaks from the aliphatic carbons, making it difficult to obtain any conclusive information. Due to the number of peaks present it is likely that either the four side chains are in different environments, and or there is more than one molecule in the asymmetric unit.

The solid-state, natural abundance  $^{15}\text{N}\{^1\text{H}\}$  full and NQS spectra for compound **2** are shown in Figure 5.

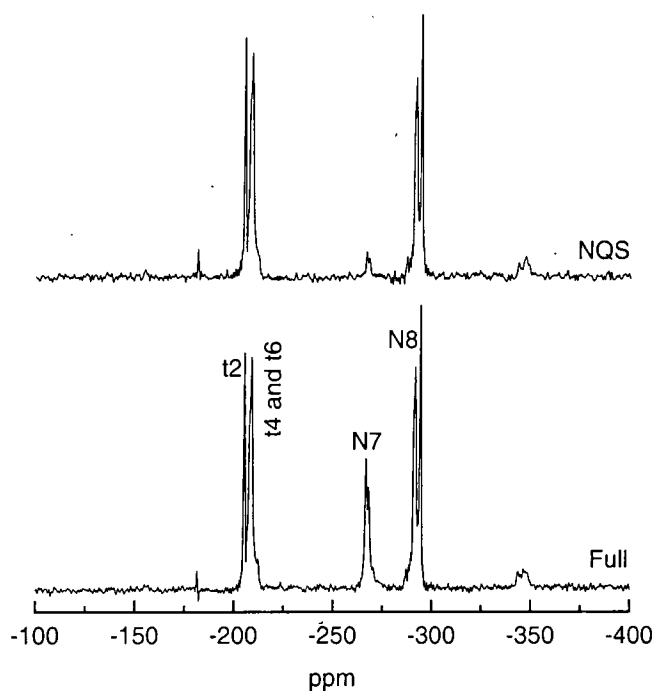


Figure 5: Solid-state  $^{15}\text{N}\{^1\text{H}\}$  full and NQS spectra of compound **2** recorded on a Varian 300 spectrometer, both using: A recycle delay of 3 s, contact time of 5 ms, 28896 acquisitions, proton decoupling power of 60 kHz and spin rate of 4.30 kHz and the NQS spectrum used a dephasing time of 200  $\mu$  s.

Assignment of the triazine nitrogen signals is uncertain but it has been shown using molecular modelling calculations by Julian Cherryman to be as indicated in Figure 5.

Two peaks are observed for N8. The two sides of the molecule are therefore different or the two sides are indistinguishable and the appearance of the spectrum is due to the presence of two molecules in the asymmetric unit. N7 gives rise to two peaks, which is consistent with there being two molecules in the asymmetric unit as suspected from observation of the  $^{13}\text{C}$  spectrum.

The solid- and solution-state  $^{15}\text{N}$  and  $^{13}\text{C}$  data for compound **2** are summarised in Table 1 and Table 2 respectively.

	$^{13}\text{C}$ chemical shift / ppm	
	$d_7$ -DMF solution	Solid
t1	164.83	163.1
t3 t5	165.86	165.7
C1	141.87	140.7
C2 C6	119.88	119.7 119.2
C3, C5	129.04	129.3 128.3 127.4
C4	121.77	121.9 120.8
a1	51.81 51.72	55.0 53.1 50.4 49.7 48.7
a2	60.81 60.78	65.1 62.0 60.9 60.0 58.2

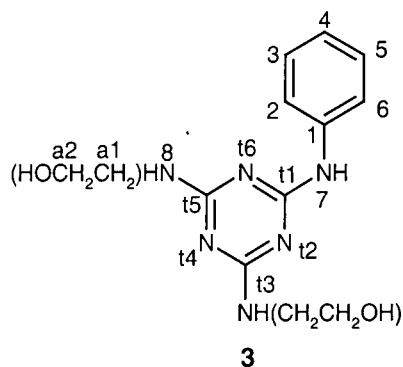
Table 2:  $^{13}\text{C}$  chemical shift information for compound **2** at ambient temperature.

	$^{15}\text{N}$ chemical shift / ppm	
	DMSO solution	Solid
t2	-206.25	-205.1
t4 t6	-206.68	-208.8
N7	-270.01	-266.7 -268.0
N8	-291.99	-291.7 -294.3

Table 1:  $^{15}\text{N}$  chemical shift information for compound **2** at ambient temperature.

Generally, solution- and solid-state chemical shifts differ by less than 2 ppm. These small variations can be attributed to changes in the local environment of the nucleus produced by changes in state. Larger differences suggest that there may be more significant effects in the environment of that nucleus brought about by changes in state such as intermolecular hydrogen bonding or stacking of aromatic rings in the solid.

## Compound 3



The  $^{13}\text{C}\{^1\text{H}\}$  full and NQS spectra of compound **3** are shown in Figure 6.

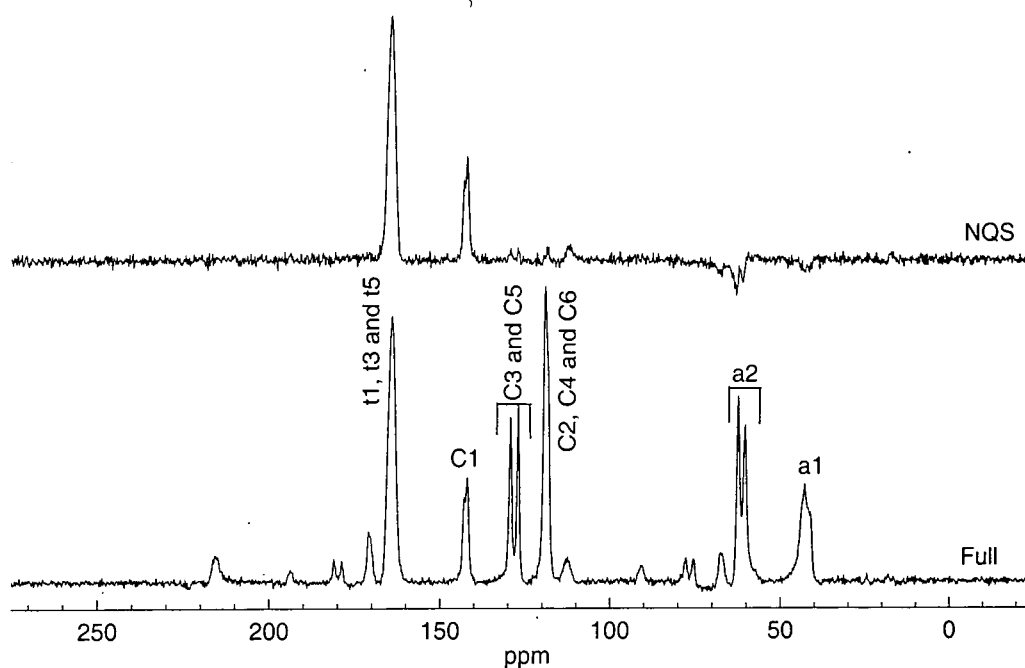
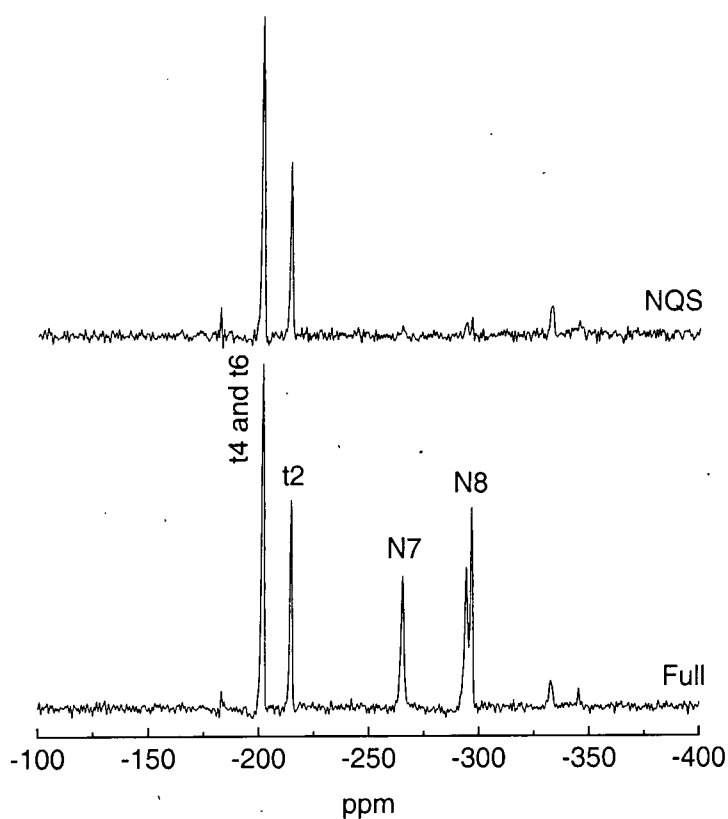


Figure 6: Solid-state  $^{13}\text{C}\{^1\text{H}\}$  full and NQS spectra of compound **3** recorded on a Varian 300 spectrometer. Full spectrum: Used a recycle delay of 5 s, contact time of 1 ms, 160 acquisitions, proton decoupling power of 60 kHz and spin rate of 4.00 kHz. NQS spectrum: Used a recycle delay of 5 s, contact time of 1 ms, 144 acquisitions, proton decoupling power of 60 kHz, spin rate of 3.87 kHz and a dephasing time of 40  $\mu\text{s}$

As with compound **2**, the carbons adjacent to nitrogen give rise to broad peaks. The triazine ring carbons cannot be distinguished; neither can C2, C4 and C6. There are two signals for the 'meta' carbons in the phenyl ring and two signals for the a2 carbons. The a1 carbon signal is also broad, suggesting more than one peak is present, but these

cannot be resolved because of broadening due to residual dipolar coupling. This suggests that the two sides of the molecule have different environments, or the two sides of the molecule are indistinguishable and there are at least two molecules in the asymmetric unit. It would be more likely that the doubling up of peaks is due to the two sides of the molecule with only one molecule in the asymmetric unit.

The solid-state, natural abundance  $^{15}\text{N}\{^1\text{H}\}$  full and NQS spectra for compound **3** are shown in Figure 7.



*Figure 7: Solid-state  $^{15}\text{N}\{^1\text{H}\}$  full and NQS spectra of compound **3** recorded on a Varian 300 spectrometer, both using: A recycle delay of 5 s, contact time of 20 ms, 5320 acquisitions, proton decoupling power of 60 kHz, spin rate of 4.00 kHz and the NQS spectrum uses a dephasing time of 200  $\mu$  s.*

As with compound **2**, the triazine peaks are assigned with reference to molecular modelling calculations by Julian Cherryman.

Two peaks are present for N8, consistent with the observations from the  $^{13}\text{C}$  spectrum where a2 gives rise to two peaks. N7 exhibits one peak suggesting there is only one molecule in the asymmetric unit as suspected.

The solid and solution-state  $^{15}\text{N}$  and  $^{13}\text{C}$  data for compound **3** are summarised in Table 3 and Table 4 respectively.

	$^{13}\text{C}$ chemical shift / ppm	
	DMF solution	Solid
t1	165.15	164.3
t3 t5	166.90	
C1	141.84	142.1
C2 C6	120.07	119.4
C3 C5	128.94	129.4
		127.1
C4	121.79	119.2
a1	43.92	43.0
a2	61.61 61.51	62.4 60.5

Table 4:  $^{13}\text{C}$  chemical shift information for compound **3** at ambient temperature.

	$^{15}\text{N}$ chemical shift / ppm	
	DMSO solution	Solid
t2	-204.10	-201.7
t4 t6		-214.2
N7	-271.30	-256.2
N8	-294.59	-294.1
		-296.5

Table 3:  $^{15}\text{N}$  chemical shift information for compound **3** at ambient temperature.

The C4 solid-state signal can be observed to change shift by 2.5 ppm compared to the solution-state shift. This carbon is at the ‘edge’ of the molecule so may be influenced more than other carbons present by molecular packing.

Powder X-ray diffraction (XRD) was used to look at this sample. The experiments were carried out and analysed by John Evans and his group using a Bruker D8 Avance X-ray diffractometer operating at 40 kV and 40 mA in capillary mode (0.5 mm capillary). The diffractometer used a Cu K- $\alpha$  radiation source with a germanium (111) monochromator adjusted to select only the  $\alpha_1$  radiation (wavelength of 1.540598 Å).

Data were collected from 3 to 65° in 2 $\theta$ , with a step size of 0.014° and a total measuring time of 48 hours. The spectrum was indexed using the Visser auto-indexing program.<sup>6</sup>

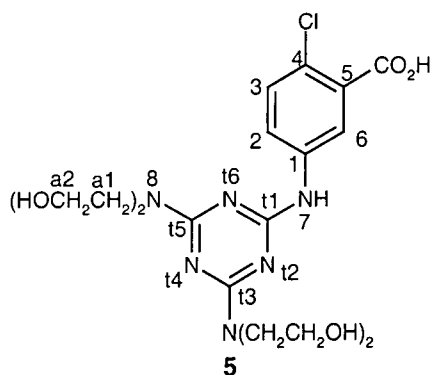
Indexing found compound **3** to be triclinic with cell parameters:

$a = 9.0008(4) \text{ \AA}$ ,  $b = 9.8955(4) \text{ \AA}$ ,  $c = 8.3450(3) \text{ \AA}$ ,  $\alpha = 91.522(2)^\circ$ ,  $\beta = 110.468(3)^\circ$  and  $\gamma = 87.000(2)^\circ$  with a cell volume of 695.18  $\text{\AA}^3$ .

The molecular volume was calculated using Cerius2 which uses the Van der Waals radius for each atom. This calculated a value of  $269.2 \pm 3.7 \text{ \AA}^3$ . If there are two molecules in the unit cell with a cell volume of 695.18  $\text{\AA}^3$  then the packing fraction is 0.77. A value between 0.6 and 0.8 is usual, so this supports the claim that there are two molecules in the unit cell. In conjunction with NMR observations, that there is one molecule in the asymmetric unit, this suggests the space group is  $P\bar{1}$ , with two molecules in the unit cell, related by an inversion centre.

Attempts at solution of the powder pattern by simulated annealing are in progress. Preliminary results show that an excellent agreement to experimental data can be obtained with a model in which the two aromatic rings are essentially coplanar, consistent with molecular modelling data in chapter 5.

## Compound 5



The solid-state  $^{13}\text{C}\{^1\text{H}\}$  full and NQS spectra for compound **5** are shown in Figure 8.

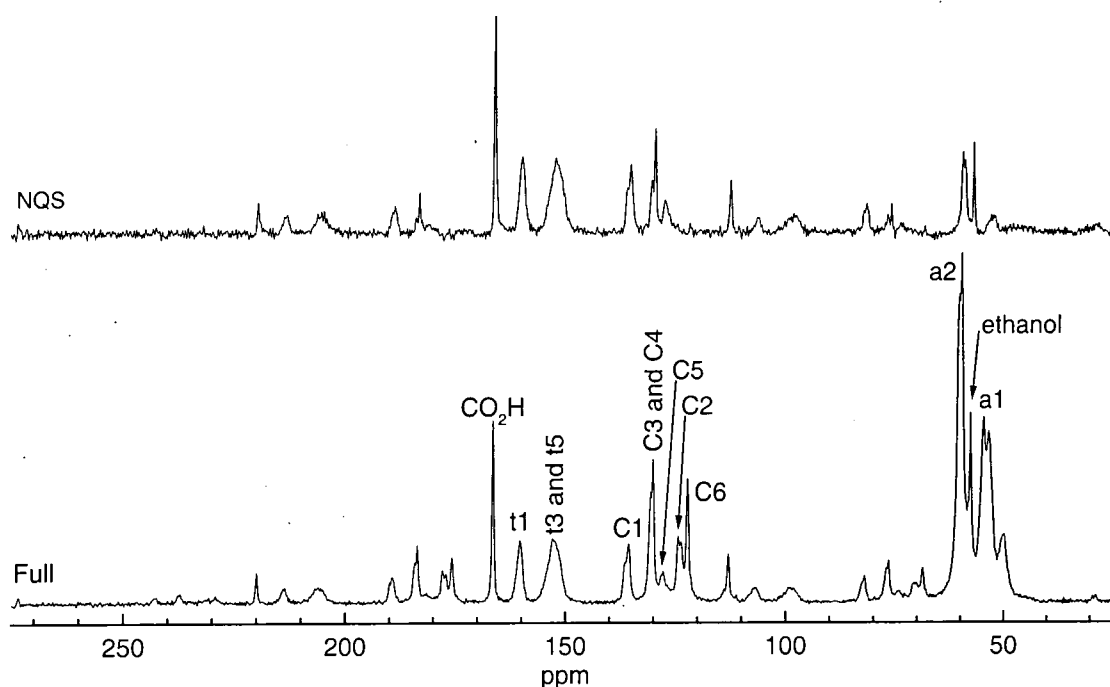


Figure 8: Solid-state  $^{13}\text{C}\{^1\text{H}\}$  full and NQS spectra of compound **5** recorded on a Varian 300 spectrometer. Full spectrum: Used a recycle delay of 2 s, contact time of 1 ms, 624 acquisitions, proton decoupling power of 60 kHz and spin rate of 4.00 kHz. NQS spectrum: Used a recycle delay of 2 s, contact time of 1 ms, 336 acquisitions, proton decoupling power of 60 kHz, spin rate of 4.00 kHz and a dephasing time of 200  $\mu\text{s}$

The signal for C1 has a slight asymmetric lineshape, characteristic of RDC. A doublet structure would be expected for C4 due to the presence of Cl but it is difficult to distinguish as there are two overlapping peaks.<sup>7</sup> It appears that all the aryl carbons are single peaks, suggesting there is only one molecule in the asymmetric unit. The aliphatic peaks show structure, but as with the other compounds it is not clear how many peaks are actually present. The a1 region is broad, again due to RDC. Up to four signals would be expected in principle if one molecule is present in the asymmetric unit.

No solution-state  $^{15}\text{N}$  spectrum was obtained. The solid-state, natural abundance  $^{15}\text{N}\{^1\text{H}\}$  full and NQS spectra for compound **5** are shown in Figure 9.

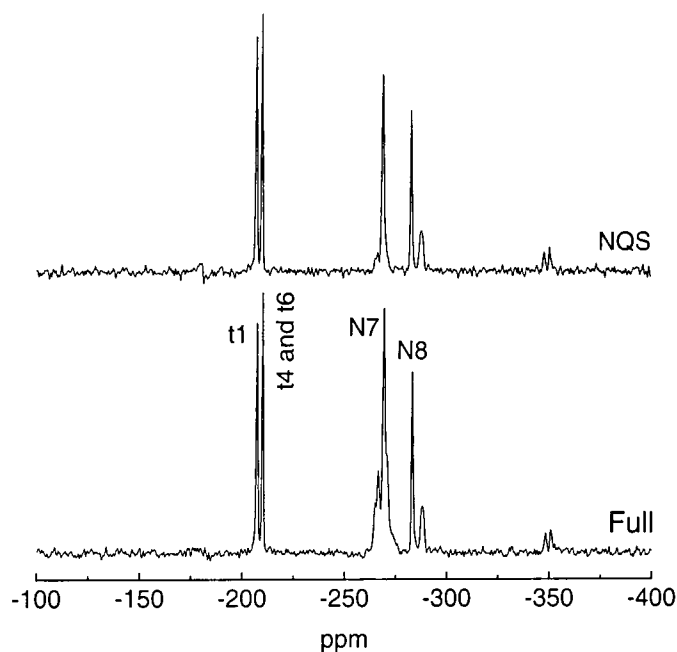


Figure 9: Solid-state  $^{15}\text{N}\{^1\text{H}\}$  full and NQS spectra of compound **5** recorded on a Varian 300 spectrometer, both using: A recycle delay of 2 s, contact time of 10 ms, 34176 acquisitions, proton decoupling power of 60 kHz, spin rate of 4.25 kHz and the NQS spectrum used a dephasing time of 200  $\mu$  s.

The  $^{15}\text{N}$  spectrum is more complex than expected and is not fully understood. Again the triazine nitrogens are tentatively assigned by molecular modelling calculations. The origin of the peak to low frequency of the N8 peak is not known. It does not appear to be due to a different magnetic environment of N8 and is likely to be an impurity. The structure apparent on the N7 peak is also not understood.

The solid-state  $^{15}\text{N}$  and solid and solution-state  $^{13}\text{C}$  data for compound **5** are summarised in Table 5 and Table 6 respectively.

	<sup>13</sup> C chemical shift / ppm	
	DMF solution	Solid
CO <sub>2</sub> H	166.99	166.5
t1	155.8b	160.4
t3, t5		152.9
C1	137.47	135.6
C2	124.33	124.4
C3	132.23	130.1
C4	132.37	130.1
C5	127.59	127.8
C6	123.02	122.2
a1	52.64	53.5
		49.9
a2	60.33	59.8
		54.7

*Table 6: <sup>13</sup>C chemical shift information for compound 5 at ambient temperature.*

	<sup>15</sup> N chemical shift / ppm
	Solid
t2	-207.3
t4, t6	-210.0
N7	-264.9
	-266.5
	-269.2
N8	-270.6
	-283.1
	-287.8

*Table 5: <sup>15</sup>N chemical shift information for compound 5 at ambient temperature.*

## 6.2.2 The Dyes Themselves

### Carbon-13

Carbon-13 solid-state spectra of many of the dyes introduced in chapter 1 were recorded. An example spectrum (for compound **9**) is the bottom one in Figure 10. It can be seen that all the peaks are broad. NQS, the middle spectrum in Figure 10, although simplifying the spectrum, does not allow unambiguous assignment, even when directly compared to the solution-state spectrum, shown at the top in Figure 10.

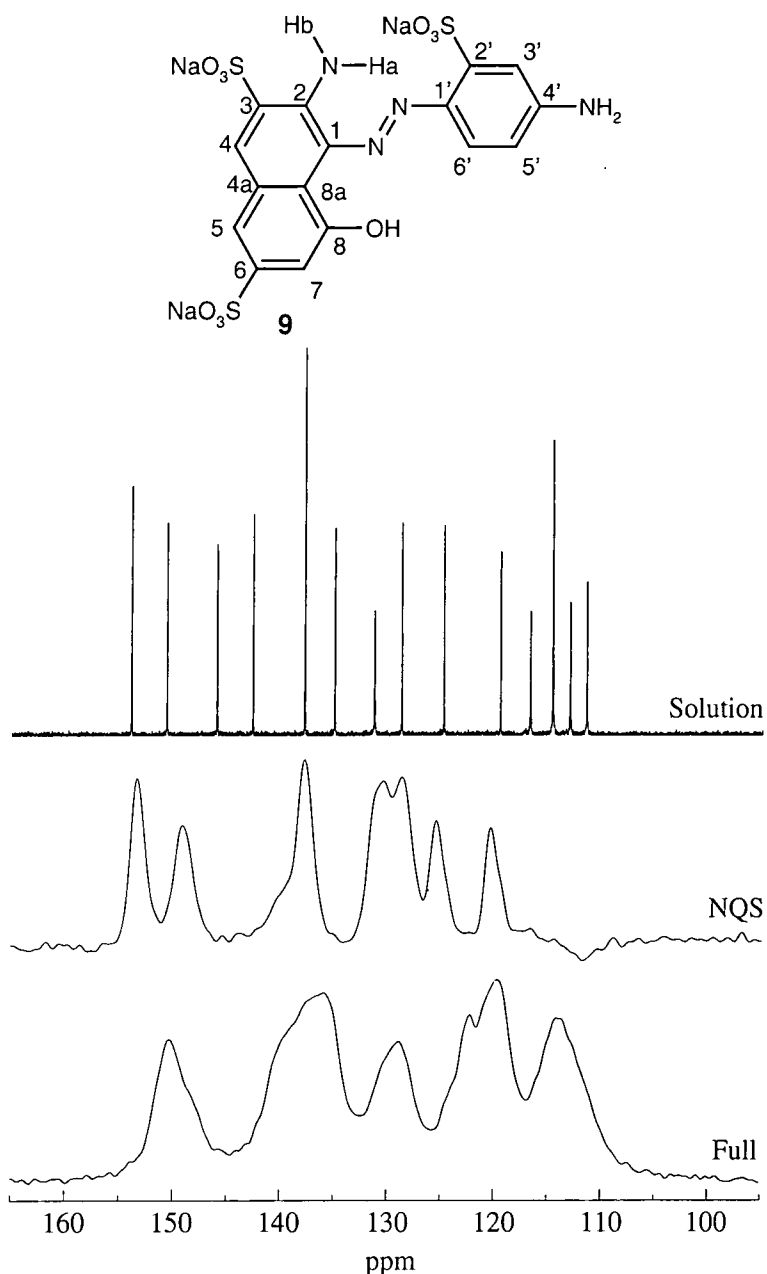


Figure 10: Carbon-13 solid-state spectrum of compound **9**. Top: Solution-state  $^{13}\text{C}\{^1\text{H}\}$  spectrum in  $d_6$ -DMSO. Middle: NQS. Bottom: Full  $^{13}\text{C}$ . Solid-state spectra were recorded on a CMX 200 spectrometer with a recycle delay of 5 s, contact time of 1 ms, decoupling power of 50 kHz, spin rate of 5.00 kHz, 1500 acquisitions and the NQS used a dephasing time of 50  $\mu$  s. The solution-state spectrum was recorded on a Bruker AMX 400 spectrometer with a pulse delay of 2 s and 5.5  $\mu$  s  $90^\circ$  pulse duration.

There are two reasons for the broadness of the spectra. The first is that there is a lot of nitrogen in these compounds leading to broadening of neighbouring carbon peaks due to residual dipolar coupling. This effect can be reduced by increasing the spectrometer field. Spectra recorded at 50.32, 75.43 and 150.92 MHz are compared in Figure 11.

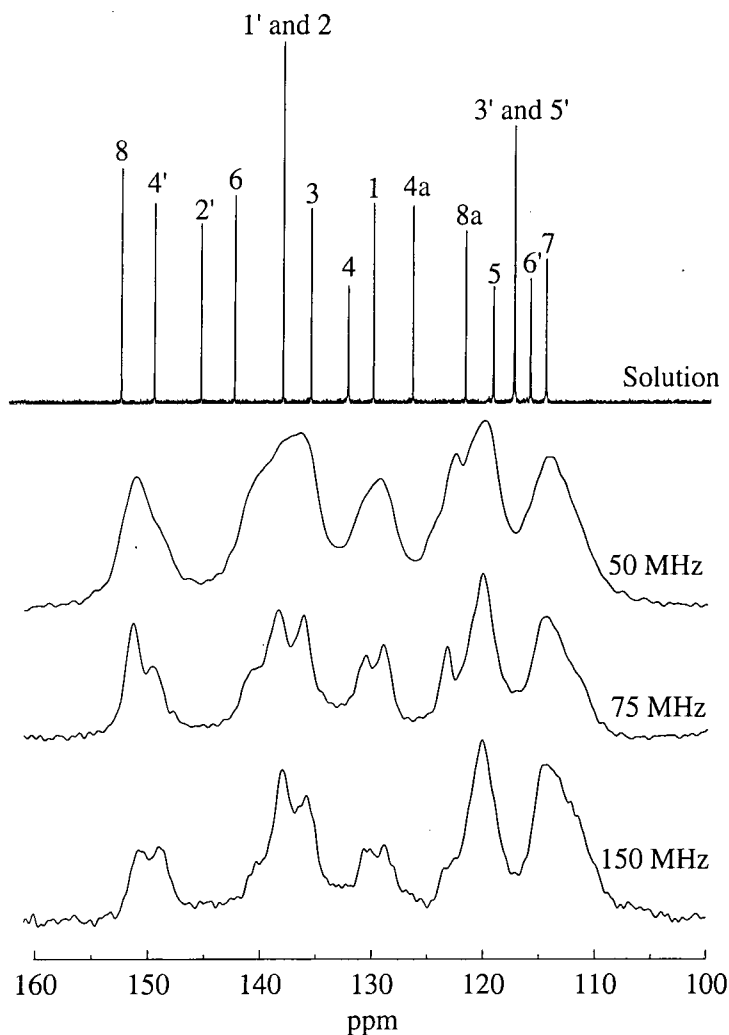
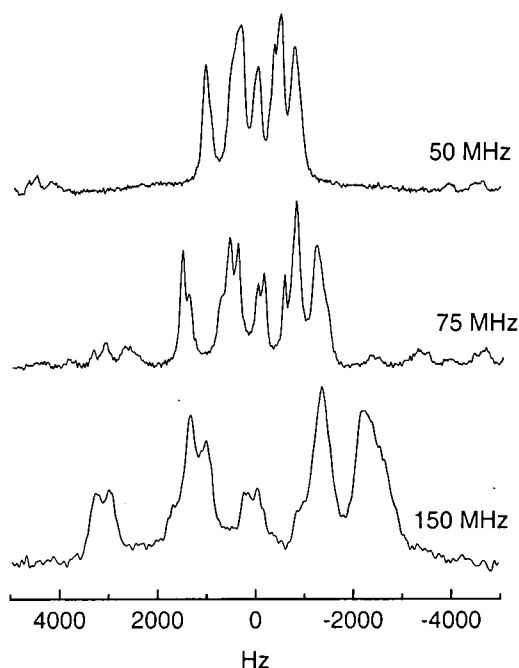


Figure 11: Carbon-13 spectra of compound **9**. Top: Solution-state spectrum in  $d_6$ -DMSO recorded on a Bruker AMX 400 spectrometer with a pulse delay of 2 s and  $5.5 \mu s$   $90^\circ$  pulse duration. Second: Solid-state spectrum recorded on a CMX 200 spectrometer using a recycle delay of 5 s, contact time of 1 ms, 1500 acquisitions, proton decoupling power of 50 kHz and spin rate of 5.00 kHz. Third: Solid-state spectrum recorded on a Varian 300 spectrometer using a recycle delay of 1 s, contact time of 1 ms, 5000 acquisitions, proton decoupling power of 60 kHz and spin rate of 4.00 kHz. Bottom: Solid-state spectrum recorded on a CMX 600 Infinity spectrometer by Alessia Portieri using a recycle delay of 10 s, contact time of 1 ms, 3008 acquisitions, proton decoupling power of 125 kHz and spin rate of 9.60 kHz.

Increasing the spectrometer field increases the spectral resolution because as well as reducing residual dipolar coupling, at 150.92 MHz there are three times as many Hz per ppm as at 50.43 MHz. If the main cause of the broadness is the amorphous nature of the sample, the improvement in resolution may not be enough to allow the observation of each peak independently as the range, in ppm, occupied by each peak will be the same.

The spectra at the three different fields are compared in Hz in Figure 12 to help understand the origin of the broadness.



*Figure 12: Solid-state  $^{13}\text{C}$  spectra of compound 9. Top: recorded on a CMX 200 spectrometer using a recycle delay of 5 s, contact time of 1 ms, 1500 acquisitions, proton decoupling power of 50 kHz and spin rate of 5.00 kHz. Middle: Recorded on a Varian 300 spectrometer using a recycle delay of 1 s, contact time of 1 ms, 1500 acquisitions, proton decoupling power of 60 kHz and a spin rate of 4.00 kHz. Bottom: Recorded on a CMX 600 Infinity spectrometer by Alessia Portieri using a recycle delay of 10 s, contact time of 1 ms, 3008 acquisitions, proton decoupling power of 125 kHz and a spin rate of 9.60 kHz.*

Increasing the spectrometer field does lead to increased resolution, but the spectrum is still far from well-resolved (none of the peaks are due to single carbons so it is not appropriate to compare linewidths at the different fields). This suggests that the major factor causing the large linewidths is the amorphous nature of the sample, but there is certainly a contribution from residual dipolar coupling. The compounds were designed to be amorphous and powder X-ray diffraction confirms this as no sharp reflections were observed.

The assignments, as far as they can be made, are shown in Table 7.

Carbon number	$^{13}\text{C}$ chemical shift / ppm	
	Solution in $d_6$ -DMSO <sup>a</sup>	Solid <sup>b</sup>
1	128.77	128.8
2	137.81	138.0
3	135.01	135.8
4	131.31	130.6
4a	124.84	125.4 <sup>c</sup>
5	116.75	120.1 or 114.6
6	142.64	149.0 or 138.0
7	111.49	114.6
8	153.93	153.1 <sup>c</sup>
8a	119.55	120.2 <sup>c</sup>
1'	137.81	138.0
2'	145.98	150.7 or 149.0
3'	114.66	114.6
4'	150.63	148.8 <sup>c</sup>
5'	114.66	114.6
6'	113.05	114.6

<sup>a</sup> The solution-state shifts quoted were recorded at 100.63 MHz.

<sup>b</sup> The solid-state shifts quoted are those recorded at 150.92 MHz except those in <sup>c</sup>. They are not necessarily the exact solid-state frequency of that carbon, they are the peaks, under which, it is thought, that the carbon signal in question lies.

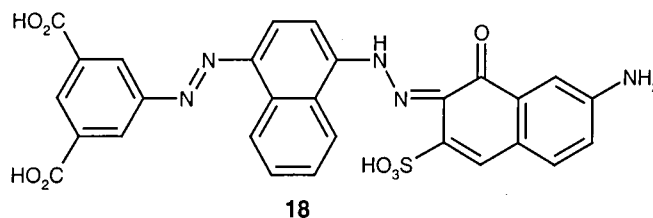
<sup>c</sup> Determined from the NQS spectrum recorded at 50.32 MHz.

*Table 7: Comparison of solution and solid-state  $^{13}\text{C}$  chemical shifts of compound 9.*

There are still many ambiguities in the assignment of the solid-state spectrum. In many cases the chemical shift of the envelope covering several carbon signals has been measured, rather than the individual shifts themselves, meaning that detailed information about the molecules in the solid state is not readily available.

Variable-temperature studies were carried out to see if the rate effects observed in solution, that were discussed in chapter 4, could be seen in the solid state, but no changes to the  $^{13}\text{C}$  spectrum could be observed. This does not mean that exchange is not occurring, but rather that its effects cannot be detected, probably due to the broadness of the signals.

The aim of the work described in this chapter was to deduce the conformation of the dyes studied in the solid state. It would be ideal to investigate their behaviour when sprayed onto a substrate, a more comparable situation to their intended use. An attempt was made to do this by spraying a 5 % by weight solution of compound **18** in water at pH 10, thinly onto silica-coated tlc plates. Once dried the dye-coated silica was scraped off the plastic backing and packed into a rotor until full.



Spectra were recorded of the dye itself, the dye coated silica and the silica only i.e. the background. These spectra are compared in Figure 13.

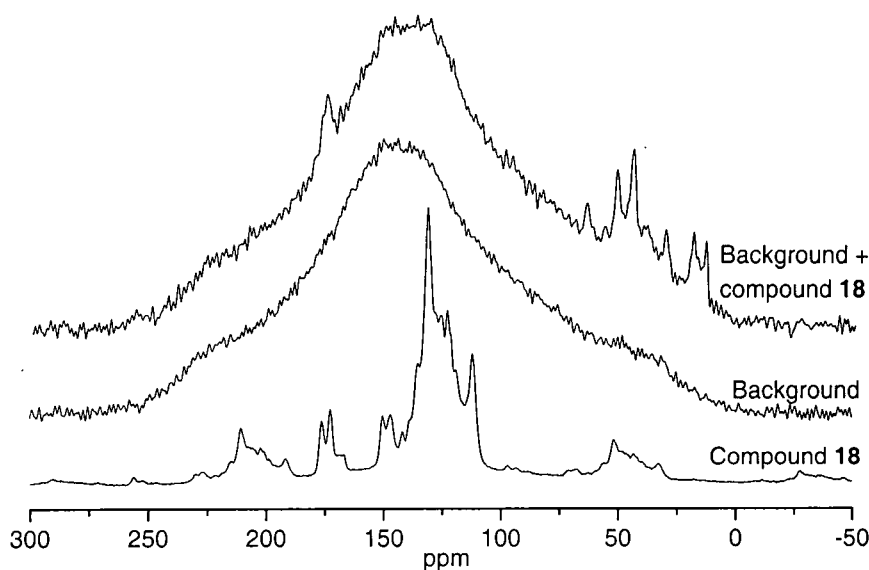


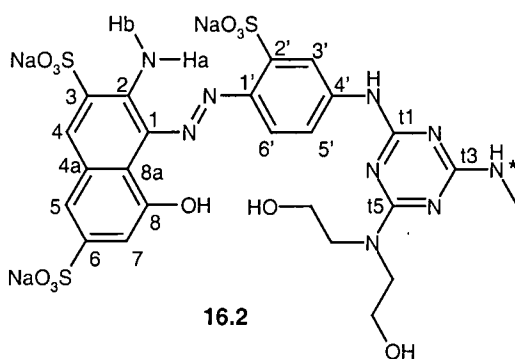
*Figure 13: Solid-state  $^{13}\text{C}$  spectra of compound **18** recorded on a CMX 200 spectrometer using a recycle delay of 5 s, contact time of 1 ms, proton decoupling power of 50 kHz and a spin rate of 4.00 kHz. Top and middle: 15812 acquisitions. Bottom: 20668 acquisitions.*

The signals originating from the dye are obscured by a large background, which is due to the very small amount of dye present. Although the rotor was full, the majority of the sample is composed of the silica substrate. Background suppression techniques could

be attempted to try to improve the spectrum but as yet these have not been carried out. In any case, signals in the aliphatic region are clearly wrong as there are no aliphatic carbons present in the sample.

### Nitrogen-15

Compound **16.2** is  $^{15}\text{N}$ -enriched in the position indicated with an asterisk shown below.



Having a  $^{15}\text{N}$  spectrum containing only one signal makes the observation of changes in the spectrum, if present, more straightforward. The peak is still fairly broad, 150 Hz at 20.28 MHz, spinning at 5 kHz. This broadness is probably due to the sample being amorphous as previously discovered. The powder pattern and spinning sideband manifold at different spinning speeds have been recorded as shown in Figure 14.

To determine the shielding anisotropy and asymmetry, the static lineshape or the sideband manifold may be used, as explained in section 6.1.1. The sets of values obtained using these different data are shown in Table 8.

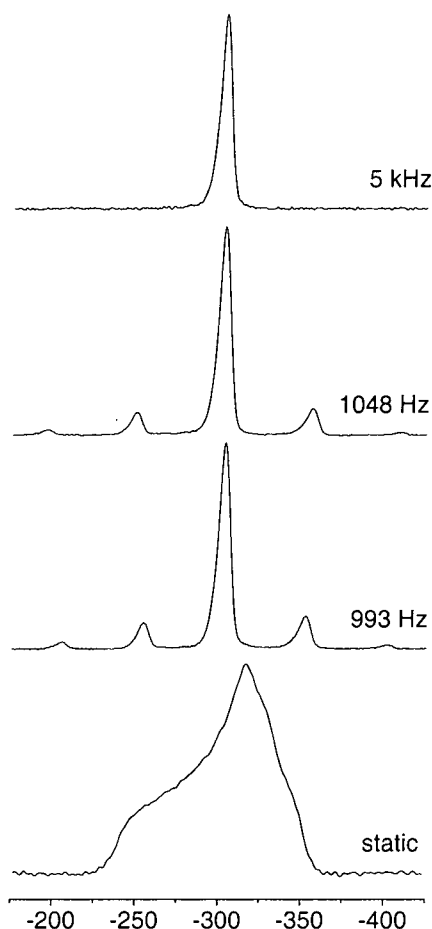


Figure 14: Static and spinning CPMAS  $^{15}\text{N}$  spectra of compound **16.2** on a CMX 200 spectrometer. Spinning speeds are as shown in the figure. All used a contact time of 1 ms, a recycle delay of 5 s and a decoupling field of 50 kHz. Top: 1036 acquisitions, second: 7200 acquisitions, third: 10080 acquisitions and bottom: 13584 acquisitions.

Spinning sideband analysis was repeated using different spin rates, using integration and peak height measurement to determine the intensities of the sidebands, and varying the number of sidebands included in the fitting. All methods provided adequate fits but the values quoted in Table 8 were believed to be the most reliable as they contained the most sidebands and appeared to be approximately the average of the other values obtained. These values used a spinning speed of 993 Hz.

The powder pattern fitting was also attempted several times using different initial starting values, estimates for the noise and number of points. The values quoted in Table 8 had the lowest  $\chi^2$  value and appeared to be consistent with the other fits produced.

	Shielding anisotropy (error) / ppm	Shielding asymmetry (error)	Linewidth / Hz
Static powder pattern fitting	-58	0.49	720
Spinning sideband fitting	-66 (0.5)	0.43 (0.009)	

Table 8: Shielding anisotropy and asymmetry values obtained for compound **16.2** using both static powder pattern lineshape and spinning sideband fitting.

The two sets of parameters outlined in Table 8 can be compared by calculating the powder pattern that would be obtained using the shielding anisotropy and asymmetry values that were found by fitting the spinning sideband manifold, and comparing it to the experimental and the fitted powder pattern. This comparison can be seen in Figure 15.

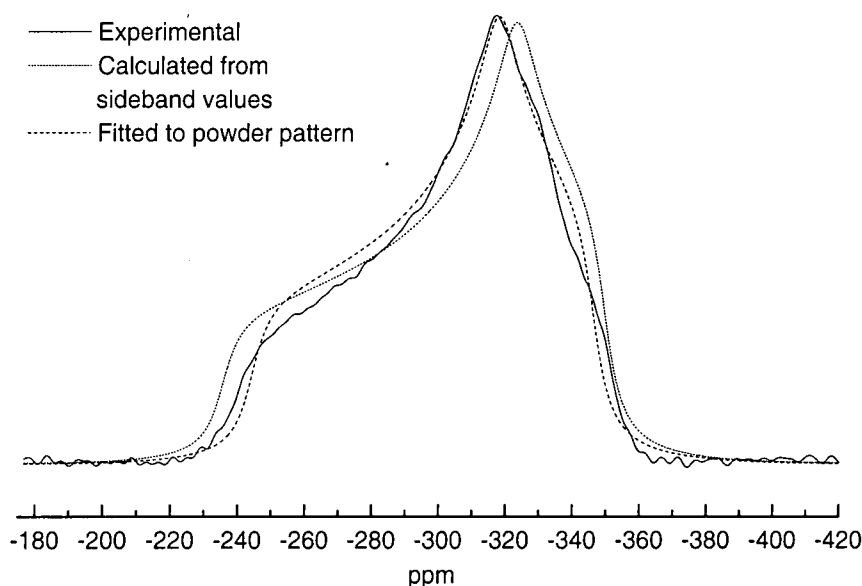
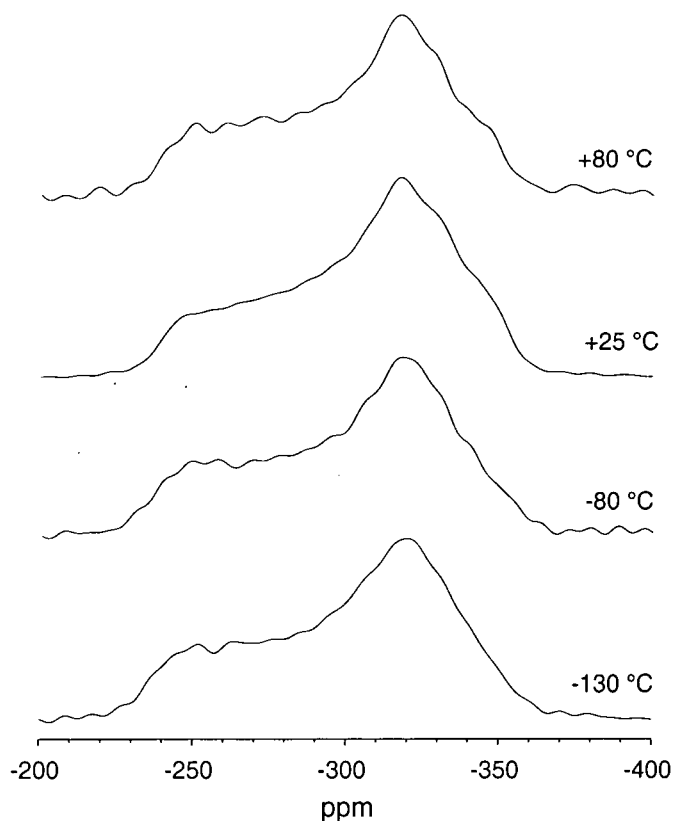


Figure 15: Experimental, fitted (iteratively to the experimental powder pattern) and simulated (using the values obtained by iteratively fitting the spinning sideband)  $^{15}\text{N}$  powder patterns for compound **16.2**. The experimental data were recorded on a CMX 200 spectrometer with a contact time of 1 ms, recycle delay of 5 s, decoupling field of 50 kHz and 13584 acquisitions.

It can be seen that neither fit particularly well to the experimental data but  $\sigma_{22}$  appears to be best obtained from the static spectrum. The value of the anisotropy calculated using the spinning sideband manifold appears to not fit the powder pattern well. Whereas the bandshape obtained by fitting the powder pattern does not fit the experimental data closely, it appears that the powder pattern bandshape is not ideal. It

was recorded several times, varying the cross polarisation condition, transmitter offset and power levels, but in all cases the result was the closely similar. The bandshape is not broad, 2600 Hz, so it is likely that the Hartmann-Hahn match will span the whole region required. Motion around the NHMe group may introduce complications in the fitting of the shielding anisotropy by both methods. The spectra were recorded at  $-130$  °C,  $-80$  °C,  $+25$  °C and  $+80$  °C, shown in Figure 16.



*Figure 16: Nitrogen-15 powder patterns of compound 16.2 recorded on a CMX 200 spectrometer. Temperatures are as shown in the figure. All spectra were recorded on a CMX 200 spectrometer with a contact time of 1 ms, recycle delay of 5 s, decoupling field of 50 kHz and 2004 acquisitions.*

The spectra shown in Figure 16 show no significant change in shape, implying that either the motion is fast at all temperatures, or motion is not occurring at all. Spectra were recorded at different temperatures for the spinning sample but again no changes were observed.

The spinning sideband profiles can be used to compare different values for the asymmetry and anisotropy. Figure 17 allows comparison between the experimental

spinning sideband heights, the iteratively fitted sideband heights and those calculated using the anisotropy and asymmetry values found when fitting the powder pattern.

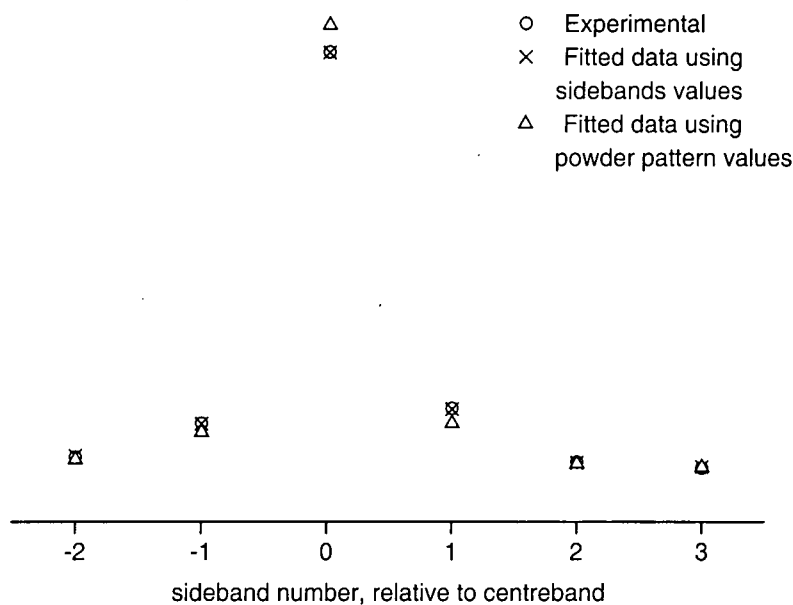


Figure 17: Experimental, fitted (iteratively to the experimental spinning sideband manifold) and simulated (using the values obtained by iteratively fitting the powder pattern)  $^{15}\text{N}$  spinning sideband manifolds for compound **16.2**. The experimental data were recorded on a CMX 200 spectrometer with a spinning speed of 1084 Hz, using a contact time of 1 ms, recycle delay of 5 s, decoupling field equivalent to 50 kHz and 7200 acquisitions.

The data obtained using the sideband manifold fit very well with the experimental points but the data calculated using the values from fitting the powder pattern do not compare as well, especially for the centreband intensity relative to the sidebands. It is thought that the values for the anisotropy and asymmetry obtained from spinning sideband analysis are more accurate than those obtained from powder pattern analysis. This is because the values obtained from the spinning sideband fit are a better fit to the powder pattern than the values obtained from the powder pattern are to the spinning sideband manifold.

**Variable Temperature  $^{15}\text{N}$   $T_{1\rho}$** 

Measurements of spin-lattice relaxation in the rotating frame ( $T_{1\rho}$ ), both with variable temperature and variable spin-lock field, can be used to give information about the rates of molecular-level motion. At the temperature where there is a minimum in  $T_{1\rho}$ , the spin-lock field can be related to the correlation time for motion and as the correlation time is linked to (for example) an exchange rate constant,  $T_{1\rho}$  can be used to probe exchange. Nitrogen-15  $T_{1\rho}$  measurements of compound **16.2** spinning at 3 kHz were carried out in the manner outlined in section 6.1.1 to see if internal rotation was occurring in the solid as it had been seen to do in solution. The results are shown in Table 9.

Temperature / °C	$^{15}\text{N}$ $T_{1\rho}$ / s
-57.4	0.032
-33.3	0.033
-9.3	0.034
6.7	0.034
24.9	0.039
46.8	0.043
70.8	0.040

Table 9: Variable temperature  $^{15}\text{N}$   $T_{1\rho}$  values of compound **16.2** spinning at 3 kHz with a  $\omega$  value of 36 kHz.

Table 9 shows that there is no significant trend of  $T_{1\rho}$  with temperature, suggesting that any motion that may be occurring is not in the range observable by this technique.

## 6.3 Conclusions

A range of compounds have been examined in the solid state using a variety of techniques:  $^{13}\text{C}$ ,  $^{15}\text{N}$ , NMR and powder XRD. Details of the solid-state structure for compound **3** have been determined using  $^{13}\text{C}$  and  $^{15}\text{N}$  NMR and powder XRD. Possibilities for the structure of compounds **2** and **5** have also been deduced from NMR spectra. The dyes themselves have been found to be amorphous, resulting in broad solid-state NMR and powder XRD spectra. Internal rotation, as discussed in chapter 4 in the solution state, does not appear to affect the solid-state spectra although it may be occurring.

## 6.4 References

- <sup>1</sup> J. R. Ascenco, L. H. Merwin, H. -P. Bai and J. C. Cherryman, unpublished.
- <sup>2</sup> M. M. Maricq and J. S. Waugh, *J. Chem. Phys.*, **70**, 3300 (1979).
- <sup>3</sup> A. C. Olivieri, *J. Magn. Reson. A*, **123**, 207 (1996).
- <sup>4</sup> P. Hodgkinson, personal communication.
- <sup>5</sup> R. K. Harris and A. C. Olivieri, *Progr. Nucl. Magn. Reson. Spectrosc.*, **24**, 435 (1992).
- <sup>6</sup> J. W. Visser, *J. Appl. Cryst.*, **2**, 89 (1969).
- <sup>7</sup> S. H. Alarcon, A. C. Olivieri, S. A. Carss, R. K. Harris, M. J. Zuriaga and G. A. Monti, *J. Magn. Reson. A*, **116**, 244 (1995).

## Chapter 7

### Future Work

At this point it is worth noting some future work that would be interesting and beneficial. This is by no means a conclusive list but contains the main issues to be considered.

In the determination of the activation parameters for compound **13**, only bandshape fitting was used. It would be useful to repeat the measurements using a higher field spectrometer, where the frequency separation is greater, so allowing SPI or SPT to be used. The wider the temperature range observed and the more methods used to measure rate constants, the more accurate the resulting activation parameters. It might also be possible to use different solvents to study compound **13**.

Compound **3** exhibits four clear peaks for the signal of NH7 at -40 °C. After recording a series of spectra at smaller temperature intervals, bandshape analysis and SPT can be used to obtain a series of rate constants and possibly activation parameters for rotation  $\beta$ .

Molecular modelling calculations were done using the HF/6-31G basis set. It would be more accurate to repeat the 'ground-state' calculation and transition-state search (now that the approximate position is known and the rotation is understood) using a higher basis set, or (even better) DFT, to take electron correlation effects into account.

More work can be done in the solid state on compounds **2**, **3** and **5** to attempt to identify the rotamers present. Variable temperature studies might allow the measurement of rotational energy barriers in the solid state. It may also be possible to deduce the number of molecules in the unit cell and more information about the crystal structure.

Powder XRD has proved very useful for compound **2** but more work has to be done to complete the solution of the crystal structure. Obtaining single-crystal information of all three compounds, **2**, **3** and **5**, would help with the interpretation of solid-state spectra. Although growing single crystals has been attempted unsuccessfully, there are many techniques and solvents that have not been tried so it is likely to be an achievable goal.

The spray study carried out with compound **18** shows a large background but suppression techniques can be attempted to enable more of the spectrum due to the dye to be observed and perhaps to make deductions about its conformation on the substrate.

---

## Appendix A

### Meetings/Research conferences Attended

- RSC Annual Congress, Young Researcher's Meeting, Durham University, UK.  
6<sup>th</sup> - 9<sup>th</sup> April 1998.
- 40<sup>th</sup> ENC, Orlando, Florida, USA.  
28<sup>th</sup> February - 4<sup>th</sup> March 1999.
- Avecia Ltd. Research Colloquia, Manchester, UK.  
30<sup>th</sup> June 2000.

### Work Presented

#### *Seminars/Oral presentations*

- Avecia Ltd.-presented update to research every three months for three years.
- Group talks-presented one per term on research or literature for three years.
- Durham University Chemistry Department Research Symposia, Durham University, UK.  
5<sup>th</sup> July 2000.  
'NMR Studies of Water-soluble Dyes'.
- Avecia Ltd. Research Colloquia, Manchester, UK.  
30<sup>th</sup> June 2000.  
'NMR and Computational Studies of Structure and Conformation of Ink-jet Magenta Dyes Which Contain Amino-substituted Triazine Rings'.

#### *Posters presented*

- 40<sup>th</sup> ENC, Orlando, USA.  
28<sup>th</sup> February - 4<sup>th</sup> March 1999.  
'NMR Studies of Exchange in Substituted Triazines'.  
Helen E. Birkett,\* Robin K. Harris and A. Margaret Chippendale.
- ICI / Durham University Chemistry Department Christmas Poster Competition, Durham University, UK.  
20<sup>th</sup> December 1999.  
'NMR Studies of Exchange in Substituted Triazines'.

## Papers published

- 'NMR studies of exchange between triazine rotamers'.  
Helen E. Birkett, Robin K. Harris, Paul Hodgkinson, Kathryn Carr, Michael H. Charlton, Julian C. Cherryman, A. Margaret Chippendale and Robert P. Glover.  
*Magn. Reson. Chem.*, **38**, 504 (2000).

## Work Outside the University

- Six three day visits to use the 600 MHz Chemagnetics spectrometer in the Physics Department, Warwick University, UK.
- Several trips to Avecia Ltd., Manchester, UK. to carry out synthesis and solution-state NMR experiments using a 400 MHz Bruker spectrometer.

## Appendix B

### Research Colloquia, Seminars and Lectures given by Invited Speakers

(\* denotes lectures attended)

(‡ denotes lectures organised personally for the Durham University Chemical Society)

#### 1997

- October 8 Prof. E. Atkins, Department of Physics, University of Bristol.  
'Advances in the control of architecture for polyamides: from nylons to genetically engineered silks to monodisperse oligoamides'.
- October 15 Dr. R. M. Ormerod, Department of Chemistry, Keele University.  
'Studying catalysis in action'.
- October 21 Prof. A. F. Johnson, IRC, Leeds.  
'Reactive processing of polymers: science and technology'.
- October 22 Prof. R. J. Puddephatt, University of Western Ontario.  
RSC Endowed Lecture.  
'Organoplatinum chemistry and catalysis'.
- October 23\* Prof. M. R. Bryce, Department of Chemistry, University of Durham.  
Inaugural lecture.  
'New tetrathiafulvalene derivatives in molecular, supramolecular and macromolecular chemistry: controlling the electronic properties of organic solids'.
- October 28 Dr. A. P. de Silva, The Queen's University, Belfast.  
'Luminescent signalling systems'.
- October 29 Prof. B. Peacock, University of Glasgow.  
'Probing chirality with circular dichroism'.
- November 5 Dr. Mimi Hii, Oxford University.  
'Studies of the Heck reaction'.
- November 11 Prof. V. Gibson, Imperial College, London.  
'Metallocene polymerisation'.
- November 12\* Dr. J. Frey, Department of Chemistry, Southampton University.  
'Spectroscopy of liquid interfaces: from bio-organic chemistry to atmospheric chemistry'.
- November 19\* Dr. G. Morris, Department of Chemistry, Manchester University.  
'Pulsed field gradient NMR techniques: Good news for the Lazy and DOSY'.

- 
- November 20 Dr. L. Spiccia, Monash University, Melbourne, Australia.  
'Polynuclear metal complexes'.
- November 25 Dr. R. Withnall, University of Greenwich.  
'Illuminated molecules and manuscripts'.
- November 26\* Prof. R. W. Richards, University of Durham.  
Inaugural lecture.  
'A random walk in polymer science'.
- December 2 Dr. C. J. Ludman, University of Durham.  
'Explosions'.
- December 3 Prof. A. P. Davis, Department of Chemistry, Trinity College Dublin.  
'Steroid-based frameworks for supramolecular chemistry'.
- December 10 Sir Gordon Higginson, former Professor of Engineering in Durham  
and retired Vice-chancellor of Southampton University.  
'1981 and all that'.
- December 10\* Prof. M. Page, Department of Chemistry, University of Huddersfield.  
'The mechanism and inhibition of beta lactamases'.

**1998**

- January 14\* Prof. D. Andrews, University of East Anglia.  
'Energy transfer and optical harmonics in molecular systems'.
- January 20\* Prof. J. Brooke, University of Lancaster.  
'What's in a formula? Some chemical controversies of the 19<sup>th</sup>  
century'.
- January 21 Prof. D. Cardin, University of Reading.  
Title unknown.
- January 27 Prof. R. Jordan, Department of Chemistry, University of Iowa, USA.  
'Cationic transition metal and main group metal alkyl complexes in  
olefin polymerisation'.
- January 28 Dr. S. Rannard, Coutaulds Coatings, Coventry.  
'The synthesis of dendrimers using highly selective chemical  
reactions'.
- February 3 Dr. J. Beacham, ICI Technology.  
'The chemical industry in the 21<sup>st</sup> century'.
- February 4\* Prof. P. Fowler, Department of Chemistry, Exeter University.  
'Classical and non-classical fullerenes'.

- 
- February 11 Prof. J. Murphy, Department of Chemistry, Strathclyde University.  
Title unknown.
- February 17\* Dr. S. Topham, ICI Chemicals and Polymers.  
'Perception of environmental risk; the river Tees, two different rivers'.
- February 18\* Prof. G. Hancock, Oxford University.  
'Surprises in the photochemistry of tropospheric ozone'.
- February 24 Prof. R. Ramage, University of Edinburgh.  
'The synthesis and folding of proteins'.
- February 25 Dr. C. Jones, Swansea University.  
'Low coordination arsenic and antimony chemistry'.
- March 4 Prof. T. C. B. McLeish, IRC of Polymer Science Technology, Leeds University.  
'The polymer physics of pyjama bottoms (or the novel rheological characterisation of long branching in entangled macromolecules)'.
- March 11\* Prof. M. J. Cook, Department of Chemistry, UEA.  
'How to make phthalocyanine films and what to do with them'.
- March 17 Prof. V. Rotello, University of Massachusetts, Amherst.  
'The interplay of recognition and redox processes – from flavoenzymes to devices'.
- March 18\* Dr. J. Evans, Oxford University.  
'Materials which contract on heating (from shrinking ceramics to bullet proof vests)'.
- October 7 Dr. S. Rimmer, Ctr Polymer, University of Lancaster.  
'New polymer colloids'.
- October 9 Prof. M. F. Hawthorne, Department of Chemistry and Biochemistry, UCLA, USA.  
RSC endowed lecture.  
Title unknown.
- October 21\* Prof. P. Unwin, Department of Chemistry, Warwick University.  
'Dynamic electrochemistry: small is beautiful'.
- October 23 Prof. J. C. Scaiano, Department of Chemistry, University of Ottawa, Canada.  
RSC endowed lecture.  
'In search of hypervalent free radicals'.
- October 26 Dr. W. Peirs, University of Calgary, Alberta, Canada.  
'Reactions of the highly electrophilic boranes  $\text{HB}(\text{C}_6\text{F}_5)_2$  and

- 
- B(C<sub>6</sub>F<sub>5</sub>)<sub>3</sub> with Zirconium and Tantalum based metallocenes’.
- October 27 Prof. A. Unsworth, University of Durham.  
In association with The North East Polymer Association.  
‘What’s a joint like this doing in a nice girl like you?’
- October 28\* Prof. J. P. S. Badyal, Department of Chemistry, University of Durham.  
Inaugural Lecture.  
‘Tailoring solid surfaces’.
- November 3 Dr. C. J. Ludman, Chemistry Department, University of Durham.  
‘Bonfire night lecture’.
- November 4 Dr. N. Kaltsoyannis, Department of Chemistry, UCL, London.  
‘Computational adventures in d and f element chemistry’.
- November 10 Dr. J. S. O. Evans, Department of Chemistry, University of Durham.  
‘Shrinking materials’.
- November 11 Dr. M. Wills, Department of Chemistry, University of Warwick.  
‘New methodology for the asymmetric transfer hydrogen of ketones’.
- November 12 Prof. S. Loeb, University of Windsor, Ontario, Canada.  
‘From macrocycles to metallo-supramolecular chemistry’.
- November 17 Dr. J. McFarlane.  
‘Nothing but sex and sudden death!’.
- November 18 Dr. R. Cameron, Department of Materials Science and Metallurgy, Cambridge University.  
‘Biodegradable polymers’.
- November 24 Dr. B. G. Davis, Department of Chemistry, University of Durham.  
‘Sugars and enzymes’.
- December 1 Prof. N. Billingham, University of Sussex.  
In association with The North East Polymer Association.  
‘Plastics in the Environment – boon or bane’.
- December 2 Dr. M. Jaspers, Department of Chemistry, University of Aberdeen.  
‘Bioactive compounds isolated from marine invertebrates and cyanobacteria’.
- December 9\* Dr. M. Smith, Department of Chemistry, Warwick University.  
‘Multinuclear solid-state magnetic resonance studies of nanocrystalline oxides and glasses’.

**1999**

- January 19 Dr. J. Mann, University of Reading.  
'The elusive magic bullet and attempts to find it'.
- January 20\* Dr. A. Jones, Department of Chemistry, University of Edinburgh.  
'Luminescence of large molecules: from conducting polymers to coral reefs'.
- January 27\* Prof. K. Wade, Department of Chemistry, University of Durham.  
'Forsight or hindsight? some borane lessons and loose ends'.
- February 3 Dr. C. Schofield, University of Oxford.  
'Studies on the stereoelectronics of enzyme catalysis'.
- February 9\* Prof. D. J. Cole-Hamilton, St. Andrews University.  
'Chemistry and the future of life of Earth'.
- February 10\* Dr. C. Bain, University of Oxford.  
'Surfactant adsorption and marangoni flow at expanding liquid surfaces'.
- February 17\* Dr. B. Horrocks, Department of Chemistry, University of Newcastle.  
'Microelectrode techniques for the study of enzymes and nucleic acids at interfaces'.
- February 23 Dr. C. Viney, Herriot-Watt.  
'Spiders, slugs and mutant bugs'.
- February 24\* Dr. A-K. Duhume, University of York.  
'Bioinorganic aspects of molybdenum transport in nitrogen-fixing bacteria'.
- March 3 Prof. B. Gilbert, Department of Chemistry, University of York.  
'Biomolecular damage by free radicals: new insights through ESR spectroscopy'.
- March 9 Dr. M. Warhurst, Chemical policy issues, Friends of the Earth.  
'Is the chemical industry sustainable'.
- March 10 Dr. A. Harrison, Department of Chemistry, University of Edinburgh.  
'Designing model magnetic materials'.
- March 17 Dr. J. Robertson, University of Oxford.  
'Recent developments in the synthesis of heterocyclic natural products'.
- May 11 Dr. J. Sodeau, University of East Anglia.  
'Ozone holes and ozone hills'.

- 
- May 12 Dr. D. Bruce, University of Exeter.  
'The synthesis and characterisation of liquid-crystalline transition metal complexes'.
- October 12<sup>\*‡</sup> Dr. S. Beckett, Nestle.  
'Chocolate for the next Millennium'.
- October 13 Prof. G. Fleet, University of Oxford.  
'Sugar lactone and amino acids'.
- October 19 Prof. K. Gloe, TU Dresden, Germany.  
'Tailor made molecules for the selective binding of metal ions'.
- October 20<sup>\*</sup> Prof. S. Lincoln, University of Adelaide.  
'Aspects of complexation and supramolecular chemistry'.
- October 25 Prof. S. Collines, University of Waterloo, Canada.  
'Methacrylate polymerisation using Zirconium enolate initiators: polymerisation mechanisms and control of polymer tacticity'.
- October 26<sup>\*‡</sup> Dr. D. Hughes, AstraZeneca.  
'Perspectives in agrochemistry'.
- October 27<sup>\*</sup> Dr. C. Braddock, Imperial College.  
'Novel catalysts for atom economic transformations'.
- November 3<sup>\*</sup> Prof. D. W. Smith, University of Waikato, NZ.  
'The strengths of C-C and C-H bonds in organic and organometallic molecules: empirical, semi-empirical and ab initio calculations'.
- November 10<sup>\*</sup> Dr. I. Samuel, Department of Physics, University of Durham.  
'Improving organic light emitting diodes by molecular, optical and device design'.
- November 16<sup>\*‡</sup> Prof. A. Holmes.  
'Conjugated polymers for the market place'.
- November 17<sup>\*</sup> Dr. J. Rourke, University of Warwick.  
'C-H activation induced by water'.
- November 18 Dr. G. Siligardi, Kings College London.  
'The use of circular dichroism to detect and characterise biomolecular interactions in solution'.
- November 23<sup>\*‡</sup> Prof. B. Caddy.  
'Trace evidence – a challenge for the forensic scientist'.
- November 24<sup>\*</sup> Prof. T. Jones, Imperial College.  
'Atomic and molecular control of inorganic and organic semiconductor thin films'.

- November 30<sup>\*‡</sup> Rev. R. Lancaster.  
'Principles and practice'.
- December 8 Prof. D. Crout, Department of Chemistry, University of Warwick.  
'More than simply sweet: carbohydrates in medicine and biology'.
- 2000**
- January 12 Prof. D. Haddleton, Department of Chemistry, University of Warwick.  
'Atom transfer polymerisation – what's all the hype about?'.
- January 19 Dr. P. R. Fielden, UMIST.  
'Miniaturised chemical analysis (lab-on-a-chip): functional or merely fashionable?'.
- January 25<sup>\*‡</sup> Prof. B. Meijer.  
'From supramolecular architecture towards functional materials'.
- January 26 Prof. S. Flisch, University of Edinburgh.  
'The challenges involved in protein glycosylation – synthesis of glycan chains and selective attachment to proteins'.
- February 2 C. Wilson, Head of crystallography, ISIS, Rutherford Appleton Laboratory.  
'Protons in motion? Neutron diffraction studies of hydrogen atoms in organic crystal structures'.
- February 9<sup>\*</sup> Dr. S. Moratti, University of Cambridge.  
'Shape and stereoselectivity in polymers'.
- February 15<sup>\*‡</sup> Prof. D. Phillips.  
'A little light relief'.
- February 16 Prof. Kocienski, University of Glasgow.  
'Asymmetric synthesis using planar chiral TT-allyl cationic complexes'.
- February 23 Dr. N. Clarke, UMIST.  
'The flow of polymer blends'.
- March 1 Prof. D. Tildsley, Unilever.  
'Computer simulation of interfaces: fact and friction'.
- March 7<sup>\*</sup> Prof. Motherwell, University College, London.  
'Curiosity and simplicity – essential ingredients for the discovery of new reactions'.

- 
- March 8 Prof. J. Courtieu, Universite de Paris-Sud, Orsay.  
'Chiral recognition through NMR in liquid crystal solvents: an order affair'.
- March 9 Dr. A. Fairbanks, Dyson-Perrins Laboratory, Oxford.  
'Selectivity in glycoside formation'.
- March 20 Prof. S. Marder, University of Arizona.  
'Design of molecules for two-photon absorption and their application to 3D polymerisation and imaging'.
- March 21 Prof. E. Rizzardo, CSIRO Mol. Sci. Victoria, Australia.  
'Designed polymers by free radical addition-fragmentation processes'.
- May 5 Prof. R. Hochstrasser, University of Pennsylvania, USA.  
'Ultrafast molecular and protein dynamics seen through their vibrations'.

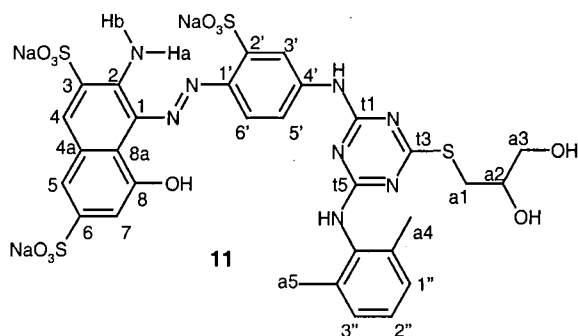
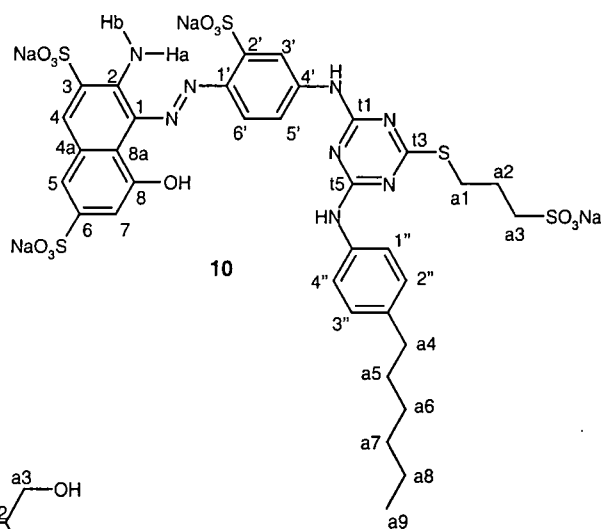
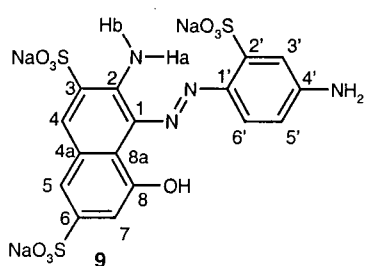
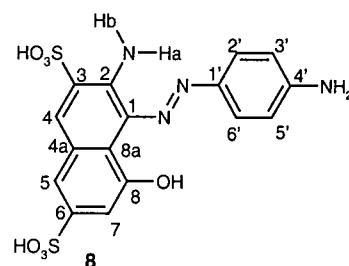
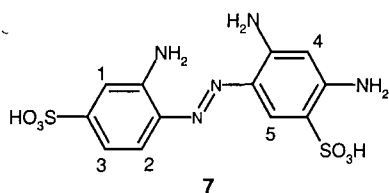
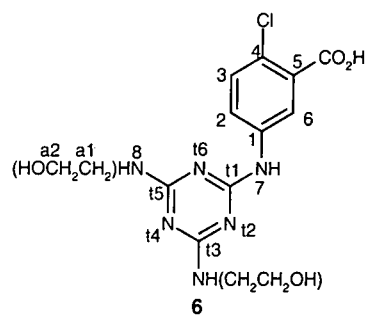
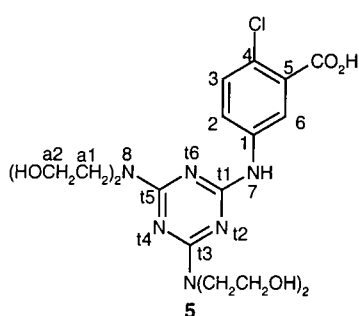
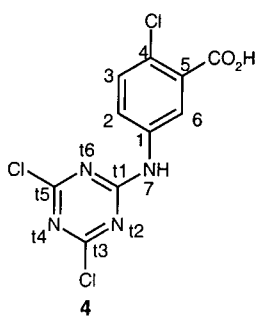
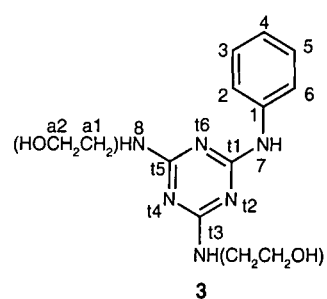
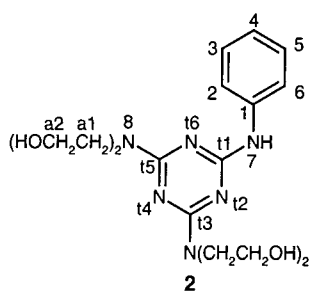
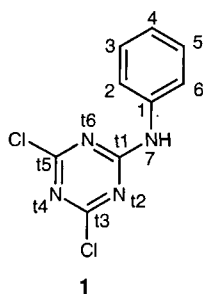
## Appendix C

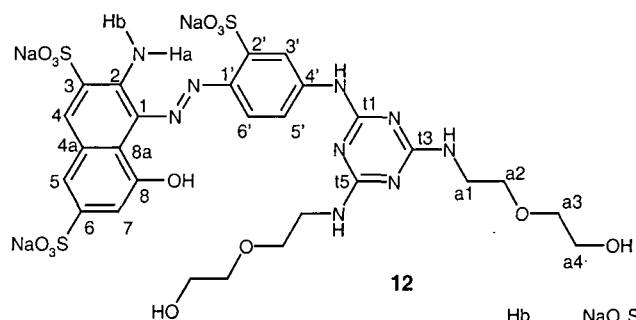
	1''	2''	3''	4''	a1	a2	a3	a4	a5	a6	a7	a8	a9
<b>10</b> rt +93 °C	7.61 7.60	7.18 7.14	7.18 7.14	7.61 7.60	3.27br 3.27	2.00br 2.04	2.50-2.62br 2.61	1.57br 2.59	1.57br 1.59	1.25br 1.28			0.83br 0.82
<b>11</b> rt +93 °C	7.16-7.20 7.11				br, impure sample br, impure sample								
<b>12</b> rt +93 °C					3.40-3.61 3.48-3.66								
<b>13</b> rt +93 °C					4.55 3.67	2.81 2.81							
<b>14</b> rt +93 °C	7.46 7.53	7.09 and 7.24 7.06 and 7.19		7.14		2.50-4.70 2.98-4.59br		1.19br 1.17	1.19br 1.17	1.19br 1.17	2.45 2.26		
<b>15</b> rt +93 °C					3.70br 3.75					3.31-3.52br 3.4-3.6			
<b>16.1</b> rt +93 °C					3.61-3.69br 3.63-3.69	2.81br 2.84							
<b>17</b> rt +93 °C					3.92-4.08 3.63-3.66								

br indicates peaks that are broad.  
First order analysis is assumed.

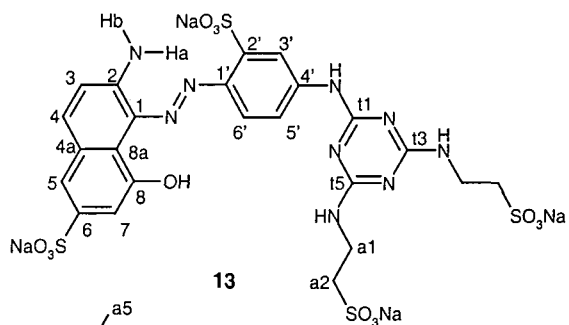
Figure 1: Side-chain  $^1\text{H}$  chemical shifts in ppm of a range of compounds in a  $0.007 \pm 0.001\text{M}$  solution in  $d_6$ -DMSO referenced to TMS all recorded on a Varian Unity Plus 300 spectrometer.

## Appendix D

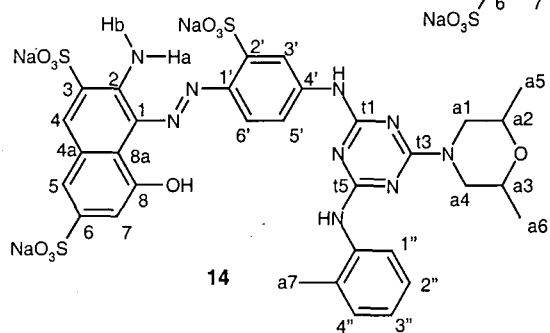




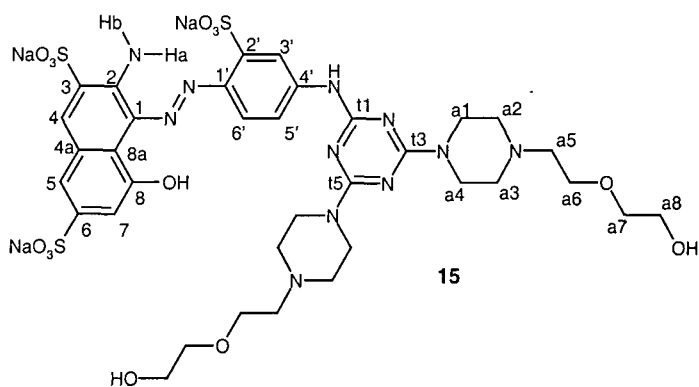
12



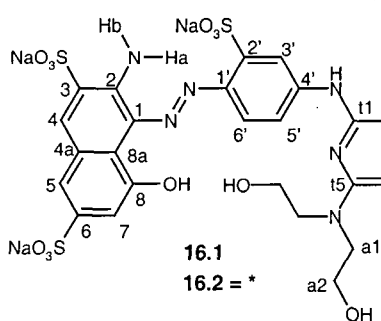
13



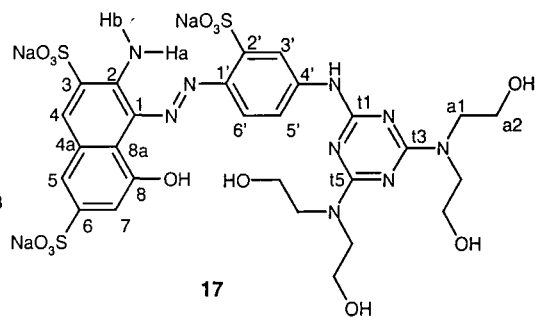
14



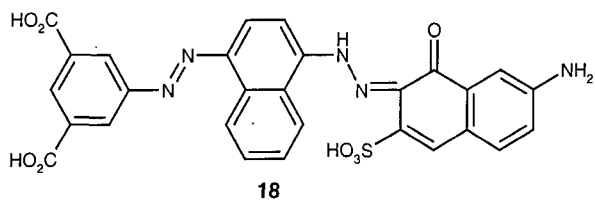
15



16.2 = \*



17



18

*When you get to the end of your rope, tie a knot and hang on.*

Franklin D. Roosevelt

